Magnetic imaging of spin waves and magnetic phase transitions with nitrogen-vacancy centers in diamond

Bertelli, I.

MAGNETIC IMAGING OF SPIN WAVES AND MAGNETIC PHASE TRANSITIONS WITH NITROGEN-VACANCY CENTERS IN DIAMOND

MAGNETIC IMAGING OF SPIN WAVES AND MAGNETIC PHASE TRANSITIONS WITH NITROGEN-VACANCY CENTERS IN DIAMOND

Proefschrift

ter verkrijging van
de graad van doctor aan de Universiteit Leiden,
op gezag van de rector magnificus prof. dr. ir. H. Bijl,
volgens besluit van het college voor promoties,
te verdedigen op woensdag 24 november 2021
klokke 16:15 uur

door

Iacopo BERTELLI

geboren te Modena (Italië)
in 1992

Promotor:

Prof. dr. J. Aarts

Co-promotor:

Dr. T. van der Sar	Technische Universiteit Delft

Promotiecommissie:

Prof. dr. Y. M. Blanter	Technische Universiteit Delft
Prof. dr. A. Chumak	University of Vienna, Austria
Dr. S. Conesa-Boj	Technische Universiteit Delft
Prof. dr. V. Jacques	University of Montpellier, France
Prof. dr. E. R. Eliel	
Prof. dr. ir. T. H. Oosterkamp	

Nederlandse Organisatie voor Wetenschappelijk Onderzoek

Printed by: Gildeprint, Enschede

About the cover: Artist's impression of a diamond, containing a nitrogen-vacancy (NV) center (which emits red light), probing a spin wave

Cover design: Iacopo Bertelli

Casimir PhD Series, Delft-Leiden 2021-39

ISBN 978-90-8593-505-6

An electronic version of this dissertation is available at
http://openaccess.leidenuniv.nl/.

Contents

1 Introduction **1**

1.1 Beyond conventional electronics: Magnonics . . . 1

1.1.1 Spin waves . . . 2

1.1.2 Spin-wave detection . . . 2

1.2 The nitrogen-vacancy center in diamond . . . 3

1.3 Thesis outline . . . 3

References . . . 5

2 NV magnetometry **17**

2.1 NV centers in diamond . . . 18

2.1.1 Electronic structure . . . 18

2.1.2 Spin-dependent optical properties . . . 18

2.1.3 Detecting NV centers: Confocal microscopy . . . 19

2.2 Magnetic field sensing with NV centers . . . 20

2.2.1 NV center in a magnetic field . . . 21

2.2.2 Electron spin resonance . . . 21

2.2.3 Detecting oscillating fields: the rotating frame . . . 23

2.2.4 Rabi oscillations . . . 25

2.2.5 T_1 Relaxometry . . . 26

2.2.6 Controlling NV centers: Setup electronics . . . 28

References . . . 29

3 Spin-wave theory **35**

3.1 Stray field of a planar magnetization . . . 36

3.2 Spin-wave dispersion . . . 37

3.2.1 Magnetization dynamics: Landau-Lifshitz-Gilbert equations . . . 37

3.2.2 Spin-wave dispersion and susceptibility . . . 40

3.2.3 Static field with an out-of-plane component . . . 43

3.3 Spin-wave excitation . . . 45

3.3.1 Inductive excitation of spin-waves . . . 45

3.4 Stray field of a spin wave . . . 48

3.5 Spin-wave detection with NV magnetometry . . . 49

3.5.1 Detecting coherent spin waves: Rabi frequency enhancement . . . 49

3.5.2 Magnetic noise generated by thermally-excited spin waves . . . 51

References . . . 53

4 Magnetic resonance imaging of spin-wave transport and interference in a magnetic insulator 57
4.1 Introduction . . . 58
4.2 Results . . . 59
4.3 Discussion . . . 64
4.4 Materials and Methods . . . 67
4.4.1 Sample Fabrication . . . 67
4.4.2 Measurement setup . . . 67
4.4.3 NV magnetometry . . . 68
4.4.4 Wavelength of the spin waves driving NV Rabi oscillations . . . 68
4.5 Supplementary Material . . . 68
4.5.1 Determination of the NV-YIG distance . . . 68
4.5.2 Determination of M_s and thickness of YIG with VNA measurements . . . 69
4.5.3 Effect of the spin wave stray field on the NV spins . . . 70
References . . . 81

5 Imaging spin-wave damping underneath metals using electron spins in diamond 85
5.1 Introduction . . . 86
5.2 Results . . . 86
5.3 Discussion . . . 93
5.4 Materials and Methods . . . 93
5.4.1 Sample fabrication . . . 93
5.4.2 NV-based imaging of spin waves . . . 93
5.5 Supplementary Material . . . 95
5.5.1 Eddy-current contribution to spin-wave damping . . . 95
5.5.2 Data fitting procedures . . . 102
References . . . 105

6 Sensing chiral magnetic noise via quantum impurity relaxometry 109
6.1 Introduction . . . 110
6.2 Results . . . 110
6.3 Discussion . . . 114
6.4 Methods . . . 114
6.5 Additional measurements . . . 115
References . . . 118

7 Magnetic imaging and statistical analysis of the metamagnetic phase transition of FeRh 121
7.1 Introduction . . . 122
7.2 Results . . . 123
7.3 Conclusions . . . 128
7.4 Materials and Methods . . . 130
7.4.1 Sample Fabrication . . . 130
7.4.2 Measurement Setup . . . 131
7.4.3 NV magnetometry . . . 131

7.5 Supplementary Material 132
References 133

8 Conclusion **137**
8.1 Conclusion 138
8.2 Outlook 138

Summary **141**

Samenvatting **143**

Sommario **145**

Acknowledgements **147**

Curriculum Vitæ **149**

List of Publications **151**

1

INTRODUCTION

1.1. BEYOND CONVENTIONAL ELECTRONICS: MAGNONICS

In the last decades, the ever-increasing technological needs have been pushing electronic devices towards their speed and size limits [1]. Therefore, researchers have tried to establish new technologies beyond conventional electronics - which relies on the diffusive motion of electric charges to process and transport information. One field that emerged is that of *spintronics* (spin-electronics), established with the discovery of the giant magneto-resistance (GMR) [2, 3]. The central idea of spintronics is that information can be encoded in the spin of an electron [4–6]. Spintronics has already delivered a number of devices that find commercial applications, including GMR-based spin valves [4], magnetic tunnel junctions based on the giant tunnel magneto-resistance [7, 8] (TMR) as read heads in storage devices [9]. Recently, the magnetic random-access memory (MRAM) based on spin-transfer [10–14] or spin-orbit torques [15–19] (STT and SOT, respectively), started replacing conventional static and dynamic random-access memories (SRAM and DRAM, respectively), in certain applications [20–22].

Compared to the spin-polarized electric currents used in most of these applications, an advantage of pure spin currents is that the motion of spins is decoupled from the motion of charges. Such diffusive charge transport is characterized by electron scattering, which leads to dissipative effects known as Joule (or Ohmic) heating [23]. The transport of pure spin information can be achieved in magnetic insulators such as yttrium-iron garnet (YIG), where coherent spin excitations (spin waves, Fig. 1.1) can propagate with ultralow dissipation [24] (i.e. with propagation distance up to several millimeters and long spin-wave coherence times [25]). The branch of spintronics that deals with information transport and processing based on spin waves is called *magnonics*, from the name of the quanta of spin waves, the magnons [23, 26].

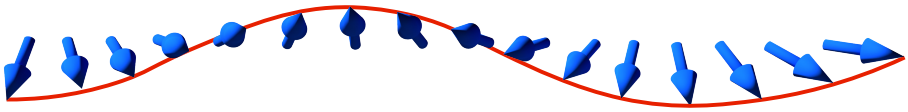

Figure 1.1: Spin wave. In a magnetic insulator, the spins (localized at lattice sites) precess around the static magnetization. The precession of neighbouring spins with a phase difference corresponds to a travelling signal, the *spin* wave.

1.1.1. SPIN WAVES

Spin waves were first predicted by Bloch almost 100 years ago as collective excitations of the spins in a ferromagnet [27]. Information transport and processing based on spin waves hold great promises [28–32], because of the several key properties of spin waves:

- Spin-wave frequencies range from the GHz to the THz regime [24], thus being well matched to the frequency of current electronic devices, but leaving plenty of room for further speed up.
- Spin-wavelengths can be as small as few nanometers, limited only by the lattice constant of the magnetic material [33], thus allowing device miniaturization.
- Unlike spin-polarized electrons, that retain information only up to the spin diffusion length (typically few tens of nanometers in metallic magnets), spin waves can propagate coherently over distances up to several millimeters [25].
- Because of their wavelike nature, information can be encoded in the phase of spin waves [34], enabling non-Boolean logic [35–39]. Parallel operation at different frequencies (i.e. multiplexing) is also possible [40–43].

Additionally, spin waves are interesting from a fundamental point of view because they show a wealth of non-linear [44–46] and non-reciprocal [47–53] effects, and they can show peculiar phenomena such as magnon condensation [54–57] and magnon supercurrents [56, 58–60].

1.1.2. SPIN-WAVE DETECTION

Because of the large interest in the physics of spin waves and their applications in information technology, many techniques have been develop to study spin waves. Among the non-local (i.e. without imaging capabilities) techniques, the most common are broadband-FMR [61], inelastic neutron scattering [62–65], the inverse spin-Hall effect [66–72] and, recently, superconducting qubits [73–76]. The leading techniques to image spin waves include Brillouin light scattering [77], scattering of x-rays [78, 79], thermal imaging [80, 81], and imaging based on the magneto-optical Kerr effect [82–84].

Because studying spin waves in magnonic devices is so important, in this thesis we develop a new technique to image spin waves relying on the detection of the spin-wave stray field with a quantum sensor [85]. Besides the high sensitivity that can be achieved

by such a sensor [86], our method can image spin waves propagating underneath metallic electrodes [87], such as those routinely used to excite spin waves inductively. The sensor we use is the electron spin localized at lattice defects in diamond, known as nitrogen-vacancy (NV) centers.

1.2. THE NITROGEN-VACANCY CENTER IN DIAMOND

Nitrogen-vacancy centers are color centers in diamond with spin-dependent optical properties [88–90]. The absence of photobleaching and the long spin lifetime at room temperature, together with the optical addressability of its spin state, have made this defect one of the most studied in the 25 years after the first report of optically detected magnetic resonance (ODMR) of individual NV centers at room temperature [91]. The applications of NV centers in quantum science and technology [92] include quantum communication [93–100], quantum computation and simulation [101–108], and quantum sensing [109]. As a quantum sensor, the NV spin has been employed to study a wide variety of living [110–115] and condensed matter systems [116–120], thanks to the combination of small size, wide operating temperature and frequency range [121], and high sensitivity to stress [122–124], temperature [110, 125, 126], electric [127, 128] and magnetic fields [129–137].

In this thesis, we use NV centers as magnetometers to characterize magnetic stray fields. A significant part of this thesis is focused on probing spin waves. To do so, we study how the NV spin dynamics is driven by the GHz spin-wave stray fields. In addition, we explore magnetic phase transitions by characterizing the stray field-dependent energy structure of the NV centers.

1.3. THESIS OUTLINE

Chapter 2 provides an introduction to magnetometry with NV centers in diamond. We start with a short description of the NV's electronic structure and spin-dependent optical properties. Then, we focus on the detection of magnetic fields, showing how to characterize static and oscillating magnetic fields, both coherent and incoherent, using NV centers.

In Chapter 3 we discuss spin waves theoretically, and derive several useful equations, including the spin-wave dispersion and the coupling between the spin-wave stray fields and the NV spin, that are necessary to understand the following chapters.

Being able to quantitatively detect coherent spin waves via their microwave stray field is an alternative and complementary way of studying spin waves compared to existing techniques. In Chapter 4 we establish a new method to image coherent spin waves using ensembles of NV spins, that allows to extract the amplitude of the spin-wave precession, and we show that imaging spin waves in monolayer magnets is within reach of our sensitivity.

Using this newly introduced technique and its ability to image spin waves underneath

metals, in Chapter 5 we characterize the excess damping caused by metallic electrodes on spin-wave propagation. We find a damping increase by roughly two orders of magnitude, which is well explained by a theoretical model we introduce.

The magnetic noise generated by a system is related to its excitations via the fluctuation-dissipation theorem, thus providing valuable insights into the spin-spin correlations, which characterize a particular magnetic phase. In Chapter 6 we detect magnetic field fluctuations generated by thermal spin waves, finding a good agreement with the model introduced in chapter 3.

One of the key strengths of NV magnetometry, i.e. its locality, can also be a drawback when addressing global properties of a system, such as the temperature of a phase transition. In Chapter 7 we apply statistical tools to overcome this challenge, focusing on the temperature-driven metamagnetic phase transition of FeRh, between the antiferro- and ferromagnetic states.

REFERENCES

[1] S. E. Thompson and S. Parthasarathy, *Moore's law: the future of Si microelectronics,* Materials Today **9**, 20 (2006).

[2] M. N. Baibich, J. M. Broto, A. Fert, F. N. V. Dau, F. Petroff, P. Etienne, G. Creuzet, A. Friederich, and J. Chazelas, *Giant Magnetoresistance of (001)Fe/(001)Cr Magnetic Superlattices,* Physical Review Letters **61**, 2472 (1988).

[3] G. Binasch, P. Grünberg, F. Saurenbach, and W. Zinn, *Enhanced magnetoresistance in layered magnetic structures with antiferromagnetic interlayer exchange,* Physical Review B **39**, 4828 (1989).

[4] I. Žutić, J. Fabian, and S. D. Sarma, *Spintronics: Fundamentals and applications,* Reviews of Modern Physics **76**, 323 (2004).

[5] S. Bader and S. Parkin, *Spintronics,* Annual Review of Condensed Matter Physics **1**, 71 (2010).

[6] A. Hirohata, K. Yamada, Y. Nakatani, L. Prejbeanu, B. Diény, P. Pirro, and B. Hillebrands, *Review on spintronics: Principles and device applications,* Journal of Magnetism and Magnetic Materials **509**, 166711 (2020).

[7] T. Miyazaki and N. Tezuka, *Giant magnetic tunneling effect in Fe/Al2O3/Fe junction,* Journal of Magnetism and Magnetic Materials **139**, L231 (1995).

[8] J. S. Moodera, L. R. Kinder, T. M. Wong, and R. Meservey, *Large Magnetoresistance at Room Temperature in Ferromagnetic Thin Film Tunnel Junctions,* Physical Review Letters **74**, 3273 (1995).

[9] J. M. Daughton, *GMR applications,* Journal of Magnetism and Magnetic Materials **192**, 334 (1999).

[10] J. C. Slonczewski, *Current-driven excitation of magnetic multilayers,* Journal of Magnetism and Magnetic Materials **159**, L1 (1996).

[11] L. Berger, *Emission of spin waves by a magnetic multilayer traversed by a current,* Physical Review B **54**, 9353 (1996).

[12] J. A. Katine, F. J. Albert, R. A. Buhrman, E. B. Myers, and D. C. Ralph, *Current-Driven Magnetization Reversal and Spin-Wave Excitations in Co/Cu/Co pillars,* Physical Review Letters **84**, 3149 (2000).

[13] T. Kawahara, K. Ito, R. Takemura, and H. Ohno, *Spin-transfer torque RAM technology: Review and prospect,* Microelectronics Reliability **52**, 613 (2012).

[14] A. V. Khvalkovskiy, D. Apalkov, S. Watts, R. Chepulskii, R. S. Beach, A. Ong, X. Tang, A. Driskill-Smith, W. H. Butler, P. B. Visscher, D. Lottis, E. Chen, V. Nikitin, and M. Krounbi, *Basic principles of STT-MRAM cell operation in memory arrays,* Journal of Physics D: Applied Physics **46**, 074001 (2013).

[15] K. Ando, S. Takahashi, K. Harii, K. Sasage, J. Ieda, S. Maekawa, and E. Saitoh, *Electric Manipulation of Spin Relaxation Using the Spin Hall Effect,* Physical Review Letters **101**, 036601 (2008).

[16] I. M. Miron, G. Gaudin, S. Auffret, B. Rodmacq, A. Schuhl, S. Pizzini, J. Vogel, and P. Gambardella, *Current-driven spin torque induced by the Rashba effect in a ferromagnetic metal layer,* Nature Materials **9**, 230 (2010).

[17] I. M. Miron, K. Garello, G. Gaudin, P.-J. Zermatten, M. V. Costache, S. Auffret, S. Bandiera, B. Rodmacq, A. Schuhl, and P. Gambardella, *Perpendicular switching of a single ferromagnetic layer induced by in-plane current injection,* Nature **476**, 189 (2011).

[18] L. Liu, C.-F. Pai, Y. Li, H. W. Tseng, D. C. Ralph, and R. A. Buhrman, *Spin-Torque Switching with the Giant Spin Hall Effect of Tantalum,* Science **336**, 555 (2012).

[19] A. Manchon, J. Železný, I. Miron, T. Jungwirth, J. Sinova, A. Thiaville, K. Garello, and P. Gambardella, *Current-induced spin-orbit torques in ferromagnetic and antiferromagnetic systems,* Reviews of Modern Physics **91**, 035004 (2019).

[20] A. D. Kent and D. C. Worledge, *A new spin on magnetic memories,* Nature Nanotechnology **10**, 187 (2015).

[21] S. Bhatti, R. Sbiaa, A. Hirohata, H. Ohno, S. Fukami, and S. N. Piramanayagam, *Spintronics based random access memory: a review,* Materials Today **20**, 530 (2017).

[22] B. Dieny, I. L. Prejbeanu, K. Garello, P. Gambardella, P. Freitas, R. Lehndorff, W. Raberg, U. Ebels, S. O. Demokritov, J. Akerman, A. Deac, P. Pirro, C. Adelmann, A. Anane, A. V. Chumak, A. Hirohata, S. Mangin, S. O. Valenzuela, M. C. Onbaşlı, M. D'Aquino, G. Prenat, G. Finocchio, L. Lopez-Diaz, R. Chantrell, O. Chubykalo-Fesenko, and P. Bortolotti, *Opportunities and challenges for spintronics in the microelectronics industry,* Nature Electronics **3**, 446 (2020).

[23] A. V. Chumak, V. I. Vasyuchka, A. A. Serga, and B. Hillebrands, *Magnon spintronics,* Nature Physics **11**, 453 (2015).

[24] V. Cherepanov, I. Kolokolov, and V. L'vov, *The saga of YIG: Spectra, thermodynamics, interaction and relaxation of magnons in a complex magnet,* Physics Reports **229**, 81 (1993).

[25] A. A. Serga, A. V. Chumak, and B. Hillebrands, *YIG magnonics,* Journal of Physics D: Applied Physics **43**, 264002 (2010).

[26] V. V. Kruglyak, S. O. Demokritov, and D. Grundler, *Magnonics,* Journal of Physics D: Applied Physics **43**, 264001 (2010).

[27] F. Bloch, *Zur Theorie des Ferromagnetismus,* Zeitschrift für Physik **61**, 206 (1930).

[28] G. Csaba, Á. Papp, and W. Porod, *Perspectives of using spin waves for computing and signal processing,* Physics Letters A **381**, 1471 (2017).

[29] A. Mahmoud, F. Ciubotaru, F. Vanderveken, A. V. Chumak, S. Hamdioui, C. Adelmann, and S. Cotofana, *Introduction to spin wave computing,* Journal of Applied Physics **128**, 161101 (2020).

[30] A. Papp, W. Porod, and G. Csaba, *Nanoscale neural network using non-linear spin-wave interference,* (2020), arXiv:2012.04594 .

[31] Q. Wang, A. V. Chumak, and P. Pirro, *Inverse-design magnonic devices,* Nature Communications **12**, 2636 (2021).

[32] A. Barman, G. Gubbiotti, S. Ladak, A. O. Adeyeye, M. Krawczyk, J. Gräfe, C. Adelmann, S. Cotofana, A. Naeemi, V. I. Vasyuchka, B. Hillebrands, S. A. Nikitov, H. Yu, D. Grundler, A. Sadovnikov, A. A. Grachev, S. E. Sheshukova, J.-Y. Duquesne, M. Marangolo, C. Gyorgy, W. Porod, V. E. Demidov, S. Urazhdin, S. Demokritov, E. Albisetti, D. Petti, R. Bertacco, H. Schulteiss, V. V. Kruglyak, V. D. Poimanov, A. K. Sahoo, J. Sinha, H. Yang, M. Muenzenberg, T. Moriyama, S. Mizukami, P. Landeros, R. A. Gallardo, G. Carlotti, J.-V. Kim, R. L. Stamps, R. E. Camley, B. Rana, Y. Otani, W. Yu, T. Yu, G. E. W. Bauer, C. H. Back, G. S. Uhrig, O. V. Dobrovolskiy, S. van Dijken, B. Budinska, H. Qin, A. Chumak, A. Khitun, D. E. Nikonov, I. A. Young, B. Zingsem, and M. Winklhofer, *The 2021 Magnonics Roadmap,* Journal of Physics: Condensed Matter **33**, 413001 (2021).

[33] T. Balashov, P. Buczek, L. Sandratskii, A. Ernst, and W. Wulfhekel, *Magnon dispersion in thin magnetic films,* Journal of Physics: Condensed Matter **26**, 394007 (2014).

[34] K.-S. Lee and S.-K. Kim, *Conceptual design of spin wave logic gates based on a Mach–Zehnder-type spin wave interferometer for universal logic functions,* Journal of Applied Physics **104**, 053909 (2008).

[35] G. Csaba, A. Papp, and W. Porod, *Spin-wave based realization of optical computing primitives,* Journal of Applied Physics **115**, 17C741 (2014).

[36] S. Klingler, P. Pirro, T. Brächer, B. Leven, B. Hillebrands, and A. V. Chumak, *Design of a spin-wave majority gate employing mode selection,* Applied Physics Letters **105**, 152410 (2014).

[37] T. Fischer, M. Kewenig, D. A. Bozhko, A. A. Serga, I. I. Syvorotka, F. Ciubotaru, C. Adelmann, B. Hillebrands, and A. V. Chumak, *Experimental prototype of a spin-wave majority gate,* Applied Physics Letters **110**, 152401 (2017).

[38] G. Talmelli, T. Devolder, N. Träger, J. Förster, S. Wintz, M. Weigand, H. Stoll, M. Heyns, G. Schütz, I. P. Radu, J. Gräfe, F. Ciubotaru, and C. Adelmann, *Reconfigurable submicrometer spin-wave majority gate with electrical transducers,* Science Advances **6**, eabb4042 (2020).

[39] Q. Wang, M. Kewenig, M. Schneider, R. Verba, F. Kohl, B. Heinz, M. Geilen, M. Mohseni, B. Lägel, F. Ciubotaru, C. Adelmann, C. Dubs, S. D. Cotofana, O. V. Dobrovolskiy, T. Brächer, P. Pirro, and A. V. Chumak, *A magnonic directional coupler for integrated magnonic half-adders,* Nature Electronics **3**, 765 (2020).

[40] A. Khitun, *Multi-frequency magnonic logic circuits for parallel data processing,* Journal of Applied Physics **111**, 054307 (2012).

[41] K. Vogt, F. Y. Fradin, J. E. Pearson, T. Sebastian, S. D. Bader, B. Hillebrands, A. Hoffmann, and H. Schultheiss, *Realization of a spin-wave multiplexer,* Nature Communications **5**, 3727 (2014).

[42] Q. Wang, P. Pirro, R. Verba, A. Slavin, B. Hillebrands, and A. V. Chumak, *Reconfigurable nanoscale spin-wave directional coupler,* Science Advances **4**, e1701517 (2018).

[43] F. Heussner, G. Talmelli, M. Geilen, B. Heinz, T. Brächer, T. Meyer, F. Ciubotaru, C. Adelmann, K. Yamamoto, A. A. Serga, B. Hillebrands, and P. Pirro, *Experimental Realization of a Passive Gigahertz Frequency-Division Demultiplexer for Magnonic Logic Networks,* Physica Status Solidi (R) **14**, 1900695 (2020).

[44] P. Krivosik and C. E. Patton, *Hamiltonian formulation of nonlinear spin-wave dynamics: Theory and applications,* Physical Review B **82**, 184428 (2010).

[45] A. V. Chumak, A. A. Serga, and B. Hillebrands, *Magnon transistor for all-magnon data processing,* Nature Communications **5**, 4700 (2014).

[46] Q. Wang, A. Hamadeh, R. Verba, V. Lomakin, M. Mohseni, B. Hillebrands, A. V. Chumak, and P. Pirro, *A nonlinear magnonic nano-ring resonator,* npj Computational Materials **6**, 1 (2020).

[47] R. Verba, V. Tiberkevich, E. Bankowski, T. Meitzler, G. Melkov, and A. Slavin, *Conditions for the spin wave nonreciprocity in an array of dipolarly coupled magnetic nanopillars,* Applied Physics Letters **103**, 082407 (2013).

[48] J. Lan, W. Yu, R. Wu, and J. Xiao, *Spin-Wave Diode,* Physical Review X **5**, 041049 (2015).

[49] T. Yu, Y. M. Blanter, and G. E. W. Bauer, *Chiral Pumping of Spin Waves,* Physical Review Letters **123**, 247202 (2019).

[50] T. Yu, C. Liu, H. Yu, Y. M. Blanter, and G. E. Bauer, *Chiral excitation of spin waves in ferromagnetic films by magnetic nanowire gratings,* Physical Review B **99**, 134424 (2019).

[51] J. Chen, T. Yu, C. Liu, T. Liu, M. Madami, K. Shen, J. Zhang, S. Tu, M. S. Alam, K. Xia, M. Wu, G. Gubbiotti, Y. M. Blanter, G. E. W. Bauer, and H. Yu, *Excitation of unidirectional exchange spin waves by a nanoscale magnetic grating,* Physical Review B **100**, 104427 (2019).

[52] M. Mohseni, R. Verba, T. Brächer, Q. Wang, D. A. Bozhko, B. Hillebrands, and P. Pirro, *Backscattering Immunity of Dipole-Exchange Magnetostatic Surface Spin Waves,* Physical Review Letters **122**, 197201 (2019).

[53] K. Szulc, P. Graczyk, M. Mruczkiewicz, G. Gubbiotti, and M. Krawczyk, *Spin-Wave Diode and Circulator Based on Unidirectional Coupling,* Physical Review Applied **14**, 034063 (2020).

[54] S. O. Demokritov, V. E. Demidov, O. Dzyapko, G. A. Melkov, A. A. Serga, B. Hillebrands, and A. N. Slavin, *Bose–Einstein condensation of quasi-equilibrium magnons at room temperature under pumping,* Nature **443**, 430 (2006).

[55] A. A. Serga, V. S. Tiberkevich, C. W. Sandweg, V. I. Vasyuchka, D. A. Bozhko, A. V. Chumak, T. Neumann, B. Obry, G. A. Melkov, A. N. Slavin, and B. Hillebrands, *Bose–Einstein condensation in an ultra-hot gas of pumped magnons,* Nature Communications **5**, 3452 (2014).

[56] D. A. Bozhko, A. A. Serga, P. Clausen, V. I. Vasyuchka, F. Heussner, G. A. Melkov, A. Pomyalov, V. S. L'vov, and B. Hillebrands, *Supercurrent in a room-temperature Bose–Einstein magnon condensate,* Nature Physics **12**, 1057 (2016).

[57] M. Schneider, T. Brächer, D. Breitbach, V. Lauer, P. Pirro, D. A. Bozhko, H. Y. Musiienko-Shmarova, B. Heinz, Q. Wang, T. Meyer, F. Heussner, S. Keller, E. T. Papaioannou, B. Lägel, T. Löber, C. Dubs, A. N. Slavin, V. S. Tiberkevich, A. A. Serga, B. Hillebrands, and A. V. Chumak, *Bose–Einstein condensation of quasiparticles by rapid cooling,* Nature Nanotechnology **15**, 457 (2020).

[58] P. Nowik-Boltyk, O. Dzyapko, V. E. Demidov, N. G. Berloff, and S. O. Demokritov, *Spatially non-uniform ground state and quantized vortices in a two-component Bose-Einstein condensate of magnons,* Scientific Reports **2**, 482 (2012).

[59] K. Nakata, K. A. van Hoogdalem, P. Simon, and D. Loss, *Josephson and persistent spin currents in Bose-Einstein condensates of magnons,* Physical Review B **90**, 144419 (2014).

[60] A. J. E. Kreil, H. Y. Musiienko-Shmarova, P. Frey, A. Pomyalov, V. S. L'vov, G. A. Melkov, A. A. Serga, and B. Hillebrands, *Experimental observation of Josephson oscillations in a room-temperature Bose-Einstein magnon condensate,* Physical Review B **104**, 144414 (2021).

[61] T. J. Silva, C. S. Lee, T. M. Crawford, and C. T. Rogers, *Inductive measurement of ultrafast magnetization dynamics in thin-film Permalloy,* Journal of Applied Physics **85**, 7849 (1999).

[62] M. T. Hutchings and E. J. Samuelsen, *Measurement of spin-wave dispersion in NiO by inelastic neutron scattering and its relation to magnetic properties,* Physical Review B **6**, 3447 (1972).

[63] J. S. Plant, *Spinwave dispersion curves for yttrium iron garnet,* Journal of Physics C: Solid State Physics **10**, 4805 (1977).

[64] H. A. Mook and D. McK Paul, *Neutron-Scattering Measurement of the Spin-Wave Spectra for Nickel,* Physical Review Letters **54**, 227 (1985).

[65] A. J. Princep, R. A. Ewings, S. Ward, S. Tóth, C. Dubs, D. Prabhakaran, and A. T. Boothroyd, *The full magnon spectrum of yttrium iron garnet,* npj Quantum Materials **2**, 63 (2017).

[66] Y. Tserkovnyak, A. Brataas, G. E. W. Bauer, and B. I. Halperin, *Nonlocal magnetization dynamics in ferromagnetic heterostructures,* Reviews of Modern Physics **77**, 1375 (2005).

[67] S. O. Valenzuela and M. Tinkham, *Direct electronic measurement of the spin Hall effect,* Nature **442**, 176 (2006).

[68] S. O. Valenzuela and M. Tinkham, *Electrical detection of spin currents: The spin-current induced Hall effect (invited),* Journal of Applied Physics **101**, 09B103 (2007).

[69] A. V. Chumak, A. A. Serga, M. B. Jungfleisch, R. Neb, D. A. Bozhko, V. S. Tiberkevich, and B. Hillebrands, *Direct detection of magnon spin transport by the inverse spin Hall effect,* Applied Physics Letters **100**, 103913 (2012).

[70] J. Sinova, S. O. Valenzuela, J. Wunderlich, C. Back, and T. Jungwirth, *Spin Hall effects,* Reviews of Modern Physics **87**, 1213 (2015).

[71] L. J. Cornelissen, J. Liu, R. A. Duine, J. B. Youssef, and B. J. Van Wees, *Long-distance transport of magnon spin information in a magnetic insulator at room temperature,* Nature Physics **11**, 1022 (2015).

[72] L. J. Cornelissen, J. Liu, B. J. van Wees, and R. A. Duine, *Spin-Current-Controlled Modulation of the Magnon Spin Conductance in a Three-Terminal Magnon Transistor,* Physical Review Letters **120**, 097702 (2018).

[73] Y. Tabuchi, S. Ishino, A. Noguchi, T. Ishikawa, R. Yamazaki, K. Usami, and Y. Nakamura, *Coherent coupling between a ferromagnetic magnon and a superconducting qubit,* Science **349**, 405 (2015).

[74] D. Lachance-Quirion, Y. Tabuchi, S. Ishino, A. Noguchi, T. Ishikawa, R. Yamazaki, and Y. Nakamura, *Resolving quanta of collective spin excitations in a millimeter-sized ferromagnet,* Science Advances **3**, e1603150 (2017).

[75] S. P. Wolski, D. Lachance-Quirion, Y. Tabuchi, S. Kono, A. Noguchi, K. Usami, and Y. Nakamura, *Dissipation-Based Quantum Sensing of Magnons with a Superconducting Qubit,* Physical Review Letters **125**, 117701 (2020).

[76] D. Lachance-Quirion, S. P. Wolski, Y. Tabuchi, S. Kono, K. Usami, and Y. Nakamura, *Entanglement-based single-shot detection of a single magnon with a superconducting qubit,* Science **367**, 425 (2020).

[77] S. O. Demokritov, B. Hillebrands, and A. N. Slavin, *Brillouin light scattering studies of confined spin waves: linear and nonlinear confinement,* Physics Reports **348**, 441 (2001).

[78] J. Raabe, G. Tzvetkov, U. Flechsig, M. Böge, A. Jaggi, B. Sarafimov, M. G. C. Vernooij, T. Huthwelker, H. Ade, D. Kilcoyne, T. Tyliszczak, R. H. Fink, and C. Quitmann, *PolLux: A new facility for soft x-ray spectromicroscopy at the Swiss Light Source,* Review of Scientific Instruments **79**, 113704 (2008).

[79] M. Baumgartner, K. Garello, J. Mendil, C. O. Avci, E. Grimaldi, C. Murer, J. Feng, M. Gabureac, C. Stamm, Y. Acremann, S. Finizio, S. Wintz, J. Raabe, and P. Gambardella, *Spatially and time-resolved magnetization dynamics driven by spin–orbit torques,* Nature Nanotechnology **12**, 980 (2017).

[80] G. E. W. Bauer, E. Saitoh, and B. J. van Wees, *Spin caloritronics,* Nature Materials **11**, 391 (2012).

[81] M. Agrawal, V. I. Vasyuchka, A. A. Serga, A. D. Karenowska, G. A. Melkov, and B. Hillebrands, *Direct Measurement of Magnon Temperature: New Insight into Magnon-Phonon Coupling in Magnetic Insulators,* Physical Review Letters **111**, 107204 (2013).

[82] Z. Q. Qiu and S. D. Bader, *Surface magneto-optic Kerr effect,* Review of Scientific Instruments **71**, 1243 (2000).

[83] Y. Acremann, C. H. Back, M. Buess, O. Portmann, A. Vaterlaus, D. Pescia, and H. Melchior, *Imaging precessional motion of the magnetization vector,* Science **290**, 492 (2000).

[84] P. Wessels, A. Vogel, J.-N. Tödt, M. Wieland, G. Meier, and M. Drescher, *Direct observation of isolated Damon-Eshbach and backward volume spin-wave packets in ferromagnetic microstripes,* Scientific Reports **6**, 22117 (2016).

[85] A. Rustagi, I. Bertelli, T. Van Der Sar, and P. Upadhyaya, *Sensing chiral magnetic noise via quantum impurity relaxometry,* Physical Review B **102**, 220403 (2020).

[86] I. Bertelli, J. J. Carmiggelt, T. Yu, B. G. Simon, C. C. Pothoven, G. E. Bauer, Y. M. Blanter, J. Aarts, and T. van der Sar, *Magnetic resonance imaging of spin-wave transport and interference in a magnetic insulator,* Science advances **6**, eabd3556 (2020).

[87] I. Bertelli, B. G. Simon, T. Yu, J. Aarts, G. E. W. Bauer, Y. M. Blanter, and T. van der Sar, *Imaging spin-wave damping underneath metals using electron spins in diamond,* Advanced Quantum Technologies , 2100094 (2021).

[88] M. W. Doherty, N. B. Manson, P. Delaney, F. Jelezko, J. Wrachtrup, and L. C. Hollenberg, *The nitrogen-vacancy colour centre in diamond,* Physics Reports **528**, 1 (2013).

[89] L. Rondin, J. P. Tetienne, T. Hingant, J. F. Roch, P. Maletinsky, and V. Jacques, *Magnetometry with nitrogen-vacancy defects in diamond,* Reports on Progress in Physics **77**, 056503 (2014).

[90] R. Schirhagl, K. Chang, M. Loretz, and C. L. Degen, *Nitrogen-Vacancy Centers in Diamond: Nanoscale Sensors for Physics and Biology,* Annual Review of Physical Chemistry **65**, 83 (2014).

[91] A. Gruber, A. Dräbenstedt, C. Tietz, L. Fleury, J. Wrachtrup, and C. Von Borczyskowski, *Scanning confocal optical microscopy and magnetic resonance on single defect centers,* Science **276**, 2012 (1997).

[92] D. D. Awschalom, R. Hanson, J. Wrachtrup, and B. B. Zhou, *Quantum technologies with optically interfaced solid-state spins,* Nature Photonics **12**, 516 (2018).

[93] T. Gaebel, M. Domhan, I. Popa, C. Wittmann, P. Neumann, F. Jelezko, J. R. Rabeau, N. Stavrias, A. D. Greentree, S. Prawer, J. Meijer, J. Twamley, P. R. Hemmer, and J. Wrachtrup, *Room-temperature coherent coupling of single spins in diamond,* Nature Physics **2**, 408 (2006).

[94] P. Neumann, N. Mizuochi, F. Rempp, P. Hemmer, H. Watanabe, S. Yamasaki, V. Jacques, T. Gaebel, F. Jelezko, and J. Wrachtrup, *Multipartite Entanglement Among Single Spins in Diamond,* Science **320**, 1326 (2008).

[95] E. Togan, Y. Chu, A. S. Trifonov, L. Jiang, J. Maze, L. Childress, M. V. G. Dutt, A. S. Sørensen, P. R. Hemmer, A. S. Zibrov, and M. D. Lukin, *Quantum entanglement between an optical photon and a solid-state spin qubit,* Nature **466**, 730 (2010).

[96] H. Bernien, B. Hensen, W. Pfaff, G. Koolstra, M. S. Blok, L. Robledo, T. H. Taminiau, M. Markham, D. J. Twitchen, L. Childress, and R. Hanson, *Heralded entanglement between solid-state qubits separated by three metres,* Nature **497**, 86 (2013).

[97] W. Pfaff, B. J. Hensen, H. Bernien, S. B. van Dam, M. S. Blok, T. H. Taminiau, M. J. Tiggelman, R. N. Schouten, M. Markham, D. J. Twitchen, and R. Hanson, *Unconditional quantum teleportation between distant solid-state quantum bits,* Science **345**, 532 (2014).

[98] B. Hensen, H. Bernien, A. E. Dréau, A. Reiserer, N. Kalb, M. S. Blok, J. Ruitenberg, R. F. L. Vermeulen, R. N. Schouten, C. Abellán, W. Amaya, V. Pruneri, M. W. Mitchell, M. Markham, D. J. Twitchen, D. Elkouss, S. Wehner, T. H. Taminiau, and R. Hanson, *Loophole-free Bell inequality violation using electron spins separated by 1.3 kilometres,* Nature **526**, 682 (2015).

[99] A. Sipahigil, R. E. Evans, D. D. Sukachev, M. J. Burek, J. Borregaard, M. K. Bhaskar, C. T. Nguyen, J. L. Pacheco, H. A. Atikian, C. Meuwly, R. M. Camacho, F. Jelezko, E. Bielejec, H. Park, M. Lončar, and M. D. Lukin, *An integrated diamond nanophotonics platform for quantum-optical networks,* Science **354**, 847 (2016).

[100] M. Pompili, S. L. N. Hermans, S. Baier, H. K. C. Beukers, P. C. Humphreys, R. N. Schouten, R. F. L. Vermeulen, M. J. Tiggelman, L. d. S. Martins, B. Dirkse, S. Wehner, and R. Hanson, *Realization of a multinode quantum network of remote solid-state qubits,* Science **372**, 259 (2021).

[101] L. Childress, M. V. G. Dutt, J. M. Taylor, A. S. Zibrov, F. Jelezko, J. Wrachtrup, P. R. Hemmer, and M. D. Lukin, *Coherent Dynamics of Coupled Electron and Nuclear Spin Qubits in Diamond,* Science **314**, 281 (2006).

[102] M. V. G. Dutt, L. Childress, L. Jiang, E. Togan, J. Maze, F. Jelezko, A. S. Zibrov, P. R. Hemmer, and M. D. Lukin, *Quantum Register Based on Individual Electronic and Nuclear Spin Qubits in Diamond,* Science **316**, 1312 (2007).

[103] T. Van Der Sar, Z. H. Wang, M. S. Blok, H. Bernien, T. H. Taminiau, D. M. Toyli, D. A. Lidar, D. D. Awschalom, R. Hanson, and V. V. Dobrovitski, *Decoherence-protected quantum gates for a hybrid solid-state spin register,* Nature **484**, 82 (2012).

[104] P. C. Maurer, G. Kucsko, C. Latta, L. Jiang, N. Y. Yao, S. D. Bennett, F. Pastawski, D. Hunger, N. Chisholm, M. Markham, D. J. Twitchen, J. I. Cirac, and M. D. Lukin, *Room-Temperature Quantum Bit Memory Exceeding One Second,* Science **336**, 1283 (2012).

[105] N. Yao, L. Jiang, A. Gorshkov, P. Maurer, G. Giedke, J. Cirac, and M. Lukin, *Scalable architecture for a room temperature solid-state quantum information processor,* Nature Communications **3**, 1 (2012).

[106] J. Cai, A. Retzker, F. Jelezko, and M. B. Plenio, *A large-scale quantum simulator on a diamond surface at room temperature,* Nature Physics **9**, 168 (2013).

[107] C. Bradley, J. Randall, M. Abobeih, R. Berrevoets, M. Degen, M. Bakker, M. Markham, D. Twitchen, and T. Taminiau, *A Ten-Qubit Solid-State Spin Register with Quantum Memory up to One Minute,* Physical Review X **9**, 031045 (2019).

[108] M. J. Degen, S. J. H. Loenen, H. P. Bartling, C. E. Bradley, A. L. Meinsma, M. Markham, D. J. Twitchen, and T. H. Taminiau, *Entanglement of dark electron-nuclear spin defects in diamond,* Nature Communications **12**, 3470 (2021).

[109] C. L. Degen, F. Reinhard, and P. Cappellaro, *Quantum sensing,* Reviews of Modern Physics **89**, 1 (2017).

[110] G. Kucsko, P. C. Maurer, N. Y. Yao, M. Kubo, H. J. Noh, P. K. Lo, H. Park, and M. D. Lukin, *Nanometre-scale thermometry in a living cell,* Nature **500**, 54 (2013).

[111] H. J. Mamin, M. Kim, M. H. Sherwood, C. T. Rettner, K. Ohno, D. D. Awschalom, and D. Rugar, *Nanoscale Nuclear Magnetic Resonance with a Nitrogen-Vacancy Spin Sensor,* Science **339**, 557 (2013).

[112] T. Staudacher, F. Shi, S. Pezzagna, J. Meijer, J. Du, C. A. Meriles, F. Reinhard, and J. Wrachtrup, *Nuclear Magnetic Resonance Spectroscopy on a (5-Nanometer)^3 Sample Volume,* Science **339**, 561 (2013).

[113] A. Sushkov, I. Lovchinsky, N. Chisholm, R. Walsworth, H. Park, and M. Lukin, *Magnetic Resonance Detection of Individual Proton Spins Using Quantum Reporters,* Physical Review Letters **113**, 197601 (2014).

[114] I. Lovchinsky, A. O. Sushkov, E. Urbach, N. P. de Leon, S. Choi, K. D. Greve, R. Evans, R. Gertner, E. Bersin, C. Müller, L. McGuinness, F. Jelezko, R. L. Walsworth, H. Park, and M. D. Lukin, *Nuclear magnetic resonance detection and spectroscopy of single proteins using quantum logic,* Science **351**, 836 (2016).

[115] J. F. Barry, M. J. Turner, J. M. Schloss, D. R. Glenn, Y. Song, M. D. Lukin, H. Park, and R. L. Walsworth, *Optical magnetic detection of single-neuron action potentials using quantum defects in diamond,* Proceedings of the National Academy of Sciences **113**, 14133 (2016).

[116] P. Neumann, J. Beck, M. Steiner, F. Rempp, H. Fedder, P. R. Hemmer, J. Wrachtrup, and F. Jelezko, *Single-Shot Readout of a Single Nuclear Spin,* Science **329**, 542 (2010).

[117] S. Kolkowitz, Q. P. Unterreithmeier, S. D. Bennett, and M. D. Lukin, *Sensing Distant Nuclear Spins with a Single Electron Spin,* Physical Review Letters **109**, 137601 (2012).

[118] M. S. Grinolds, M. Warner, K. De Greve, Y. Dovzhenko, L. Thiel, R. L. Walsworth, S. Hong, P. Maletinsky, and A. Yada, *Subnanometre resolution in three-dimensional magnetic resonance imaging of individual dark spins,* Nature Nanotechnology **9**, 279 (2014).

[119] S. J. DeVience, L. M. Pham, I. Lovchinsky, A. O. Sushkov, N. Bar-Gill, C. Belthangady, F. Casola, M. Corbett, H. Zhang, M. Lukin, H. Park, A. Yacoby, and R. L. Walsworth, *Nanoscale NMR spectroscopy and imaging of multiple nuclear species,* Nature Nanotechnology **10**, 129 (2015).

[120] M. H. Abobeih, J. Randall, C. E. Bradley, H. P. Bartling, M. A. Bakker, M. J. Degen, M. Markham, D. J. Twitchen, and T. H. Taminiau, *Atomic-scale imaging of a 27-nuclear-spin cluster using a quantum sensor,* Nature **576**, 411 (2019).

[121] F. Casola, T. van der Sar, and A. Yacoby, *Probing condensed matter physics with magnetometry based on nitrogen-vacancy centres in diamond,* Nature Reviews Materials **3**, 17088 (2018).

[122] S. Hsieh, P. Bhattacharyya, C. Zu, T. Mittiga, T. J. Smart, F. Machado, B. Kobrin, T. O. Höhn, N. Z. Rui, M. Kamrani, S. Chatterjee, S. Choi, M. Zaletel, V. V. Struzhkin, J. E. Moore, V. I. Levitas, R. Jeanloz, and N. Y. Yao, *Imaging stress and magnetism at high pressures using a nanoscale quantum sensor,* Science **366**, 1349 (2019).

[123] P. Kehayias, M. J. Turner, R. Trubko, J. M. Schloss, C. A. Hart, M. Wesson, D. R. Glenn, and R. L. Walsworth, *Imaging crystal stress in diamond using ensembles of nitrogen-vacancy centers,* Physical Review B **100**, 174103 (2019).

[124] D. A. Broadway, B. C. Johnson, M. S. J. Barson, S. E. Lillie, N. Dontschuk, D. J. McCloskey, A. Tsai, T. Teraji, D. A. Simpson, A. Stacey, J. C. McCallum, J. E. Bradby, M. W. Doherty, L. C. L. Hollenberg, and J.-P. Tetienne, *Microscopic Imaging of the Stress Tensor in Diamond Using in Situ Quantum Sensors,* Nano Letters **19**, 4543 (2019).

[125] D. M. Toyli, C. F. de las Casas, D. J. Christle, V. V. Dobrovitski, and D. D. Awschalom, *Fluorescence thermometry enhanced by the quantum coherence of single spins in diamond,* Proceedings of the National Academy of Sciences **110**, 8417 (2013).

[126] P. Neumann, I. Jakobi, F. Dolde, C. Burk, R. Reuter, G. Waldherr, J. Honert, T. Wolf, A. Brunner, J. H. Shim, D. Suter, H. Sumiya, J. Isoya, and J. Wrachtrup, *High-Precision Nanoscale Temperature Sensing Using Single Defects in Diamond,* Nano Letters **13**, 2738 (2013).

[127] F. Dolde, H. Fedder, M. W. Doherty, T. Nöbauer, F. Rempp, G. Balasubramanian, T. Wolf, F. Reinhard, L. C. Hollenberg, F. Jelezko, and J. Wrachtrup, *Electric-field sensing using single diamond spins,* Nature Physics **7**, 459 (2011).

[128] J. Michl, J. Steiner, A. Denisenko, A. Bülau, A. Zimmermann, K. Nakamura, H. Sumiya, S. Onoda, P. Neumann, J. Isoya, and J. Wrachtrup, *Robust and Accurate Electric Field Sensing with Solid State Spin Ensembles,* Nano Letters **19**, 4904 (2019).

[129] J. M. Taylor, P. Cappellaro, L. Childress, L. Jiang, D. Budker, P. R. Hemmer, A. Yada, R. Walsworth, and M. D. Lukin, *High-sensitivity diamond magnetometer with nanoscale resolution,* Nature Physics **4**, 810 (2008).

[130] G. Balasubramanian, I. Y. Chan, R. Kolesov, M. Al-Hmoud, J. Tisler, C. Shin, C. Kim, A. Wojcik, P. R. Hemmer, A. Krueger, T. Hanke, A. Leitenstorfer, R. Bratschitsch, F. Jelezko, and J. Wrachtrup, *Nanoscale imaging magnetometry with diamond spins under ambient conditions,* Nature **455**, 648 (2008).

[131] J. R. Maze, P. L. Stanwix, J. S. Hodges, S. Hong, J. M. Taylor, P. Cappellaro, L. Jiang, M. V. Dutt, E. Togan, A. S. Zibrov, A. Yada, R. L. Walsworth, and M. D. Lukin, *Nanoscale magnetic sensing with an individual electronic spin in diamond,* Nature **455**, 644 (2008).

[132] P. Maletinsky, S. Hong, M. S. Grinolds, B. Hausmann, M. D. Lukin, R. L. Walsworth, M. Loncar, and A. Yacoby, *A robust scanning diamond sensor for nanoscale imaging with single nitrogen-vacancy centres,* Nature Nanotechnology **7**, 320 (2012).

[133] M. S. Grinolds, S. Hong, P. Maletinsky, L. Luan, M. D. Lukin, R. L. Walsworth, and A. Yada, *Nanoscale magnetic imaging of a single electron spin under ambient conditions,* Nature Physics **9**, 215 (2013).

[134] J.-P. Tetienne, T. Hingant, J.-V. Kim, L. H. Diez, J.-P. Adam, K. Garcia, J.-F. Roch, S. Rohart, A. Thiaville, D. Ravelosona, and V. Jacques, *Nanoscale imaging and control of domain-wall hopping with a nitrogen-vacancy center microscope,* Science **344**, 1366 (2014).

[135] L. Thiel, D. Rohner, M. Ganzhorn, P. Appel, E. Neu, B. Müller, R. Kleiner, D. Koelle, and P. Maletinsky, *Quantitative nanoscale vortex imaging using a cryogenic quantum magnetometer,* Nature Nanotechnology **11**, 677 (2016).

[136] I. Gross, W. Akhtar, V. Garcia, L. J. Martínez, S. Chouaieb, K. Garcia, C. Carrétéro, A. Barthélémy, P. Appel, P. Maletinsky, J. V. Kim, J. Y. Chauleau, N. Jaouen, M. Viret, M. Bibes, S. Fusil, and V. Jacques, *Real-space imaging of non-collinear antiferromagnetic order with a single-spin magnetometer,* Nature **549**, 252 (2017).

[137] L. Thiel, Z. Wang, M. A. Tschudin, D. Rohner, I. Gutiérrez-Lezama, N. Ubrig, M. Gibertini, E. Giannini, A. F. Morpurgo, and P. Maletinsky, *Probing magnetism in 2D materials at the nanoscale with single-spin microscopy,* Science **364**, 973 (2019).

2

NV MAGNETOMETRY

Nitrogen-vacancy (NV) centers are atomic defects in diamond, whose electronic spin can be controlled and readout with a combination of optical and microwave excitation. Their non-invasive character and sensitivity to GHz magnetic fields makes them well suited to study the dynamic excitations of magnetic systems, such as spin waves. In Chapters 4-7 we use these sensors to study thermal and coherent spin waves, and to characterize a meta-magnetic phase transition. In this chapter we discuss the properties of NV centers that are required to understand these experiments.

This chapter is divided into two parts. In the first part (Section 2.1) we introduce the physics and working principles of nitrogen-vacancy centers in diamond, concluding with a description of the confocal microscope used to optically detect them. In the second part (Section 2.2) we consider an NV center in a magnetic field and express its Hamiltonian in a form that is useful to understanding Chapter 3 and the results of Chapters 6-5 (Section 2.2.1). We then explain how NV centers can be used as sensors of static (Section 2.2.2), coherently oscillating (Section 2.2.3-2.2.4) and incoherent (Section 2.2.5) magnetic fields. All these measurement techniques are the foundation upon which the results of this thesis are built. We conclude with a description of the electronic setup used to control and detect the NV spin state (Section 2.2.6).

2.1. NV CENTERS IN DIAMOND

Several extensive reviews treat the physics of NV centers in depth [1–3]. In this section we briefly describe the electronic structure of an NV center and how this is related to its spin-dependent optical properties, starting point of understanding the working principles of NV magnetometry.

2

2.1.1. ELECTRONIC STRUCTURE

Nitrogen-vacancy (NV) centers are point defects in the diamond lattice consisting of a substitutional nitrogen atom adjacent to a missing carbon atom (Fig. 2.1a). They can occur with the N-V axis oriented along any of the four ⟨111⟩ directions of the diamond lattice. This defect has a C_{3V} symmetry with axis along the N-V direction and can exist in the neutral NV^0 or charged NV^- states [4]. The electronic structure of NV^0 is composed of five unpaired electrons, two from the nitrogen and three from the carbon atoms nearest-neighbour to the vacancy [5, 6]. An additional electron can be trapped by the defect, resulting in NV^- [6]. This charge state is the one typically used for sensing applications because of its photophysics (see next section). In the rest of this thesis we focus exclusively on the negatively charged state and simply denote it "NV", for clarity.

The energy level scheme of NV centers (Fig. 2.1b) consists of triplet ground and excited states and intermediate singlet states [7][1]. Both $S = 1$ triplet levels are split into $m_s = |0\rangle$ and $m_s = |\pm 1\rangle$ states (where m_s indicates the spin projection along the NV quantization axis) by the spin-spin interaction, resulting in a ground (excited) state zero-field splitting $D \approx 2.87$ GHz ($D_{ES} \approx 1.42$ GHz).

2.1.2. SPIN-DEPENDENT OPTICAL PROPERTIES

Among many existing lattice defects, NV centers in diamond have gained importance for sensing because of the relation between their spin and optical properties [10].

The photoluminescence emission spectrum of NVs (Fig. 2.1c) shows a zero-phonon line (ZPL) at 637 nm and a broad phonon sideband (PSB). The PSB is related to transitions in which one phonon is excited/absorbed in addition to a photon at the ZPL. Thus, the PSB allows the non-resonant optical excitation with a green laser. Once excited, the NV can relax either through a spin-conserving optical transition or non-radiatively by inter-system crossing (ISC) via the singlet states.

The $m_s = |0\rangle$ state has a lower ISC shelving rate to the singlet states than $m_s = |\pm 1\rangle$ [7, 11]. Additionally, the singlet states preferentially decay toward $m_s = |0\rangle$ [2]. These spin-selective processes have the net effect of populating the $m_s = |0\rangle$ state to a high degree upon optical pumping, which allows for optical initialization into $m_s = |0\rangle$. For the same reasons, the optical transition is significantly brighter when the spin is in the $m_s = |0\rangle$ state. This spin-dependent photoluminescence forms the basis for the optical detection of the NV spin state, upon which a large part of the field of NV magnetometry

[1] The number of singlet states has not been determined clearly, with predictions and experiments reporting between two [8] and three [9], but the actual number can be generally neglected to the purpose of NV magnetometry.

is built [1–3, 12].

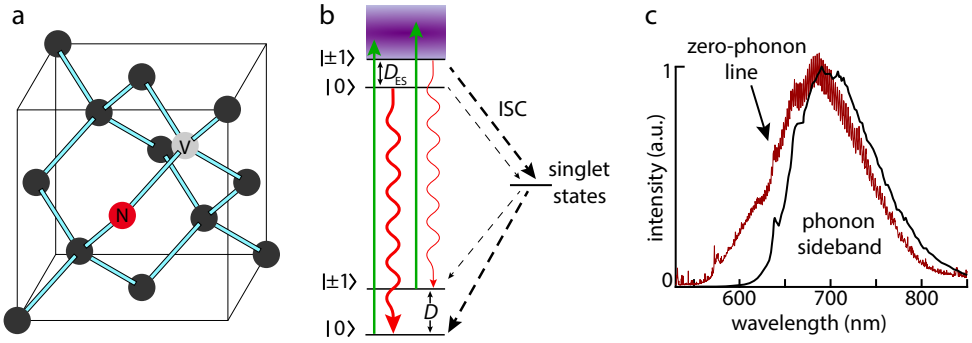

Figure 2.1: Structural, electronic and optical properties of NV centers. (**a**) Atomic structure of an NV defect in the diamond lattice. Carbon atoms are represented as dark grey spheres, while the vacancy (nitrogen atom) is represented as a light gray (red) sphere. (**b**) Energy level scheme of an NV center. The zero-field splitting in the ground (excited) state is $D = 2.87$ GHz ($D_{ES} = 1.4$ GHz) at room temperature. The green arrows represent spin-conserving non-resonant optical excitation with a green laser (515 nm) from the ground states to the phonon sideband (shaded in purple). The red wiggly arrows indicate decay via spin-conserving optical transitions, while the black dashed lines indicate non-radiative relaxation paths via inter-system crossing (ISC). The weight of the lines indicates the relative strength of the transition. (**c**) Photoemission spectrum of NV centers. Red line: spectrum of the NV ensemble used for the measurements of Chapter 4-5 and 7, measured with green excitation at 515 nm. Black line: spectrum of reference NV^- center [13], showing a zero-phonon line (ZPL) at 637 nm and a broad phonon sideband between 650 and 800 nm. The additional luminescence of the NV ensemble compared to the reference NV^- is attributed to the presence of centers in the netural NV^0 state.

2.1.3. DETECTING NV CENTERS: CONFOCAL MICROSCOPY

One way of optically addressing single NV centers is with a confocal microscope [14]. A sketch of one of the two confocal microscopes built to perform the experiments in this thesis is shown in Fig. 2.2a. A green laser beam (wavelength 515 nm) is focused to a diffraction-limited spot by an objective with high numerical aperture (NA=0.95, typically). The excited NV center emits photoluminescence (PL), which is collected via the same objective and separated from the green excitation by a dichroic mirror and optical filters. The PL is successively focused through a pinhole (diameter 50 μm) before being focused on the sensor of an avalanche photodiode (APD) with ≤ 250 dark counts per second. The pinhole ensures that only light emitted from a point in a confocal plane can reach the APD. Blocking the out-of-focus light increases the signal-to-background ratio, allowing for the detection of single NV centers (Fig. 2.2b).

The second setup built (with a heating sample-stage, used for the experiments of Chapter 7) employs a fiber-coupled Si-PIN photodiode, instead of an APD. The photodiode

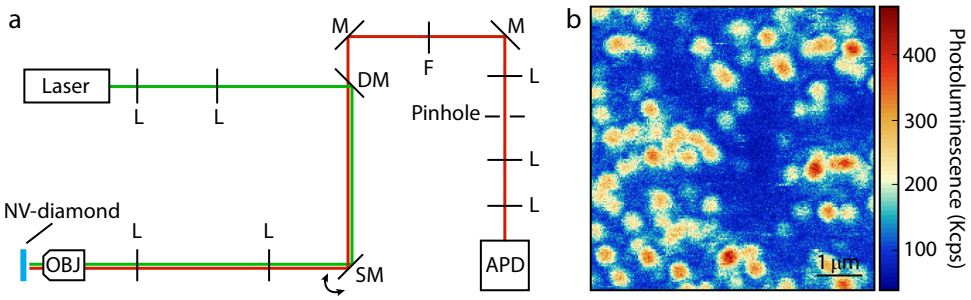

Figure 2.2: Detecting single NV centers with confocal microscopy. a) Sketch of the setup. A laser (*Cobolt 06-MLD 515 nm*) emits green light toward a dichroic mirror (DM, cutoff at 607 nm) after passing through a beam expander composed of two lenses (L). The dichroic mirror reflects the green light, which reaches a scanning mirror (*Thorlabs GVS212/M*) and the NV-diamond after a second beam-expander and a large-NA objective (*Olympus MPlanApo 50X*, NA=0.95). The NV centers emit broadband red light that is collected by the same objective and follows the excitation path backward until the dichroic mirror, where it is transmitted to the APD single-photon counting module(*Excelitas SPCM-AQRH-13* and successively *Laser Components COUNT-NIR-100*) after being filtered (F, long-pass) focused through the pinhole (diameter 50 µm). (**b**) Photoluminescence image of a diamond containing single NV centers, visible as high-PL circular spots.

has a dark current that corresponds to a higher background signal, but also much higher saturation power, which is well suited to working with ensembles of NVs. No pinhole is used because the core of the multimode optical fiber (diameter ~ 50 µm) spatially filters the incoming light in a similar way.

2.2. MAGNETIC FIELD SENSING WITH NV CENTERS

In this section we describe how to sense static and oscillating magnetic fields using NV centers. We start by expressing the NV center Hamiltonian in a magnetic field in a form that is useful to the remainder of this thesis (Section 2.2.1). We then discuss the electron spin resonance (ESR) technique, used to characterize static fields and to probe the power of the microwave field driving the NV center (Section 2.2.2). Afterwards, we introduce the idea of a rotating reference frame (Section 2.2.3), which introduces the idea that a circularly-polarized magnetic field of a certain handedness only drives one of the two NV ground-state transitions. Additionally, analyzing the action of oscillating fields in the rotating frame makes it easier to understand pulsed measurement schemes, used to induce Rabi oscillations (Section 2.2.4) and perform T_1 relaxometry (Section 2.2.5). In the rest of this thesis, we use both kind of measurements to detect and characterize GHz oscillating fields. In Section 2.2.6 we show the electronics setup that allows to manipulate and probe the NV spin state.

2.2.1. NV CENTER IN A MAGNETIC FIELD

Both ground and excited states are spin triplets with zero-field splitting between $|0\rangle$ and $|\pm 1\rangle$ states. In a static magnetic field $\mathbf{B}$, the $m_s = |-1\rangle$ and $m_s = |+1\rangle$ are additionally split because of the Zeeman interaction [15], so that the NV center energy spectrum in the electronic ground state is determined by the Hamiltonian (in a reference frame with z along the NV axis)[2]

$$\mathscr{H} = DS_z^2 + \gamma \mathbf{B}\cdot\mathbf{S} \tag{2.1}$$

where $\gamma = 2\pi \cdot 28$ MHz/mT is the electronic gyromagnetic ratio and $\mathbf{S} = [S_x, S_y, S_z]$ are the Pauli spin operators for a spin-1 system, with

$$S_x = \frac{1}{\sqrt{2}}\begin{pmatrix} 0 & 1 & 0 \\ 1 & 0 & 1 \\ 0 & 1 & 0 \end{pmatrix}, \quad S_y = \frac{1}{\sqrt{2}}\begin{pmatrix} 0 & -i & 0 \\ i & 0 & -i \\ 0 & i & 0 \end{pmatrix}, \quad S_z = \begin{pmatrix} 1 & 0 & 0 \\ 0 & 0 & 0 \\ 0 & 0 & -1 \end{pmatrix}. \tag{2.2}$$

Substituting these in Eq. 2.1, we obtain the Hamiltonian in matrix form:

$$\mathscr{H} = \begin{pmatrix} D+\gamma B_z & \frac{\gamma}{\sqrt{2}}(B_x - iB_y) & 0 \\ \frac{\gamma}{\sqrt{2}}(B_x + iB_y) & 0 & \frac{\gamma}{\sqrt{2}}(B_x - iB_y) \\ 0 & \frac{\gamma}{\sqrt{2}}(B_x + iB_y) & D-\gamma B_z \end{pmatrix}. \tag{2.3}$$

A static magnetic field that is oriented exactly along the NV z axis causes a linear shift of the two ESR frequencies $\omega_\pm = D \pm \gamma B_z$. At the same field, NV centers belonging to different families show a different shift (Fig. 2.3a), because they experience a transverse field. Diagonalizing the Hamiltonian yields its eigenvalues ($\lambda_{i=1,2,3}$), from which the ESR frequencies can be determined as $\omega_{+(-)} = \lambda_1 - \lambda_{2(3)}$. These frequencies can be experimentally detected by measuring the electron spin resonance (ESR) spectrum (next section).

Let us now rewrite the Hamiltonian in a form that is useful when considering oscillating fields (Section 2.2.3). Because the $|-1\rangle \leftrightarrow |+1\rangle$ transition is dipole-forbidden[3], we can treat the three-level system of Eq. 2.3 as two effective two-level systems (selecting the upper-left or bottom-right corners of the matrix). The full Hamiltonian can then be rewritten using the spin-1/2 Pauli matrices $\boldsymbol{\sigma} = (\sigma_x, \sigma_y, \sigma_z)$[4] as

$$\mathscr{H}_\pm = \frac{\omega_\pm}{2}(I \pm \sigma_z) + \frac{\gamma}{\sqrt{2}}(B_x\sigma_x + B_y\sigma_y) \tag{2.4}$$

where I is the identity matrix.

2.2.2. ELECTRON SPIN RESONANCE

When performing an NV-based measurement, we usually start by detecting and characterizing the strength and direction of the static field at the NV location. This is done

[2] We neglect strains and electric fields, which lead to additional terms in the Hamiltonian [3, 16, 17]. We neglect these effects because they play a minor role for the relatively large magnetic fields considered in this thesis.

[3] These states are coupled by quadrupolar magnetic fields, dipolar electric fields, and mechanical strain [18–21].

[4] $\sigma_x = \begin{pmatrix} 0 & 1 \\ 1 & 0 \end{pmatrix}, \sigma_y = \begin{pmatrix} 0 & -i \\ i & 0 \end{pmatrix}, \sigma_z = \begin{pmatrix} 1 & 0 \\ 0 & -1 \end{pmatrix}$.

by determining the electron spin resonance (ESR) transitions of the NV center(s) used for sensing. Characterizing the ESR transitions is also the first step of any procedure to probe oscillating fields, because knowing the resonances allows to apply microwave pulses of the appropriate frequencies. Additionally, the contrast of ESR transitions provides information regarding the strength of the oscillating field that is resonantly driving the NV center.

DETECTION OF A STATIC FIELD

Transitions between $m_s = |0\rangle$ and $m_s = |\pm 1\rangle$ (both in the ground and excited states) can be induced by a GHz magnetic field that is resonant with an ESR transition $\omega_\pm$ (we study this in detail in Section 2.2.3). In the easiest implementation, an ESR experiment consists of the simultaneous and continuous excitation with light and microwaves[5], of which the frequency is varied, while the emitted photons are collected. When the drive frequency is resonant with either of the ESR transitions, the NV spin is driven from the bright $|0\rangle$ into the dark $|\pm\rangle$ states, such that the NV photoluminesce is reduced. Typical ESR spectra are shown in Fig. 2.3b-c for single NVs and NV ensembles, respectively.

We perform ESR experiments in order to determine the strength and orientation of a static magnetic field at the NV location, by inverting Eq. 2.1. The resulting magnetic field components parallel ($B_\parallel$) and perpendicular ($B_\perp$) to the N-V axis can be written as [23]

$$B_\parallel = \frac{\sqrt{-(D+\omega_+-2\omega_-)(D+\omega_--2\omega_+)(D+\omega_++\omega_-)}}{3\gamma\sqrt{3D}}, \tag{2.5}$$

$$B_\perp = \frac{\sqrt{-(2D-\omega_+-\omega_-)(2D-\omega_++2\omega_-)(2D-\omega_-+2\omega_+)}}{3\gamma\sqrt{3D}}. \tag{2.6}$$

The angle between the NV axis and the field can thus be calculated as $\theta = \arctan(B_\perp / B_\parallel)$.

The procedure of extracting the field strength and angle is used in Chapter 7 to detect local magnetic field variations due to the presence of magnetic domains and domain walls. It is also used to calibrate the magnetic field at the NV location (since we always apply the bias field with a small permanent magnet) whenever a new sample is mounted in the setup.

CHARACTERIZATION OF THE OSCILLATING FIELD MAGNITUDE

The width and contrast of each ESR dip in the spectrum are influenced by several parameters, which include the power of the optical and microwave excitation and the lifetime of the energy levels. The contrast C of an ESR dip can be expressed as [24]

$$C = C_0 \frac{B_{AC,\perp}^2}{B_{AC,\perp}^2 + \Phi} \tag{2.7}$$

[5] ESR can also be measured with a pulsed scheme ("dark ESR") in order to avoid broadening of the transitions induced by the continuous laser excitation [22].

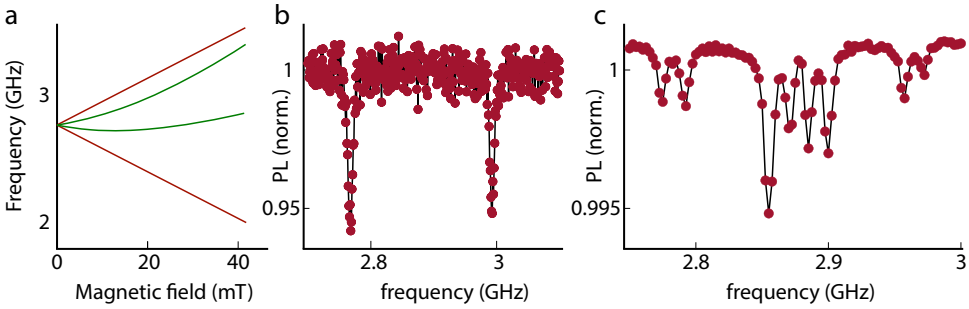

Figure 2.3: Electron spin resonance. (**a**) Magnetic field-evolution of the eight ESR transitions of an NV ensemble. When the field is oriented exactly along one NV family (red lines), the other three families are degenerate because they experience the same misaligned field (green lines). (**b**) ESR spectrum of a single NV center for $B_{\parallel} \sim 4$ mT, $B_{\perp} \sim 5$ mT. (**c**) ESR spectrum of an NV ensemble for a field misaligned with all four NV families. $(B_x, B_y, B_z) \approx (0.6(1), 4.0(1), 0.5(1))$ mT.

where C_0 is the maximum attainable contrast of an ESR transition (roughly $20-25\%$ for single NVs and $2-3\%$ for ensembles), B_{AC} is the amplitude of the magnetic field oscillating at the ESR frequency, perpendicular to the NV axis, and Φ is a parameter that depends on the optical excitation and relaxation time of the NV spin[6]. For small microwave power, when all other parameters are constant, the contrast is a sensitive tool to characterize variations of the strength of the oscillating field. In Chapters 4 and 5 we use this property to spatially image the stray field of spin waves. To obtain quantitative results, we measure Rabi oscillations instead (Section 2.2.4).

2.2.3. DETECTING OSCILLATING FIELDS: THE ROTATING FRAME

In this section we transform the NV Hamiltonian into a rotating frame of reference. This treatment shows that the two NV ESR transitions are driven by circularly-polarized magnetic fields of opposite handedness. Additionally, because it removes the time dependence from the Hamiltonian, it facilitates the understanding of the complex motion of a spin subject to both a static and an oscillating field .

We define a rotating wavefunction $\psi_{R_\pm} = e^{\pm i\omega t\sigma_z/2}\psi$, and use the time-dependent Schrödinger's equation

$$i\hbar\frac{\partial\psi}{\partial t} = \mathscr{H}\psi \tag{2.8}$$

to obtain

$$\frac{\partial\psi}{\partial t} = e^{\mp i\omega t\sigma_z/2}\frac{\partial\psi_{R_\pm}}{\partial t} \mp i\omega\sigma_z\psi_{R_\pm}/2 = -\frac{i}{\hbar}\mathscr{H}e^{\mp i\omega t\sigma_z/2}\psi_{R_\pm}. \tag{2.9}$$

[6] For typical values of the T_1 and T_2^* relaxation rates and optical power P_{opt}, $\Phi = \frac{2}{\gamma}\Gamma_p\Gamma_c$, where Γ_p (Γ_c) is the optically-induced polarization (relaxation) rate [24]. They both depend on $s = P_{\text{opt}}/P_{\text{sat}}$ as $\Gamma_{p(c)} = \Gamma^{\infty}_{p(c)}\left(\frac{s}{s+1}\right)$, where P_{sat} is the optical power at saturation of the NV luminescence (i.e. half of the maximum attainable PL) and $\Gamma^{\infty}_{p(c)}$ is the polarization (relaxation) rate at saturation [24]. Depending on the optical power P_{opt}, $\Phi \approx 10^{13} - 10^{14}$ Hz [24].

Rewriting this, we can obtain a new Schrödinger's equation for the rotating wavefunction:

$$\frac{\partial \psi_{R_\pm}}{\partial t} = -i(e^{\pm i\omega t\sigma_z/2}\mathcal{H}e^{\mp it\sigma_z/2} \mp \omega\sigma_z/2)\psi_{R_\pm} = -\frac{i}{\hbar}\mathcal{H}_{R_\pm}\psi_{R_\pm}. \tag{2.10}$$

Thus, the new Hamiltonian in the frame that is rotating synchronously with the wavefunction is given by

$$\mathcal{H}_{R_\pm} = e^{\pm i\omega t\sigma_z/2}\mathcal{H}e^{\mp i\omega t\sigma_z/2} \mp \omega\sigma_z/2. \tag{2.11}$$

We can now analyze the NV center in a static field (along the z axis) and consider what happens when we apply an oscillating field in the xy plane. Such transverse field can generally be elliptically polarized, such that it can be written as sum of two counter-rotating circular components of amplitude B_R and $B_{R'}$:

$$B_{AC} = \frac{1}{\sqrt{2}}B_R\left[\cos(\omega t)\sigma_x + \sin(\omega t)\sigma_y\right] + \frac{1}{\sqrt{2}}B_{R'}\left[\cos(\omega t)\sigma_x - \sin(\omega t)\sigma_y\right] \tag{2.12}$$

$$= \frac{1}{\sqrt{2}}\cos(\omega t)\sigma_x(B_R + B_{R'}) + \frac{1}{\sqrt{2}}\sin(\omega t)\sigma_y(B_R - B_{R'}). \tag{2.13}$$

We can transform the two-level Hamiltonian (Eq. 2.4) in the rotating frame, using Eq. 2.11

$$\mathcal{H}'_\pm = e^{\pm i\omega t\sigma_z/2}\mathcal{H}_\pm e^{\mp i\omega t\sigma_z/2} \mp \omega\sigma_z/2 = \frac{I\omega_\pm}{2} \mp \frac{\sigma_z\Delta_\pm}{2} + e^{\pm i\omega t\sigma_z/2}(\gamma B_{AC})e^{\mp i\omega t\sigma_z/2}, \tag{2.14}$$

where $\Delta_\pm = \omega - \omega_\pm$ is the detuning between the NV transition and the drive field. Working out the matrix products, we obtain

$$\mathcal{H}'_+ = \frac{I\omega_+}{2} + \frac{1}{\sqrt{2}}B_R\sigma_x + \frac{1}{\sqrt{2}}B_{R'}\left[\sigma_x\cos(2\omega t) - \sigma_y\sin(2\omega t)\right] - \frac{\sigma_z\Delta_+}{2}, \tag{2.15}$$

$$\mathcal{H}'_- = \frac{I\omega_-}{2} + \frac{1}{\sqrt{2}}B_{R'}\sigma_x + \frac{1}{\sqrt{2}}B_R\left[\sigma_x\cos(2\omega t) + \sigma_y\sin(2\omega t)\right] + \frac{\sigma_z\Delta_-}{2}. \tag{2.16}$$

For $\mathcal{H}'_+$ ($\mathcal{H}'_-$), when $|2\omega - \Delta_+| \gg B_R$ ($|2\omega - \Delta_-| \gg B_{R'}$) we can disregard the terms oscillating at 2ω (rotating wave approximation [25])[7], such that the spin dynamic in the new frame is driven by the $B_{R(R')}$ component, which appears static in the frame rotating at $+\omega(-\omega)$ (Fig. 2.4).

Importantly, Eqs. 2.15-2.16 show that the $\omega\pm$ transitions are driven by circularly-polarized magnetic fields of opposite handedness. This turns out to be crucial to the detection and characterization of spin waves of Chapters 4-6, because they generate fields that are circularly polarized (see Chapter 3 for the derivation of spin-wave stray fields), so that spin waves propagating to the right (left) drive almost exclusively the $|0\rangle \leftrightarrow |-1\rangle$ ($|0\rangle \leftrightarrow |+1\rangle$) transition.

Since each transition is driven by a circularly-polarized field of a certain handedness, a linearly-polarized field (such as that of a wire or a microstrip) drives both transitions equally, because it can be expressed as the sum of two counter-rotating circular components.

[7] These components only cause minor modifications, known as Bloch-Siegert effects [26, 27], which are only relevant when the amplitude of the oscillating field is strong compared to its detuning from the ESR transition.

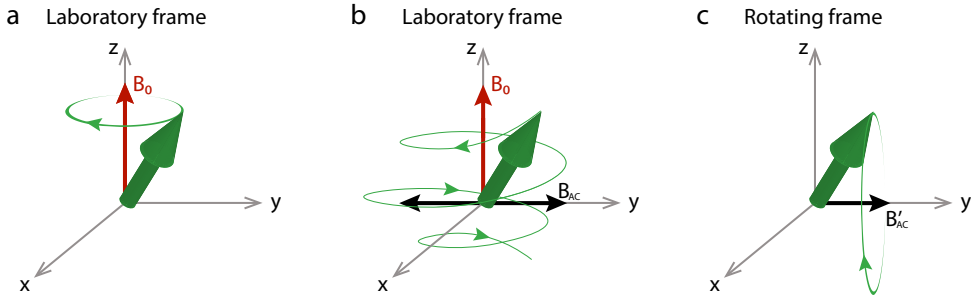

Figure 2.4: Electron spin in a magnetic field. (**a**) In the laboratory frame, an electron spin subjected to a static magnetic field precesses around it. (**b**) When a resonant oscillating field is applied in the transverse plane, the spin rotates around the vector sum of the two fields, following a complicated trajectory. (**c**) In a reference frame rotating at the same frequency of the spin and transverse field, the trajectory is much simpler: the spin "Rabi" precesses around the transverse field, which in this frame appears static.

2.2.4. RABI OSCILLATIONS

We see from Eqs. 2.15-2.16 that B_R ($B_{R'}$) has become static in the rotating frame. As such, this transverse field drives "Rabi" oscillations [28, 29] with frequency

$$\Omega_{\pm} = \sqrt{\Omega_R^2 + \Delta_{\pm}^2}, \tag{2.17}$$

where $\Omega_R = \gamma B_{R(R')}/\sqrt{2}$. At resonance (i.e. $\Delta_{\pm} = 0$), $\Omega = \Omega_{R(R')}$. To ensure resonance between the ESR transition and the applied oscillating field, we always perform an ESR measurement before exciting Rabi oscillations. However, when the Rabi frequency is below ~ 5 MHz, we must take into account that the ESR transition is actually split in two transitions (separated by ~ 3 MHz) by the nuclear hyperfine interaction of the nitrogen atoms used to create the NV center by ^{15}N implantation [30]. Thus, the field we apply is detuned from each hyperfine-split transition by ~ 1.5 MHz. This situation occurs in Chapter 4 (Fig. 4.2).

Measuring Rabi oscillations allows to quantify $B_{R(R')}$, i.e. the amplitude of the oscillating field driving NV centers. We can perform a Rabi measurement using the pulsed control scheme shown in Fig. 2.5a. Microwave bursts of increasing duration rotate the NV spin between the $|0\rangle$ (high luminescence) and the $|\pm 1\rangle$ states (Fig. 2.5b). We calculate the Rabi frequency from the period of the luminescence oscillations.

Knowing the Rabi frequency, we can calibrate the duration of a microwave burst that would prepare the NV spin in the $|-1\rangle$ or $|+1\rangle$ state (known as π pulse because, in the rotating frame, a spin prepared along $= z$ rotates by an angle π until $-z$) by choosing a pulse length that corresponds to the first minimum in the Rabi oscillation measurement (Fig. 2.5). Similarly, a $\pi/2$ pulse brings the spin on the xy plane, where the spin

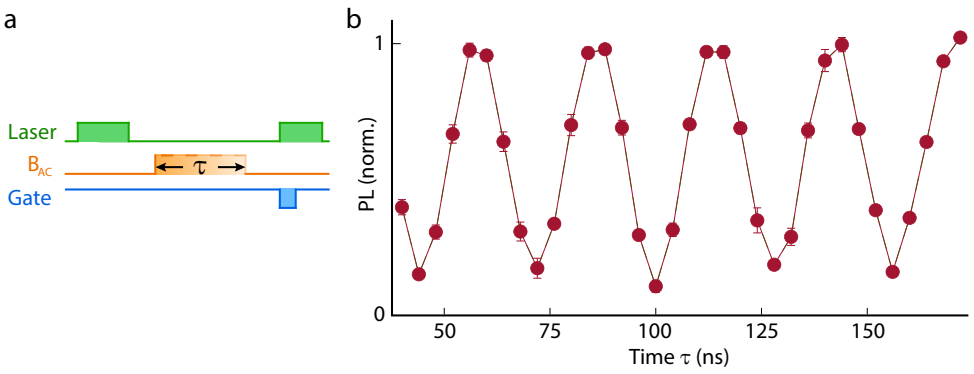

Figure 2.5: Rabi oscillations measurement. (**a**) Pulse sequence used to measure Rabi oscillations. Green laser pulses are used to initialize and read out the NV spin state. A resonant microwave burst of variable duration τ induces Rabi rotations of the NV spin. The emitted photons are counted during the first 400 ns of the second laser pulse. (**b**) Typical result of a Rabi oscillation experiment. As a function of the microwave pulse length, the NV spin state rotates between the $|0\rangle$ (high PL) and the $|\pm 1\rangle$ (low PL) states. The signal does not start from 1 because the first pulse has non-zero duration ($\sim$ 40 ns).

is dephased by slow variations of the static field[8] or, in the case of NV ensembles, local field variations over the detection volume (i.e. the laser spot with size determined by the diffraction limit).

We use pulsed control of the NV spin in Chapter 4 in a time-of-flight experiment on spin waves and in Chapter 6 to characterize the longitudinal relaxation time of the NV spin (this kind of measurements is known as "relaxometry").

2.2.5. T_1 RELAXOMETRY

Measuring Rabi oscillations allows the calibration of the duration of pulses used to deterministically prepare the NV spin in any coherent state. Measuring the time evolution of coherent states enables to characterize the source of the magnetic field responsible for the system dynamics. Advanced sequences of $\pi/2$ and π pulses can be used to, e.g., selectively lock-in to a magnetic field of a certain frequency while filtering out all other components [10, 31–37], deterministically enable or disable the influence of a system on the probe [38–41], and characterize dephasing and decoherence processes [38, 42].

In this thesis, we employ π pulses to measure the velocity of spin waves (Chapter 4) and the longitudinal NV relaxation rate as a result of magnetic-noise-induced decoherence

[8] Here, fields are "slow" when they are quasi-static, i.e. almost constant during a single measurement but varying over many repetitions. Some examples are the effective field due to the statistical polarization of the spins in the NV environment, such as the nuclear spins of the neighbouring ^{13}C atoms, as well as the electron spins of other substitutional nitrogen atoms [43].

(Chapter 6). The measurement protocol for the NV relaxation rate simply consists of preparing the NV spin in one of the three eigenstates and monitoring how long it takes to relax to the stationary situation (i.e. the NV spending 1/3 of time in each state). We prepare the spin in $|0\rangle$ by optical pumping. We apply a subsequent π pulse on the $\omega_{\pm}$ transition to flip the spin into the $|\pm 1\rangle$ states. The pulse sequence is shown in Fig. 2.6a.

The NV-spin relaxation dynamics can be described by a rate-equation model, where the time-evolution of the population $\mathbf{P}(t)$ of the three ground states can be expressed as [23, 44]

$$\frac{d\mathbf{P}(t)}{dt} = \mathbf{\Gamma}\mathbf{P}(t) = \begin{pmatrix} -(\Gamma_{-1,0}+\Gamma_{-1,+1}) & \Gamma_{0,-1} & \Gamma_{+1,-1} \\ \Gamma_{-1,0} & -(\Gamma_{0,-1}+\Gamma_{0,+1}) & \Gamma_{+1,0} \\ \Gamma_{-1,+1} & \Gamma_{0,+1} & -(\Gamma_{+1,0}+\Gamma_{+1,-1}) \end{pmatrix} \mathbf{P}(t) \quad (2.18)$$

where $\Gamma_{i,j} = \Gamma_{j,i}$ is the transition rate between states $|i\rangle$ and $|j\rangle$ and we set $\Gamma_{-1,+1} = 0$ because magnetic field noise does not directly couple these states (see previous section). The system dynamics is therefore described by only two rates ($\Gamma_{0,-1} := \Gamma_-$ and $\Gamma_{0,+1} := \Gamma_+$):

$$\mathbf{\Gamma} = \begin{pmatrix} -\Gamma_- & \Gamma_- & 0 \\ \Gamma_- & -(\Gamma_- + \Gamma_+) & \Gamma_+ \\ 0 & \Gamma_+ & -\Gamma_+ \end{pmatrix}. \quad (2.19)$$

Fig. 2.6b shows a typical relaxation measurements of the three spin states in a system where $\Gamma_- \neq \Gamma_+$. Measuring the time-relaxation of the three states and fitting the data to the model (Eq.2.20) allows to extract the two relaxation rates $\Gamma_{\pm}$.

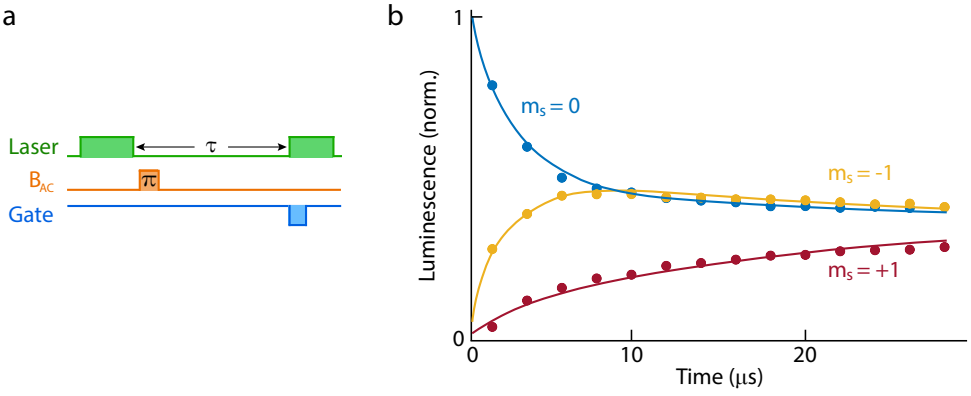

Figure 2.6: Relaxation measurement. (**a**) Pulse sequence for a relaxometry measurement. A green laser pulse prepares the NV spin in the $|0\rangle$ state. A π pulse (on either transition) can prepare the NV spin in the ± 1 states. After a waiting time τ, the spin state is read out during the first 400 ns of a laser pulse. (**b**) Typical NV relaxation measurement of the three states. In this case, the relaxation rate Γ_- is much larger than Γ_+ (data from Chapter 6).

The relaxation rates can be expressed in term of field-field correlators[9]. We start from

[9] In this thesis we only consider magnetic noise generated by the fluctuations of the magnetic field of thermally-

Eq. 2.4, considering a static field along the NV z axis and a resonant field oscillating in the xy plane. Using linear perturbation theory, the relaxation rates are given by [23, 46–49]

$$\Gamma_{\pm} = \frac{\gamma^2}{2} \int_{-\infty}^{+\infty} \mathrm{d}t e^{i\omega_{\pm} t} \langle B_{\pm}(t) B_{\mp}(0) \rangle \,. \tag{2.20}$$

where $\langle ... \rangle$ indicates ensemble averaging over the realizations of the field fluctuations.

In Chapter 3 we derive the NV relaxation rates caused by thermally-excited incoherent magnons, which generate magnetic fluctuations at the $\omega_{\pm}$ ESR frequencies and result in a large increase of the NV relaxation rates.

2.2.6. CONTROLLING NV CENTERS: SETUP ELECTRONICS

The oscillating magnetic field used to induce NV spin transitions in the ground state is generated inductively, throughout this thesis, by current running through a wire (i.e. a bonding wire pushed close to the sample, as in Chapters 4, 6, 7) and/or a Ti/Au microstrip fabricated on a magnetic substrate (as in Chapters 4 and 5). This microwave current is generated by two microwave sources and amplified, if necessary. A programmable pulse generator controls the timing of such microwave bursts, of the laser excitation, and of the readout window. Additionally, the pulse generator triggers the data acquisition by the data-acquisition card (DAQ). Fig. 2.7 shows the electronic elements and connections of the setup.

excited spin waves. In magnetic systems, these fluctuations are typically much larger than other components. In non-magnetic systems, the dominating noise source can be electronic transport [45].

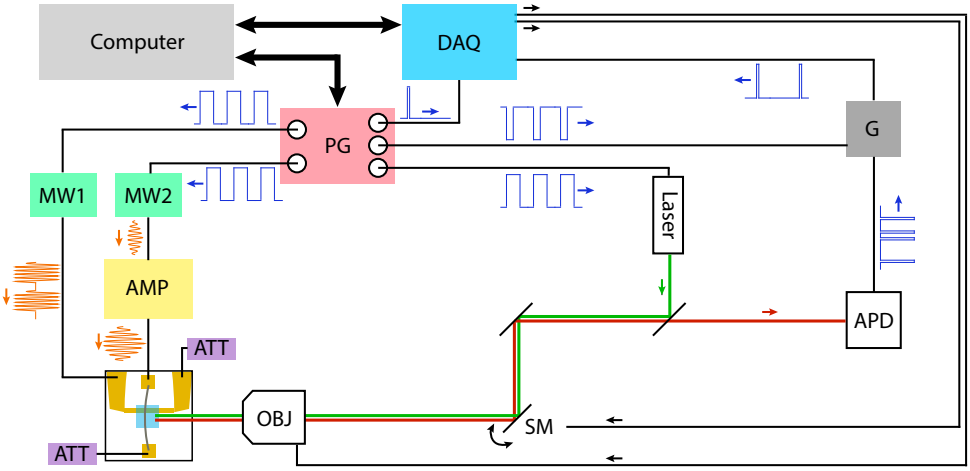

Figure 2.7: Sketch of the electronic setup. The whole electronic setup is controlled via a computer (top left corner), that communicates with a National Instrument data-acquisition (DAQ) card (*NI PCIe-6343*). This card supplies DC voltages to control the scanning mirror (SM), the in-plane sample position and the piezo-actuated stage (*PIFOC Piezo X-drive*) that controls the distance between the objective (OBJ) and the sample. Additionally, the DAQ card is used to count the pulses generated by the avalanche photodetector (APD) when a photon is collected. Before reaching the DAQ card, such pulses pass through a pull-up resistor (G, for "gate"). When the "counter gate" output of the pulse generator (PG, *PulseBlasterESR-PRO-500*) is low (high) the APD pulses (don't) reach the counter on the DAQ card. Additionally, the PG generates pulses to trigger data acquisition (the DAQ card stores counts until a new trigger is received), and controls the laser and two microwave sources (MW1 and MW2, both *Rohde & Schwarz SGS100A*). The signal from MW1 typically reaches a microstrip on the sample, while the one from MW2 reaches a bonding wire after being amplified by a high-power broadband amplifier (*AR 30 W 1-6 GHz*). After reaching the sample, each microwave channel is terminated with a 50 Ω-impedance attenuator and terminator.

REFERENCES

[1] M. W. Doherty, N. B. Manson, P. Delaney, F. Jelezko, J. Wrachtrup, and L. C. Hollenberg, *The nitrogen-vacancy colour centre in diamond,* Physics Reports **528**, 1 (2013).

[2] L. Rondin, J. P. Tetienne, T. Hingant, J. F. Roch, P. Maletinsky, and V. Jacques, *Magnetometry with nitrogen-vacancy defects in diamond,* Reports on Progress in Physics **77**, 056503 (2014).

[3] R. Schirhagl, K. Chang, M. Loretz, and C. L. Degen, *Nitrogen-Vacancy Centers in Diamond: Nanoscale Sensors for Physics and Biology,* Annual Review of Physical Chemistry **65**, 83 (2014).

[4] Y. Mita, *Change of absorption spectra in type-Ib diamond with heavy neutron irradiation,* Physical Review B **53**, 11360 (1996).

[5] J. H. Loubser and J. A. Van Wyk, *Electron spin resonance in the study of diamond,* Reports on Progress in Physics **41**, 1201 (1978).

[6] M. W. Doherty, N. B. Manson, P. Delaney, and L. C. L. Hollenberg, *The negatively charged nitrogen-vacancy centre in diamond: the electronic solution,* New Journal of Physics **13**, 25019 (2011).

[7] L. Robledo, H. Bernien, T. Van der Sar, and R. Hanson, *Spin dynamics in the optical cycle of single nitrogen-vacancy centres in diamond,* New Journal of Physics **13**, 025013 (2011).

[8] V. M. Acosta, E. Bauch, M. P. Ledbetter, A. Waxman, L. S. Bouchard, and D. Budker, *Temperature dependence of the nitrogen-vacancy magnetic resonance in diamond,* Physical Review Letters **104**, 070801 (2010).

[9] Y. Ma, M. Rohlfing, and A. Gali, *Excited states of the negatively charged nitrogen-vacancy color center in diamond,* Physical Review B **81**, 041204 (2010).

[10] C. L. Degen, F. Reinhard, and P. Cappellaro, *Quantum sensing,* Reviews of Modern Physics **89**, 1 (2017).

[11] J.-P. Tetienne, L. Rondin, P. Spinicelli, M. Chipaux, T. Debuisschert, J.-F. Roch, and V. Jacques, *Magnetic-field-dependent photodynamics of single NV defects in diamond: an application to qualitative all-optical magnetic imaging,* New Journal of Physics **14**, 103033 (2012).

[12] F. Casola, T. van der Sar, and A. Yacoby, *Probing condensed matter physics with magnetometry based on nitrogen-vacancy centres in diamond,* Nature Reviews Materials **3**, 17088 (2018).

[13] J. Jeske, D. W. Lau, X. Vidal, L. P. McGuinness, P. Reineck, B. C. Johnson, M. W. Doherty, J. C. McCallum, S. Onoda, F. Jelezko, T. Ohshima, T. Volz, J. H. Cole, B. C. Gibson, and A. D. Greentree, *Stimulated emission from nitrogen-vacancy centres in diamond,* Nature Communications **8**, 370 (2017).

[14] A. Gruber, A. Dräbenstedt, C. Tietz, L. Fleury, J. Wrachtrup, and C. Von Borczyskowski, *Scanning confocal optical microscopy and magnetic resonance on single defect centers,* Science **276**, 2012 (1997).

[15] S. Blundell, *Magnetism in Condensed Matter* (Oxford, 2001).

[16] E. Van Oort and M. Glasbeek, *Electric-field-induced modulation of spin echoes of N-V centers in diamond,* Chemical Physics Letters **168**, 529 (1990).

[17] F. Dolde, H. Fedder, M. W. Doherty, T. Nöbauer, F. Rempp, G. Balasubramanian, T. Wolf, F. Reinhard, L. C. Hollenberg, F. Jelezko, and J. Wrachtrup, *Electric-field sensing using single diamond spins,* Nature Physics **7**, 459 (2011).

[18] N. B. Manson, X.-F. He, and P. T. H. Fisk, *Raman heterodyne detected electron-nuclear-double-resonance measurements of the nitrogen-vacancy center in diamond,* Optics Letters **15**, 1096 (1990).

[19] E. R. Macquarrie, T. A. Gosavi, N. R. Jungwirth, S. A. Bhave, and G. D. Fuchs, *Mechanical spin control of nitrogen-vacancy centers in diamond,* Physical Review Letters **111**, 227602 (2013).

[20] P. V. Klimov, A. L. Falk, B. B. Buckley, and D. D. Awschalom, *Electrically driven spin resonance in silicon carbide color centers,* Physical Review Letters **112**, 087601 (2014).

[21] B. A. Myers, A. Ariyaratne, and A. C. Jayich, *Double-Quantum Spin-Relaxation Limits to Coherence of Near-Surface Nitrogen-Vacancy Centers,* Physical Review Letters **118**, 197201 (2017).

[22] P. Neumann, R. Kolesov, V. Jacques, J. Beck, J. Tisler, A. Batalov, L. Rogers, N. B. Manson, G. Balasubramanian, F. Jelezko, and J. Wrachtrup, *Excited-state spectroscopy of single NV defects in diamond using optically detected magnetic resonance,* New Journal of Physics **11**, 013017 (2009).

[23] T. van der Sar, F. Casola, R. Walsworth, and A. Yacoby, *Nanometre-scale probing of spin waves using single-electron spins.* Nature communications **6**, 7886 (2015).

[24] A. Dréau, M. Lesik, L. Rondin, P. Spinicelli, O. Arcizet, J. F. Roch, and V. Jacques, *Avoiding power broadening in optically detected magnetic resonance of single NV defects for enhanced dc magnetic field sensitivity,* Physical Review B **84**, 195204 (2011).

[25] C. P. Slichter, *Principles of Magnetic Resonance* (Springer, 1990).

[26] F. Bloch and A. Siegert, *Magnetic resonance for nonrotating fields,* Physical Review **57**, 522 (1940).

[27] J. Tuorila, M. Silveri, M. Sillanpää, E. Thuneberg, Y. Makhlin, and P. Hakonen, *Stark effect and generalized Bloch-Siegert shift in a strongly driven two-level system,* Physical Review Letters **105**, 257003 (2010).

[28] W. G. Breiland, H. C. Brenner, and C. B. Harris, *Coherence in multilevel systems. I. Coherence in excited states and its application to optically detected magnetic resonance in phosphorescent triplet states ,* Journal of Chemical Physics **62**, 3458 (1975).

[29] F. Jelezko, T. Gaebel, I. Popa, A. Gruber, and J. Wrachtrup, *Observation of Coherent Oscillations in a Single Electron Spin,* Physical Review Letters **92**, 076401 (2004).

[30] J. R. Rabeau, P. Reichart, G. Tamanyan, D. N. Jamieson, S. Prawer, F. Jelezko, T. Gaebel, I. Popa, M. Domhan, and J. Wrachtrup, *Implantation of labelled single nitrogen vacancy centers in diamond using* ^{15}N*,* Applied Physics Letters **88**, 023113 (2006).

[31] L. Viola, S. Lloyd, and E. Knill, *Universal control of decoupled quantum systems,* Physical Review Letters **83**, 4888 (1999).

[32] F. Jelezko, T. Gaebel, I. Popa, M. Domhan, A. Gruber, and J. Wrachtrup, *Observation of coherent oscillation of a single nuclear spin and realization of a two-qubit conditional quantum gate,* Physical Review Letters **93**, 130501 (2004).

[33] T. Gaebel, M. Domhan, I. Popa, C. Wittmann, P. Neumann, F. Jelezko, J. R. Rabeau, N. Stavrias, A. D. Greentree, S. Prawer, J. Meijer, J. Twamley, P. R. Hemmer, and J. Wrachtrup, *Room-temperature coherent coupling of single spins in diamond,* Nature Physics **2**, 408 (2006).

[34] L. Childress, M. V. Gurudev Dutt, J. M. Taylor, A. S. Zibrov, F. Jelezko, J. Wrachtrup, P. R. Hemmer, and M. D. Lukin, *Coherent dynamics of coupled electron and nuclear spin qubits in diamond,* Science **314**, 281 (2006).

[35] T. Staudacher, F. Shi, S. Pezzagna, J. Meijer, J. Du, C. A. Meriles, F. Reinhard, and J. Wrachtrup, *Nuclear magnetic resonance spectroscopy on a (5-nanometer)3 sample volume,* Science **339**, 561 (2013).

[36] S. J. Devience, L. M. Pham, I. Lovchinsky, A. O. Sushkov, N. Bar-Gill, C. Belthangady, F. Casola, M. Corbett, H. Zhang, M. Lukin, H. Park, A. Yacoby, and R. L. Walsworth, *Nanoscale NMR spectroscopy and imaging of multiple nuclear species,* Nature Nanotechnology **10**, 129 (2015).

[37] I. Lovchinsky, J. D. Sanchez-Yamagishi, E. K. Urbach, S. Choi, S. Fang, T. I. Andersen, K. Watanabe, T. Taniguchi, A. Bylinskii, E. Kaxiras, P. Kim, H. Park, and M. D. Lukin, *Magnetic resonance spectroscopy of an atomically thin material using a single-spin qubit,* Science **355**, 503 (2017).

[38] R. Hanson, V. V. Dobrovitski, A. E. Feiguin, O. Gywat, and D. D. Awschalom, *Coherent dynamics of a single spin interacting with an adjustable spin bath,* Science **320**, 352 (2008).

[39] T. Van Der Sar, Z. H. Wang, M. S. Blok, H. Bernien, T. H. Taminiau, D. M. Toyli, D. A. Lidar, D. D. Awschalom, R. Hanson, and V. V. Dobrovitski, *Decoherence-protected quantum gates for a hybrid solid-state spin register,* Nature **484**, 82 (2012).

[40] M. H. Abobeih, J. Randall, C. E. Bradley, H. P. Bartling, M. A. Bakker, M. J. Degen, M. Markham, D. J. Twitchen, and T. H. Taminiau, *Atomic-scale imaging of a 27-nuclear-spin cluster using a quantum sensor,* Nature **576**, 411 (2019).

[41] B. B. Zhou, P. C. Jerger, K. H. Lee, M. Fukami, F. Mujid, J. Park, and D. D. Awschalom, *Spatiotemporal Mapping of a Photocurrent Vortex in Monolayer MoS2 Using Diamond Quantum Sensors,* Physical Review X **10**, 011003 (2020).

[42] G. De Lange, Z. H. Wang, D. Ristè, V. Dobrovitski, and R. Hanson, *Universal dynamical decoupling of a single solid-state spin from a spin bath,* Science **330**, 60 (2010).

[43] G. De Lange, T. Van Der Sar, M. Blok, Z. H. Wang, V. Dobrovitski, and R. Hanson, *Controlling the quantum dynamics of a mesoscopic spin bath in diamond,* Scientific Reports **2**, 1 (2012).

[44] A. Jarmola, V. M. Acosta, K. Jensen, S. Chemerisov, and D. Budker, *Temperature- and magnetic-field-dependent longitudinal spin relaxation in nitrogen-vacancy ensembles in diamond,* Physical Review Letters **108**, 197601 (2012).

[45] S. Kolkowitz, A. Safira, A. A. High, R. C. Devlin, S. Choi, Q. P. Unterreithmeier, D. Patterson, A. S. Zibrov, V. E. Manucharyan, H. Park, and M. D. Lukin, *Probing Johnson noise and ballistic transport in normal metals with a single-spin qubit,* Science **347**, 1129 (2015).

[46] A. Suter, M. Mali, J. Roos, and D. Brinkmann, *Mixed magnetic and quadrupolar relaxation in the presence of a dominant static Zeeman Hamiltonian,* Journal of Physics: Condensed Matter **10**, 5977 (1998).

[47] B. Flebus and Y. Tserkovnyak, *Quantum-Impurity Relaxometry of Magnetization Dynamics,* Physical Review Letters **121**, 187204 (2018).

[48] S. Chatterjee, J. F. Rodriguez-Nieva, and E. Demler, *Diagnosing phases of magnetic insulators via noise magnetometry with spin qubits,* Physical Review B **99**, 104425 (2019).

[49] A. Rustagi, I. Bertelli, T. Van Der Sar, and P. Upadhyaya, *Sensing chiral magnetic noise via quantum impurity relaxometry,* Physical Review B **102**, 220403 (2020).

3

SPIN-WAVE THEORY

Spin waves are collective excitations of spins in magnetic materials. In this chapter we derive expressions that are useful and recurrent in Chapters 4-6. We start by calculating the dipolar field of a planar magnetization (Section 3.1), which we need in the following sections. Starting from the Landau-Lifshits-Gilbert (LLG) equation, in Section 3.2 we derive the spin-wave susceptibility, and from that the spin-wave dispersion. We then examine which spin-wave modes are efficiently excited inductively (Section 3.3), calculate the stray fields that spin waves generate (Section 3.4) and finally show how these fields can be detected using NV magnetometry (Section 3.5) via measuring Rabi oscillations and T_1 relaxometry. Importantly, from the last three sections stem equations regarding the coupling of the stray field of a microstrip with the spin waves, and of the spin-wave stray field with NV centers.

3.1. STRAY FIELD OF A PLANAR MAGNETIZATION

In this section we calculate the dipolar stray field generated by a planar magnetization. This result is needed in Sections 3.2 and 3.4, where we derive the spin-wave dispersion and the stray field of a spin wave, respectively.

The magnetic field of a single magnetic dipole $\mathbf{m}$, located at the origin, is given by

$$\mathbf{B}(\mathbf{r}) = \mu_0 \mathbf{\Gamma}(\mathbf{r})\mathbf{m}, \tag{3.1}$$

where $\mathbf{\Gamma}(\mathbf{r})$ is the dipolar tensor, given by

$$\mathbf{\Gamma}(\mathbf{r}) = \frac{1}{4\pi|\mathbf{r}|^5}\begin{pmatrix} 2x^2-y^2-z^2 & 3xy & 3xz \\ 3xy & 2y^2-x^2-z^2 & 3yz \\ 3xz & 3yz & 2z^2-x^2-y^2 \end{pmatrix}. \tag{3.2}$$

For a magnetization $\mathbf{M}(\mathbf{r})$, the stray field is given by

$$\mathbf{B}(\mathbf{r}) = \mu_0 \int \mathrm{d}\mathbf{r}' \mathbf{\Gamma}(\mathbf{r}-\mathbf{r}')\mathbf{M}(\mathbf{r}'), \tag{3.3}$$

where the components of the dipolar tensor $\mathbf{\Gamma}(\mathbf{r}-\mathbf{r}')$ are derivatives of the Coulomb's kernel

$$\Gamma_{\alpha\beta}(\mathbf{r}-\mathbf{r}') = \frac{\partial}{\partial\alpha}\frac{\partial}{\partial\beta'}\frac{1}{4\pi|\mathbf{r}-\mathbf{r}'|} \quad \text{with } \alpha,\beta = x,y,z. \tag{3.4}$$

Later on, we analyze spin waves (in thin films) that are characterized by their wavevector. Thus, it is convenient here to remove the convolution in Eq. 3.3 by taking the 2D Fourier transform in the film plane (yz)[1]

$$\mathbf{B}(\mathbf{k},x) = \mu_0 \int \mathrm{d}x' \mathbf{\Gamma}(\mathbf{k},x-x')\mathbf{M}(\mathbf{k},\mathbf{x}'), \tag{3.5}$$

where $\mathbf{k} = k_y\hat{\mathbf{y}} + k_z\hat{\mathbf{z}}$ is in the film plane. Using [1, 2]

$$\nabla^2 \frac{1}{4\pi|\mathbf{r}-\mathbf{r}'|} = \delta(\mathbf{r}-\mathbf{r}') \tag{3.6}$$

and the identity [1–3]

$$\frac{1}{|\mathbf{r}-\mathbf{r}'|} = 2\pi \int \frac{\mathrm{d}\mathbf{k}}{k} e^{-k|x-x'|} e^{i\mathbf{k}(\boldsymbol{\rho}-\boldsymbol{\rho}')}, \tag{3.7}$$

where $\mathbf{k}$ and $\boldsymbol{\rho} = y\hat{\mathbf{y}} + z\hat{\mathbf{z}}$ are in the infinite yz plane, we obtain the Fourier transform of Eq. 3.4

$$\Gamma_{\alpha\beta}(\mathbf{k},x-x') = \frac{1}{2}\begin{cases} e^{-k|x-x'|}k - 2\delta(x-x') & \text{for } \alpha=\beta=x, \\ -e^{-k|x-x'|}\frac{k_\alpha k_\beta}{k} & \text{for } \alpha,\beta = y,z, \\ -e^{-k|x-x'|}\mathrm{sign}(x-x')\,i\,k_\alpha & \text{for } \alpha = y,z \text{ and } \beta = x. \end{cases} \tag{3.8}$$

[1] We are considering a thin film with infinite lateral dimensions.

Because we consider thin films, we assume that the magnetization $\mathbf{M} = \mathbf{m}M_s$ does not vary across the film thickness[2]: $\mathbf{m}(\mathbf{k},\mathbf{x}') = \mathbf{m}(\mathbf{k})$. We can now integrate Eq. 3.5 over the film thickness t, where the only x'-dependent components are the $\Gamma_{\alpha\beta}$, so that the dipolar field at x is

$$\mathbf{B}(\mathbf{k},\mathbf{x}) = \mu_0 M_s \int_{-t}^{0} \mathrm{d}x' \mathbf{\Gamma}(\mathbf{k}, x-x')\mathbf{m}(\mathbf{k}) = \mu_0 M_s \overline{\mathbf{\Gamma}}(\mathbf{k}, x)\mathbf{m}(\mathbf{k}), \tag{3.9}$$

where $\overline{(...)}$ indicates spatial averaging over the film thickness. Carrying out the integration for $\mathbf{r} > \mathbf{r}'$ (i.e. above the film)[3] results in

$$\overline{\mathbf{\Gamma}}(\mathbf{k}, x) = \int_{-t}^{0} \mathrm{d}x' \mathbf{\Gamma}(\mathbf{k}, x-x') = \frac{1}{2} e^{-kx}(1-e^{-kt}) \begin{pmatrix} -1 & i\sin\phi & i\cos\phi \\ i\sin\phi & \sin^2\phi & \sin\phi\cos\phi \\ i\cos\phi & \sin\phi\cos\phi & \cos^2\phi \end{pmatrix}, \tag{3.10}$$

where we expressed $\mathbf{k}$ in terms of its polar coordinates k and ϕ ($\phi = 0$ corresponds to the z axis).

Below the magnetic film, $\mathrm{sign}(x-x')$ in Eq. 3.8 changes sign, so that $\Gamma_{xy}, \Gamma_{yx}, \Gamma_{xz}, \Gamma_{zx}$ also change sign. It will become clear in Section 3.4 that this result is important to understand the chirality of NV-based detection of spin waves with $\phi = \pm\pi/2$.

3.2. SPIN-WAVE DISPERSION

The relation between the frequency of an excitation and its wavelength is known as dispersion. The gradient of the dispersion, called group velocity, denotes the direction in which energy is transported in the system. In this section we derive the transverse dynamic susceptibility of a thin magnetic film from the Landau-Lifshitz-Gilbert (LLG) equation. From the susceptibility, we find expressions for the spin-wave dispersion and damping. The LLG equation phenomenologically describes the damped motion of the magnetization in an effective magnetic field, composed of several contributions, such as the Zeeman, exchange, and dipolar interactions. In Section 3.3 we use the spin-wave susceptibility to calculate the magnetization excited inductively by a microwave stripline.

3.2.1. MAGNETIZATION DYNAMICS: LANDAU-LIFSHITZ-GILBERT EQUATIONS

We consider an external static magnetic field $\mathbf{B_0}$ applied along z ($\mathbf{B_0} = B_0\hat{\mathbf{z}}$) (Fig. 3.1), which forces the static magnetization parallel to z[4,5]. The magnetization evolves in time

[2] This assumption is valid in the limit $kt \ll 1$, where t is the film thickness, which is the case for the magnetization profiles in this thesis.

[3] For $x > x'$, we use $\int_{-t}^{0} \mathrm{d}x' e^{-k|x-x'|} = \int_{-t}^{0} \mathrm{d}x' e^{-kx} e^{kx'} = e^{-kx}\frac{1-e^{-kt}}{k}$.

[4] We disregard the crystalline anisotropy, because it is small for the magnets considered in this thesis (Ni, YIG) [4].

[5] In the experiments of Chapters 4-5, the static field is applied along the axis of one NV center family, which forms a $\sim 35°$ angle with the z axis. However, the fields we apply in spin-wave experiments are always smaller than ~ 30 mT, such that the out-of-plane component is smaller than ~ 17.3 mT. Since the saturation magnetization of YIG is 178 mT at room temperature, the static magnetization tilts out-of-plane by less than $\mathrm{atan}(17.3/178) \sim 5.6°$. In Chapter 6, the system considered is nickel, whose saturation magnetization is ~5 times higher, but we also apply fields up to ~ 60 mT. We treat the case of a tilted magnetization is Section 3.2.3.

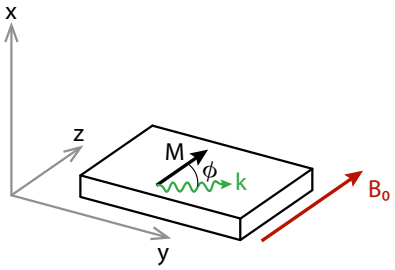

Figure 3.1: Geometry of the system. A thin film in the yz plane is magnetized along z by the static magnetic field $\mathbf{B_0}$. Spin waves propagate with wavevector $\mathbf{k}$ at angle ϕ from $\mathbf{M}$.

following the Landau-Lifshitz-Gilbert (LLG) equation [5]:

$$\frac{\mathrm{d}\mathbf{m}}{\mathrm{d}t} = -\gamma \mathbf{m} \times \mathbf{B}_{\mathrm{eff}} - \alpha \frac{\mathrm{d}\mathbf{m}}{\mathrm{d}t} \times \mathbf{m}, \tag{3.11}$$

where α is the Gilbert damping parameter (we study changes of α due to increased damping in Chapter 5) and $\mathbf{B}_{\mathrm{eff}}$ is the effective magnetic field (including both static and dynamic contributions). The first term after the equal sign in Eq. 3.11 induces the precession of $\mathbf{m}$ around $\mathbf{B}_{\mathrm{eff}}$ (Fig. 3.2). The second term induces a rotation of $\mathbf{m}$ toward $\mathbf{B}_{\mathrm{eff}}$, with rate given by α, and is therefore a damping term. Here, $\mathbf{B}_{\mathrm{eff}}$ is the sum of the external fields and the effective fields due to dipolar and exchange contributions (both static and oscillating):

$$\mathbf{B}_{\mathrm{eff}} = \mathbf{B}_0 + \mathbf{B}_{\mathrm{AC}} + \mathbf{B}_{\mathrm{dem}} + \mathbf{B}_{\mathrm{ex}} \tag{3.12}$$

where $\mathbf{B}_{\mathrm{AC}}$ is an external oscillating field used to excite spin waves, $\mathbf{B}_{\mathrm{dem}}$ is the demagnetizing (i.e. dipolar) field and $\mathbf{B}_{\mathrm{ex}}$ the exchange field. We evaluate each contribution in the following sections.

ZEEMAN INTERACTION

The Zeeman energy associated with the external magnetic field is

$$F_Z = -\mathbf{M} \cdot \mathbf{B}_0 = M_s \mathbf{m} \cdot \mathbf{B}_0. \tag{3.13}$$

Defining $\omega_B = \gamma B_0$, the Zeeman contribution to the effective field is

$$B_{0,z} = \frac{\omega_B}{\gamma}. \tag{3.14}$$

EXCHANGE INTERACTION

The exchange interaction is short-ranged (i.e. few nanometers) and, in a magnet with negligible anisotropy constants such as YIG [4], the exchange energy density can be considered isotropic:

$$F_{\mathrm{ex}}(\mathbf{r}) = \frac{D}{2} \sum_{i,j=x,y,z} \left(\frac{\partial m_i(\mathbf{r})}{\partial j} \right)^2. \tag{3.15}$$

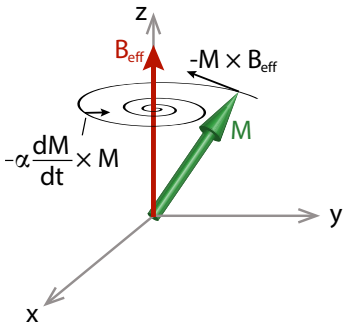

Figure 3.2: Time evolution of the magnetization according to the LLG equation. The magnetization **M** precesses around the effective field $\mathbf{B}_{\text{eff}}$ (which is static, in this sketch). The damping term forces **M** towards $\mathbf{B}_{\text{eff}}$.

where D is the exchange constant. Its Fourier transform over the in-plane coordinates y, z is

$$F_{\text{ex}}(\mathbf{k}, x) = -k^2 D\left[m_y^2(\mathbf{k}, x) + m_z^2(\mathbf{k}, x)\right] + \frac{D}{2}\sum_{i=x,y,z}\left(\frac{\partial m_i(\mathbf{k}, x)}{\partial x}\right)^2, \tag{3.16}$$

where $\mathbf{k}$ is the spin-wavevector (in the yz plane). For a constant magnetization over the film thickness, the last term vanishes. Thus, the exchange energy contributes an effective field with Cartesian components:

$$B_{\text{ex},i} = -\frac{1}{M_s}\frac{\partial F}{\partial m_i} = -\frac{\omega_{\text{ex}}}{\gamma}k^2 m_i(\mathbf{k}, x), \tag{3.17}$$

where we defined $\omega_{\text{ex}} = \gamma D / M_s$

DIPOLAR INTERACTION

The dipolar interaction is long ranged and strongly anisotropic, unlike the short-ranged, isotropic exchange interaction. Therefore, the dipolar contribution leads to an anisotropic spin-wave dispersion at long wavelengths: spin waves propagating perpendicularly to the static magnetization generate a larger stray (i.e. dipolar) field than those propagating parallel to it, which costs energy.

We use the results of Section 3.1 to calculate the demagnetizing field

$$\mathbf{B}_{\text{dem}}(\mathbf{r}) = \mu_0 M_s \int \Gamma(\mathbf{r} - \mathbf{r}')\mathbf{m}(\mathbf{r}')\mathrm{d}\mathbf{r}', \tag{3.18}$$

which can be seen as the field felt by a spin, due to the dipolar field of all the other spins in the system.
In k-space, after averaging over the film thickness, from Eq. 3.9 we obtain

$$\overline{\mathbf{B}}_{\text{dem}}(\mathbf{k}) = \mu_0 M_s \frac{1}{t}\int_{-t}^{0} \mathrm{d}x\Gamma(\mathbf{k}, x)\mathbf{m}(\mathbf{k}) = \mu_0 M_s \overline{\Gamma}(\mathbf{k})\mathbf{m}(\mathbf{k}), \tag{3.19}$$

where $\overline{(...)}$ indicates averaging over the thickness. Using Eq. 3.8 and

$$\frac{1}{t}\int_{-t}^{0}\int_{-t}^{0} \mathrm{d}x'\mathrm{d}x e^{-k|x-x'|} = \frac{2}{k}(1-\frac{1-e^{-kt}}{kt}) = \frac{2}{k}f(kt), \tag{3.20}$$

$$\frac{1}{t}\int_{-t}^{0}\int_{-t}^{0} \mathrm{d}x'\mathrm{d}x \mathrm{sign}(x-x')e^{-k|x-x'|} = 0, \tag{3.21}$$

$$\frac{1}{t}\int_{-t}^{0}\int_{-t}^{0} \mathrm{d}x'\mathrm{d}x \delta(x-x') = 1, \tag{3.22}$$

we arrive at

$$\overline{\mathbf{B}}_{\mathrm{dem}}(\mathbf{k}) = \mu_0 M_s \begin{pmatrix} f(kt)-1 & 0 & 0 \\ 0 & \frac{-k_y^2}{k^2}f(kt) & \frac{-k_y k_z}{k^2}f(kt) \\ 0 & \frac{-k_y k_z}{k^2}f(kt) & \frac{-k_z^2}{k^2}f(kt) \end{pmatrix} \begin{pmatrix} m_x(\mathbf{k}) \\ m_y(\mathbf{k}) \\ m_z(\mathbf{k}) \end{pmatrix}, \tag{3.23}$$

which can be re-written as

$$\overline{\mathbf{B}}_{\mathrm{dem}}(\mathbf{k}) = \mu_0 M_s \begin{pmatrix} f-1 & 0 & 0 \\ 0 & -f\sin^2\phi & -f\sin\phi\cos\phi \\ 0 & -f\sin\phi\cos\phi & -f\cos^2\phi \end{pmatrix} \begin{pmatrix} m_x(\mathbf{k}) \\ m_y(\mathbf{k}) \\ m_z(\mathbf{k}) \end{pmatrix}, \tag{3.24}$$

where ϕ is the in-plane angle between $\mathbf{m}$ and $\mathbf{k}$. Thus, the dipolar contribution to the effective field in the LLG equations (Eq. 3.12) reads

$$\mathbf{B}_{\mathrm{dem}}(\mathbf{k}) = \frac{\omega_{\mathrm{dem}}}{\gamma}\overline{\mathbf{\Gamma}}(k)\mathbf{m}(\mathbf{k}), \tag{3.25}$$

where we defined

$$\omega_{\mathrm{dem}} = \gamma\mu_0 M_s. \tag{3.26}$$

3.2.2. SPIN-WAVE DISPERSION AND SUSCEPTIBILITY

Having evaluated the contributions to $\mathbf{B}_{\mathrm{eff}}$, we can now calculate the spin-wave dispersion. To do so, we Fourier-transform the LLG equation (Eq. 3.11) into the frequency domain, and linearize it by assuming that $m_z = \sqrt{1-m_x^2-m_y^2} \approx 1$, yielding

$$-i\omega m_x = -\gamma(B_{\mathrm{eff},z}m_y - B_{\mathrm{eff},y}) + i\alpha\omega m_y, \tag{3.27}$$

$$-i\omega m_y = -\gamma(B_{\mathrm{eff},x} - B_{\mathrm{eff},z}m_x) - i\alpha\omega m_x. \tag{3.28}$$

Using Eq. 3.12 and $\Gamma_{xy} = \Gamma_{yx} = 0$ (from Eq. (3.24)) we obtain

$$\gamma B_{\mathrm{eff},x} = \omega_{\mathrm{dem}}(f-1)m_x - \omega_{\mathrm{ex}}k^2 m_x + \gamma B_{\mathrm{AC},x}, \tag{3.29}$$

$$\gamma B_{\mathrm{eff},y} = -\omega_{\mathrm{dem}} f\sin^2\phi m_y - \omega_{\mathrm{ex}}k^2 m_y + \gamma B_{\mathrm{AC},y}, \tag{3.30}$$

$$\gamma B_{\mathrm{eff},z} = \omega_B. \tag{3.31}$$

Defining

$$\omega_0 = \omega_B + \omega_{\text{ex}} k^2, \tag{3.32}$$

$$\omega_2 = \omega_0 + \omega_{\text{dem}}(1-f), \tag{3.33}$$

$$\omega_3 = \omega_0 + \omega_{\text{dem}} f \sin^2\phi, \tag{3.34}$$

we obtain Eqns. (3.27-3.28) in matrix form:

$$\begin{pmatrix} \omega_2 - i\alpha\omega & i\omega \\ -i\omega & \omega_3 - i\alpha\omega \end{pmatrix} \begin{pmatrix} m_x \\ m_y \end{pmatrix} = \gamma \begin{pmatrix} B_{AC,x} \\ B_{AC,y} \end{pmatrix}. \tag{3.35}$$

Inverting Eq. (3.35) gives the susceptibility tensor

$$\boldsymbol{\chi} = \frac{\gamma}{(\omega_2 - i\alpha\omega)(\omega_3 - i\alpha\omega) - \omega^2} \begin{pmatrix} \omega_3 - i\alpha\omega & -i\omega \\ i\omega & \omega_2 - i\alpha\omega \end{pmatrix}. \tag{3.36}$$

The matrix elements of the susceptibility tensor describe the response of the magnetization to a transverse magnetic drive field. The prefactor, with a Lorentzian-like form, peaks at a (k- and ϕ-dependent) resonance frequency, and has a width that is governed by α. We can find the spin-wave dispersion by solving

$$\Lambda = \omega^2 - (\omega_2 - i\alpha\omega)(\omega_3 - i\alpha\omega) = 0, \tag{3.37}$$

with solutions

$$\omega = -i\alpha\frac{\omega_2+\omega_3}{2(1+\alpha^2)} \pm \sqrt{\frac{4\omega_2\omega_3 - \alpha^2(\omega_2+\omega_3)^2}{4(1+\alpha^2)}}. \tag{3.38}$$

The real (imaginary) part of this equation gives the dispersion ω_{sw} (linewidth $\Delta\omega_{sw}$)

$$\omega_{sw} \approx \sqrt{\omega_2\omega_3}, \tag{3.39}$$

$$\Delta\omega_{sw} \approx \alpha\frac{\omega_2+\omega_3}{2}, \tag{3.40}$$

where we neglected the α^2 terms, since usually $\alpha < 0.01$. The ellipticity of the magnetization precession is given by

$$\eta = \left|\frac{\chi_{xx}}{\chi_{yx}}\right| \approx \sqrt{\frac{\omega_3}{\omega_2}}. \tag{3.41}$$

Interestingly, the dispersion of spin waves is strongly anisotropic due to the ϕ-dependence of ω_3 (Fig. 3.3). We can consider three important cases:

- The mode with $k = 0$ is spatially uniform, and known as ferromagnetic resonance (FMR). Its frequency follows from Eq. 3.39, and is given by[6]

  $$\omega_{sw} = \sqrt{\omega_B(\omega_B + \omega_{\text{dem}})} = \gamma\sqrt{B_0(B_0 + \mu_0 M_s)}, \tag{3.42}$$

  which is known as Kittel's law [6].
  A typical way of studying this mode is with microwave absorption measurements, such as cavity- or broadband-FMR, which often aim at characterizing the width of the absorption dip to extract the saturation magnetization and (changes in) the Gilbert damping parameter (see Chapter 4 for an example of such measurements).

[6] For $k = 0$, $f \to 0$, so that $\omega_2 \to \omega_B + \omega_{\text{dem}}$ and $\omega_3 \to \omega_B$.

- Spin-waves propagating parallel to the magnetization ($\phi = 0; \pi$) are known as backward-volume spin waves (BVSW), because of the negative group velocity at small **k**. Their dispersion reads

$$\omega_{sw} = \sqrt{\omega_0[\omega_0 + \omega_{\text{dem}}(1-f)]}, \tag{3.43}$$

  and is plotted in Fig. 3.3b (red line).

- Spin waves propagating perpendicular to the magnetization ($\phi = \pm\pi/2$) are known as Damon-Eshbach spin waves (DESW) [7, 8], surface spin waves, and often described with the adjective "chiral" (blue line in Fig. 3.3b). The reasons for these names are historical: the article in Ref. [7], by Eshbach and Damon, is the first to identify and study these modes that are confined to the surface in YIG crystals of macroscopic dimensions. However, the vertical confinement of these modes is on the order of the spin-wavelength (they decay exponentially with depth), so that in films thinner than ~ 1 μm, this confinement is effectively negligible for micron-sized spin waves. The "chiral" aspect will become clear in this chapter (Sections 3.4-3.5). Their dispersion reads

$$\omega_{sw} = \sqrt{[\omega_0 + f\omega_{\text{dem}}][\omega_0 + (1-f)\omega_{\text{dem}}]}. \tag{3.44}$$

In the rest of this thesis, we use "BV" and "DE" to indicate the propagation direction of the spin waves with respect to the static magnetization.

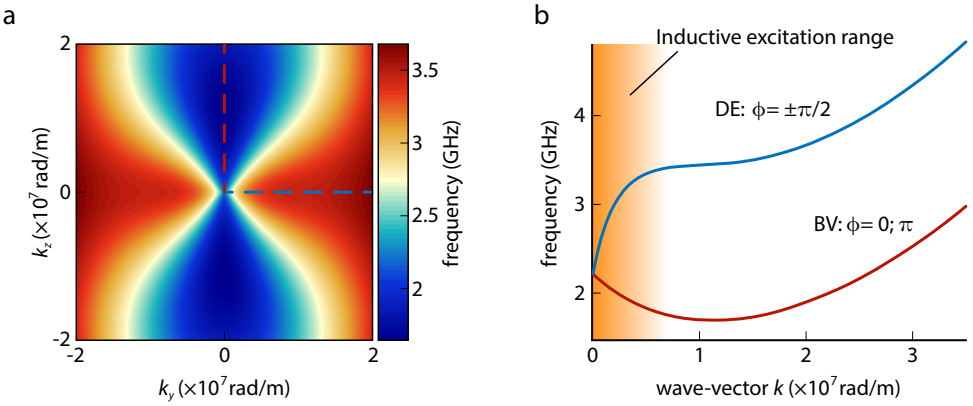

Figure 3.3: Spin-wave dispersion. (**a**) 2D spin-wave dispersion for $B_0 = 30$ mT. The frequency of a spin wave strongly depends on it propagation angle (ϕ) with respect to the static magnetization (**M**). For backward-volume spin waves (along the dashed red line), the frequency decreases with increasing wavevector (the dispersion slope corresponds to the group velocity, from which the name "backward"). For Damon-Eshbach spin waves (dashed blue line), the group velocity is always positive. (**b**) Linecuts of (a), corresponding to the DE (blue line) and BV (red line) spin waves. The shaded orange area indicates which wave-vector values are easily excited inductively.

INTRINSIC HANDEDNESS OF THE MAGNETIZATION PRECESSION

A single, isolated magnetic moment precesses around the static field always with a particular handedness, performing a circular motion with direction governed by the first cross-product in the LLG equation (Eq. 3.11). In a magnet, however, a spin also feels the field generated by its neighbours (demagnetizing field). As a result, the precessional motion becomes elliptical, as described by Eq. 4.15. However, this motion retains the same preferential handedness. It is important to keep this in mind before deriving the spin-wave excitation efficiency by a microstrip (Section 3.3). In that section we shall find out that such phenomenon has a momentum-locking character that, together with this preferential handedness of the magnetization precession, results in very spatially-asymmetric spin-wave excitation.

We can see this preferred precession handedness of the magnetization by disregarding the terms with α and the dipolar terms in ω_2 and ω_3[7], so that both are equal to ω_0, and the dispersion $\omega \sim \omega_0$. From Eq. 3.36 we obtain

$$\frac{m_x}{m_y} = \frac{B_x\omega_0 - iB_y\omega_0}{iB_x\omega_0 + B_y\omega_0}. \tag{3.45}$$

Clearly, $m_y = im_x$: the precession is right-circularly polarized. Considering the dipolar terms we just disregarded, the polarization becomes right-handed elliptical (i.e. the out-of-plane component m_x is smaller than m_y), which can be seen as linear superposition of right- and left-circularly polarized fields, of which the right- component is larger. We see in Section 3.3 why this is important.

3.2.3. STATIC FIELD WITH AN OUT-OF-PLANE COMPONENT

So far we considered $\mathbf{B}_0$ and $\mathbf{M}$ along z. We now generalize these results to the case of a magnetic field applied with out-of-plane angle θ_B (from the z axis), which lifts the magnetization out of plane by θ. In this case, it is convenient to consider the system in the magnet frame, i.e. with z' rotated out-of-plane from z around y by θ (Fig. 3.4).

The changes to the results of the previous section are to the Zeeman and the dipolar contributions. The former becomes [3]

$$B_0, z = \frac{\omega_B}{\gamma} \rightarrow \frac{\omega_B}{\gamma}\cos(\theta_B - \theta). \tag{3.46}$$

The demagnetizing field can be obtained applying a rotation matrix

$$\mathbf{R}(\theta) = \begin{pmatrix} \cos\theta & 0 & -\sin\theta \\ 0 & 1 & 0 \\ \sin\theta & 0 & \cos\theta \end{pmatrix} \tag{3.47}$$

such that $\mathbf{m}' = \mathbf{R}(\theta)\mathbf{m}$ and $\mathbf{m} = \mathbf{R}^T(\theta)\mathbf{m}'$.

[7] At very large k, this is a good approximation.

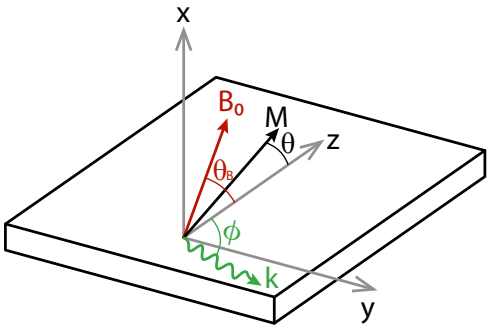

Figure 3.4: System geometry for a magnetic field along the NV axis. A magnetic field applied at an out-of-plane angle $\theta_B = \theta_{NV}$ tilts the magnetization out of plane by a smaller angle θ.

The rotated form of the dipolar tensor $\mathbf{\Gamma'} = \mathbf{R\Gamma R}^T$ reads

$$\begin{pmatrix} (f-1)\cos^2\theta - f\sin^2\theta\cos^2\phi & f\sin\theta\sin\phi\cos\phi & \sin\theta\cos\theta(f-1+f\cos^2\phi) \\ f\sin\theta\sin\phi\cos\phi & -f\sin^2\phi & -f\cos\theta\sin\phi\cos\phi \\ \sin\theta\cos\theta(f-1+f\cos^2\phi) & -f\cos\theta\sin\phi\cos\phi & (f-1)\sin^2\theta - f\cos^2\theta\cos^2\phi \end{pmatrix}. \tag{3.48}$$

This modifies Eqns. 3.29 into

$$\gamma B'_{\text{eff},x} = \omega_{\text{dem}}\left\{\left[(f-1)\cos^2\theta - f\sin^2\theta\cos^2\phi\right]m'_x + f\sin\theta\sin\phi\cos\phi m'_y\right\} - \omega_{\text{ex}}k^2 m'_x + \gamma B_{\text{AC},x'}, \tag{3.49}$$

$$\gamma B'_{\text{eff},y} = \omega_{\text{dem}}\left[f\sin\theta\sin\phi\cos\phi m'_x - f\sin^2\phi m'_y\right] - \omega_{\text{ex}}k^2 m'_y + \gamma B_{\text{AC},y'}, \tag{3.50}$$

$$\gamma B'_{\text{eff},z} = \omega_B\cos(\theta_B - \theta) - \omega_{\text{dem}}\sin^2\theta, \tag{3.51}$$

where the last term in Eq. 3.51 is $\Gamma_{zz}(k=0)$, since m'_z is spatially homogeneous. The LLG equations in matrix form then read

$$\begin{pmatrix} \omega_2 - i\alpha\omega & -\omega_1 + i\omega \\ -\omega_1 - i\omega & \omega_3 - i\alpha\omega \end{pmatrix}\begin{pmatrix} m'_x \\ m'_y \end{pmatrix} = \gamma\begin{pmatrix} B_{AC,x'} \\ B_{AC,y'} \end{pmatrix}, \tag{3.52}$$

with

$$\omega_0 = \omega_B\cos(\theta_B - \theta) + \omega_{\text{ex}}k^2 - \omega_{\text{dem}}\sin^2\theta, \tag{3.53}$$

$$\omega_1 = \omega_{\text{dem}} f\sin\theta\sin\phi\cos\phi, \tag{3.54}$$

$$\omega_2 = \omega_0 + \omega_{\text{dem}}\left[(1-f)\cos^2\theta + f\sin^2\theta\cos^2\phi)\right], \tag{3.55}$$

$$\omega_3 = \omega_0 + \omega_{\text{dem}} f\sin^2\phi. \tag{3.56}$$

The susceptibility then reads

$$\chi = \frac{\gamma}{(\omega_2 - i\alpha\omega)(\omega_3 - i\alpha\omega) - \omega_1^2 - \omega^2}\begin{pmatrix} \omega_3 - i\alpha\omega & -\omega_1 + i\omega \\ -\omega_1 - i\omega & \omega_2 - i\alpha\omega \end{pmatrix} \tag{3.57}$$

and, disregarding the terms with α, the dispersion is given by

$$\omega_{sw} = \sqrt{\omega_2 \omega_3 - \omega_1^2}, \tag{3.58}$$

while the linewidth is unchanged.

3.3. SPIN-WAVE EXCITATION

Spin waves can be excited using several methods, such as thermally [9–11], by light pulses [12], mechanically via magnetoelastic coupling [13, 14], by spin pumping via the spin-Hall effect [15, 16] or FMR-driving [17], via spin-orbit [18] and spin-transfer torques [19, 20], and inductively [21–25]. In this thesis we always use the last method because 1) we already have the necessary circuit elements, which we use to drive NV centers and 2) it allows to drive spin-waves that are coherent and monochromatic[8].

In the next section we show how certain magnetization patterns and dynamics are excited using the monochromatic microwave field from a microwave stripline. We shall find out that only spin waves with specific values of $\mathbf{k}$ can be excited, and that the excitation efficiency depends on the direction and handedness/chirality of the modes.

3.3.1. INDUCTIVE EXCITATION OF SPIN-WAVES

We saw previously that the precession of the magnetization around its equilibrium position possesses a certain intrinsic handedness. In this section we shall find out that a microstrip stray field is also circularly-polarized with handedness that depends on the wave-vector $\mathbf{k}$. The combined result of these two phenomena is a strong spatial asymmetry in the spin-wave excitation.

In this thesis we use current-carrying circuit elements to generate an oscillating magnetic field $\mathbf{B}$ that excites oscillations of the magnetization $\mathbf{M}$[9]

$$\mathbf{M}(\mathbf{r}) = \frac{1}{\mu_0} \int d\mathbf{r}' \boldsymbol{\chi}(\mathbf{r}, \mathbf{r}') \mathbf{B}(\mathbf{r}'). \tag{3.59}$$

We can remove the convolution in the yz plane with a 2D Fourier transform that yields, in the mixed position and momentum space

$$\mathbf{M}(x, \mathbf{k}, \omega) = \frac{1}{\mu_0 t} \int_{-t}^{0} dx' \boldsymbol{\chi}(x, x', \mathbf{k}, \omega) \mathbf{B}(x', \mathbf{k}, \omega), \tag{3.60}$$

where $\boldsymbol{\chi}$ is the magnetic susceptibility tensor from Eq. 3.36.

We start from the stray field generated by a current distribution $\mathbf{J}$, using Ampere's law [1]

$$\mathbf{B}(\mathbf{r}) = \frac{\mu_0}{4\pi} \int d\mathbf{r}' \mathbf{J}(\mathbf{r}') \times \frac{\mathbf{r} - \mathbf{r}'}{|\mathbf{r} - \mathbf{r}'|^3} = \frac{\mu_0}{4\pi} \nabla \times \int d\mathbf{r}' \frac{\mathbf{J}(\mathbf{r}')}{|\mathbf{r} - \mathbf{r}'|}. \tag{3.61}$$

[8] The range of $\mathbf{k}$ excited depends on the spin-wave linewidth, since the signal generated by the microwave source is extremely narrow (i.e. ~ kHz width for a GHz signal).

[9] Strictly speaking, in Eq. 3.59-3.60 $\mathbf{B}$ should be substituted by $\mu_0 \mathbf{H}$. However, we use $\mathbf{B}$ for simplicity.

where μ_0 is the magnetic permeability of vacuum. Because $\nabla \cdot \mathbf{B} = 0$, $\mathbf{B}$ can be written as the curl of a vector potential $\mathbf{A}$:

$$\mathbf{B}(\mathbf{r}) = \nabla \times \mathbf{A}(\mathbf{r}). \tag{3.62}$$

From Eq. 3.61 we get

$$\mathbf{A}(\mathbf{r},\omega) = \frac{\mu_0}{4\pi}\int \mathrm{d}\mathbf{r}' \frac{\mathbf{J}(\mathbf{r}',\omega)e^{ik|\mathbf{r}-\mathbf{r}'|}}{|\mathbf{r}-\mathbf{r}'|}, \tag{3.63}$$

where $k = \omega/c = \sqrt{k_x^2+k_y^2+k_z^2}$ with c the speed of light. We consider a microstrip of width w, length L and thickness h with current flowing parallel to z, thus $\mathbf{A} = A\hat{\mathbf{z}}$, so that $B_z = 0$.

Eq. 3.62 then becomes

$$(B_x, B_y) = (\partial A_z/\partial y, \partial A_z/\partial x). \tag{3.64}$$

Substituting the Weyl identitity[10] and carrying out the differentiation and integration, we obtain the Fourier components of the stray field in reciprocal space [28]:

$$B_{x(y)}(x,k_y,k_z) = 2i\mu_0 J(\omega)\frac{e^{-ik_x x}}{k_x}\frac{e^{ik_x h}-1}{k_{x(y)}}\sin\left(k_y\frac{w}{2}\right)\sin(k_z\frac{L}{2})\frac{e^{-ik_z z}}{k_z}, \tag{3.65}$$

where $z = 0$ is located at the center of the microstrip. At the few-GHz frequency we consider in the experiments, $k = \omega/c \ll 100$ rad/m, while typical spin-wavevectors for our experiments are $10^5 - 10^7$ rad/m, so that $k_x = \sqrt{k^2-k_y^2-k_z^2} \to i\sqrt{k_y^2+k_z^2} = i\kappa$. Thus,

$$B_x(x,k_y,k_z) = -2i\mu_0 J(\omega)e^{\kappa x}\frac{e^{-\kappa h}-1}{\kappa^2}\sin\left(k_y\frac{w}{2}\right)\sin(k_z\frac{l}{2})\frac{e^{-ik_z z}}{k_z}, \tag{3.66}$$

$$B_y(x,k_y,k_z) = 2\mu_0 J(\omega)e^{\kappa x}\frac{e^{-\kappa h}-1}{\kappa k_y}\sin\left(k_y\frac{w}{2}\right)\sin(k_z\frac{l}{2})\frac{e^{-ik_z z}}{k_z}. \tag{3.67}$$

These expressions for the field of a microstrip are useful for further calculations and offer the following insights:

- Only certain values of the spin-wavevector can be excited with a microstrip. Specifically, when an integer number of wavelengths fits under the microstrip width ($k = n\cdot 2\pi/w$), the excitation efficiency vanishes. A wire that is very long in a certain direction (z in all experiments) can efficiently excite only large wavenumbers (i.e. with wavelength ~larger than the length) in the same direction. Similarly, it is less efficient to excite spin waves with wavelength below 1 µm with strips that are wider than a micrometer (Fig. 3.5). This difficulty in exciting nanometer-sized spin waves is a drawback of inductive spin-wave excitation.

- The polarization of the microstrip field depends on the value of $\mathbf{k}$. Because $B_x = -iB_y k_y/\kappa$ (from Eqs. 3.66-3.67), we can identify two interesting situations:

[10] The Weyl identity is [26, 27] $\frac{e^{ik\sqrt{(x-x')^2+(y-y')^2+(z-z')^2}}}{\sqrt{(x-x')^2+(y-y')^2+(z-z')^2}} = \frac{i}{2\pi}\int \mathrm{d}k_y \mathrm{d}k_z \frac{e^{ik_x|x-x'|+ik_y(y-y')+ik_z(z-z')}}{k_x}$.

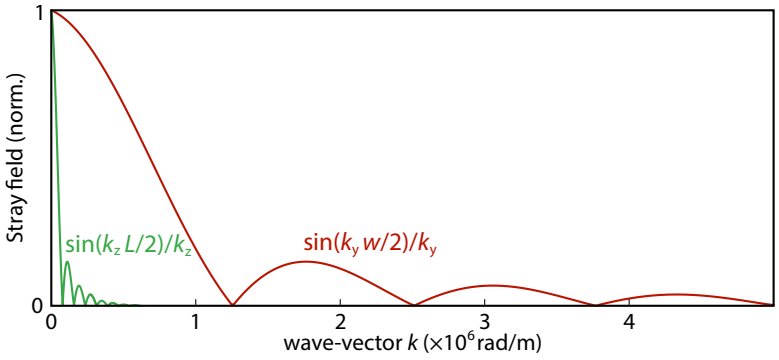

Figure 3.5: Effect of the microstrip shape on the stray field. A microstrip of length $L = 100$ μm (along z) and width $w = 5$ μm (along y) can excite spin waves with large k_y (red line) and small k_z (green line).

  - When $|k_z| \gg |k_y|$ (BV waves), $|B_x| \ll |B_y|$, so that the field is linearly polarized along $\hat{\mathbf{y}}$.

  - When $|k_y| \gg |k_z|$ (DE waves), $B_x \to -i\,\mathrm{sign}(k_y)B_y$ represents a circularly polarized field[11] with opposite handedness for $\pm k_y$ (Fig. 3.6a): Even though the stripline field is linearly polarized at each location, its right-circular (left-circular) component couples only to modes propagating with wavevector $+k_y$ ($-k_y$).

- Spin waves are preferentially excited in certain directions, i.e. their amplitude depends on $\mathbf{k}$. For $|k_y| \gg |k_z|$ we have

  - For $+k_y$, from $B_y = iB_x$ and Eq. 3.36 follows that $m_y = im_x/\eta$, where $\eta = |m_x|/|m_y|$ has been defined in Section 3.2.2, and[12]

$$m_y \approx B_y\omega_2(1+\eta). \tag{3.68}$$

  - For $-k_y$, from $B_y = -iB_x$ follows that $m_y = -im_x/\eta$, with

$$m_y \approx B_y\omega_2(1-\eta). \tag{3.69}$$

  Thus, we see from Eq. 3.68-3.69 that the spin-wave amplitude is strongly asymmetric: spin waves with circular precession (i.e. $\eta = 1$) are exclusively excited with $+k_y$,

[11] Using Jones matrices [29], we can write an oscillating field as $B = \begin{pmatrix} B_x \\ B_y e^{i\varphi} \end{pmatrix}$. A field for which $B_y = \pm iB_x$ can be written as $B = B_x \begin{pmatrix} 1 \\ \pm i \end{pmatrix} = \begin{pmatrix} 1 \\ e^{\pm i\pi/2} \end{pmatrix}$, such that B_y trails (leads) B_x by $\pi/2$: the field is right-circularly (left-circularly) polarized.

[12] Here we are again disregarding the terms in α in Eq. 3.36.

thus propagating along $+y$. As the precession becomes more elliptical, the left-propagating spin waves are also excited, but with very low efficiency. This strongly asymmetric excitation of DE waves by a microstrip can be seen in Chapters 4-5.

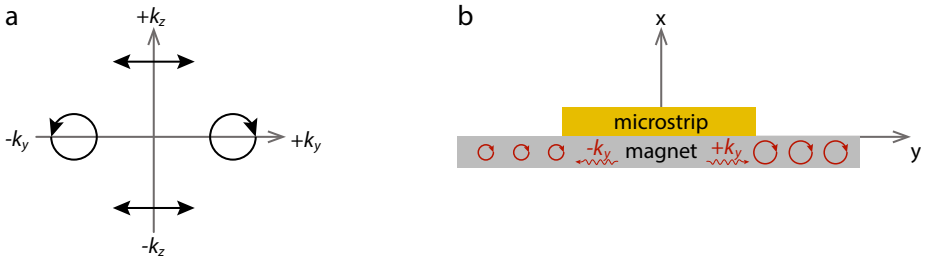

Figure 3.6: Chiral inductive excitation of DESW by a microstrip field. (**a**) For $\mathbf{k} = \pm k_z$, the microstrip field (black arrows) is linearly polarized along y. For $\mathbf{k} = +k_y(-k_y)$, the field is right(left)-circularly polarized in the xy plane. (**b**) The right(left)-propagating spin waves (in red) are excited with large (small) amplitude.

From the susceptibility (Eq. 3.36) and the microstrip field (Eqs. 3.66-3.67), we can calculate the dynamic magnetization in $k-$space using Eq. 3.60, and Fourier-transforming back into real space yields

$$M_i(\boldsymbol{\rho}, t) = \frac{1}{4\pi^2}\int\int \mathrm{d}\mathbf{k} e^{i\mathbf{k}\cdot\boldsymbol{\rho}-i\omega t} M_i(x,\mathbf{k}), \tag{3.70}$$

where $\boldsymbol{\rho} = (y,z)$.

3.4. STRAY FIELD OF A SPIN WAVE

We can now derive the stray field of a spin wave of in-plane wavevector $\mathbf{k}$ and frequency $\omega/2\pi$ from Eqs. 3.9-3.10:

$$B_{sw,x}(x,\mathbf{k}) = \frac{\mu_0 M_s}{2} e^{-kx}(1-e^{-kt})\left(-m_x(\mathbf{k}) + i\sin\phi m_y(\mathbf{k})\right), \tag{3.71}$$

$$B_{sw,y}(x,\mathbf{k}) = \frac{\mu_0 M_s}{2} e^{-kx}(1-e^{-kt})\left(i\sin\phi m_x(\mathbf{k}) + \sin^2\phi m_y(\mathbf{k})\right), \tag{3.72}$$

$$B_{sw,z}(x,\mathbf{k}) = \frac{\mu_0 M_s}{2} e^{-kx}(1-e^{-kt})\left(i\cos\phi m_x(\mathbf{k}) + \sin\phi\cos\phi m_y(\mathbf{k})\right), \tag{3.73}$$

where again $\sin\phi = k_y/k$ and $\cos\phi = k_z/k$, so that $B_{sw,y} = -i(k_y/k)B_{sw,x}$ and $B_{sw,z} = -i(k_z/k)B_{sw,x}$.

Because we use NV centers to study spin waves via their stray fields, these results are central to this thesis. Let's examine a few interesting cases:

- For $\phi = 0(\pi)$ (BV geometry), $B_{sw,y} = 0$ and $B_{sw,z} = -(+)iB_{sw,x}$. In the xy plane, however, this field is linearly polarized.

- In the DE geometry the situation is dramatically different.
  For $\phi = +\pi/2$ the spin waves propagate with $+k_y$, therefore $m_y = i\,m_x/\eta$ (from Section 3.3) and $B_{sw,y} = -iB_{sw,x}$. This field is circularly polarized in the xy plane, with handedness opposite to that of the microstrip stray field, which excited the spin-waves along $+k_y$ in the first place (Eqs. 3.66-3.67).

- For $\phi = -\pi/2$, $B_{sw,y} = +iB_{sw,x}$. Because these modes propagate toward $-k_y$, they are characterized by $m_y = -i\,m_x/\eta$. Using this relation, we see that both $B_{sw,x}$ and $B_{sw,y}$ vanish (remembering that the formula for the stray fields holds above the magnetic film, while below the film the terms containing i change sign, see Section. 3.1).

Let's summarize the importance of these results (Fig. 3.7):

- The right-propagating DE spin waves ($+k_y$) generate a stray field above the magnetic film that is left-circularly polarized. If there was an ensemble of NV centers above the film, with axes parallel to the magnetic z axis, the spin-wave field would have the correct handedness to drive the $0 \leftrightarrow -1$ NV transition of those NVs on the right of the microstrip, and would not drive the $0 \leftrightarrow +1$ transition. However, there is usually an angle between the two axes, so that the field drives the $0 \leftrightarrow +1$ transition as well.

- The left-propagating spin waves are not efficiently excited and generate a left-circularly polarized stray field below the film. Above the film, the field is zero for $\eta = 1$, and non-zero for smaller ellipticity, but with opposite handedness, such that it can drive the $0 \leftrightarrow +1$ NV transition.

- BV waves generate a field in the xz plane. Its projection onto the xy plane (relevant to NV driving) is a linear field (for any out-of-plane angle between the NV and the magnet), which drives both transitions with equal efficiency.

3.5. SPIN-WAVE DETECTION WITH NV MAGNETOMETRY

In this section we derive the effect of the stray field of coherent (Section 3.5.1) and thermal (Section 3.5.2) spin waves on the NV center spin state.

3.5.1. DETECTING COHERENT SPIN WAVES: RABI FREQUENCY ENHANCEMENT

In Chapter 4 we measure the NV Rabi frequency induced by the stray field of spin waves to image them and ultimately extract the amplitude of the spin-wave oscillations. In Chapter 5 we detect a change in spin-wave damping by measuring the spatial variations of the Rabi frequency. In this section we derive the Rabi frequency induced by the spin-wave stray field.

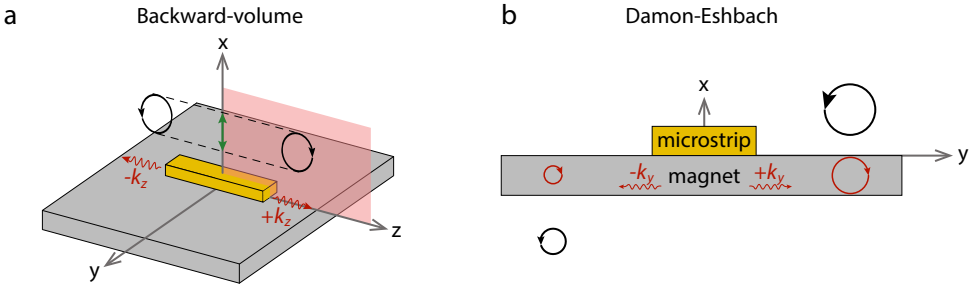

Figure 3.7: Momentum-locked spin-wave handedness. (**a**) Backward-volume spin waves (red arrows) generate fields that are circularly-polarized in the xz plane (black arrows). In the xy plane, the field is linearly polarized (green arrow). (**b**) Damon-Eshbach spin waves (red arrows) are excited with different amplitudes on the two sides of the stripline. The field they generate (black arrows) is circularly-polarized in the xy plane, with handedness opposite to that of the spin precession. Right-propagating spin waves generate a large left-circular field above the magnetic film. Conversely, left-propagating spin waves (less efficiently excited) generate a left-circular field below the film. If we consider spin waves with an elliptical precession (i.e. $\eta < 1$), a small field component is present also below (above) the film, on the right (left) side, that has the opposite handedness of the component above (below).

We know from 2.17 that the $\omega_\pm$ transition is driven by a resonant magnetic field that is circularly polarized in the plane perpendicular to the NV axis, inducing Rabi rotations with frequency $\Omega_R^\pm = \gamma|B_x \mp iB_y|/\sqrt{2}$. We can use the results of the previous section for the spin-wave field, but we need to transform them into the NV reference frame (rotated by θ_{NV} from z toward x about y). To do so, we use the rotation matrix of Eq. 3.47 to obtain the $\mathbf{B}_+$ component in the NV frame:

$$|\mathbf{B}_+^{NV}| = |B_x \cos\theta_{NV} - B_z \sin\theta_{NV} + iB_y|. \tag{3.74}$$

For spin waves propagating along $+k_y$, we obtain

$$\Omega_R^\pm = |B_{sw}^0 m_y| \frac{\gamma\sqrt{\eta^2 + \sin^2\phi}}{\sqrt{2}} \sqrt{(\cos\theta_{NV} \pm \sin\phi)^2 + \sin^2\theta_{NV}\cos^2\phi}, \tag{3.75}$$

where $B_{sw}^0 = \mu_0 M_s e^{-kx}(1 - e^{-kt})/2$.

We see that, for BVSWs ($\phi = 0, \pi$), $\Omega_R^\pm = |B_{sw}^0 m_y \eta/\sqrt{2}|$, so that $\omega_\pm$ are driven equally. Moreover, when the waves are very elliptical[13] (small η) the spin-wave driving of the NV transitions decreases correspondingly.

For $\phi = \pi/2$, $\Omega_R^\mp = |B_{sw}^0 m_y|\sqrt{\eta^2 + 1}|\cos\theta_{NV} \pm 1|/\sqrt{2}$. As previously introduced, for $\theta_{NV} = 0$, the spin-wave field is circularly polarized in the NV-xy axis and only drives ω^-.

[13] At large wavelengths, the out-of-plane component is much smaller than the in-plane one [28].

In Chapter 4 we build on this model, considering the additional stray field components of a microwave stripline and of a bonding wire, used as antenna, to extract the precession amplitude of DE spin waves from experiments. In Chapter 5 we monitor the spatial decay of the Rabi frequency to characterize the spin-wave damping induced by metallic electrodes.

3.5.2. MAGNETIC NOISE GENERATED BY THERMALLY-EXCITED SPIN WAVES

Even in absence of direct driving, incoherent spin waves are thermally excited because of the finite temperature. Such spin waves generate fluctuating magnetic fields that act as noise and can induce relaxation of the NV spin states. In Chapter 6, we probe these magnetic fluctuations in a nickel thin film using NV relaxometry. In this section we derive the magnetic field noise generated by these thermal spin-waves, and calculate the NV relaxation rates they induce.

The system considered is a thin magnetic film in the yz plane. A single NV center is located at distance d above the film, with axis oriented in the xz plane at an angle θ_{NV} from z. A static field is applied along the NV axis, which lifts the magnetization of the film out of plane by an angle θ. From Eq. 3.9, 3.10, and the rotation matrix $\mathbf{R}(\theta)$ (Eq. 3.47) the dipolar field in the NV frame is given by

$$\mathbf{B}_{NV} = M_s \mathbf{R}(\theta_{NV}) \mathbf{\Gamma}(\mathbf{k}) \mathbf{R}^{\mathbf{T}}(\theta) \mathbf{m}'(\mathbf{k}) = M_s \mathbf{\Gamma}^{\text{eff}}(\mathbf{k}) \mathbf{m}'(\mathbf{k}). \tag{3.76}$$

Substituting into Eq. 2.20, we can express the relaxation rates as an integral over k-space [3]

$$\Gamma_{\mp} = \frac{\gamma^2 M_s^2}{2} \int \frac{\mathrm{d}\mathbf{k}}{(2\pi)^2} \sum_{i,j=\{x,y\}} \Gamma^{\text{eff}}_{\pm i}(\mathbf{k}) \Gamma^{\text{eff}}_{\mp j}(-\mathbf{k}) C_{ij}(\mathbf{k}, \omega_{\mp}), \tag{3.77}$$

where the elements of the dipolar tensor $\Gamma^{\text{eff}}_{\pm i} = \Gamma^{\text{eff}}_{xi} \pm i\Gamma^{\text{eff}}_{yi}$ and C_{ij} is the Fourier transform of the magnetization correlator [3, 30]

$$C_{ij}(\mathbf{r}-\mathbf{r}', t-t') = \left\langle m'_i(\mathbf{r}, t) m'_j(\mathbf{r}', t') \right\rangle. \tag{3.78}$$

The magnetization correlations are governed by the dispersion and the band occupation, determined by the temperature T. Defining $D_{\text{th}} = \alpha k_B T/(\gamma M_s t)$, with k_B the Boltzmann constant, we can express the C_{ij} as [3]

$$C_{ij}(\mathbf{k}, \omega) = 2D_{\text{th}} \sum_{\rho=\{x,y\}} \chi_{i\rho}(\mathbf{k}, \omega) \chi_{j\rho}(-\mathbf{k}, -\omega), \tag{3.79}$$

where χ_{ij} are the elements of the susceptibility in Eq. 3.57 (for $\theta_B = \theta_{NV}$).

In the next chapter we see that these equations agree quite well with the measured relaxation rates. Unlike previous models [17, 31, 32], which only included in-plane oscillations of the magnetization (thus, the spin-wave fields were linearly polarized, coupling equally well to both NV ESR transitions), this model includes the handedness of the spin-waves and their fields, which therefore couple differently to the two NV ESR transitions. Thus, this model can be applied without arbitrary scaling constant to account for the

different rates at $\omega_{\pm}$. We use this in Chapter 6 to calculate the NV relaxation rate as a function of the static field (Fig. 3.8).

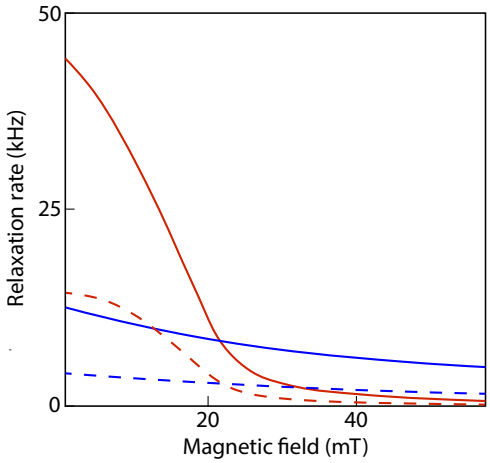

Figure 3.8: NV relaxation rate as a function of magnetic field. Red (blue) lines: calculated relaxation rate of the $|0\rangle \leftrightarrow |-1\rangle$ ($|0\rangle \leftrightarrow |+1\rangle$) transition, for a distance of 200 nm (solid lines) and 300 nm (dashed lines) between an NV center and a nickel film of thickness 40 nm.

REFERENCES

[1] J. D. Jackson, *Classical Electrodynamics* (Wiley, New York, 1998).

[2] K. Y. Guslienko and A. N. Slavin, *Magnetostatic Greens functions for the description of spin waves in finite rectangular magnetic dots and stripes,* Journal of Magnetism and Magnetic Materials **323**, 2418 (2011).

[3] A. Rustagi, I. Bertelli, T. Van Der Sar, and P. Upadhyaya, *Sensing chiral magnetic noise via quantum impurity relaxometry,* Physical Review B **102**, 220403 (2020).

[4] D. D. Stancil and A. Prabhakar, *Spin waves* (Springer, New York, 2009).

[5] T. L. Gilbert, *A phenomenological theory of damping in ferromagnetic materials,* IEEE Transactions on Magnetics **40**, 3443 (2004).

[6] C. Kittel, *Introduction to Solid State Physics*, 8th ed. (Wiley, 2005).

[7] J. R. Eshbach and R. W. Damon, *Surface magnetostatic modes and surface spin waves,* Physical Review **118**, 1208 (1960).

[8] R. W. Damon and J. R. Eshbach, *Magnetostatic modes of a ferromagnet slab,* Journal of Physics and Chemistry of Solids **19**, 308 (1961).

[9] K. Uchida, S. Takahashi, K. Harii, J. Ieda, W. Koshibae, K. Ando, S. Maekawa, and E. Saitoh, *Observation of the spin Seebeck effect,* Nature **455**, 778 (2008).

[10] J. Xiao, G. E. Bauer, K. C. Uchida, E. Saitoh, and S. Maekawa, *Theory of magnon-driven spin Seebeck effect,* Physical Review B **81**, 214418 (2010).

[11] M. Schneider, T. Brächer, D. Breitbach, V. Lauer, P. Pirro, D. A. Bozhko, H. Y. Musiienko-Shmarova, B. Heinz, Q. Wang, T. Meyer, F. Heussner, S. Keller, E. T. Papaioannou, B. Lägel, T. Löber, C. Dubs, A. N. Slavin, V. S. Tiberkevich, A. A. Serga, B. Hillebrands, and A. V. Chumak, *Bose–Einstein condensation of quasiparticles by rapid cooling,* Nature Nanotechnology **15**, 457 (2020).

[12] T. Kampfrath, A. Sell, G. Klatt, A. Pashkin, S. Mährlein, T. Dekorsy, M. Wolf, M. Fiebig, A. Leitenstorfer, and R. Huber, *Coherent terahertz control of antiferromagnetic spin waves,* Nature Photonics **5**, 31 (2011).

[13] M. Weiler, L. Dreher, C. Heeg, H. Huebl, R. Gross, M. S. Brandt, and S. T. Goennenwein, *Elastically driven ferromagnetic resonance in nickel thin films,* Physical Review Letters **106**, 117601 (2011).

[14] X. Li, D. Labanowski, S. Salahuddin, and C. S. Lynch, *Spin wave generation by surface acoustic waves,* Journal of Applied Physics **122**, 43904 (2017).

[15] L. J. Cornelissen, J. Liu, R. A. Duine, J. B. Youssef, and B. J. Van Wees, *Long-distance transport of magnon spin information in a magnetic insulator at room temperature,* Nature Physics **11**, 1022 (2015).

[16] L. J. Cornelissen, J. Liu, B. J. van Wees, and R. A. Duine, *Spin-Current-Controlled Modulation of the Magnon Spin Conductance in a Three-Terminal Magnon Transistor,* Physical Review Letters **120**, 097702 (2018).

[17] C. Du, T. van der Sar, T. X. Zhou, P. Upadhyaya, F. Casola, H. Zhang, M. C. Onbasli, C. A. Ross, R. L. Walsworth, Y. Tserkovnyak, and A. Yacoby, *Control and local measurement of the spin chemical potential in a magnetic insulator,* Science **357**, 195 (2017).

[18] M. Collet, X. De Milly, A. Kelly, V. V. Naletov, R. Bernard, P. Bortolotti, J. B. Youssef, V. E. Demidov, S. O. Demokritov, J. L. Prieto, M. Muñoz, V. Cros, A. Anane, G. De Loubens, and . O. Klein, *Generation of coherent spin-wave modes in yttrium iron garnet microdiscs by spin-orbit torque,* Nature Communications **7**, 10377 (2016).

[19] S. I. Kiselev, J. C. Sankey, I. N. Krivorotov, N. C. Emley, R. J. Schoelkopf, R. A. Buhrman, and D. C. Ralph, *Microwave oscillations of a nanomagnet driven by a spin-polarized current,* Nature **425**, 380 (2003).

[20] K. J. Lee, A. Deac, O. Redon, J. P. Nozières, and B. Dieny, *Excitations of incoherent spin-waves due to spin-transfer torque,* Nature Materials **3**, 877 (2004).

[21] C. Kittel, *On the theory of ferromagnetic resonance absorption,* Physical Review **73**, 155 (1948).

[22] L. R. Walker, *Magnetostatic modes in ferromagnetic resonance,* Physical Review **105**, 390 (1957).

[23] S. O. Demokritov, V. E. Demidov, O. Dzyapko, G. A. Melkov, A. A. Serga, B. Hillebrands, and A. N. Slavin, *Bose-Einstein condensation of quasi-equilibrium magnons at room temperature under pumping,* Nature **443**, 430 (2006).

[24] C. W. Sandweg, Y. Kajiwara, A. V. Chumak, A. A. Serga, V. I. Vasyuchka, M. B. Jungfleisch, E. Saitoh, and B. Hillebrands, *Spin pumping by parametrically excited exchange magnons,* Physical Review Letters **106**, 216601 (2011).

[25] I. S. Maksymov and M. Kostylev, *Broadband stripline ferromagnetic resonance spectroscopy of ferromagnetic films, multilayers and nanostructures,* Physica E: Low-Dimensional Systems and Nanostructures **69**, 253 (2015).

[26] L. Novotny and B. Hecht, *Principles of nano-optics*, 2nd ed. (Cambridge University Press, Cambridge, 2006).

[27] H. Weyl, *Ausbreitung elektromagnetischer Wellen über einem ebenen Leiter,* Annalen der Physik **365**, 481 (1919).

[28] I. Bertelli, J. J. Carmiggelt, T. Yu, B. G. Simon, C. C. Pothoven, G. E. Bauer, Y. M. Blanter, J. Aarts, and T. van der Sar, *Magnetic resonance imaging of spin-wave transport and interference in a magnetic insulator,* Science advances **6**, eabd3556 (2020).

[29] E. Hecht, *Optics*, 4th ed. (Pearson, 2002).

[30] B. Flebus and Y. Tserkovnyak, *Quantum-Impurity Relaxometry of Magnetization Dynamics,* Physical Review Letters **121**, 187204 (2018).

[31] T. van der Sar, F. Casola, R. Walsworth, and A. Yacoby, *Nanometre-scale probing of spin waves using single-electron spins,* Nature Communications **6**, 1 (2015).

[32] C. M. Purser, V. P. Bhallamudi, F. Guo, M. R. Page, Q. Guo, G. D. Fuchs, and P. C. Hammel, *Spinwave detection by nitrogen-vacancy centers in diamond as a function of probe-sample separation,* Applied Physics Letters **116**, 202401 (2020).

4

MAGNETIC RESONANCE IMAGING OF SPIN-WAVE TRANSPORT AND INTERFERENCE IN A MAGNETIC INSULATOR

Spin waves — the elementary excitations of magnetic materials — are prime candidate signal carriers for low-dissipation information processing. Being able to image coherent spin-wave transport is crucial for developing interference-based spin-wave devices. We introduce magnetic resonance imaging of the microwave magnetic stray fields that are generated by spin waves as a new approach for imaging coherent spin-wave transport. We realize this approach using a dense layer of electronic sensor spins in a diamond chip, which combines the ability to detect small magnetic fields with a sensitivity to their polarization. Focusing on a thin-film magnetic insulator, we quantify spin-wave amplitudes, visualize spin-wave dispersion and interference, and demonstrate time-domain measurements of spin-wave packets. We theoretically explain the observed anisotropic spin-wave patterns in terms of chiral spin-wave excitation and stray-field coupling to the sensor spins. Our results pave the way for probing spin waves in atomically thin magnets, even when embedded between opaque materials.

This chapter has been published in *Science Advances* **6**, eabd3556 (2020) by **I. Bertelli**, J. J. Carmiggelt, T. Yu, B. G. Simon, C. C. Pothoven, G. E. W. Bauer, Y. M. Blanter, J. Aarts, T. van der Sar.

4.1. INTRODUCTION

Over the last few decades, the desire to understand and control spin transport, and to use it in information technology, has invigorated the field of spintronics. A central goal of the field is to provide information processing based on the spin of the electron instead of its charge and thereby avoid the heating associated with charge currents. As heating is currently the main obstacle for increasing computational speed, spin-based information processing may provide the next transformative change in information technology.

Promising signal carriers for low-dissipation information transport are spin waves [1, 2] — the collective spin excitations of magnetic materials. Spin waves exist even in electrically insulating magnets, where they are able to propagate inherently free of the dissipative motion of charge. They can have nanometer wavelengths and gigahertz frequencies well suited for chip-scale device technologies and interference-based spin-wave logic circuits [2]. Consequently, a growing research field focuses on spin-wave devices such as interconnects, interferometers, transistors, amplifiers, and spin-torque oscillators [3–7].

Being able to image coherent spin waves in thin-film magnets is crucial for developing spin-wave device technology. Leading techniques for imaging coherent spin waves, such as transmission x-ray microscopy [8, 9], Brillouin light scattering [10], and Kerr microscopy [11], rely on a spin-dependent optical response of a magnetic material. Here, we introduce a new approach: phase-sensitive magnetic resonance imaging of the microwave magnetic stray fields generated by coherent spin waves. We realize this approach using a layer of electronic sensor spins in a diamond chip as imaging platform (Fig. 4.1A). These spins enable quantitative measurements of microwave magnetic fields including their polarization, making the approach well suited for spin-wave imaging in magnetic thin films.

Focusing on a ~200-nm-thick magnetic insulator, we quantify spin-wave amplitudes, visualize the spin-wave dispersion, and demonstrate time-domain measurements of spin-wave packets. We observe unidirectional emission of spin waves that autofocus, interfere, and produce chiral magnetic stray fields with a handedness that matches that of the natural precession of the sensor spins. We present a theoretical analysis of the chiral spin-wave excitation and stray-field coupling to the sensor spins and show that it accurately describes the observed spatial spin-wave maps.

We detect the magnetic fields generated by spin waves using electron spins associated with nitrogen-vacancy (NV) lattice defects in diamond [12]. These spins can be initialized and read out optically and manipulated with high fidelity by microwaves. Over the last decade, NV magnetometry has emerged as a powerful platform for probing static and dynamic magnetic phenomena in condensed matter systems [13]. Key is an NV-sample distance tunable between 10 and 1000 nm that is well matched with the length scales of spin textures such as magnetic domain walls, cycloids, vortices, and skyrmions [14–16] as well as those of dynamic phenomena such as spin waves [17–21]. Recent experiments demonstrated that NV magnetometry has the sensitivity required for imaging the static magnetization of monolayer van der Waals magnets [22]. Here, we develop

NV-based magnetic resonance imaging into a platform for studying coherent spin waves via the gigahertz magnetic fields that they generate.

4.2. RESULTS

Our imaging platform consists of a diamond chip hosting a dense layer of shallowly implanted NV spins. We position this chip onto a thin film of yttrium iron garnet (YIG) — a ferrimagnetic insulator with record-high magnetic quality (Fig. 4.1A-B) [23]. The typical distance between the diamond and the magnetic film is ~ 1 µm (Supplementary Material). We excite spin waves using microwave striplines microfabricated onto the YIG. When the spin-wave frequency matches an NV electron spin resonance (ESR) frequency, the oscillating magnetic stray field B_{SW} drives NV spin transitions [17, 19] that we detect through the NV's spin-dependent photoluminescence (Materials and Methods). By tuning the external static magnetic field B_0, we sweep the NV ESR frequencies through the spin-wave band, thereby probing spin waves with different wavelength (Fig. 4.1C).

We start by characterizing the NV photoluminescence as a function of B_0 and the frequency ω_{MW} of a microwave drive current sent through the stripline, at a distance of ~ 5 µm from the stripline edge (Fig. 4.1D). This microwave current not only generates an oscillating magnetic field that drives ESR transitions of the NV spins directly but also excites spin waves in the YIG film that can drive NV ESR transitions via their magnetic stray field (Fig. 4.1A). The dips in the observed NV photoluminescence correspond to the ESR frequencies of the NV spins in the diamond (Fig. 4.1D; Materials and Methods). We observe an enhanced contrast for the ω_- transition when $B < B_0^{(2)}$. In this region, the excited spin waves efficiently drive the ω_- ESR transition.

We image the spin waves excited by the stripline in the YIG film by characterizing the contrast of the ω_- ESR transition as a function of the distance to the stripline (Fig. 4.2A). We do so by tuning the magnetic field such that the ω_- frequency is 2.17 GHz, i.e., 160 MHz above the bottom of the spin-wave band, thereby exciting spin waves in the film. To gain the phase sensitivity required for detecting the individual wavefronts of these propagating spin waves, we let their stray field interfere with an additional, externally applied microwave magnetic field B_{REF} that is spatially homogeneous and has the same frequency (Materials and Methods). As formulated mathematically below, this interference leads to a spatial standing-wave pattern in the total magnetic field that drives the NV ESR transition with a spatial periodicity equal to the spin-wave wavelength. We can thus rapidly visualize the spin waves by measuring the ratio between the NV photoluminescence with and without applied microwaves (Fig. 4.2A).

Quantifying the amplitude of a spin wave is a challenging task for any technique because the coupling between spin wave and probe is often not well known. With NV magnetometry, however, we accurately measure the microwave magnetic field generated by a spin wave as described by Maxwell's equations. We can therefore determine the amplitude of a spin wave of known direction and ellipticity with high confidence by solving a well-defined inverse problem.

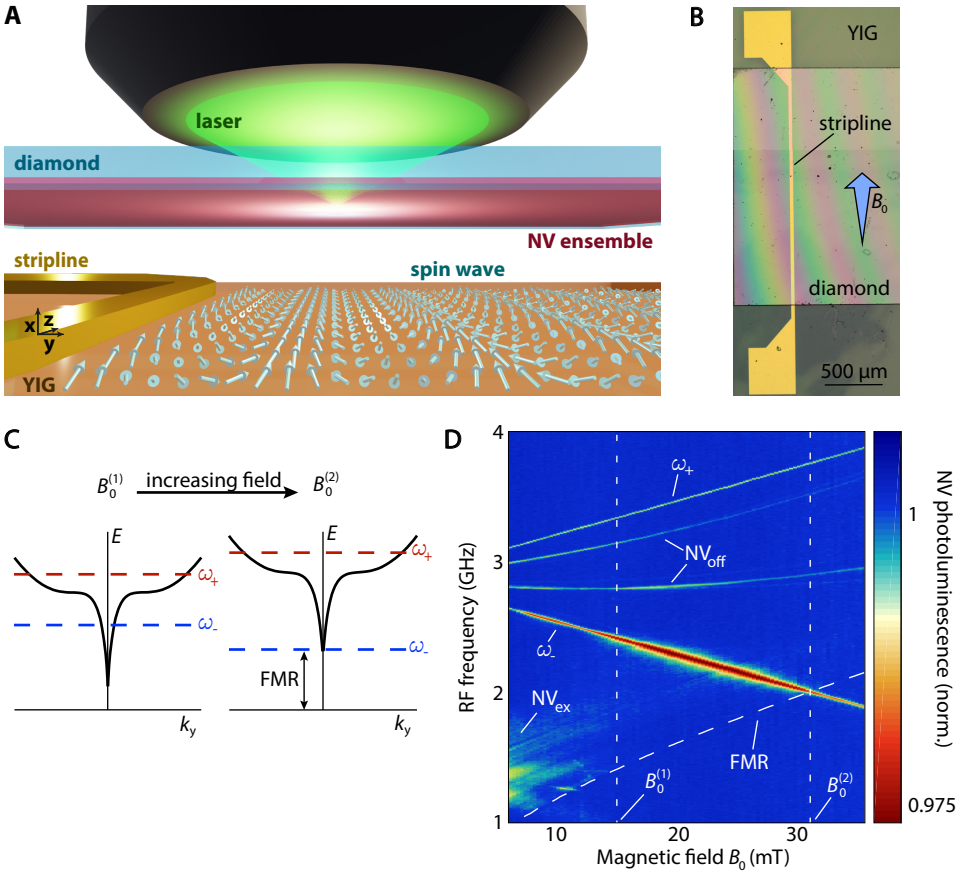

Figure 4.1: Imaging spin waves using NV spins in diamond. (**A**) A diamond hosting a layer of NV spins implanted at 20 nm below its surface is placed onto a film of YIG (thickness of 245 nm) grown on gadolinium gallium garnet (GGG). The NVs detect the magnetic fields of stripline-excited spin waves. (**B**) NV-containing diamond (thickness of ~ 40 µm) on YIG with gold stripline. B_0 is applied along the stripline at $\phi = 35°$ relative to the sample plane, aligning it with one of the four possible NV orientations. (**C**) The NV ESR frequencies $\omega_\pm$ are swept over the Damon-Eshbach spin-wave dispersion (black line) by tuning B_0. For any $B_0^{(1)} < B_0^{(2)}$, ω_- is resonant with spin waves of finite wavelength. At $B_0 < B_0^{(2)}$, ω_- is resonant with the ferromagnetic resonance (FMR). (**D**) Normalized NV photoluminescence versus B_0 and microwave drive frequency, measured at ~ 5 µm from a 2.5 µm-wide stripline. Indicated are the electronic ground-state ESR transitions $\omega_\pm$ (NV_{off}) of the NVs aligned (not aligned) with B_0. An electronic excited-state ESR transition (NV_{ex}) is visible because of the continuous optical and microwave excitation and identified through its location at $\omega_+/2$ [12]. The FMR is calculated from the independently determined saturation magnetization (Supplementary Material).

To illustrate the concept, we formulate the magnetic stray field of a spin wave traveling perpendicularly to the static magnetization (such as the one in Fig. 4.2B) in the reference frame depicted in Fig. 4.1A with transverse magnetization

$$\mathbf{m}_\perp(y) = m_\perp^0 \mathrm{Re}\left\{e^{i(k_y y-\omega t)}(\hat{\mathbf{y}} - i\eta\hat{\mathbf{x}})\right\} \tag{4.1}$$

where k_y, ω, and η are the wave number, angular frequency, and ellipticity of the spin wave, respectively; t is the time; and hats denote unit vectors. This spin wave produces a magnetic stray field above the film that rotates in the xy plane (see the Supplementary Material and [24]).

$$\mathbf{B}_{SW}(y) = -B_{SW}^0 \mathrm{Re}\left\{e^{i(k_y y-\omega t)}(\hat{\mathbf{y}} + i\,\mathrm{sgn}(k_y)\hat{\mathbf{x}})\right\} \tag{4.2}$$

where $B_{SW}^0 = \mu_0 m_\perp^0 \left[1+\mathrm{sgn}(k_y)\eta\right]|\mathbf{k}|d e^{-|k_y|x_0}/2$, x_0 is the NV-YIG distance, and d is the thickness of the YIG film.

The handedness of $\mathbf{B}_{SW}$ is opposite to that of $\mathbf{m}_\perp$ for a spin wave traveling to the right (i.e., with $k_y > 0$; as in Fig. 4.2B), which drives the ω_- (rather than the ω_+) NV spin transition (Supplementary Material). Moreover, the amplitude B_{SW}^0 depends on the propagation direction and degree of ellipticity η of the spin wave: Those traveling to the right (left) generate a stronger field above (below) the magnetic film. Therefore, only the ω_- transition of NV centers to the right of the stripline in Fig. 4.2B is excited (Supplementary Material). The resulting NV spin rotation rate (Rabi frequency) ω_{Rabi} is determined by the interference between the spin-wave field and the reference field B_{REF}

$$\omega_{Rabi} = \sqrt{2}\gamma|B_{SW}^0 \cos^2\left(\frac{\phi}{2}\right)e^{ik_y y} - B_{REF}| \tag{4.3}$$

where $\phi = 35°$ is the angle with respect to (w.r.t.) the film of the NV centers used in Fig. 4.2 and $\gamma/2\pi = 28$ GHz/T is the (modulus of the) electron gyromagnetic ratio. Fitting the data in Fig. 4.2B by Eq. 4.3(including a spatial decay; see the Supplementary Material), we extract a spin-wave amplitude $m_\perp^0 = 0.033(1)\ M_s$ at the location of the stripline and a decay length of 1.2(1) mm, corresponding to a Gilbert damping parameter $1.2(1)\cdot 10^{-4}$, which is similar to the typically reported $1\cdot 10^{-4}$ for films of similar thickness [25].

By tuning the externally applied magnetic field, we sweep the NV ESR frequency through the spin-wave band and access spin waves with different wavelengths (Fig. 4.3A), as schematically described in Fig. 4.1C. In Fig. 4.3A-B, we visualize the individual spin-wave fronts using the interference between the direct stripline field and the stray field of the propagating spin wave. We extract the spin-wave dispersion from the frequency dependence of the wavelength (Fig. 4.3C). This dispersion matches the one calculated using values of the saturation magnetization M_s and film thickness d determined by independent measurements (Supplementary Material).

Travelling spin-wave packets can be used for pulsed quantum control of distant spins such as those of the NV centers [19, 20]. Understanding the distance-dependent response of the spins to an applied control sequence requires knowledge of the spin-wave

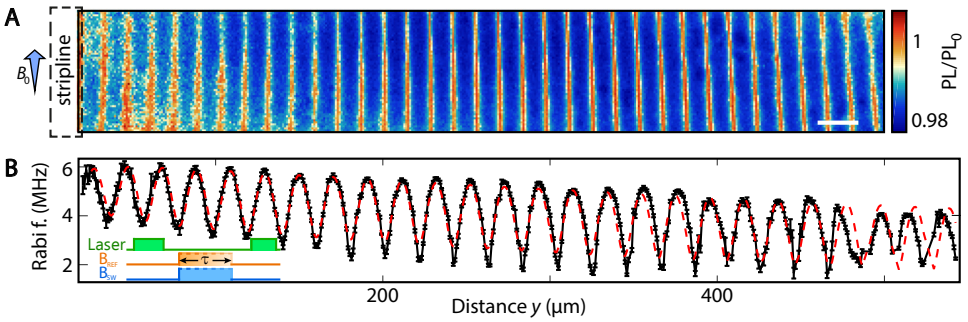

Figure 4.2: Imaging coherent spin waves. (**A**) Spatial ESR contrast at $B_0 = 25$ mT when a spin wave of frequency $\omega_{SW} = \omega_- = 2\pi \times 2.17$ GHz is excited by a microwave current in the stripline (length of 2 mm, width of 30 μm, and thickness of 200 nm) at the left image edge. The NV photoluminescence with applied microwaves (PL) is normalized to that without applied microwaves (PL$_0$). The NV-YIG distance at the stripline was 1.8(2) μm, determined by measuring the field of a DC stripline current (Supplementary Material). Scale bar, 20 μm. (**B**) Rabi frequency $\omega_{Rabi}/2\pi$ versus distance from the stripline. $\omega_{SW} = \omega_- = 2\pi \times 2.11$ GHz, $B_0 = 27$ mT. In (A) and (B), the microwaves were split between the stripline and a bonding wire, located ≈100 μm above the YIG and oriented along y to generate a spatially homogeneous field B_{REF}, creating an interference pattern (see text). Red line: Fit to a model including the field of the stripline, the bonding wire, and the spin waves (section 4.5.3.3). Inset: Measurement sequence. Laser pulses (1 μs) are used to initialize and read out the NV spins. Microwave pulses (duration τ) drive Rabi oscillations. ω_{Rabi} was calculated from the measured $\omega_{Rabi,0}$ using $\omega_{Rabi} = \sqrt{\omega_{Rabi,0}^2 - \Delta^2}$ to account for a $\Delta = 2\pi \times 1.5$ MHz detuning between the drive frequency and the two hyperfine-split ESR resonances caused by the ^{15}N nuclear spin.

group velocity. We demonstrate a time-domain characterization of the spin-wave propagation using pulsed control of the NV spins (Fig. 4.3D-E). In our measurement scheme (Fig. 4.3D), the NV spins at a target distance from the stripline are prepared in $m_s = 0$ using a green laser pulse. A spin-wave pulse (excited by the stripline) flips the NV spins into the dark $m_s = -1$ state only if it arrives either before or after a set of two reference pulses acting on the $0 \leftrightarrow +1$ transition (generated by a wire above the sample), resulting in low photoluminescence upon spin readout. In contrast, if the spin-wave pulse reaches the NVs between the two reference pulses, then it does not affect the NV spins because they are in $m_s = +1$ due to the first reference pulse. The second reference pulse subsequently flips the spin back to the bright $m_s = 0$ state, resulting in high photoluminescence upon spin readout. Measurements as a function of time between spin-wave and reference pulses and distance from the stripline reveal the spin-wave packet in the time domain and allow the extraction of the group velocity (Fig. 4.3E). We find a velocity of 3.6(2) km/s at a frequency of 2.169 GHz and a wavelength of 12 μm, consistent with the YIG spin-wave dispersion.

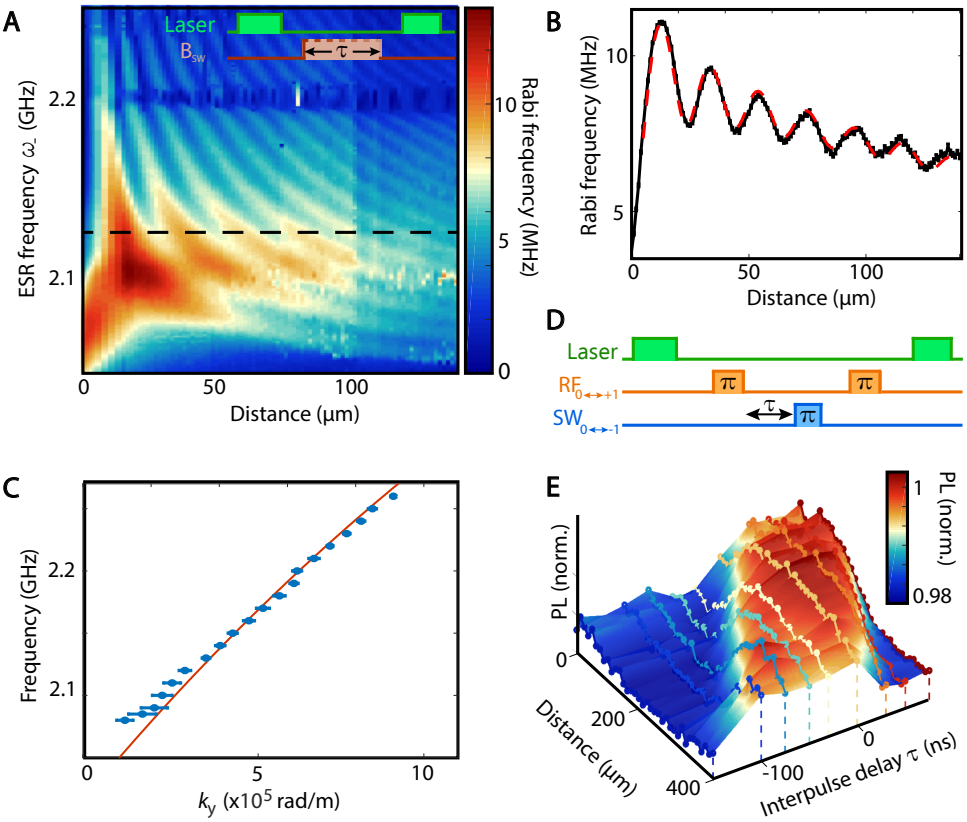

Figure 4.3: Spin-wave dispersion in the space and time domains. (**A**) NV Rabi frequency versus microwave drive frequency and distance from the stripline. The feature at 2.2 GHz matches the first perpendicular spin-wave mode (Supplementary Material). Inset: Measurement sequence. (**B**) Linecut of (A) with fit (red line) at 2.119 GHz. (**C**) Blue dots: Spin-wave frequency versus wave number extracted from (A). Red line: Calculated spin-wave dispersion. (**D**) Pulse sequence for studying spin-wave packets in the time domain [see text for details; data in (E)]: Laser pulses (1 μs) are used for NV spin initialization and readout. Two reference (RF) π pulses separated by 100 ns are applied at the $0 \leftrightarrow +1$ ESR frequency via a wire above the sample. After a time τ from the end of the first RF pulse, a spin wave–mediated π-pulse (SW) is generated at the $0 \leftrightarrow -1$ ESR frequency. (**E**) Normalized NV photoluminescence (PL) during the first 400 ns of the laser readout pulse [see (D)] versus distance from the stripline and delay time π. Negative τ indicates a spin-wave packet generated before the first RF pulse. For example, for $\tau = -100$ ns (i.e., the spin-wave pulse is generated 100 ns before the first RF pulse), the signal rises at 360 μm, indicating a spin-wave group velocity of 3.6 km/s. Circles, data; colored surface, interpolation.

The 2-mm-long stripline used in Figs. 4.2 and 4.3 corresponds to an effectively one-dimensional situation. We now turn to spin waves injected by a shorter stripline with a length comparable to the scanned area (Fig. 4.4A). We observe a focused emission pattern that is dominated by spin-wave beams traveling at specific angles (Fig. 4.4B-C). Such "caustics" occur when the dispersion is strongly anisotropic [26, 27]. They can be understood in terms of stationary points in the isofrequency curves in reciprocal space (Fig. 4.4D). In optics, such an isofrequency curve $k_z = k_z(k_y)$ is called "slowness" curve, because it is perpendicular to the group velocity $\mathbf{v}_G = \nabla_{\mathbf{k}}\omega(\mathbf{k})$. The states for which the angle of the group velocity $\theta = -\arctan(dk_z(k_y)/dk_y)$ is stationary along the curve, i.e., when $d\theta/dk_y \propto d^2k_z(k_y)/dk_y^2 = 0$, dominate emission, generating high-intensity spin-wave beams. The external magnetic field and the drive frequency can tune the beam direction and intensity [26, 27], providing opportunities to optimize the efficiency of spin wave–mediated magnetic field driving of distant spins at target locations.

Last, we image the interference between spin waves excited by two adjacent striplines on the YIG chip (Fig. 4.4, E and F), which shows rich interference patterns radiating from the three crossing points of the main caustics (i.e., ~ 80 μm from the striplines edge). The strongly anisotropic spin-wave dispersion causes a triangular "dark" region between the striplines in which no spin waves are detected, because spin waves traveling at small angles with respect to the equilibrium magnetization direction or having large wave numbers are neither efficiently excited (when the wavelength is shorter than the half-width of the stripline) nor efficiently detected due to the ~ 1 μm NV-sample distance. The downward directionality of the observed spin-wave patterns has two causes: The chiral spin-wave field has the correct handedness to drive the ω_- NV transition, and the handedness of the stripline field excites downward-propagating spin waves more efficiently (Supplementary Material). We note that these waves are not intrinsically directional because their wavelength far exceeds the film thickness [28], in contrast with Damon-Eshbach surface waves in thick films [29]. The observed directionality and interference patterns agree well with linear response calculations of the nonlocal dynamic susceptibility and the spatial profile of the microwave drive field, as described in the Supplementary Material. These quantitative measurements of the spin wave–generated rotating magnetic stray fields illustrate the power of NV-based magnetic resonance imaging in magnonics.

4.3. DISCUSSION

Our results demonstrate that ensembles of NV spins in diamonds enable quantitative, phase-sensitive magnetic imaging of coherent spin waves in thin-film magnets. A theoretical analysis explains the NV sensor signals in terms of the rotating stray fields generated by spin waves that are excited unidirectionally by the stripline magnetic field. In contrast to other spin-wave imaging techniques, our technique images spin waves by their microwave magnetic stray fields. This does not require a specific spin-photon or spin-electron interaction and enables imaging spin waves through optically opaque materials. These capabilities provide new opportunities, e.g., for studying top-gated materials and the interaction of spin waves with magnetic and nonmagnetic materials placed

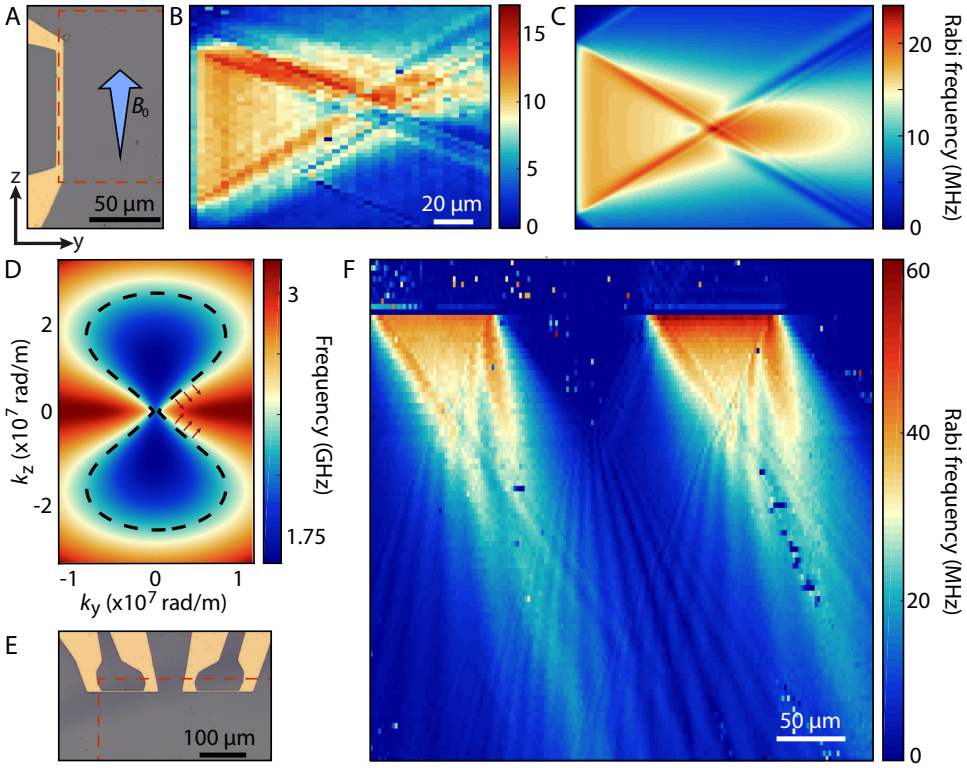

Figure 4.4: Imaging interference and caustics of spin waves excited by one and two short striplines. (**A**) Optical micrograph of the stripline (width of 5 µm) used to excite spin waves. The dashed red lines indicate the region where (B) is acquired. (**B**) Rabi frequency map corresponding to the dashed region of (A) for $B_0 = 27.1$ mT and $\omega/2\pi = 2.11$ GHz. The small asymmetry is attributed to a small misalignment of B_0 with respect to the striplines. (**C**) Simulation of the emission pattern observed in (B). (**D**) Calculated two-dimensional spin-wave dispersion relation $\omega(k_y, k_z)/2\pi$ at $B_0 = 20.5$ mT. The dashed line is an isofrequency contour at 2.292 GHz, indicating which wave vectors can be excited at this frequency and field. Red arrows indicate the direction of the spin-wave caustics. (**E**) Optical micrographs of the two injector striplines of width 2.5 µm. The dashed lines indicates the region where (F) is acquired. (**F**) Rabi frequency map under simultaneous driving of the two striplines, showing unidirectional excitation of autofocused spin-wave patterns that interfere and drive NV Rabi oscillations via their chiral magnetic stray fields.

on top of a magnetic film, which play an important role for spin-wave excitation and damping and form the basis for nonreciprocal devices [30]. NV magnetometry also allows high-resolution imaging of electric currents [31], enabling spatial studies of the interaction between spin waves and charge transport.

Both the NV-sample distance and the optical resolution of our microscope limit the resolution of our technique. The typical NV-magnet distances are here 0.5 to 2 μm (limited by, e.g., dust particles), comparable to our diffraction-limited optical resolution. Shallow NV centers in diamond chips that are wafer-bonded to (i.e., in direct contact with) a magnetic sample should allow the detection of spin waves with wavelengths comparable to the implantation depth of the NV centers of a few nanometers [32]—albeit without phase sensitivity. This requires resonance between the spin waves and the NV sensors, e.g., by tuning a magnetic field and/or magnetic anisotropies. This may be difficult for magnetically hard materials. We can probe nonresonant spin waves by detecting the Stark shift that they impart on the sensor spins [33] or by detecting intraband spin-wave transitions using NV spin relaxometry [34]. Phase-sensitive imaging of spin waves with wavelengths below the diffraction limit could be enabled using specialized NV control sequences such as phase encoding schemes [35]. Furthermore, the techniques presented here are directly transferrable to single-NV scanning probe microscopes with real-space resolution on the 10-nm scale [36].

Our results pave the way for studying spin waves in other magnetic material systems such as magnetic nanodevices and atomically thin magnets. NV magnetometry works at cryogenic temperatures [37–39], allowing studies of magnets with low Curie temperatures such as complex oxide or van der Waals magnets. Because the dipole density per unit area $M_s d = 3.6 \cdot 10^3$ μ_B/nm^2 of the YIG film studied here is only about two orders of magnitude above the 16 μ_B/nm^2 of the monolayer van der Waals magnet CrI_3 [22], the magnetic stray fields generated by spin waves in such monolayer magnets are within the sensitivity range of NV-based magnetic imaging. The sensitivity of our technique is rooted in measuring the sum of a reference field and the spin-wave field. A good strategy for measuring weak spinwave fields is to apply a strong reference field and measure the variations in the Rabi frequency caused by the spin-wave field, because Rabi frequency variations of ~ 100 kHz can easily be detected (the average error bar in Fig. 2B is 75 kHz). We can further increase the sensitivity by applying a stronger reference field, which decouples the NV spin from noise sources [40]. Increasing the microwave drive current and reducing the NV-sample distance (for instance, by depositing a van der Waals material directly onto the diamond [41]) would further increase the detection capability.

ACKNOWLEDGEMENTS

Funding: This work was supported by the Dutch Research Council (NWO) as part of the Frontiers of Nanoscience (NanoFront) program through NWO Projectruimte grant 680.91.115, JSPS KAKENHI grant no. 19H006450, and Kavli Institute of Nanoscience Delft.

Author contributions: I.B., J.J.C., and T.v.d.S. designed the experiment. I.B. fabricated the diamond-YIG samples, realized the imaging setup, performed the NV measurements,

and analyzed the data. B.G.S. prepared the diamonds. C.C.P. performed the vector network analyzer (VNA) measurements, for which J.J.C. fabricated the samples. T.Y., Y.M.B., and G.E.W.B. developed the theoretical model describing spin-wave caustics and interference. I.B. and T.v.d.S. wrote the manuscript with help from all coauthors. J.A. contributed to the discussions of the results and the manuscript.
Competing interests: The authors declare that they have no competing interests.
Data and materials availability: All data contained in the figures are available at Zenodo.org with the identifier 10.5281/zenodo.4005488. Additional data related to this paper may be requested from the authors.

4.4. MATERIALS AND METHODS

4.4.1. SAMPLE FABRICATION

The diamond samples used in this work are chemical vapor deposition (CVD)–grown, electronic-grade type IIa diamonds (Element 6), laser-cut, and polished down to 2 mm × 2 mm × 0.05 mm chips (Almax easyLab). These chips were cleaned with nitric acid, and the top ~ 5 μm were removed using inductively-coupled plasma (ICP) reactive ion etching (30 min Ar/Cl, 20 min O_2) to mitigate polishing damage. The chips were subsequently implanted with ^{15}N ions at 6 keV with a dose of 1 $\times 10^{13}$ ions/cm^2 (INNOViON), tri-acid cleaned (mixture of nitric, sulfuric, and perchloric acid, 1:1:1), annealed at 800°C for 4 hours at 10^{-6} mbar, and tri-acid cleaned again to remove possibly graphitized layers on the surface, resulting in an estimated density of NV centers of ~ 1×10^{11} NV/cm^2 at a depth of ~10 to 20 nm.

The YIG films were 245 nm thick, grown on gadolinium gallium garnet (GGG) substrates by liquid-phase epitaxy (Matesy GmbH). Before stripline fabrication, the YIG/GGG chips were sonicated in acetone and cleaned for a few seconds in an O_2 descum plasma to remove contaminants. Striplines for spin-wave excitation were fabricated directly onto the YIG films by e-beam lithography using a PMMA(A8 495)/PMMA(A3 950) double-layer resist and subsequent e-beam evaporation of Cr/Au (5 nm/200 nm). To attach an NV-containing diamond to the YIG film, a small droplet of isopropanol was deposited onto the YIG, on top of which a diamond chip was placed, with the NV surface facing down. The diamond chip was gently pressed down until the isopropyl alcohol had evaporated [42]. The resulting NV-YIG distance was measured to be 1.8(2) μm (see fig. 4.5).

4.4.2. MEASUREMENT SETUP

The optical setup used for all the measurements was a homebuilt confocal microscope. A 515-nm laser (Cobolt 06-MLD) was used for optical excitation of the NV centers, focused to a diffraction-limited spot by an Olympus 50×, numerical aperture = 0.95 objective. The NV luminescence was collected by the same objective, separated from the excitation light by a Semrock dichroic mirror and long-pass filter (617 nm cutoff), spatially filtered by a pinhole, and detected using a single-photon counting module (Laser Components). The microwaves signals used for driving NVs and spin waves were generated using Rohde & Schwarz microwave generators (SGS100A). The reference field B_{REF} used to produce the interference pattern in Fig. 4.2 was generated by a wire located ~ 200 μm

above the diamond and oriented perpendicularly to the stripline. To simultaneously drive the pair of striplines in Fig. 4, the microwave excitation was split using a Mini-Circuits power combiner (ZFRSC-123-S+). A National Instruments data acquisition card was used for triggering the data acquisition, while a SpinCore programmable pulse generator (PulseBlaster ESR-PRO 500) was used to control the timing sequences of the laser excitation, microwaves, and detection window. The photons were collected during the first 300 to 400 ns of the laser readout pulse, which was kept fixed to 1 µs. All measurements were performed at room temperature.

4.4.3. NV MAGNETOMETRY

The NV spins are initialized and read out using nonresonant optical excitation at 515 nm. To measure NV spin rotations (Rabi oscillations), we first apply a ~ 1 µs green laser pulse to polarize the NV spin into the $m_s = 0$ state. A subsequently applied microwave magnetic field resonant with an NV ESR frequency drives Rabi oscillations between the corresponding NV spin states ($m_s = 0$ and -1 in Fig. 4.2B). The NV spin state is read out by applying a laser pulse and measuring the spin-dependent photoluminescence that results from spin-selective nonradiative decay via a metastable singlet state. The ESR frequencies of the four NV families (Fig. 4.1D) in a magnetic field B_0 are determined by the NV spin Hamiltonian $H = DS_z^2 + \gamma \mathbf{B}_0 \cdot \mathbf{S}$, where γ is the electron gyromagnetic ratio, D is the zero-field splitting (2.87 GHz), and $S_{(i=x,y,z)}$ is the Pauli spin matrices for a spin 1. We apply the magnetic field B_0 using a small permanent magnet (diameter, 1 cm; height, 2 cm).

4.4.4. WAVELENGTH OF THE SPIN WAVES DRIVING NV RABI OSCILLATIONS

We excite spin waves at a frequency that matches the ω_- ESR transition of the NV spins, allowing us to detect the spin waves via the resulting NV Rabi oscillations. Hence, for a given field B_0 applied along the NV axis, the wave number of the spin waves driving Rabi oscillations is determined by equating the NV frequency $\omega_-/2\pi = D - \gamma B_0$ to the spin-wave frequency given by the spin-wave dispersion (eq. 4.14)

$$\frac{\omega(B_0,k)}{\gamma\mu_0 M_s} = \sqrt{\left(\frac{B_0\cos\theta}{\mu_0 M_s} + \alpha_{ex}k^2 + \frac{1-e^{-|k_y|d}}{|k_y|d}\right)\left(\frac{B_0\cos\theta}{\mu_0 M_s} + \alpha_{ex}k^2 + \frac{k_y^2}{k^2}\left(1 - \frac{1-e^{-|k_y|d}}{|k_y|d}\right)\right)} \tag{4.4}$$

where k is the SW wave number; k_y is its in-plane component perpendicular to the static magnetization; μ_0 is the magnetic permeability of vacuum; and M_s, $\alpha_{ex} = 3.0 \cdot 10^{-16}$ m^2, and d are the YIG saturation magnetization, exchange constant [23], and thickness, respectively.

4.5. SUPPLEMENTARY MATERIAL

4.5.1. DETERMINATION OF THE NV-YIG DISTANCE

The distance x_0 between the YIG surface and the NV sensing layer is an important parameter for the reconstruction of spin-wave amplitude from the detected field (Fig. 4.2) of the main text). We determined x_0 by sending a DC current I_{DC} through the stripline and characterizing the resulting magnetic field $\mathbf{B}_{DC}(x_0, y)$ using the NV sensing layer.

This field causes spatially dependent shifts in the NV ESR frequencies (Fig. 4.5A-B) from which we can extract x_0 as described next. Considering an infinitely thin stripline of width w with its center at $x = y = 0$, the stripline field is given by

$$\mathbf{B}_{DC}(x_0, y) = \frac{\mu_0 I_{DC}}{2\pi w}\left(\frac{1}{2}\ln\left(\frac{x_0^2 + (y + w/2)^2}{x_0^2 + (y - w/2)^2}\right)\hat{\mathbf{x}} + \arctan\left(\frac{w x_0}{x_0^2 + y^2 - (w/2)^2}\right)\hat{\mathbf{y}}\right) \tag{4.5}$$

To facilitate the analysis of the ESR spectra, we also applied a small bias field $\mathbf{B}_0$ to increase the splitting of the 8 ESR transitions of the 4 NV families. From the total field $\mathbf{B} = \mathbf{B}_0 + \mathbf{B}_{DC}$, we calculate the ESR frequencies for the 4 NV families by diagonalizing the NV spin Hamiltonian $H = DS_z^2 + \gamma(B_\parallel S_z + B_\perp S_x)$, where $B_\parallel$ is the projection of $\mathbf{B}$ onto the NV axis and $B_\perp = \sqrt{B^2 - B_\parallel^2}$. From the fit to this model (Fig. 4.5C), we extract $\mathbf{B_0}$ = (0.461(3), 3.568(3), 0.626(3)) mT, D = 2.872(1) GHz and x_0 = 1.8(2) µm. For the sample in Fig. 4 we used an alternative, optical method to determine the distance, focusing the excitation laser first on the YIG surface and then on the NV layer, reading off the change in the position of the microscope objective from its closed-loop piezo-controller, measuring $x_{0,\text{Sample2}}$ = 1.0(3) µm.

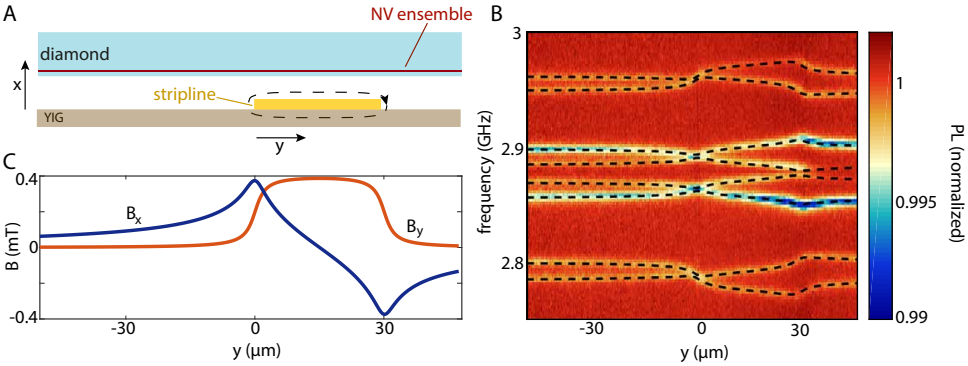

Figure 4.5: Determination of the YIG-NV distance. (**A**) Idea of the measurement. The diamond is located at a height x above the current-carrying stripline fabricated on the YIG. ESR spectra are measured along a line perpendicular to the stripline. The current in the stripline generates a magnetic field (dashed black line), causing a shift of the NV ESR frequencies. (**B**) NV ESR spectra measured along a line oriented perpendicularly to the stripline (which is located between $y = 0$ and $y = 30$ µm). The eight dips in the photoluminescence (PL) are caused by the ESR transitions of the four NV families having different orientations in the diamond crystal lattice. (**C**) Stripline magnetic field in the NV layer corresponding to the values extracted from the fit.

4.5.2. DETERMINATION OF M_s AND THICKNESS OF YIG WITH VNA MEASUREMENTS

The YIG saturation magnetization M_s and thickness d are important parameters for analyzing the spin-wave dispersion. Here we describe the extraction of these parameters

using vector network analyzer (VNA) measurements.

We flip-chip a YIG chip on the central conductor of a coplanar waveguide (CPW) and use a VNA to measure the microwave transmission S_{21} through the CPW as a function of a magnetic field B_0 applied in-plane and parallel to the central conductor of the CPW (Fig. 4.6 A). When the frequency matches the YIG FMR, energy is absorbed and S_{21} decreases. We extract $M_s = 1.42(1) \cdot 10^5$ A/m by fitting the data with the Kittel equation $\omega = \gamma\sqrt{B_0(B_0 + \mu_0 M_s)}$.

We determine the thickness of the YIG chip from the frequency of the first perpendicular standing spin-wave mode (PSSW) [43].To extract the frequency of the first PSSW, we measure the spin-wave mediated transmission of microwaves between two striplines using the VNA (Fig. 4.6 B-C). The PSSW manifests as a small dip in the transmission (indicated by the dashed black line in Fig. 4.6 B and the black arrow in Fig. 4.6 D). To extract the thickness d, we calculate the PSSW frequency at each field for fixed M_s and different values of the thickness using [44]. The best match is reached for $d = 245(5)$ nm.

4.5.3. EFFECT OF THE SPIN WAVE STRAY FIELD ON THE NV SPINS

In this section we derive the NV Rabi frequency due to the stray fields from spin waves excited in the YIG by a stripline carrying an oscillating current. In section 4.5.3.2 we present the magnetization profile excited by the stripline magnetic field, based on the spin susceptibility of the YIG. In section 4.5.3.3 we provide the dipolar field generated by the magnetization oscillations at the NV centers and determine their Rabi frequency by evaluating the efficiency of the field in driving the NV spins, including the chirality of the spin-wave field. In section 4.5.3.6, we extend the results obtained to the case of two adjacent striplines and calculate the interference pattern. Our theoretical framework captures and explains several effects visible in the data, such as the spin wave focussing and caustics beams, as well as the interference fringes.

MODEL AND PARAMETERS

We use the reference frame depicted in Fig. 4.1 of the main text. Additionally, the length, width and thickness of the stripline are referred to as l, w and δ, respectively, the thickness of the yttrium iron garnet (YIG) film is d, and the NV-YIG distance is x_0. The static magnetic field B_0 is always applied at a ϕ=35° angle with respect to the sample plane and parallel to the striplines. Because B_0 in the experiments of Figs. 4.2-4.4 does not exceed 27 mT, which is much smaller than the YIG saturation magnetization $\mu_0 M_s \approx 178$ mT, the static magnetization of the film only tilts out of plane by a small angle $B_0 \sin\phi/(\mu_0 M_s) \lessapprox 5°$. We therefore disregard the out-of-plane component of the static magnetizaton and magnetic field B_0 in the calculations. We use the parameters $w = 2.5$ µm, $\delta = 200$ nm, $l = 88$ µm, $d = 245$ nm and $x_0 = 1$ µm. The striplines in Fig. 4.4E-F of the main text are 110 µm apart and driven with a phase difference of π.

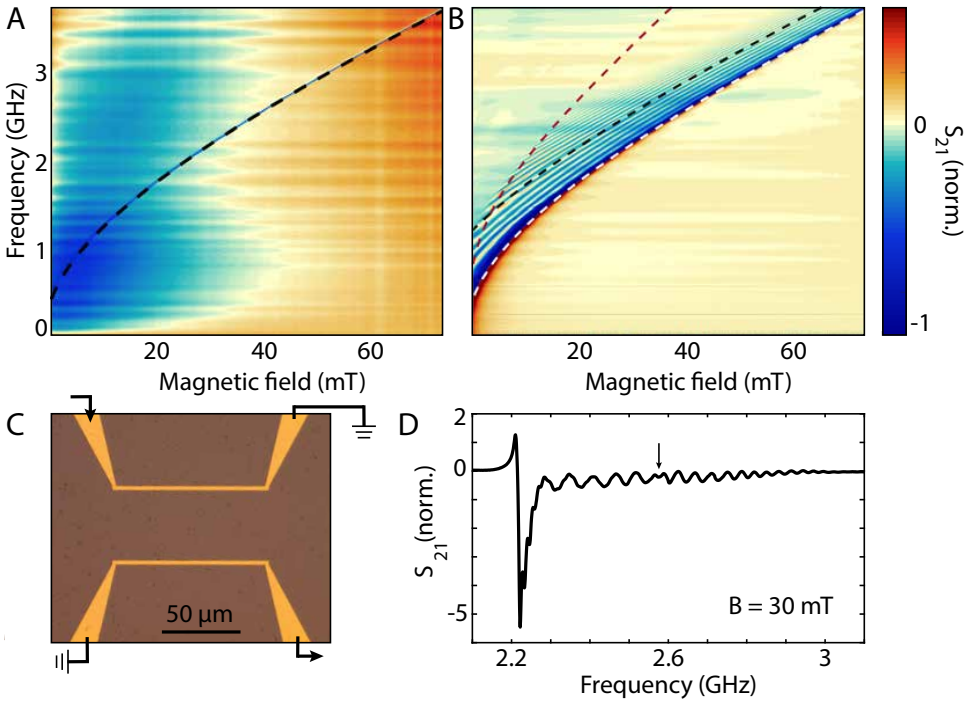

Figure 4.6: VNA-FMR detection of spin waves to determine M_s and thickness of the YIG chip. (**A**) Transmission $S_{21}(B,\omega)$ through the central conductor of a CPW on top of which a YIG chip is placed. The absorption of YIG at the FMR (dark blue line in the data) is extremely sharp (FWHM<10 MHz). The dashed black line is calculated using the extracted value of $M_s = 1.42 \cdot 10^5$ A/m. (**B**) $S_{21}(B,\omega)$ mediated by spin waves across the device shown in (C). The white and black dashed lines are the calculated frequencies of the FMR and 1st-order PSSW, respectively. The red dashed line indicates a frequency that is twice that of the calculated band minimum. Above this frequency, three-magnon scattering becomes allowed, which may contribute to the observed vanishing of the spin-wave mediated transmission above this frequency. (**C**) Device used to obtain the measurement in (B). The two gold striplines fabricated on YIG and connected to the input and output of the VNA as indicated by the arrows. Stripline width = 2.5 µm, thickness = 200 nm. (**D**) Vertical linecut of (B) at 30 mT, showing the FMR absorption dip followed by several oscillations and the PSSW, indicated by the black arrow.

MAGNETIZATION EXCITED BY A MICROWAVE STRIPLINE OF FINITE LENGTH

Stripline magnetic field

Two striplines $i = \{1,2\}$ carrying a current density $\mathbf{J}_i(\mathbf{r},\omega)$ with frequency ω generate the vector potentials [45]

$$\mathbf{A}_i(\mathbf{r},\omega) = \frac{\mu_0}{4\pi}\int d\mathbf{r}'\mathbf{J}_i(\mathbf{r}',\omega)\frac{e^{ik|\mathbf{r}-\mathbf{r}'|}}{|\mathbf{r}-\mathbf{r}'|}, \tag{4.6}$$

parallel to the direction of the current (the z-direction). μ_0 is the vacuum permeability and $k = \omega/c$. Substituting the Weyl identity [46],

$$\frac{e^{ik\sqrt{(x-x')^2+(y-y')^2+(z-z')^2}}}{\sqrt{(x-x')^2+(y-y')^2+(z-z')^2}} = \frac{i}{2\pi}\int dk_y dk_z \frac{e^{ik_x|x-x'|+ik_y(y-y')+ik_z(z-z')}}{k_x}, \tag{4.7}$$

where $k = \sqrt{k_x^2+k_y^2+k_z^2}$ (and hence $k_x = \sqrt{k^2-k_y^2-k_z^2}$), the Fourier components of the magnetic field $\mu_0(H_x,H_y)^{(i)} = (\partial A_z/\partial y, -\partial A_z/\partial x)^{(i)}$ in reciprocal space are

$$H_x^{(i)}(x;k_y,k_z) = 2iJ_i(\omega)\frac{e^{-ik_x x}}{k_x}\frac{e^{ik_x\delta}-1}{k_x}\sin\left(k_y\frac{w}{2}\right)\frac{\sin(k_z l_i/2)}{k_z}e^{-ik_z z_i}, \tag{4.8}$$

$$H_y^{(i)}(x;k_y,k_z) = 2iJ_i(\omega)\frac{e^{-ik_x x}}{k_x}\frac{e^{ik_x\delta}-1}{k_y}\sin\left(k_y\frac{w}{2}\right)\frac{\sin(k_z l_i/2)}{k_z}e^{-ik_z z_i}, \tag{4.9}$$

where $k_x = \sqrt{(\omega/c)^2-k_y^2-k_z^2}$, z_i are the z-coordinates of the centers of the striplines and the total current is given by $J_i w\delta$. The generated magnetic field is perpendicular to the stripline axis, i.e. $H_z = 0$, and $k_x H_x(x;k_y,k_z) = k_y H_y(x;k_y,k_z)$. Since $l \gg w$, the magnetic field oscillates as function of k_z with a short period of $4\pi/l$, while it oscillates with k_y with a much longer period of $4\pi/w$ (Fig. 4.7 A). For a frequency $\omega/(2\pi) \sim 2$ GHz, $k_0 \equiv \omega/c = 4.19$ rad/m with characteristic wavelength $\lambda_0 = 2\pi/k_0 = 0.15$ m. The wavelength of the excited spin waves is much smaller than this scale, indicating that $\sqrt{k_y^2+k_z^2} \gg \omega/c$. Thus, $k_x \to i\sqrt{k_y^2+k_z^2} = i\kappa$. With $\kappa\delta \ll 1$:

$$\begin{aligned} H_x^{(i)}(x;k_y,k_z) &= -2iJ_i(\omega)e^{\kappa x}\frac{e^{-\kappa\delta}-1}{\kappa^2}\sin\left(k_y\frac{w}{2}\right)\frac{\sin(k_z l_i/2)}{k_z}e^{-ik_z z_i}, \\ H_y^{(i)}(x;k_y,k_z) &= 2J_i(\omega)e^{\kappa x}\frac{e^{-\kappa\delta}-1}{\kappa k_y}\sin\left(k_y\frac{w}{2}\right)\frac{\sin(k_z l_i/2)}{k_z}e^{-ik_z z_i}. \end{aligned} \tag{4.10}$$

The magnetic field distribution in $\mathbf{k}$-space is plotted in Fig. 4.7 A for the sample dimensions specified above, emphasizing the fast k_z oscillations. A microwave excitation with field components $h_x = \pm i h_y$ is circularly polarized. The relation

$$H_x(x;k_y,k_z) = -i(k_y/\kappa)H_y(x;k_y,k_z). \tag{4.11}$$

implies that when $|k_y| \ll |k_z|$, $|H_x| \ll |H_y|$, so the radiation is nearly linearly-polarized along the $\hat{\mathbf{y}}$-direction (in momentum space). On the other hand, when $|k_y| \gg |k_z|$, $H_x(x;k_y,k_z) \to$

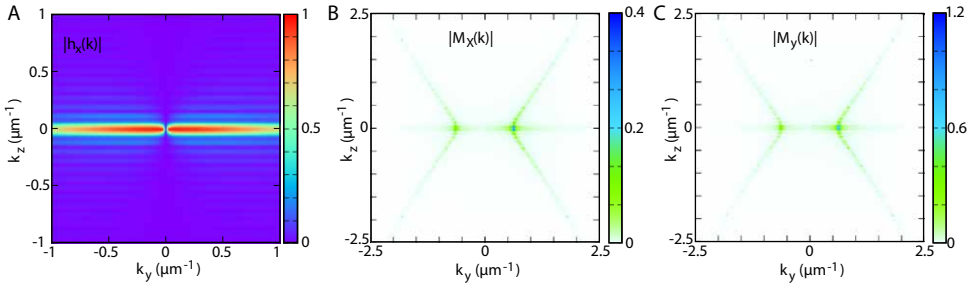

Figure 4.7: Drive field and excited magnetization in reciprocal space. **(A)** $x-$component of the magnetic field generated by the stripline in momentum space. **(B)-(C)** Resulting transverse magnetization amplitude, for $\alpha_G = 1\times10^{-4}$, $\omega = 2.29$ GHz, $\mu_0 M_s = 0.178$ T, and applied magnetic field $B_0 = 20$ mT. Note the different scales used for plotting $|M_x|$ and $|M_y|$.

$-i\mathrm{sgn}(k_y)H_y(x;k_y,k_z)$ is nearly right- (left-) circularly polarized for positive (negative) k_y. The polarization-momentum locking of the stripline magnetic field is responsible for the chiral pumping of circularly-polarized spin waves [24, 30, 47].

Excited magnetization

The stripline magnetic field excites spin waves in the YIG film. In the mixed position and momentum space, the dynamic magnetization $\mathbf{M}(x,\mathbf{k},\omega)$ reads in linear response [24, 30, 47]

$$M_\alpha(x,\mathbf{k},\omega) = \frac{1}{d}\int_{-d}^{0} dx'\,\chi_{\alpha\beta}(x,x',\mathbf{k},\omega)H_\beta(x',\mathbf{k},\omega) \tag{4.12}$$

where we sum over repeated Cartesian indices $\alpha,\beta = \{x,y,z\}$. γ is the electron gyromagnetic ratio and the spin susceptibility reads [24]

$$\chi_{\alpha\beta}(x,x',\mathbf{k},\omega) = -\gamma\mu_0 M_s m_\alpha^{\mathbf{k}}(x)m_\beta^{\mathbf{k}*}(x')\frac{1}{\omega-\omega_{\mathbf{k}}+i\Gamma_{\mathbf{k}}}. \tag{4.13}$$

Here, $m_\alpha^{\mathbf{k}}(x)$ characterize the ellipticity of the magnetization precession associated with the spin waves (see Eq. (4.15) and Eq. (4.17)), and $\Gamma_{\mathbf{k}} = 2\alpha_G\omega_{\mathbf{k}}$ is the Gilbert damping of the spin waves with frequency $\omega_{\mathbf{k}}$.

For the parameters of our experiments, the spin waves are in the dipolar-exchange regime with strongly anisotropic dispersion. For the long wavelengths considered here, the magnetization is homogeneous across the film thickness, which allows for an analytical treatment. The spin-wave dispersion for free magnetization boundary conditions reads [24, 30, 47]

$$\omega_{\mathbf{k}} = \gamma\mu_0 M_s\sqrt{\left[\Omega_H+\alpha_{\mathrm{ex}}k^2+1-f(|k_y|)\right]\left[\Omega_H+\alpha_{\mathrm{ex}}k^2+(k_y^2/k^2)f(|k_y|)\right]}, \tag{4.14}$$

where α_{ex} is the exchange stiffness, $\Omega_H \equiv B_0 \cos(\phi)/\mu_0 M_s$, and

$$f(|k_y|) = 1 - \frac{1}{|k_y|d} + \frac{1}{|k_y|d}\exp(-|k_y|d).$$

At long wavelengths, m_x and m_y are homogeneous across the film thickness and given by

$$m_x = \sqrt{\frac{\mathscr{D}+1}{(\mathscr{D}-1)}}, \quad m_y = i\sqrt{\frac{\mathscr{D}-1}{(\mathscr{D}+1)}}, \tag{4.15}$$

with

$$\mathscr{D} = \frac{1/2 - (1/2)\left(1 + k_y^2/k^2\right) f(|k_y|)}{\omega_{\mathbf{k}}/(\mu_0\gamma M_s) - \left(\Omega_H + \alpha_{\text{ex}}k_y^2 + 1/2\right) + (1/2)\left(1 - k_y^2/k^2\right) f(|k_y|)}. \tag{4.16}$$

We define the ellipticity parameter

$$\eta = \frac{|m_x|}{|m_y|} = \frac{\mathscr{D}+1}{\mathscr{D}-1}. \tag{4.17}$$

In the dipolar regime, the spin waves precess elliptically. When $\mathbf{k} \to 0$, $f(|k_y|) \to 0$, $\omega_{\mathbf{k}} \to \mu_0\gamma M_s\sqrt{\Omega_H(\Omega_H+1)}$ (corresponding to the FMR frequency), $\mathscr{D} \to -1-2\Omega_H-2\sqrt{\Omega_H(\Omega_H+1)}$. When $\Omega_H \to 0$ with a small static magnetic field, $\mathscr{D} \to -1-2\sqrt{\Omega_H}$, $|m_y| \gg |m_x|$, leading to a (nearly) linearly-polarized Kittel mode. When k is large, the exchange interaction dominates and the spin waves are right-circularly polarized.

We plot the calculated excited transverse magnetization amplitude in momentum space in Fig. 4.7B-C with parameters similar to those in Fig. 4F of the main text, i.e. $M_s = 1.42 \cdot 10^5$ A/m, $\alpha_G = 1 \times 10^{-4}$, $\omega/2\pi = 2.29$ GHz. The momentum distribution of the resonantly excited spin waves reflects the hyperboles formed by the cut through the anisotropic spin wave dispersion at the given frequency. The excitation becomes unidirectional when the spin waves are circularly-polarized [24, 47], in which case only those with positive values of k_y are excited. Due to the YIG thickness much smaller than the wavelengths considered, this chirality is not the intrinsic one of Damon-Eshbach surface modes, which exist only in much thicker films

The real part of the inverse Fourier transform of Eq. (4.12) gives the observable spatiotemporal magnetization

$$\mathbf{M}_\alpha(\boldsymbol{\rho}, t) = \frac{1}{4\pi^2}\iint d\mathbf{k} e^{i\boldsymbol{\rho}\cdot\mathbf{k} - i\omega t}\mathbf{M}_\alpha(x, \mathbf{k}) \tag{4.18}$$

with $\boldsymbol{\rho} = (y, z)$. Using this equation, we calculate a snapshot of the dynamic magnetization when spin waves are driven by a stripline as in Fig. 4 of the main text (Fig. 4.8). We observe interference of spin waves with frequency ω. Triangular areas of weak and strong excitation exist at the sides and in front of the stripline, respectively, with a spin wave focus point at the vertex of the latter triangle. These features can be understood from the anisotropy of the spin wave dispersion that leads to a critical opening angle of available spin wave momenta at a given frequency.

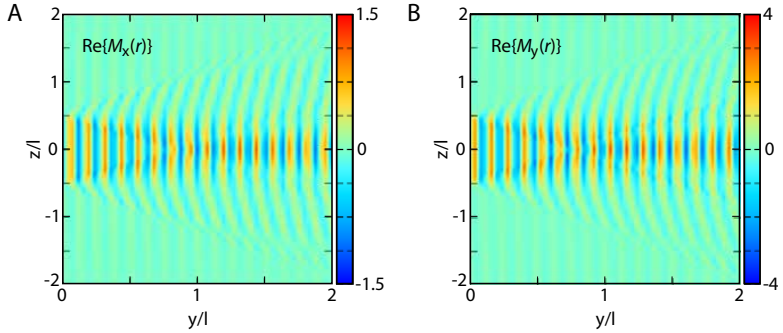

Figure 4.8: Spatial profile of the excited magnetization. Spatial profile of the out-of-plane (A) and in-plane **(B)** of the transverse magnetization oscillations excited by a single stripline, located at $y = 0$ between $z/l = -0.5$ and $z/l = +0.5$.

DIPOLAR FIELD AND RABI FREQUENCY

When the frequency of the magnetic stray field generated by a spin wave matches an NV ESR frequency, it can drive Rabi rotations of the NV spin if it has a circularly polarized component of the correct handedness. Here we describe the spin-wave induced Rabi driving of the NV spins.

Dipolar field generated by an oscillating magnetization

The magnetic field generated by a magnetization pattern can be calculated using Coulomb's law [45]

$$\mathbf{B}_\beta(\mathbf{r},t) = \frac{\mu_0}{4\pi}\partial_\beta\partial_\alpha \int d\mathbf{r}' \frac{\mathbf{M}_\alpha(\mathbf{r}',t)}{|\mathbf{r}-\mathbf{r}'|}. \tag{4.19}$$

By substituting the magnetization from Eq. (4.18) and using the Coulomb integral

$$\int d\mathbf{r}' \frac{e^{i\mathbf{k}\cdot\boldsymbol{\rho}'} f(x')}{|\mathbf{r}-\mathbf{r}'|} = \frac{2\pi}{k} e^{i\mathbf{k}\cdot\boldsymbol{\rho}} \int dx' e^{-|x-x'|k} f(x'), \tag{4.20}$$

where $k = |\mathbf{k}|$, we obtain the magnetic field above the film ($x > 0$) [24, 30, 47]

$$B_{SW,x}(x,\mathbf{k},t) = \frac{\mu_0}{2} e^{-kx-i\omega t}(1-e^{-kd})\left(M_x(\mathbf{k}) - i\frac{k_y}{k}M_y(\mathbf{k})\right), \tag{4.21}$$

with $B_{SW,y}(\mathbf{k}) = -i(k_y/k)B_{SW,x}(\mathbf{k})$, and $B_{SW,z}(\mathbf{k}) = -i(k_z/k)B_{SW,x}(\mathbf{k})$. Thus, when $|k_z| \ll |k_y|$, $B_{SW,y}(\mathbf{k}) = -i\,\mathrm{sign}(k_y)B_{SW,x}(\mathbf{k})$, i.e. the polarization and momentum are locked. $B_{SW,(x,y)}$ vanishes for negative k_y when the spin waves are right circularly-polarized since $M_x(\mathbf{k}) - iM_y(\mathbf{k})k_y/k \to 0$ [24, 47]. The right-forward dipolar field is left-circularly polarized.

In real space, the stray field generated by the spin wave is given by the real part of the inverse Fourier transform

$$\mathbf{B}_{SW}(x,\boldsymbol{\rho},t) = \frac{1}{4\pi^2}\iint e^{i\boldsymbol{\rho}\cdot\mathbf{k}}\mathbf{B}_{SW}(x,\mathbf{k},t)d\mathbf{k}. \tag{4.22}$$

A snapshot of the spin-wave stray field at a distance x_0 above the film is plotted in Fig. 4.9. Since the distance to the film is much smaller than the relevant wavelengths, the interference pattern of the spin waves is well resolved. We note that $|B_{SW,z}| \ll |B_{SW,x}|, |B_{SW,y}|$ because the excited spin waves propagate almost perpendicular to the stripline. The strong chirality (unidirectionality) is caused by both the stripline magnetic field (see in Fig. 4.7) and the stray field from the spin waves [24, 30, 47]. All Cartesian vector components exert a torque on the NV center spin, which is oriented at an angle to the film. The dipolar field shows a focal point with large amplitude, which can be controlled by tuning the magnetic field and stripline frequency, which could be interesting for spintronic applications.

The field of a spin wave that is characterized by $|k_z| \ll |k_y|$ (therefore $\mathbf{k} \perp \mathbf{M}$, corresponding to a Damon-Eshbach geometry and an effectively one-dimensional configuration) is given by ($x > 0$)

$$\mathbf{B}_{SW}(x,\mathbf{k},t) = -\frac{\mu_0}{2} e^{-kx-i\omega t}(1-e^{-kd}) M_y(\mathbf{k}) \left(1+\text{sign}(k_y)\eta\right)\left(\hat{\mathbf{y}} + i\,\text{sign}(k_y)\hat{\mathbf{x}}\right), \tag{4.23}$$

where we used $M_x = -i\eta M_y$. To arrive at the equations given in the main text, we calculate the field of a traveling spin wave given by the real part of $\mathbf{m}_\perp = m_\perp^0 e^{i(k_0 y-\omega t)}(\hat{\mathbf{y}} - i\eta\hat{\mathbf{x}})$. The Fourier transform of the y-component is

$$M_y(k_y) = m_\perp^0 2\pi\delta(k_y - k_0). \tag{4.24}$$

Substituting into Eq. (4.23) and taking the inverse Fourier transform, we get Eq.(4.2) of the main text

$$\mathbf{B}_{\text{SW}}(y) = -\text{Re}[\frac{\mu_0 m_\perp^0}{2} e^{-|k_0|x_0} e^{i(k_0 y-\omega t)}(1-e^{-|k_0|d})(1+\text{sign}(k_0)\eta)(\hat{\mathbf{y}} + i\,\text{sign}(k_0)\hat{\mathbf{x}})] \tag{4.25}$$

$$= -\text{Re}[B_{SW}^0 e^{i(k_0 y-\omega t)}(\hat{\mathbf{y}} + i\,\text{sign}(k_0)\hat{\mathbf{x}})] \tag{4.26}$$

Calculation of the Rabi frequency

The dynamic magnetic field generated by the spin waves can induce transitions between the spin states of the NV center when its frequency matches an NV ESR frequency as described by the NV spin Hamiltonian. We write the dynamic part of the magnetic field as

$$\mathbf{B}_{\text{SW}}(y) = \text{Re}[(B_x\hat{\mathbf{x}} + B_y\hat{\mathbf{y}} + B_z\hat{\mathbf{z}})e^{-i\omega t}] \tag{4.27}$$

In the local coordinates of the NV center, with the z'-direction along the applied static magnetic field (therefore along the NV axis), the field amplitudes becomes

$$B_{x'} = B_x\cos\phi - B_z\sin\phi, \tag{4.28}$$

$$B_{y'} = B_y, \tag{4.29}$$

$$B_{z'} = B_z\cos\phi + B_x\sin\phi. \tag{4.30}$$

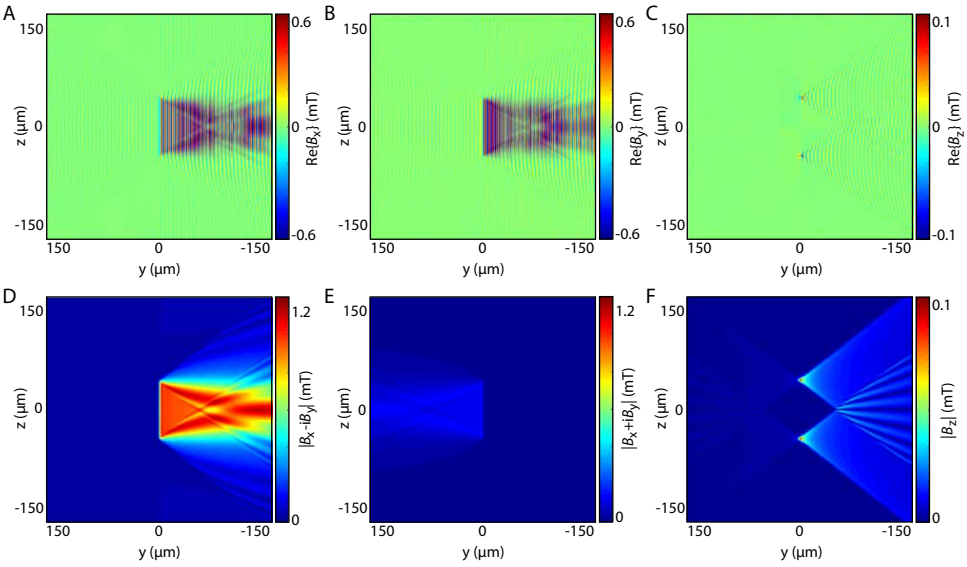

Figure 4.9: Spatial profile of the dipolar field generated by spin waves. Snapshot of the stray field in real space at $t = 0$ for a microwave driving with a frequency $\omega = 2.29$ GHz and a stripline current of 0.7 mA at a distance x_0 above the film. The stripline is located at $y = 0$, $z \in [-40, 40]$ μm. The damping coefficient is $\alpha_G = 10^{-4}$.

The Hamiltonian describing the NV spin dynamics is given by

$$H_{\mathrm{NV}} = DS_z^2 + \gamma \mathbf{B}' \cdot \mathbf{S} \tag{4.31}$$

where $\mathbf{S} = (S_x, S_y, S_z)$ are the Pauli matrices for a spin 1 and $D/2\pi = 2.87$ GHz is the zero-field frequency. The two magnetic-dipole allowed transitions between the $m_s = 0$ and the $m_s = \pm 1$ states are driven by magnetic fields of opposite handedness. When the magnetic-field frequency ω matches one of the NV ESR frequencies $D \pm \gamma B_0$, the NV spin will Rabi oscillate between the corresponding $m_s = 0$ and $m_s = \pm 1$ states with a Rabi frequency given by

$$\omega_R^{\pm} = \frac{\gamma}{\sqrt{2}} \left| B_{x'} \pm i B_{y'} \right|. \tag{4.32}$$

We use Eq. (4.32) to calculate the spin-wave induced Rabi frequency caused by the spatial magnetization profile shown in Fig. 4.8. The Rabi frequency closely resembles the spatial magnetization profile, including the presence of caustic beams and a focal point (Fig. 4.10).

When the NV ω_- transition is driven by a resonant Damon-Eshbach spin wave with $k_0 > 0$, we get

$$\omega_R^- = \sqrt{2}\gamma B_{\mathrm{SW}}^0 \cos^2 \frac{\phi}{2}. \tag{4.33}$$

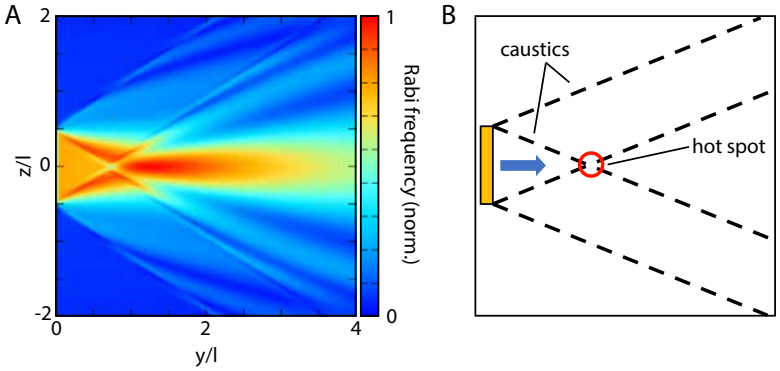

Figure 4.10: Calculated spatial map of the Rabi frequency for a single stripline. **(A)** Rabi frequency calculated from the dipolar field without the (small) direct contribution from the stripline at $y = 0$ and $z/l \in [-0.5, 0.5]$. **(B)** Schematics indicating the emergence of caustic spin-wave beams and the "hot spot" where energy gets focussed.

If the NV spin is also driven by a magnetic field that is given by $\mathrm{Re}[\mathbf{B}_{\mathrm{REF}} e^{-i\omega t}]$, we get

$$\omega_R^- = \frac{\gamma}{\sqrt{2}} \left| 2B_{\mathrm{SW}}^0 e^{ik_0 y} \cos^2 \frac{\phi}{2} + B_{\mathrm{REF,x'}} - iB_{\mathrm{REF,y'}} \right|. \tag{4.34}$$

from which follows Eq. 4.3 of the main text. Including a damping parameter into Eq. (4.34), we fit the data of Fig. 2B of the main text, from which we extract the spin-wave amplitude $m_\perp^0$ (using the ellipticity parameter calculated with Eq. (4.17)) and the spin-wave damping:

$$\omega_R^- = \frac{\gamma}{\sqrt{2}} \left| 2B_{\mathrm{SW}}^0 e^{ik_0 y - y/y_0} \cos^2 \frac{\phi}{2} + e^{i\theta} B_{\mathrm{REF}} \right|. \tag{4.35}$$

Here, y_0 is the spin-wave decay length from which the Gilbert damping parameter is extracted using $y_0 = v_g/(2\omega\alpha_G)$, with v_g the group velocity, leading to $\alpha_G = 1.2(1) \cdot 10^{-4}$. The main contribution to the uncertainty is caused by the uncertainty in the NV-YIG distance, which we measured to be 1.8(2) µm (see section 4.5.1) at the location of the stripline and which increases by about 0.4 µm/mm as estimated from the optical interference fringes visible in Fig. 1B of the main text (the distance change between two fringes is given by $\lambda_0/2$, with λ_0 the wavelength of the light in air). Using Eq. (4.35), we also fitted the data shown in Fig. 3B of the main text, with B_{REF} given by Eq. (4.5).

EFFECT OF MAGNETIC FIELD MISALIGNMENT ON THE OBSERVED SPIN-WAVE PATTERNS

To explain the asymmetry along $\hat{\mathbf{z}}$ of the observed spin-wave patterns in Fig. 4, we repeat the calculation of Fig. 4C with the introduction of a 5° misalignment between the static field and the stripline (Fig. 4.11). The tilt is from the $\hat{\mathbf{z}}$ toward the $-\hat{\mathbf{y}}$ axis.

INFLUENCE OF THE SPIN-WAVE PROPAGATION DIRECTION ON THE FIELD PROFILE

As previously explained (Eq. (4.32)), right(left)-propagating spin waves generate a circularly-polarized field with handedness that drives the ω_- (ω_+) transition. Moreover, for perfectly circular polarization, the right(left)-propagating waves only generate a field above

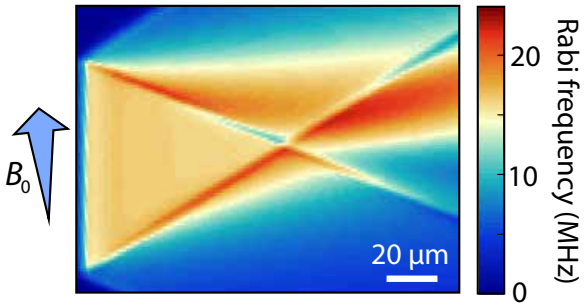

Figure 4.11: Effect of a small angle between the stripline and the in-plane component of the static field $\mathbf{B_0}$. Calculated spatial map of the Rabi frequency when the in-plane projection of the static field (B_0) is oriented at a 5° angle from the stripline.

(below) the film, which can be simply explained by cancellation of the field contributions of neighbouring spins (Fig. 4.12). For elliptical polarization, the field suppression is not complete.

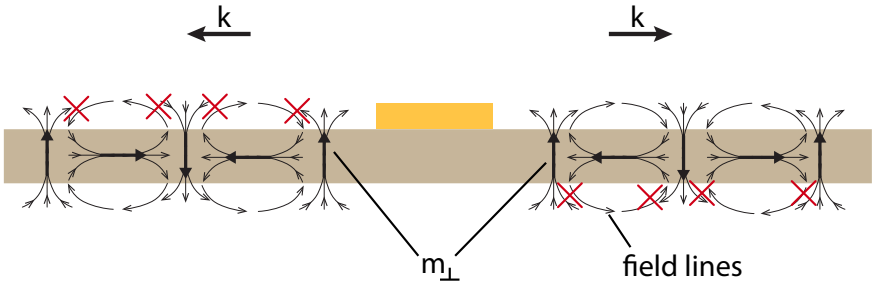

Figure 4.12: Magnetic field generated by spin waves propagating to the left and right. The magnetic stray field generated by a spin wave is the sum of the fields generated by the individual precessing spins in the magnet. The phases of the spin waves traveling to the right interfere constructively/destructively above/below the film, and vice versa for spin waves traveling to the left.

INTERFERENCE BETWEEN SPIN WAVES GENERATED BY TWO ADJACENT STRIPLINES

Finally, we calculate the interference pattern generated by two striplines on the YIG film, with centers separated by 200 µm. With $l_1 = 100$ µm and $l_2 = -100$ µm in Eq. (4.10) and considering the π phase difference between the two striplines

$$H_x(x;k_y,k_z) = -2iJ(\omega)e^{\kappa x}\frac{e^{-\kappa\delta}-1}{\kappa^2}\sin\left(k_y\frac{w}{2}\right)\frac{\sin(k_z l/2)}{k_z}(e^{-ik_z z_1}-e^{-ik_z z_2}), \tag{4.36}$$

$$H_y(x;k_y,k_z) = 2J(\omega)e^{\kappa x}\frac{e^{-\kappa\delta}-1}{\kappa k_y}\sin\left(k_y\frac{w}{2}\right)\frac{\sin(k_z l/2)}{k_z}(e^{-ik_z z_1}-e^{-ik_z z_2}). \tag{4.37}$$

By substitution into Eqs. (4.12) and (4.21), we obtain the Rabi frequencies of the NV center in Figure 4.13. The spin-wave interference is clearly reflected in the Rabi frequency.

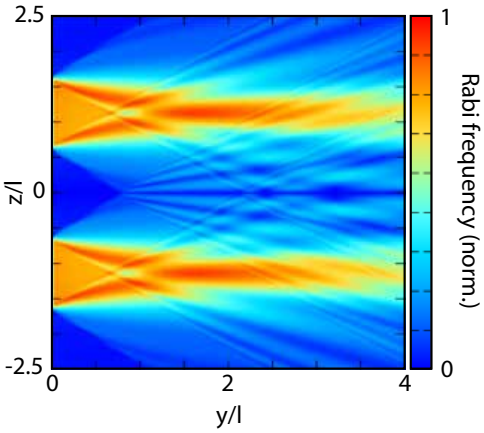

Figure 4.13: Calculated spatial map of the Rabi frequency induced by two adjacent striplines. We observe interference of spin waves generated by two striplines located at $y = 0$ for $z \in \pm[0.5, 1.5]$.

REFERENCES

[1] V. V. Kruglyak, S. O. Demokritov, and D. Grundler, *Magnonics,* Journal of Physics D: Applied Physics **43**, 264001 (2010).

[2] A. V. Chumak, V. I. Vasyuchka, A. A. Serga, and B. Hillebrands, *Magnon spintronics,* Nature Physics **11**, 453 (2015).

[3] K. Vogt, F. Y. Fradin, J. E. Pearson, T. Sebastian, S. D. Bader, B. Hillebrands, A. Hoffmann, and H. Schultheiss, *Realization of a spin-wave multiplexer,* Nature Communications **5**, 3727 (2014).

[4] A. V. Chumak, A. A. Serga, and B. Hillebrands, *Magnon transistor for all-magnon data processing,* Nature Communications **5**, 4700 (2014).

[5] L. J. Cornelissen, J. Liu, B. J. van Wees, and R. A. Duine, *Spin-Current-Controlled Modulation of the Magnon Spin Conductance in a Three-Terminal Magnon Transistor,* Physical Review Letters **120**, 097702 (2018).

[6] V. E. Demidov, H. Ulrichs, S. V. Gurevich, S. O. Demokritov, V. S. Tiberkevich, A. N. Slavin, A. Zholud, and S. Urazhdin, *Synchronization of spin Hall nano-oscillators to external microwave signals.* Nature communications **5**, 3179 (2014).

[7] Q. Wang, P. Pirro, R. Verba, A. Slavin, B. Hillebrands, and A. V. Chumak, *Reconfigurable nanoscale spin-wave directional coupler,* Science Advances **4**, e1701517 (2018).

[8] T. Warwick, K. Franck, J. B. Kortright, G. Meigs, M. Moronne, S. Myneni, E. Rotenberg, S. Seal, W. F. Steele, H. Ade, A. Garcia, S. Cerasari, J. Denlinger, S. Hayakawa, A. P. Hitchcock, T. Tyliszczak, J. Kikuma, E. G. Rightor, H. J. Shin, and B. P. Tonner, *A scanning transmission x-ray microscope for materials science spectromicroscopy at the advanced light source,* Review of Scientific Instruments **69**, 2964 (1998).

[9] V. Sluka, T. Schneider, R. A. Gallardo, A. Kákay, M. Weigand, T. Warnatz, R. Mattheis, A. Roldán-Molina, P. Landeros, V. Tiberkevich, A. Slavin, G. Schütz, A. Erbe, A. Deac, J. Lindner, J. Raabe, J. Fassbender, and S. Wintz, *Emission and propagation of 1D and 2D spin waves with nanoscale wavelengths in anisotropic spin textures,* Nature Nanotechnology **14**, 328 (2019).

[10] T. Sebastian, K. Schultheiss, B. Obry, B. Hillebrands, and H. Schultheiss, *Micro-focused Brillouin light scattering: imaging spin waves at the nanoscale,* Frontiers in Physics **3**, 35 (2015).

[11] Y. Acremann, C. H. Back, M. Buess, O. Portmann, A. Vaterlaus, D. Pescia, and H. Melchior, *Imaging precessional motion of the magnetization vector,* Science **290**, 492 (2000).

[12] L. Rondin, J. P. Tetienne, T. Hingant, J. F. Roch, P. Maletinsky, and V. Jacques, *Magnetometry with nitrogen-vacancy defects in diamond,* Reports on Progress in Physics **77**, 056503 (2014).

[13] F. Casola, T. van der Sar, and A. Yacoby, *Probing condensed matter physics with magnetometry based on nitrogen-vacancy centres in diamond,* Nature Reviews Materials **3**, 17088 (2018).

[14] I. Gross, W. Akhtar, V. Garcia, L. J. Martínez, S. Chouaieb, K. Garcia, C. Carrétéro, A. Barthélémy, P. Appel, P. Maletinsky, J. V. Kim, J. Y. Chauleau, N. Jaouen, M. Viret, M. Bibes, S. Fusil, and V. Jacques, *Real-space imaging of non-collinear antiferromagnetic order with a single-spin magnetometer,* Nature **549**, 252 (2017).

[15] L. Rondin, J.-P. Tetienne, S. Rohart, A. Thiaville, T. Hingant, P. Spinicelli, J.-F. Roch, and V. Jacques, *Stray-field imaging of magnetic vortices with a single diamond spin.* Nature communications **4**, 2279 (2013).

[16] Y. Dovzhenko, F. Casola, S. Schlotter, T. X. Zhou, F. Büttner, R. L. Walsworth, G. S. Beach, and A. Yacoby, *Magnetostatic twists in room-temperature skyrmions explored by nitrogen-vacancy center spin texture reconstruction,* Nature Communications **9**, 2712 (2018).

[17] T. van der Sar, F. Casola, R. Walsworth, and A. Yacoby, *Nanometre-scale probing of spin waves using single-electron spins.* Nature communications **6**, 7886 (2015).

[18] C. Du, T. van der Sar, T. X. Zhou, P. Upadhyaya, F. Casola, H. Zhang, M. C. Onbasli, C. A. Ross, R. L. Walsworth, Y. Tserkovnyak, and A. Yacoby, *Control and local measurement of the spin chemical potential in a magnetic insulator,* Science **357**, 195 (2017).

[19] P. Andrich, C. F. de las Casas, X. Liu, H. L. Bretscher, J. R. Berman, F. J. Heremans, P. F. Nealey, and D. D. Awschalom, *Long-range spin wave mediated control of defect qubits in nanodiamonds,* npj Quantum Information **3**, 28 (2017).

[20] D. Kikuchi, D. Prananto, K. Hayashi, A. Laraoui, N. Mizuochi, M. Hatano, E. Saitoh, Y. Kim, C. A. Meriles, and T. An, *Long-distance excitation of nitrogen-vacancy centers in diamond via surface spin waves,* Applied Physics Express **10**, 103004 (2017).

[21] C. S. Wolfe, V. P. Bhallamudi, H. L. Wang, C. H. Du, S. Manuilov, R. M. Teeling-Smith, a. J. Berger, R. Adur, F. Y. Yang, and P. C. Hammel, *Off-resonant manipulation of spins in diamond via precessing magnetization of a proximal ferromagnet,* Physical Review B **89**, 180406 (2014).

[22] L. Thiel, Z. Wang, M. A. Tschudin, D. Rohner, I. Gutiérrez-Lezama, N. Ubrig, M. Gibertini, E. Giannini, A. F. Morpurgo, and P. Maletinsky, *Probing magnetism in 2D materials at the nanoscale with single-spin microscopy,* Science **364**, 973 (2019).

[23] A. A. Serga, A. V. Chumak, and B. Hillebrands, *YIG magnonics,* Journal of Physics D: Applied Physics **43**, 264002 (2010).

[24] T. Yu, Y. M. Blanter, and G. E. W. Bauer, *Chiral Pumping of Spin Waves,* Physical Review Letters **123**, 247202 (2019).

[25] C. Dubs, O. Surzhenko, R. Linke, A. Danilewsky, U. Brückner, and J. Dellith, *Sub-micrometer yttrium iron garnet LPE films with low ferromagnetic resonance losses,* Journal of Physics D: Applied Physics **50**, 204005 (2017).

[26] T. Schneider, A. A. Serga, A. V. Chumak, C. W. Sandweg, S. Trudel, S. Wolff, M. P. Kostylev, V. S. Tiberkevich, A. N. Slavin, and B. Hillebrands, *Nondiffractive subwavelength wave beams in a medium with externally controlled anisotropy,* Physical Review Letters **104**, 197203 (2010).

[27] R. Gieniusz, H. Ulrichs, V. D. Bessonov, U. Guzowska, A. I. Stognii, and A. Maziewski, *Single antidot as a passive way to create caustic spin-wave beams in yttrium iron garnet films,* Applied Physics Letters **102**, 102409 (2013).

[28] M. Mohseni, R. Verba, T. Brächer, Q. Wang, D. A. Bozhko, B. Hillebrands, and P. Pirro, *Backscattering Immunity of Dipole-Exchange Magnetostatic Surface Spin Waves,* Physical Review Letters **122**, 197201 (2019).

[29] J. R. Eshbach and R. W. Damon, *Surface magnetostatic modes and surface spin waves,* Physical Review **118**, 1208 (1960).

[30] J. Chen, T. Yu, C. Liu, T. Liu, M. Madami, K. Shen, J. Zhang, S. Tu, M. S. Alam, K. Xia, M. Wu, G. Gubbiotti, Y. M. Blanter, G. E. W. Bauer, and H. Yu, *Excitation of unidirectional exchange spin waves by a nanoscale magnetic grating,* Physical Review B **100**, 104427 (2019).

[31] J. P. Tetienne, N. Dontschuk, D. A. Broadway, A. Stacey, D. A. Simpson, and L. C. Hollenberg, *Quantum imaging of current flow in graphene,* Science Advances **3**, e1602429 (2017).

[32] T. Rosskopf, A. Dussaux, K. Ohashi, M. Loretz, R. Schirhagl, H. Watanabe, S. Shikata, K. M. Itoh, and C. L. Degen, *Investigation of surface magnetic noise by shallow spins in diamond,* Physical Review Letters **112**, 147602 (2014).

[33] C. Wei, A. S. Windsor, and N. B. Manson, *A strongly driven two-level atom revisited: Bloch-Siegert shift versus dynamic Stark splitting,* Journal of Physics B: Atomic, Molecular and Optical Physics **30**, 21 (1997).

[34] B. Flebus and Y. Tserkovnyak, *Quantum-Impurity Relaxometry of Magnetization Dynamics,* Physical Review Letters **121**, 187204 (2018).

[35] K. Arai, C. Belthangady, H. Zhang, N. Bar-Gill, S. J. Devience, P. Cappellaro, A. Yada, and R. L. Walsworth, *Fourier magnetic imaging with nanoscale resolution and compressed sensing speed-up using electronic spins in diamond,* Nature Nanotechnology **10**, 859 (2015).

[36] G. Balasubramanian, I. Y. Chan, R. Kolesov, M. Al-Hmoud, J. Tisler, C. Shin, C. Kim, A. Wojcik, P. R. Hemmer, A. Krueger, T. Hanke, A. Leitenstorfer, R. Bratschitsch, F. Jelezko, and J. Wrachtrup, *Nanoscale imaging magnetometry with diamond spins under ambient conditions,* Nature **455**, 648 (2008).

[37] L. Thiel, D. Rohner, M. Ganzhorn, P. Appel, E. Neu, B. Müller, R. Kleiner, D. Koelle, and P. Maletinsky, *Quantitative nanoscale vortex imaging using a cryogenic quantum magnetometer,* Nature Nanotechnology **11**, 677 (2016).

[38] M. Pelliccione, A. Jenkins, P. Ovartchaiyapong, C. Reetz, E. Emmanouilidou, N. Ni, and A. C. Bleszynski Jayich, *Scanned probe imaging of nanoscale magnetism at cryogenic temperatures with a single-spin quantum sensor,* Nature Nanotechnology **11**, 700 (2016).

[39] E. Schaefer-Nolte, F. Reinhard, M. Ternes, J. Wrachtrup, and K. Kern, *A diamond-based scanning probe spin sensor operating at low temperature in ultra-high vacuum,* Review of Scientific Instruments **85**, 013701 (2014).

[40] J. M. Cai, B. Naydenov, R. Pfeiffer, L. P. McGuinness, K. D. Jahnke, F. Jelezko, M. B. Plenio, and A. Retzker, *Robust dynamical decoupling with concatenated continuous driving,* New Journal of Physics **14**, 113023 (2012).

[41] S. E. Lillie, N. Dontschuk, D. A. Broadway, D. L. Creedon, L. C. Hollenberg, and J. P. Tetienne, *Imaging Graphene Field-Effect Transistors on Diamond Using Nitrogen-Vacancy Microscopy,* Physical Review Applied **12**, 024018 (2019).

[42] S. Bogdanović, M. S. Liddy, S. B. Van Dam, L. C. Coenen, T. Fink, M. Lončar, and R. Hanson, *Robust nano-fabrication of an integrated platform for spin control in a tunable microcavity,* APL Photonics **2**, 126101 (2017).

[43] M. A. Schoen, J. M. Shaw, H. T. Nembach, M. Weiler, and T. J. Silva, *Radiative damping in waveguide-based ferromagnetic resonance measured via analysis of perpendicular standing spin waves in sputtered permalloy films,* Physical Review B **92**, 184417 (2015).

[44] B. A. Kalinikos and A. N. Slavin, *Theory of dipole-exchange spin wave spectrum for ferromagnetic films with mixed exchange boundary conditions,* Journal of Physics C: Solid State Physics **19**, 7013 (1986).

[45] J. D. Jackson, *John wiley & sons* (Wiley, New York, 1998).

[46] L. Novotny and B. Hecht, *Principles of nano-optics* (Cambridge University Press, Cambridge, 2006).

[47] T. Yu, C. Liu, H. Yu, Y. M. Blanter, and G. E. Bauer, *Chiral excitation of spin waves in ferromagnetic films by magnetic nanowire gratings,* Physical Review B **99**, 134424 (2019).

5

IMAGING SPIN-WAVE DAMPING UNDERNEATH METALS USING ELECTRON SPINS IN DIAMOND

Spin waves in magnetic insulators are low-damping signal carriers that could enable a new generation of spintronic devices. The excitation, control, and detection of spin waves by metal electrodes is crucial for interfacing these devices to electrical circuits. It is therefore important to understand metal-induced damping of spin-wave transport, but characterizing this process requires access to the underlying magnetic films. Here we show that spins in diamond enable imaging of spin waves that propagate underneath metals in magnetic insulators, and then use this capability to reveal a 100-fold increase in spin-wave damping. By analyzing spin-wave-induced currents in the metal, we derive an effective damping parameter that matches these observations well. We furthermore detect buried scattering centers, highlighting the technique's power for assessing spintronic device quality. Our results open new avenues for studying metal - spin-wave interaction and provide access to interfacial processes such as spin-wave injection via the spin-Hall effect.

This chapter has been published in *Advanced quantum technologies* 2100094 (2021) by **I. Bertelli**, B. G. Simon, T. Yu, J. Aarts, G. E. W. Bauer, Y. M. Blanter, T. van der Sar.

5.1. INTRODUCTION

Spin waves are collective, wave-like excitations of the spins in magnetic materials[1]. The field of magnon spintronics aims at using these waves as signal carriers in information processing devices[2]. Since its recent inception, the field has matured rapidly[3] and successfully realized prototypical spin-wave devices that implement logical operations[4–8]. In such devices, the spin waves are typically excited inductively[4–8] or via spin-pumping based on the spin-Hall effect[9, 10], using electric currents in metal electrodes that are deposited on top of thin-film magnetic insulators. As such, it is a key challenge to understand the interaction between the metals and the spin waves in the magnetic insulators, but this requires the ability to study the buried magnetic films and is hampered by the opacity of the metals to optical probes.

We address this challenge using magnetic imaging based on electron spins in diamond[11]. Metal films of sub-skin-depth thickness are transparent for microwave magnetic fields, which enables imaging of spin waves traveling underneath the metals by detecting their magnetic stray fields. We demonstrate this ability by imaging spin waves that travel underneath 200-nm-thick metal electrodes in a thin film of the magnetic insulator yttrium iron garnet (YIG). We find that the spatial spin-wave profiles under the metals reveal a surprisingly strong metal-induced spin-wave damping. By introducing the spin-wave-induced currents in the metal self-consistently into the Landau-Lifshitz-Gilbert (LLG) equation, we derive an analytical expression for the spin wave damping that matches our experimental observations without free parameters. We demonstrate that this eddy-current-induced damping mechanism dominates up to a threshold frequency above which three-magnon scattering becomes allowed and increases damping further.

Our imaging platform is an ensemble of shallowly implanted nitrogen-vacancy (NV) centers in diamond (Fig. 5.1a). NV centers are lattice defects with an $S = 1$ electron spin that can be polarized by optical excitation, controlled by microwaves, and read out through spin-dependent photoluminescence[12, 13]. Since NV centers can exist within ~ 10 nm from the surface of diamond[14], they can be brought within close proximity to a material of interest. Combined with an excellent sensitivity to magnetic fields[13], these properties make NV spins well suited for stray-field probing of spins and currents in condensed matter systems[15].

5.2. RESULTS

To image propagating spin waves, we place a diamond membrane containing a layer of NV centers implanted $\sim 10-20$ nm below the diamond surface onto a YIG film equipped with 200 nm thick gold microstrips (Methods). Passing a microwave current through a microstrip generates a magnetic field that excites spin waves in the YIG (Fig. 5.1a). These waves create a magnetic stray field that interferes with the direct microstrip field, leading to a spatial standing-wave pattern in the total amplitude of the oscillating magnetic field[11]. We spatially map this amplitude by locally measuring the contrast of the NV electron spin resonance (ESR) transitions. By changing the drive frequency while adjusting the static magnetic field (B_0) to maintain resonance with the NV ESR frequency

(Methods), we can excite and detect spin waves with wavevectors either along or perpendicular to the static magnetization M (Fig. 5.1b-c). The spin waves are clearly visible both underneath and next to the gold microstrips (Fig. 5.1b-d).

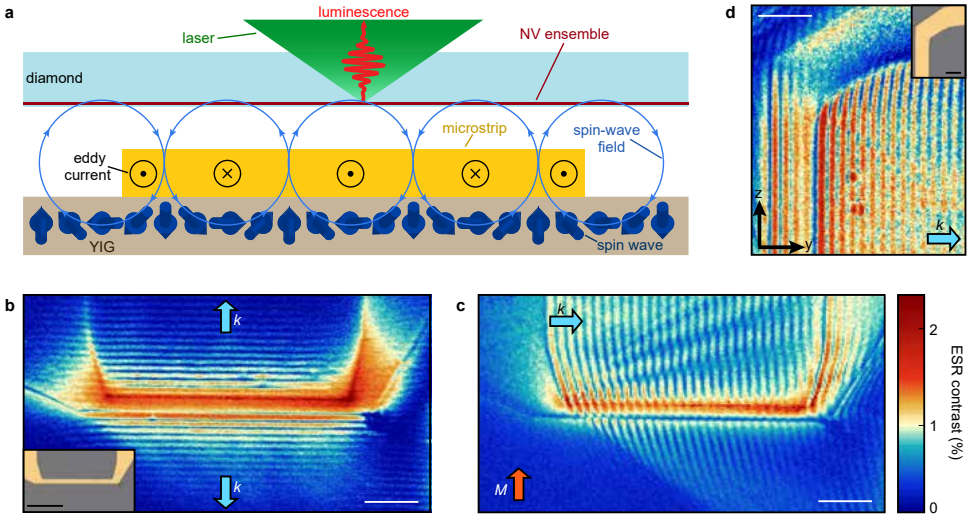

Figure 5.1: Magnetic imaging of microstrip excited spin waves using electron spins in diamond. (**a**) Idea of the experiment. An ensemble of nitrogen-vacancy (NV) centers in a diamond chip is used to image the magnetic stray fields generated by spin waves in a YIG thin film. The ability to image spin waves underneath metals is used to study the metal-induced spin-wave damping. (**b**)-(**d**) Spatial maps of the NV electron spin resonance (ESR) contrast when exciting spin waves resonant with an NV ESR transition. The oscillations result from the interference of the spin-wave and direct microstrip fields. The magnetization (**M**) points along z. The directions of the predominantly excited spin-wave vectors (**k**) are indicated. Scale bars: 20 µm. (**b**) Backward volume waves ($\mathbf{k} \parallel \mathbf{M}$), excited by applying a drive frequency $\omega/2\pi = 1.934$ GHz that is 0.17 GHz below the FMR at $B_0 = 33.5$ mT. Inset: micrograph of the sample (scale bar: 40 µm). (**c**) Spin waves in the Damon-Eshbach configuration ($\mathbf{k} \perp \mathbf{M}$) excited by applying a drive frequency $\omega/2\pi = 2.590$ GHz that is 1.12 GHz above the FMR at $B = 15$ mT. (**d**) Spin waves underneath and next to a gold microstrip used for spin-wave excitation (inset). Scale bars: 20 µm. As the skin depth of a 2.5 GHz magnetic field in gold is ~1.6 µm, spin waves are clearly visible underneath the 200 nm gold film.

To characterize the metal-induced spin-wave damping, we start by analyzing the spatial spin-wave profiles underneath and next to a gold microstrip that we use to excite spin waves (Fig. 5.2a). We select a section of microstrip that is far away from corners (> 100 µm) to avoid edge effects. We apply a static magnetic field with in-plane component along the microstrip direction and a drive frequency between 100-600 MHz above the ferromagnetic resonance (FMR), resulting in directional spin-wave emission with a large (small) spin-wave amplitude to the right (left) of the microstrip (Fig. 5.2a).This directionality is characteristic of microstrip-driven spin waves traveling perpendicularly to the magnetization and is a result of the handedness of the microstrip drive field and

the precessional motion of the spins in the magnet[16, 17]. We spatially quantify the amplitude of the local microwave magnetic field generated by the spin waves by measuring the rotation rate (Rabi frequency) of the NV spins[18]. The spatial oscillations in the measured NV Rabi frequency result from the interference between the microstrip and spin-wave fields[11]. The spin-wavelength is directly visible from the spatial period of these oscillations. We observe a rapid decay of the oscillations underneath the microstrip (Fig. 5.2b), even though the microstrip field is approximately constant in this region (Fig. 5.2c). We can thus conclude that this decay is caused by the decay of the spin-wave amplitude. In contrast, the decrease of the amplitude away from the microstrip follows the decay of the direct microstrip field (Fig. 5.2c).

By fitting the measured spatial decay in- and outside the microstrip region we can extract the additional spin-wave damping caused by the metal (Supplementary Sections 5.5.1 and 5.5.2). An accurate description of the measured NV Rabi frequencies (Fig. 5.2a-c) is only possible if we allow for different damping constants in- and outside the microstrip region (see also Supplementary Figure 5.5). We find that the damping underneath the gold microstrip (Fig. 5.2d, red diamonds) exceeds the damping next to the microstrip (yellow squares) by approximately two orders of magnitude .

We argue that the observed strong spin-wave damping underneath the metal is caused by eddy currents that are induced by the oscillating magnetic stray field of the spin waves. Eddy currents have been reported to cause linewidth broadening of ferromagnetic resonances in cavity and stripline-based experiments[19–25]. However, revealing their effect on propagating spin waves, which is important for information transport, has remained an outstanding challenge. We model the effect of the spin-wave-induced currents by including their magnetic field self-consistently into the LLG equation (Supplementary Sections 5.5.1.4 and 5.5.1.5). Doing so, we find that a metal film of thickness t increases the damping to $\alpha = \alpha_G + \alpha_m$, with α_G the intrinsic "Gilbert" damping and

$$\alpha_m = \gamma \frac{\mu_0^2 M_s g^2(k) t h}{4\rho} \frac{(1+\eta)^2}{1+\eta^2} \tag{5.1}$$

with γ the electron gyromagnetic ratio, μ_0 the vacuum permeability, M_s and h the YIG saturation magnetization and thickness, respectively, k the spin-wavenumber, ρ the metal resistivity, and η the spin-wave ellipticity. This expression is derived under the assumption of a homogeneous magnetization across the film thickness t, which becomes strictly valid in the thin-film limit $kt \ll 1$. The form factor $g(k) = (1-e^{-kh})(1-e^{-kt})/(k^2 th) \approx 1-k(t+h)$ arises from spatially averaging the dipolar and eddy-current stray fields over the thicknesses of the YIG and metal films. An analysis equating the magnetic energy losses to the power dissipated in the metal yields the same expression (Supplementary Section 5.5.1.7). We plot Eq. 5.1 and its thin-film limit in Fig. 5.2d using $\rho = 2.44 \cdot 10^{-8}$ Ωm for the resistivity of gold[26], finding a good agreement with the damping extracted from the various sets of data without free parameters. The finite width w of the stripline can be disregarded when $kw \gg 1$ (Supplementary Sections 5.5.1.6 and 5.5.1.7), as is the case in Fig. 5.2d. Accounting for a non-homogeneous magnetization may be achieved via micromagnetic simulations[16]

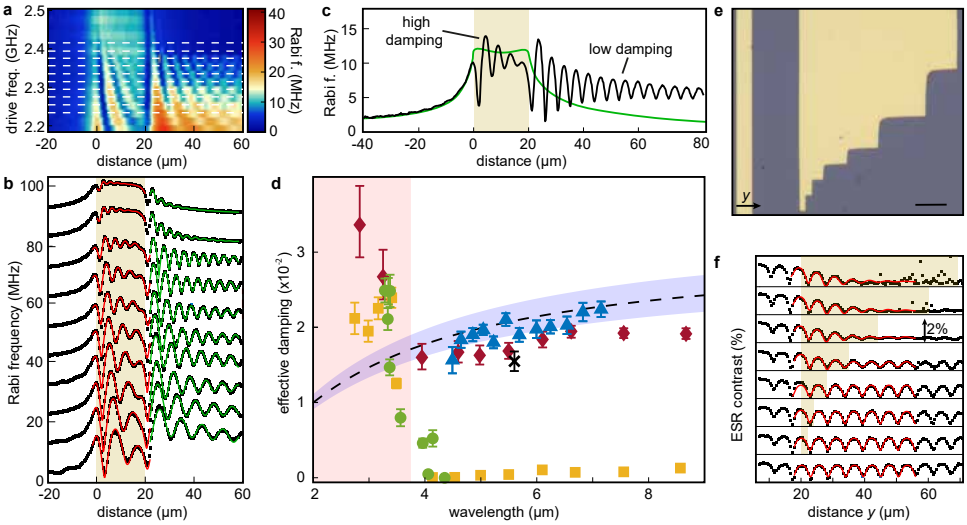

Figure 5.2: Characterizing metal-induced spin-wave damping. (**a**) Imaging spin waves underneath and next to a gold microstrip located between 0-20 μm vs drive frequency. Color scale: measured NV Rabi frequency. (**b**) Linecuts along dashed lines in (a). Black squares: data. Dashed red (green) lines: fits in (next to) the microstrip region. Traces offset by 10 MHz for clarity. (**c**) Measured NV Rabi frequency (black line) and calculated contribution to it from the direct microstrip field (green line) at drive frequency 2.361 GHz, B_0 = 18.2 mT. (**d**) Extracted spin-wave damping versus spin-wavelength for different devices. Yellow squares (red diamonds): device in (a-b), next to (under) the microstrip. Black cross: data from Fig. 5.2e-f. Blue triangles: wavelength-dependent damping underneath gold structure (Fig. 5.2e, Supplementary Fig. 5.6). Green circles: data from Fig. 5.3. Error bars: ±1 s.d. fit uncertainty. Dashed black line: theoretical model (Eq. 5.1) with shaded purple area indicating 10% uncertainty in gold resistivity. Shaded red area: three-magnon scattering region. (**e**) Micrograph of microstrip and gold structure used in (f). Scale bar: 10 μm. (**f**) ESR contrast along sections of varying length of the gold structure in (e). For each trace, the shaded yellow area indicates the gold structure length. The right microstrip edge is located at y = 5 μm. B = 20.3 mT, drive frequency $\omega/2\pi$ = 2.302 GHz, spin-wavelength= 5.6(2) μ. Black squares: data (for clarity, each trace is offset by 2%). Red lines: fits to a model that calculates the ESR contrast by summing the microstrip and spin-wave fields (Supplementary Section 5.5.2).

To corroborate the origin of the damping enhancement, we image spin waves propagating underneath a 200-nm-thick gold island deposited next to a microstrip (Fig. 5.2e-f). We observe a progressively decreasing spin-wave amplitude for increasing travel distance under the gold, with an average characteristic decay length of $y_0 = 9(1)$ µm extracted by fitting the top three traces in Fig. 5.2f. We characterize the wavelength dependence by varying the drive frequency (Supplementary Fig. 5.6). The corresponding damping values are reported in Fig. 5.2d (black cross and blue triangles) and agree well with Eq. 5.1.

Both in- and outside the stripline region, we observe a sudden increase in damping above a threshold frequency $\omega_T/2\pi \sim 2.39$ GHz (Fig. 5.2a). We characterize this increase in detail by zooming in to the threshold frequency (Fig. 5.3a-b) and extracting the damping parameter as a function of the wavelength (Fig. 5.2d, green circles). For the spin waves outside the microstrip region, the increase occurs in a ~10 MHz frequency range of the order of the intrinsic spin-wave linewidth.

By analyzing the known spin-wave dispersion of our YIG thin film (Supplementary Section 5.5.1.3), it becomes clear that the observed increase in damping above ω_T is a result of three-magnon scattering – a process in which one magnon decays into two of half the frequency and opposite wavevectors[27] (Fig. 5.3c): When the drive frequency is increased to above ω_T, three-magnon scattering becomes allowed because $\omega_T/2$ starts to exceed the bottom of the spin wave band (ω_{min}) (Fig. 5.3c and Supplementary Fig. 5.7). The onset of three-magnon scattering was previously identified using Brillouin light scattering[28]. Our real-space imaging approach reveals its dramatic effect on the spatial spin-wave decay length important for spin-wave transport. These measurements highlight that damping caused by three-magnon scattering limits the frequency range within which coherent spin waves in YIG thin films can serve as low-damping carriers to $\omega_{min} < \omega < 2\omega_{min}$.

Finally, we demonstrate that the ability to study spin waves underneath metals also enables the detection of hidden spin-wave scattering centers, highlighting the applicability of this approach for assessing the quality of buried magnetic films in multilayer systems. As an example, we show the scattering patterns produced by defects underneath the metal electrodes used for spin-wave excitation (Fig. 5.4a-b). The defects produce characteristic v-shaped patterns, resulting from preferential scattering into the "caustic" directions that are associated with the anisotropic dispersion[29], making the source of these spin-wave beams clearly identifiable. NV-based spin-wave imaging could therefore be used as a diagnostic tool for magnetic quality, even when the material of interest is buried under metallic layers in a heterostructure.

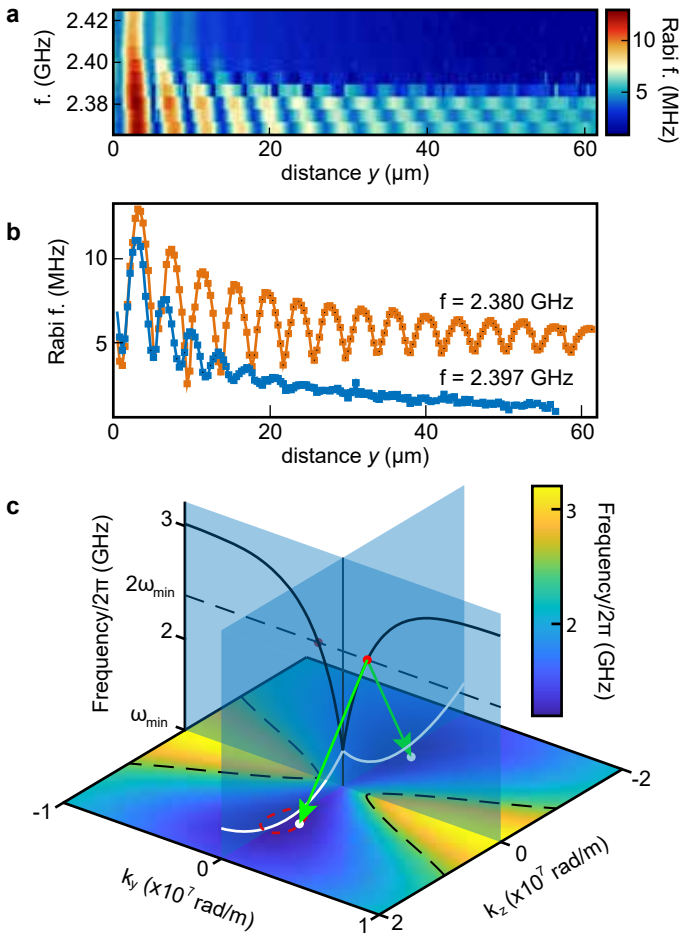

Figure 5.3: Spatial decay of propagating spin waves caused by three-magnon scattering. (**a**) NV Rabi frequency vs spin-wave drive frequency and distance from the edge of the microstrip used for spin-wave excitation. Above a threshold frequency $\omega_T/2\pi \sim 2.39$ GHz, the spin-wave damping increases strongly. (**b**) Linecuts of (a) below and above the threshold frequency. When the driving is below the threshold frequency (orange squares and curve), the decrease of the oscillation amplitude follows the decrease of the microstrip field. Above the threshold frequency (blue squares and curve), the spin-wave propagation distance is strongly reduced. (**c**) Calculated spin-wave dispersion for our 235 nm YIG film. The solid black and white lines show the dispersion along the y and z directions, respectively. The microwave drive excites spin waves propagating along y (red dot, Damon-Eshbach configuration). Above the threshold frequency ($\omega_T = 2\omega_m in$), scattering of one magnon in this mode into two backward-volume magnons (along z, white dots) near the band minimum becomes allowed (red dashed line corresponds to ~ 20 MHz above ω_{min}).

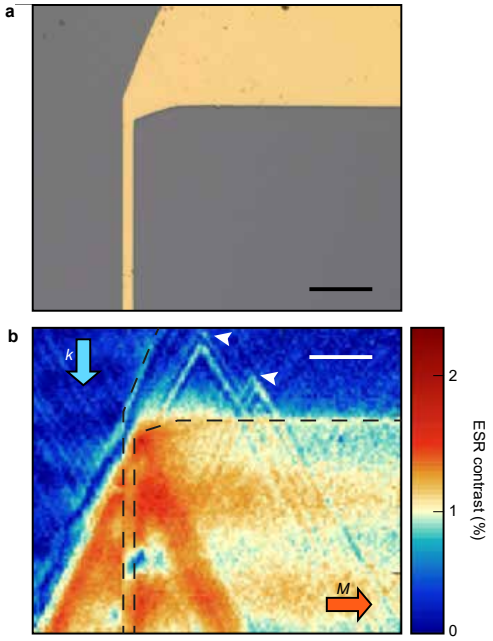

Figure 5.4: Imaging defect-induced spin-wave scattering underneath a 200 nm metal film. (**a**) Micrograph of the gold microstrip used in (b). Scale bar: 20 μm. (**b**) Spatial maps of the NV ESR contrast for $B_0 = 27.5$ mT and drive frequency $\omega/2\pi = 2.099$ GHz. Two scattering centers (white arrows) are located near the top edge of the image (not clearly identifiable from (a)), as deduced by the scattered caustic beams. Dashed black line: edge of the gold structure. The directions of the magnetization (**M**) and the predominant wavevector (**k**) excited by the microstrip are indicated. Scale bar: 20 μm.

5.3. DISCUSSION

In conclusion, we characterized the damping enhancement of spin waves that propagate under metallic electrodes used for spin-wave control, and showed that the increase is well explained by a model that introduces the spin-wave-induced currents into the LLG equation. The ability to detect spin waves underneath metals opens up several exciting new possibilities for studying the interaction between metals and magnets. One example is studying the spectral properties of temperature- or chemical-potential-driven magnon condensates underneath gates in magnon transistors[8, 30, 31]. Additionally, varying the thickness of the metal and/or magnetic films, or using spacer layers, enables a characterization of interfacial effects such as damping and anti-damping of magnons controlled by the spin-Hall effect in heavy metal electrodes. Furthermore, characterizing the screening of the spin-wave stray fields by a metal enables measuring its magnetic susceptibility at well-defined wavenumbers and extracting material parameters such as skin depth, conductivity and permeability. Finally, the ability to reveal buried scattering centers provides a new tool for assessing the quality of magnetic interfaces and spin-wave devices.

5.4. MATERIALS AND METHODS

5.4.1. SAMPLE FABRICATION

The diamond chip used in this work measured $2 \times 2 \times 0.05\text{–mm}^3$ and had an estimated NV density of $10^3/\ \mu\text{m}^2$ created via ion implantation at a depth of ~10-20 nm below the diamond surface (see fabrication details in[11]). The YIG film was 235 nm thick, grown on a 500 μm-thick GGG substrate via liquid phase epitaxy (Matesy gmbh). The saturation magnetization was previously measured[11] to be $M_s = 1.42 \cdot 10^5$ A/m. To mount the NV-diamond, we deposit a drop of isopropanol onto the YIG and place the diamond on top with the NV-surface facing down, while gently pressing down until the IPA has evaporated. The resulting diamond-YIG distance is limited by small particles (e.g. dust). We extract an NV-YIG distance of 1.6(1) μm from the measured maps of the NV Rabi oscillations.

5.4.2. NV-BASED IMAGING OF SPIN WAVES

NV centers are optically addressed using a home-built confocal microscope with a 515 nm laser, an NA=0.95 objective for laser focusing/photon collection, and an avalanche photodiode for NV photon detection (for details of the setup, see[11]). The ESR transition of the NV centers used in this work for spin-wave imaging is tuned by a magnetic field B_0 according to $\omega = D - \gamma B_0$ where $\gamma/2\pi = 28$ GHz/T is the electron gyromagnetic ratio and $D/2\pi = 2.87$ GHz is the zero-field splitting. In all experiments in Figs. 2-4, the magnetic field is oriented at a 54° angle with respect to the sample-plane normal and with an in-plane projection along the microwave stripline, thus aligning it with one of the four possible crystallographic orientations of the NV centers in the diamond. The fields used in this work are below ~25 mT, much smaller than the YIG saturation magnetization ($\mu_0 M_s = 178$ mT), therefore the YIG magnetization tilts out of plane by less than 5°[11]. We measure Rabi oscillations by applying a ~ 1 μs laser pulse to polarize the NV spin into

the $m_s = 0$ state, applying a microwave magnetic field at the NV ESR frequency, and reading out the final spin state through the NV's spin-dependent photoluminescence[13].

ACKNOWLEDGEMENTS

The authors thank Tao Yu for discussions.
Funding: This work was supported by the Dutch Research Council (NWO) as part of the Frontiers of Nanoscience (NanoFront) program through NWO Projectruimte grant 680.91.115.
Author contributions: I.B. and T.S. designed the experiment. B.S. prepared the diamond membrane. I.B. realized the NV magnetometry setup, fabricated the sample and performed the measurements. G.E.W.B., T.S and Y.M.B. developed the theoretical model. J.A. commented on the manuscript. I.B and T.S. analyzed the data and wrote the manuscript with help from all co-authors.
Data and materials availability: All data contained in the figures will be made available at 10.5281/zenodo.4726771 upon publication. Additional data related to this paper may be requested from the authors.
Competing interests: The authors declare no competing interest.

5.5. SUPPLEMENTARY MATERIAL

5.5.1. EDDY-CURRENT CONTRIBUTION TO SPIN-WAVE DAMPING

In this section we derive the additional spin-wave damping caused by the spin-wave-induced eddy currents in a nearby metallic layer. We use the Landau-Lifshitz-Gilbert (LLG) equation to evaluate the various components of the effective magnetic field and find solutions in the absence of additional damping. Then, we evaluate the spin-wave field inside the metal, derive the eddy currents excited by that field, and calculate the additional field component that acts back on the spin-waves, leading to an expression for the effective damping. Last, we consider the finite width of the metal film in the y direction and include this into the effective damping result.

We consider a thin film of a magnetic insulator (i.e. YIG) in the yz plane, between $-t < x < 0$, with unit magnetization $\mathbf{m}(\mathbf{r})$ oriented along z in equilibrium and saturation magnetization M_s. The bias magnetic field is applied along z. The system is translationally invariant along z.

LLG EQUATION

The LLG equation is [32]

$$\dot{\mathbf{m}} = -\gamma \mathbf{m} \times [\mathbf{B}_{\text{eff}} + \mathbf{B}_{\text{AC}}] - \alpha \dot{\mathbf{m}} \times \mathbf{m}, \tag{5.2}$$

where $\mathbf{B}_{\text{AC}}$ is the microstrip magnetic field, γ is the gyromagnetic ratio, α is the Gilbert damping and the effective magnetic field is

$$B_{\text{eff},\alpha} = -\frac{1}{M_s}\frac{\partial F}{\partial m_\alpha}, \tag{5.3}$$

where $\alpha = x, y, z$. We will now evaluate the various components of the effective magnetic field. We will assume that the spin-wavelength is much larger than the film thickness ($kt \ll 1$) such that we can approximate the magnetization to be homogeneous across the film thickness.

The free energy density includes contributions from the external field $\mathbf{B}_0$, the demagnetizing field $\mathbf{B}_{\text{d}}$, and the exchange interaction:

$$F = -M_s \mathbf{m} \cdot (\mathbf{B}_0 + \mathbf{B}_d/2) + \frac{D}{2} \sum_{\alpha,\beta=x,y,z} \left(\frac{\partial m_\alpha}{\partial \beta}\right)^2, \tag{5.4}$$

with D the spin stiffness. We define, for convenience, $\omega_B = \gamma B_0$, $\omega_M = \gamma \mu_0 M_s$, and $\omega_D = \frac{\gamma D}{M_s}$.

EVALUATING THE CONTRIBUTIONS TO THE EFFECTIVE MAGNETIC FIELD

Zeeman energy

The Zeeman energy associated with the external magnetic field $\mathbf{B}_0 = \omega_B \hat{\mathbf{z}}/\gamma$ is

$$F_z = -M_s \mathbf{m} \cdot \mathbf{B}_0. \tag{5.5}$$

Exchange energy

The exchange energy density in YIG is isotropic

$$F_{\text{ex}}(\mathbf{r}) = \frac{D}{2} \sum_{\alpha,\beta=x,y,z} \left(\frac{\partial m_\alpha(\mathbf{r})}{\partial \beta} \right)^2. \tag{5.6}$$

Its Fourier transform over the in-plane coordinates y, z is:

$$F_{\text{ex}}(\mathbf{k}, x) = -k^2 D(m_y^2(\mathbf{k}, x) + m_z^2(\mathbf{k}, x)) + \frac{D}{2} \sum_{\alpha=x,y,z} \left(\frac{\partial m_\alpha(\mathbf{k}, x)}{\partial x} \right)^2. \tag{5.7}$$

For a constant magnetization over the film thickness, the exchange energy contributes an effective field with Cartesian components:

$$B_{\text{D},\alpha} = -\frac{1}{M_s} \frac{\partial F}{\partial m_\alpha} = -\frac{\omega_D}{\gamma} k^2 m_\alpha(\mathbf{k}, x). \tag{5.8}$$

5

Demagnetizing field

The magnetic field generated by a magnetization $M_s\mathbf{m}(\mathbf{r})$ is given by [33]:

$$\mathbf{B}(\mathbf{r}) = \mu_0 M_s \int \Gamma(\mathbf{r} - \mathbf{r}')\mathbf{m}(\mathbf{r}')d\mathbf{r}', \tag{5.9}$$

where $\Gamma(\mathbf{r} - \mathbf{r}')$ is the real-space dipolar tensor, with components that are derivatives of the "Coulomb kernel":

$$\Gamma_{\alpha\beta}(\mathbf{r}) = \frac{\partial^2}{\partial\alpha\partial\beta} \frac{1}{4\pi|\mathbf{r}|}, \quad \text{with} \quad \alpha, \beta = x, y, z. \tag{5.10}$$

The 2D Fourier transform of Eq. (5.9) is [1]:

$$\mathbf{B}(\mathbf{k}, x) = \mu_0 M_s \int \Gamma(\mathbf{k}, x - x')\mathbf{m}(\mathbf{k}, x')dx', \tag{5.11}$$

where $\mathbf{k} = (k_y, k_z)$ and with magnetization

$$\mathbf{m}(\mathbf{r}) = \begin{cases} \mathbf{m}(y, z) & \text{for } -t < x < 0 \\ 0 & \text{elsewhere} \end{cases}. \tag{5.12}$$

The demagnetizing field, averaged over the film thickness, is given by:

$$\overline{\mathbf{B}}(\mathbf{k}) = \mu_0 M_s \frac{1}{t} \int_{-t}^{0} \int_{-t}^{0} \Gamma(\mathbf{k}, x - x')dx'dx\mathbf{m}(\mathbf{k}) = \mu_0 M_s \overline{\Gamma}(\mathbf{k})\mathbf{m}(\mathbf{k}), \tag{5.13}$$

[1] We define $g(k_x) = \int g(x)e^{-ik_x x}dx$ and $g(x) = \frac{1}{2\pi} \int g(k_x)e^{ik_x x}dk_x$

where the overline indicates averaging over the thickness. The components of the dipolar tensor in Fourier space are:

$$\Gamma_{\alpha\beta}(\mathbf{k},x)=\frac{1}{2}\begin{cases}e^{-k|x|}k-2\delta(x) & \text{for } \alpha=\beta=x,\\ -e^{-k|x|}\frac{k_\alpha k_\beta}{k} & \text{for } \alpha,\beta=y,z,\\ -e^{-k|x|}\text{sign}(x)ik_\alpha & \text{for } \alpha=y,z \text{ and } \beta=x.\end{cases} \tag{5.14}$$

Using

$$\frac{1}{t}\int_{-t}^{0}\int_{-t}^{0}e^{-k|x-x'|}dx'dx=\frac{2}{k}(1-\frac{1-e^{-kt}}{kt})=\frac{2}{k}f(kt), \tag{5.15}$$

$$\frac{1}{t}\int_{-t}^{0}\int_{-t}^{0}\text{sign}(x-x')e^{-k|x-x'|}dx'dx=0, \tag{5.16}$$

$$\frac{1}{t}\int_{-t}^{0}\int_{-t}^{0}\delta(x-x')dx'dx=1, \tag{5.17}$$

we arrive at

$$\overline{\mathbf{B}}(\mathbf{k})=\mu_0 M_s\begin{pmatrix}f(kt)-1 & 0 & 0\\ 0 & \frac{-k_y^2}{k^2}f(kt) & \frac{-k_y k_z}{k^2}f(kt)\\ 0 & \frac{-k_y k_z}{k^2}f(kt) & \frac{-k_z^2}{k^2}f(kt)\end{pmatrix}\begin{pmatrix}m_x(\mathbf{k})\\ m_y(\mathbf{k})\\ m_z(\mathbf{k})\end{pmatrix}, \tag{5.18}$$

with $f(kt)\rightarrow kt/2$ for $kt\ll 1$.

SPIN-WAVE SUSCEPTIBILITY

The linearized Eq. (5.2) in the frequency domain reads:

$$-i\omega m_x=-\gamma(B_z m_y-B_y)+i\alpha\omega m_y, \tag{5.19}$$

$$-i\omega m_y=-\gamma(B_x-B_z m_x)-i\alpha\omega m_x. \tag{5.20}$$

Using $\mathbf{B}=\mathbf{B}_{\text{eff}}+\mathbf{B}_{\text{AC}}$ and with $\Gamma_{xy}=\Gamma_{yx}=0$ (from Eq. (5.18)) we obtain

$$\gamma B_x=\omega_M(f-1)m_x-\omega_D k^2 m_x+\gamma B_{\text{AC},x}, \tag{5.21}$$

$$\gamma B_y=-\omega_M f\sin^2\phi m_y-\omega_D k^2 m_y+\gamma B_{\text{AC},y}, \tag{5.22}$$

$$\gamma B_z=\omega_B, \tag{5.23}$$

where ϕ is the angle between the wave vector $\mathbf{k}$ and $\mathbf{B}_{\text{eff}}$. With

$$\omega_0=\omega_B+\omega_D k^2, \tag{5.24}$$

$$\omega_2=\omega_0+\omega_M(1-f), \tag{5.25}$$

$$\omega_3=\omega_0+\omega_M f\sin^2\phi, \tag{5.26}$$

we obtain Eqns. (5.19-5.20) in matrix form:

$$\begin{pmatrix}\omega_2-i\alpha\omega & i\omega\\ -i\omega & \omega_3-i\alpha\omega\end{pmatrix}\begin{pmatrix}m_x\\ m_y\end{pmatrix}=\gamma\begin{pmatrix}B_{AC,x}\\ B_{AC,y}\end{pmatrix}. \tag{5.27}$$

Inverting Eq. (5.27) gives the susceptibility

$$\chi = \frac{\gamma}{(\omega_2 - i\alpha\omega)(\omega_3 - i\alpha\omega) - \omega^2} \begin{pmatrix} \omega_3 - i\alpha\omega & -i\omega \\ i\omega & \omega_2 - i\alpha\omega \end{pmatrix}. \tag{5.28}$$

It is singular when:

$$\Lambda = (\omega_2 - i\alpha\omega)(\omega_3 - i\alpha\omega) - \omega^2 = 0. \tag{5.29}$$

The real parts of the solutions of this quadratic equation give the spin wave dispersion $\omega_{sw} = \sqrt{\omega_2\omega_3}$, plotted in Fig. 3c of the main text. In Fig. 3c, the solid lines indicate the dispersion for spin waves propagating along $\pm z$ (i.e., $\phi = 0$ and $\phi = \pi$) and along $\pm y$ (i.e., $\phi = \pm\pi/2$). The spin-wave linewidth $\alpha(\omega_2 + \omega_3)/2$ follows from the imaginary part of Eq. (4.14), and the ellipticity of the magnetization precession is given by

$$\eta = \left|\frac{\chi_{xx}}{\chi_{yx}}\right|_{(\omega=\omega_{sw})} = \sqrt{\frac{\omega_3}{\omega_2}}. \tag{5.30}$$

Applying the bias field B_0 along $\theta_{B_0} = 34°$ as in the experiments changes $\omega_0 \rightarrow \omega_B \cos\theta_{B_0} + \omega_D k^2$, but does not introduce additional terms in the susceptibility for B_0 much smaller than the demagnetizing field ($B_0 \ll \mu_0 M_s$), as in this work.

5

EDDY-CURRENT-INDUCED SPIN-WAVE DAMPING

In this section, we introduce the field generated by eddy currents into the LLG equation. We first derive the eddy currents in a metal film (parallel to the yz plane and located between $0 < x < h$) induced by the spin-wave stray field. The eddy currents in turn generate a magnetic field $\mathbf{B}_e$ that couples back into the LLG equation, which should be solved self-consistently. We focus on spin waves travelling in the $+y$-direction, such that $k = k_y$ (thus $\phi = \pi/2$). Our films are much thinner than the magnetic skin depth (1.7 μm for gold at 2 GHz) such that the dipolar stray fields are not screened significantly. Because the film is thin, we neglect eddy currents in the out-of-plane direction. The in-plane eddy currents are induced by the out-of-plane component of the magnetic field, given by (see Eq. (5.14)):

$$\overline{B}_x = \frac{\mu_0 M_s}{2} \frac{1}{h} \int_0^h dx \int_{-t}^0 dx' k e^{-k(x-x')} (m_x - i m_y) \tag{5.31}$$

$$= \frac{\mu_0 M_s}{2} k t g (m_x - i m_y), \tag{5.32}$$

where the overbar denotes an average over the metal (h) thickness. Here,

$$g = \frac{(1 - e^{-kh})}{kh} \frac{(1 - e^{-kt})}{kt}. \tag{5.33}$$

For an infinitely thin film, $g \rightarrow 1$. From Faraday's law, $\overline{B}_x$ generates a charge current :

$$J_z = \sigma E_z = \sigma \frac{\omega}{k_y} \overline{B}_x = \omega \frac{\sigma \mu_0 M_s t}{2} g (m_x - i m_y), \tag{5.34}$$

where σ is the conductivity and E_z the electromotive force. As we will further discuss in 5.5.1.6, this equation is valid in the limit $kw \gg 1$, with w the width of the film, since we used a Fourier transform over y and did not specify boundary conditions. In Fig. 2d of the main text, $w = 20$ μm and $\lambda < 9$ μm, such that $kw > 14$.

Field generated by the eddy currents

The current J_z generates a field $\mathbf{B}_e$ inside the YIG film. Its average over the YIG thickness is

$$\overline{B}_{e,x} = i\frac{\mu_0 J_z h}{2} g = i\omega \frac{\mu_0^2 M_s \sigma}{4} th \cdot g^2 (m_x - i m_y), \tag{5.35}$$

$$\overline{B}_{e,y} = i\overline{B}_{e,x}, \tag{5.36}$$

which we can rewrite as

$$\gamma \overline{B}_{e,x} = i\omega \alpha_m (m_x - i m_y), \tag{5.37}$$

$$\gamma \overline{B}_{e,y} = -\alpha_m \omega (m_x - i m_y), \tag{5.38}$$

where

$$\alpha_m = \gamma \frac{\mu_0^2 M_s \sigma}{4} th \cdot g^2 \tag{5.39}$$

is a dimensionless factor that turns out to be the eddy current contribution to the damping as discussed in the next section. Because the equation was derived under the approximation of a homogeneous magnetization across the film thickness it is valid in the thin-film limit $kt, kh \ll 1$ where $g^2(k) \to 1 - k(t+h)$. The factor $g^2(k)$ arises from averaging the dipolar and eddy current stray fields over the thicknesses of the metal and magnet films. Including a non-homogeneous magnetization across the film thickness may be achieved via micromagnetic simulations. In Fig. 2d of the main text, $0.16 < kt < 0.37$ (for $4\ \mu\text{m} < \lambda < 9\ \mu\text{m}$.)

SOLUTIONS TO THE LLG EQUATIONS WITH EDDY CURRENTS

We now incorporate $\mathbf{B}_e$ into the LLG equation by adding it to Eqs. (5.21-5.23) for $\phi = \pi/2$

$$\gamma B_x = -(\omega_M (1-f) + \omega_D k^2) m_x + \alpha_m \omega \left(i m_x + m_y\right) + \gamma B_{AC,x}, \tag{5.40}$$

$$\gamma B_y = -(\omega_M f + \omega_D k^2) m_y - \alpha_m \omega \left(m_x - i m_y\right) + \gamma B_{AC,y}, \tag{5.41}$$

$$\gamma B_z = \omega_B. \tag{5.42}$$

The linearized LLG equations (5.19-5.20) become

$$-i\omega m_x = -(\omega_3 - i(\alpha + \alpha_m)\omega) m_y - \alpha_m \omega m_x + \gamma B_{AC,y}, \tag{5.43}$$

$$-i\omega m_y = (\omega_2 - i(\alpha + \alpha_m)\omega) m_x - \alpha_m \omega m_y - \gamma B_{AC,x}, \tag{5.44}$$

where ω_2 and ω_3 are given in Eqs. (5.24-5.26). In matrix form:

$$\begin{pmatrix} \omega_2 - i(\alpha+\alpha_m)\omega & (i-\alpha_m)\omega \\ -(i-\alpha_m)\omega & \omega_3 - i(\alpha+\alpha_m)\omega \end{pmatrix} \begin{pmatrix} m_x \\ m_y \end{pmatrix} = \gamma \begin{pmatrix} B_{AC,x} \\ B_{AC,y} \end{pmatrix}. \tag{5.45}$$

The resulting susceptibility is singular when

$$\Lambda = (\omega_2 - i(\alpha+\alpha_m)\omega)(\omega_3 - i(\alpha+\alpha_m)\omega) + (i-\alpha_m)^2 \omega^2 = 0. \tag{5.46}$$

Solving this quadratic equation and disregarding terms of order α^2 leads to

$$\omega = \sqrt{\omega_2\omega_3} - i\left[\alpha_m\sqrt{\omega_2\omega_3} + (\alpha+\alpha_m)\frac{\omega_2+\omega_3}{2}\right]. \tag{5.47}$$

We observe that including the eddy currents yields the same spin-wave dispersion $\omega_{sw} = \sqrt{\omega_2\omega_3}$, but renormalizes the linewidth according to

$$\alpha\frac{\omega_2+\omega_3}{2} \to \alpha_m\left[\sqrt{\omega_2\omega_3} + \frac{\omega_2+\omega_3}{2}\right], \tag{5.48}$$

where we assumed $\alpha_m \gg \alpha$. The eddy-current-induced damping can thus be included into Eq. (5.2) by setting

$$\alpha = \alpha_e = \alpha_m\frac{\sqrt{\omega_2\omega_3} + \frac{\omega_2+\omega_3}{2}}{\frac{\omega_2+\omega_3}{2}} = \alpha_m\frac{(1+\eta)^2}{1+\eta^2}. \tag{5.49}$$

Substituting Eq. (5.39) leads to Eq. 1 in the main text. In section 5.5.1.7 we find the same expression using an alternative derivation.

5

METAL FILM OF FINITE WIDTH

We now consider a metal strip with finite width w along y. The effective orbital magnetization of the eddy currents induced by the spin-wave field points in the x-direction and is determined by the Maxwell-Faraday equation:

$$\frac{\partial^2 m_z^{eff}}{\partial y^2} = -i\omega\sigma\bar{B}_x(y), \quad \text{with} \quad j_z = -\partial m_z^{eff}/\partial y, \tag{5.50}$$

where $\bar{B}_x(y)$ is the stray field of a spin wave travelling in the $+y$ direction, Fourier transformed over time but not over coordinates. It is given by (c.f. Eq. (5.32))

$$\bar{B}_x(y) = \frac{\mu_0 M_s}{2} ktg(m_x - i m_y). \tag{5.51}$$

Introducing the notations $m_{x,y} = m_{x,y}^{(0)} e^{iky}$, the solution of Eq. (5.50) is

$$m_x^{eff} = \alpha_k\left(e^{iky} - [1+iky]\frac{\sin\frac{kw}{2}}{\frac{kw}{2}}\right), \tag{5.52}$$

with

$$\alpha_k = i\omega\sigma\frac{\mu_0 M_s t}{2k} g_k(m_x^0 - i m_y^0). \tag{5.53}$$

The eddy-current field averaged over the magnetic film thickness, cf. Eq. (5.35) is:

$$B_{e\alpha}(y) = \frac{1}{t}\int_{-t}^{0} dx B_{e\alpha}(x,y) = \int\frac{dq}{2\pi} B_{e\alpha}(q) e^{iqy}, \tag{5.54}$$

where

$$B_{e\alpha}(q) = \frac{\mu_0 M_s}{t}\int_{-t}^{0} dx \int_0^h dx' \int_{-\infty}^{\infty} dy dz e^{\prime -iqy} \int_{-w/2}^{w/2} dy' \Gamma_{\alpha x}(\mathbf{r},\mathbf{r}') m_x^{eff}(\mathbf{r}'). \tag{5.55}$$

Note that it does not depend on z. Using

$$\int_{-\infty}^{\infty} dy'dz' \frac{e^{iky'}}{\sqrt{(x-x')^2+y'^2+z'^2}} = \frac{2\pi}{|k|} e^{-|k(x-x')|}, \tag{5.56}$$

from Eq. (5.55) we obtain

$$B_{e\alpha}(q) = \mu_0 M_s \alpha_k |q| h g_{|q|} \left\{ \frac{\sin[(k-q)w/2]}{k-q} - 2\frac{\sin(qw/2)\sin(kw/2)}{qwk} + \right. \tag{5.57}$$

$$\left. -\frac{2}{wq^2}\sin\frac{kw}{2}\left[\sin\frac{qw}{2} - \frac{qw}{2}\cos\frac{qw}{2}\right]\right\} \tag{5.58}$$

and $B_{e,y}(q) = (iq/|q|)B_{e,x}(q)$. In the wide-strip limit $\lim_{w\to\infty} k^{-1}\sin(kw/2) \to \pi\delta(k)$ such that, back in the real-space and time domains,

$$B_{e\alpha}(y,\tau) = \frac{i\omega\sigma\mu_0^2 M_s}{4} e^{-i\omega\tau} th(m_x^0 - i m_y^0)(g_k^2 e^{iky} - \frac{2\pi}{w}\delta(k)). \tag{5.59}$$

The last term reflects that a spatially homogeneous mode does not induce eddy currents. The finite width can be neglected when $kw \gg 1$, in which case we get the same result as Eq. (5.39). In Fig. 2d of the main text, $kw > 14$.

5

EFFECTIVE MAGNETIC DAMPING

The effective damping parameter can be derived alternatively by equating the magnetic and external energy losses [34]. According to the LLG equation the power density per area of a dynamic magnetization for a scalar Gilbert damping constant reads

$$p^{(m)}(y) = -\int \left(\dot{\mathbf{M}}\cdot\mathbf{B}_{\text{eff}}\right) dx = -\frac{\alpha_G M_s}{\gamma}\int \dot{\mathbf{m}}^2 dx, \tag{5.60}$$

where the integral is over the magnetic film thickness. In our geometry the power loss density of a spin wave mode $\mathbf{m}_i$ with index i that solves the linearized LLG with frequency ω_i is then

$$p_i^{(m)}(y) = \frac{\alpha_G M_s}{\gamma}\omega_i^2 \int [(m_i^{(x)})^2 + (m_i^{(y)})^2] dx, \tag{5.61}$$

In the limit $kt \ll 1$, we can replace i by the wave number k of the spin wave in the y direction. The time (τ)-dependent magnetization

$$\mathbf{m}_k = m_k \begin{pmatrix} \eta_k \cos(ky-\omega\tau) \\ \sin(ky-\omega\tau) \end{pmatrix} \tag{5.62}$$

leads to the time-averaged dissipation

$$p_i^{(m)}(y) = \frac{\alpha_G M_s}{\gamma}\omega_k^2 \frac{1+\eta_k^2}{2}\int m_k^2(x,y)\, dx, \tag{5.63}$$

We model the energy loss per unit of length under the strip by a phenomenological damping parameter α'_k as

$$P_k^{(m)} = tw\frac{\alpha'_k M_s}{\gamma}\omega_k^2 \frac{1+\eta_k^2}{2}\overline{m_k^2}, \tag{5.64}$$

where the over-bar indicates the spatial average over the film thickness t. Assuming that the magnetic skin depth is much larger than the thickness of the strip h, the stray field averaged over the strip thickness above the film and $k > 0$ reads

$$\bar{B}_x = M_s \mu_0 t k \frac{1+\eta_k}{2} \overline{m_k} \cos\left(ky - \omega\tau\right). \tag{5.65}$$

This field generates an electromotive force (emf) E_z according to $\partial_y E_z = -\partial_\tau \bar{B}_x$:

$$E_z(y) = -\int_0^y \partial_\tau \bar{B}_x dy' \tag{5.66}$$

$$= M_s \mu_0 t \frac{1+\eta_k}{2} \overline{m_k} \omega \left[\cos(ky - \omega\tau) - cos(\omega\tau)\right] + \mathrm{C}. \tag{5.67}$$

The emf does not drive a net charge current since the metal strip is part of a high impedance circuit.

$$J_z = \sigma t \int_0^w E_z(y) = 0 \tag{5.68}$$

then fixes the integration constant C. The time-averaged ($\langle\cdots\rangle$) integrated Ohmic loss per unit length of the wire then reads

$$P_k^{(\Omega)} = h\sigma \int_0^w \langle |E_z|^2 \rangle \, dy \tag{5.69}$$

$$= \sigma \left(\mu_0 t \overline{m_k} \omega\right)^2 hw \left(\frac{2\cos kw + k^2 w^2 - 2}{2\left(kw\right)^2}\right). \tag{5.70}$$

We can now determine the effective damping by setting $P_k^{(\Omega)} \equiv P_k^{(m)}$.

$$\alpha_k' = \gamma M_s h t \sigma \mu_0^2 \frac{\overline{m_k}^2}{\overline{m_k^2}} \frac{2\cos kw + k^2 w^2 - 2}{2\left(kw\right)^2} \frac{(1+\eta_k)^2}{2(1+\eta_k^2)}. \tag{5.71}$$

In the long-wavelength and wide-metal-strip regime $w^{-1} \ll k \ll t^{-1}$, $\overline{m_k}^2 \approx \overline{m_k^2}$ and $\eta_k \approx \eta$,

$$\alpha_e' = \gamma M_s h t \sigma \mu_0^2 \frac{(1+\eta)^2}{4(1+\eta^2)} \tag{5.72}$$

agrees with Eq. (5.49). We note that the scalar α_m' should be interpreted as an appropriate average over the Gilbert damping tensor elements that can be in principle determined by the same procedure.

5.5.2. DATA FITTING PROCEDURES

EXTRACTING THE DAMPING FROM THE MEASURED RABI FREQUENCY TRACES

To fit the measured Rabi frequencies (Fig. 2a-c of the main text) and extract the spin-wave damping, we follow the procedure described in [11]. In this procedure, we first calculate the magnetic field generated by a microwave current in a microstrip propagating along z, given by $\mathbf{B_{AC}} = (B_{AC,x}\hat{\mathbf{x}} + B_{AC,y}\hat{\mathbf{y}})$. We then calculate the resulting magnetization dynamics in Fourier space using $\mathbf{m}(\mathbf{k}) = \chi(\mathbf{k})\mathbf{B}_{\mathrm{AC}}(\mathbf{k})$. From $\mathbf{m}(\mathbf{k})$, we calculate the stray

field of the spin waves at the location of the NV sensing layer. We then sum (vectorially) the spin-wave and microstrip fields and calculate the resulting NV Rabi frequency. Free fitting parameters are the microwave current through the microstrip, the spin-wave damping, and a ~ 1 MHz spatially homogeneous offset to account for the field generated by the leads delivering the current to the stripline.

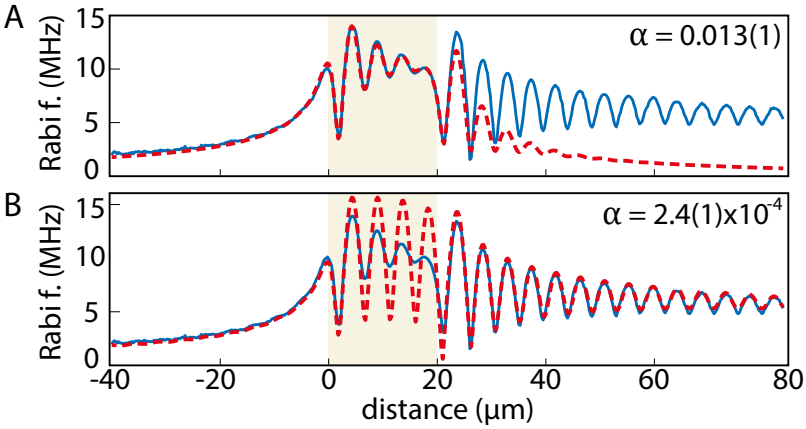

Figure 5.5: Highlighting the different spin-wave damping underneath and next to the microstrip. Solid blue lines: data trace from Fig. 2c of the main text. Dashed red lines: calculated Rabi frequencies for high (A) and low (B) values of the damping. The calculations use a single value of the damping for the entire spatial range. The high-damping calculation (panel A) only matches the data well in the microstrip region. The low-damping calculation (panel B) only matches the data next to the microstrip. The microstrip is indicated by shaded yellow color.

Figure 5.5 shows two example traces calculated using this procedure (red dashed lines) and compares these to a measured trace (blue line) of Fig. 2c of the main text. In both A and B, the calculated traces use a single value of the damping for the entire spatial range. These plots highlight that the measured data in the microstrip region are only described well for a large value of the damping, while the data next to the microstrip are only described well for a low value of the damping.

EXTRACTING THE DAMPING UNDER THE GOLD STRUCTURE

To extract the spatial decay length of the spin waves y_{decay} underneath the gold structure from spatial measurements of the ESR contrast $C(y)$ (Fig. 2e-f of the main text and Supplementary Fig. 5.6) we describe $C(y)$ using

$$C(y) = C_0 \frac{\Omega^2(y)}{\Omega^2(y)+1}, \tag{5.73}$$

where C_0 is the known maximum ESR contrast and $\Omega(y)$ is a normalized NV Rabi frequency resulting from the sum of the spin-wave and direct microstrip fields:

$$\Omega(y) = \left| iAe^{i(k(y-y_0)}e^{-(y-y_{\text{struct}})/y_{decay}} + \frac{B}{y-y_0} \right|. \tag{5.74}$$

Here, y_0 and y_{struct} are the known locations of the edges of the microstrip and gold structure, respectively (see Fig. 2e of the main text), and A, B, and y_{decay} are extracted from the fits. The spatial decay length y_{decay} is given by the linewidth of the susceptibility in k-space and can therefore be related to the damping parameter α by Taylor expanding $\omega_{sw}(k) \approx \omega_{sw}(k_0) + v_g(k-k_0)$ in Eq. (4.14) to get:

$$\Lambda = 2\omega_{sw}\left(v_g(k-k_0) - i\alpha\frac{\omega_2+\omega_3}{2}\right). \tag{5.75}$$

Solving $\Lambda = 0$, we find

$$k = k_0 + i\alpha\frac{\omega_2+\omega_3}{2v_g}, \tag{5.76}$$

which yields the relation between the spatial decay length and α

$$y_{decay} = \frac{2v_g}{\alpha(\omega_2+\omega_3)}, \tag{5.77}$$

where we calculate ω_2 and ω_3 (defined in Eqs. (5.25) and (5.26)) and the spin-wave group velocity v_g from the spin-wave dispersion.
This fit procedure is used to extract the damping from the data in Fig. 2f of the main text, as well as to determine the frequency dependence of the damping underneath the gold structure, for which the data traces and fits are shown in Fig. 5.6. The extracted values of the damping are plotted in Fig. 2d of the main text.

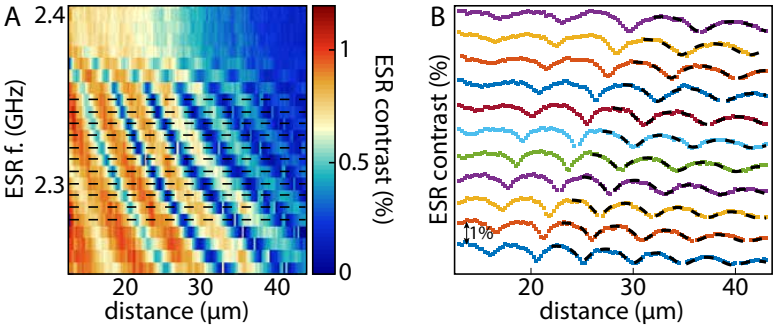

Figure 5.6: Spin-wave damping under gold structure. (**A**) ESR contrast vs distance for different spin-wave frequencies under the gold structure shown in Fig. 2e of the main text. Dashed black lines: linecuts shown in (B). (**B**) Colored lines: linecuts of (A). Dashed black lines: fits. The fitting range was chosen such that it starts at the first peak for which a decay is visible.

THREE-MAGNON SCATTERING THRESHOLD

The three-magnon scattering process is enabled for spin waves of frequency at least twice that of the bottom of the spin-wave band (ω_{min}), which shifts with the applied magnetic field. In the main text, we see this threshold at ~2.39 GHz (Fig. 3). From the spin-wave dispersion (Eq. (4.14)), we find that this frequency corresponds to the frequency at which the ω_- NV ESR transition and $2\omega_{\text{min}}$ cross (Fig. 5.7).

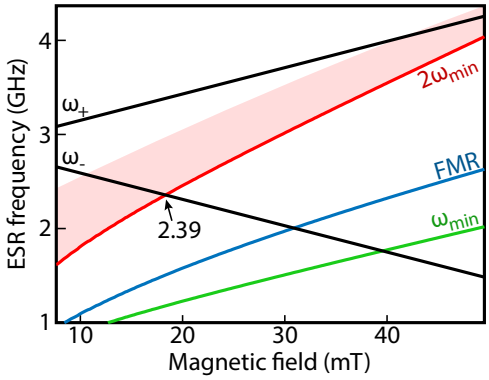

Figure 5.7: Calculated three-magnon scattering threshold frequency vs magnetic field applied along the NV axis. For frequencies above $2\omega_{\text{min}}$ (shaded red area), scattering of one DE spin wave into two BV waves of frequency close to the band minimum (ω_{min}, solid green line) becomes possible. Solid black lines (indicated as $\omega_{\pm}$) represent the NV ESR transitions. ω_{-} and $2\omega_{\text{min}}$ cross at a frequency close to 2.39 GHz, as shown in Fig. 3 of the main text. Solid blue line: FMR of YIG.

5

REFERENCES

[1] D. D. Stancil and A. Prabhakar, *Spin Waves* (Springer, 2009).

[2] A. V. Chumak, V. I. Vasyuchka, A. A. Serga, and B. Hillebrands, *Magnon spintronics,* Nature Physics **11**, 453 (2015).

[3] A. Barman, G. Gubbiotti, S. Ladak, A. O. Adeyeye, M. Krawczyk, J. Gräfe, C. Adelmann, S. Cotofana, A. Naeemi, V. I. Vasyuchka, B. Hillebrands, S. A. Nikitov, H. Yu, D. Grundler, A. Sadovnikov, A. A. Grachev, S. E. Sheshukova, J.-Y. Duquesne, M. Marangolo, C. Gyorgy, W. Porod, V. E. Demidov, S. Urazhdin, S. Demokritov, E. Albisetti, D. Petti, R. Bertacco, H. Schulteiss, V. V. Kruglyak, V. D. Poimanov, A. K. Sahoo, J. Sinha, H. Yang, M. Muenzenberg, T. Moriyama, S. Mizukami, P. Landeros, R. A. Gallardo, G. Carlotti, J.-V. Kim, R. L. Stamps, R. E. Camley, B. Rana, Y. Otani, W. Yu, T. Yu, G. E. W. Bauer, C. H. Back, G. S. Uhrig, O. V. Dobrovolskiy, S. van Dijken, B. Budinska, H. Qin, A. Chumak, A. Khitun, D. E. Nikonov, I. A. Young, B. Zingsem, and M. Winklhofer, *The 2021 Magnonics Roadmap,* Journal of Physics: Condensed Matter , (in press) (2021).

[4] T. Fischer, M. Kewenig, D. A. Bozhko, A. A. Serga, I. I. Syvorotka, F. Ciubotaru, C. Adelmann, B. Hillebrands, and A. V. Chumak, *Experimental prototype of a spin-wave majority gate,* Applied Physics Letters **110**, 152401 (2017).

[5] G. Talmelli, T. Devolder, N. Träger, J. Förster, S. Wintz, M. Weigand, H. Stoll, M. Heyns, G. Schütz, I. P. Radu, J. Gräfe, F. Ciubotaru, and C. Adelmann, *Reconfigurable submicrometer spin-wave majority gate with electrical transducers,* Science Advances **6**, eabb4042 (2020).

[6] Q. Wang, M. Kewenig, M. Schneider, R. Verba, F. Kohl, B. Heinz, M. Geilen,

M. Mohseni, B. Lägel, F. Ciubotaru, C. Adelmann, C. Dubs, S. D. Cotofana, O. V. Dobrovolskiy, T. Brächer, P. Pirro, and A. V. Chumak, *A magnonic directional coupler for integrated magnonic half-adders,* Nature Electronics **3**, 765 (2020).

[7] A. V. Chumak, A. A. Serga, and B. Hillebrands, *Magnon transistor for all-magnon data processing,* Nature Communications **5**, 4700 (2014).

[8] L. J. Cornelissen, J. Liu, B. J. van Wees, and R. A. Duine, *Spin-Current-Controlled Modulation of the Magnon Spin Conductance in a Three-Terminal Magnon Transistor,* Physical Review Letters **120**, 097702 (2018).

[9] J. Sinova, S. O. Valenzuela, J. Wunderlich, C. H. Back, and T. Jungwirth, *Spin Hall effects,* Reviews of Modern Physics **87**, 1213 (2015).

[10] L. J. Cornelissen, J. Liu, R. A. Duine, J. B. Youssef, and B. J. Van Wees, *Long-distance transport of magnon spin information in a magnetic insulator at room temperature,* Nature Physics **11**, 1022 (2015).

[11] I. Bertelli, J. J. Carmiggelt, T. Yu, B. G. Simon, C. C. Pothoven, G. E. Bauer, Y. M. Blanter, J. Aarts, and T. van der Sar, *Magnetic resonance imaging of spin-wave transport and interference in a magnetic insulator,* Science advances **6**, eabd3556 (2020).

[12] A. Gruber, A. Dräbenstedt, C. Tietz, L. Fleury, J. Wrachtrup, and C. Von Borczyskowski, *Scanning confocal optical microscopy and magnetic resonance on single defect centers,* Science **276**, 2012 (1997).

[13] L. Rondin, J. P. Tetienne, T. Hingant, J. F. Roch, P. Maletinsky, and V. Jacques, *Magnetometry with nitrogen-vacancy defects in diamond,* Reports on Progress in Physics **77**, 056503 (2014).

[14] T. Rosskopf, A. Dussaux, K. Ohashi, M. Loretz, R. Schirhagl, H. Watanabe, S. Shikata, K. M. Itoh, and C. L. Degen, *Investigation of surface magnetic noise by shallow spins in diamond,* Physical Review Letters **112**, 147602 (2014).

[15] F. Casola, T. van der Sar, and A. Yacoby, *Probing condensed matter physics with magnetometry based on nitrogen-vacancy centres in diamond,* Nature Reviews Materials **3**, 17088 (2018).

[16] M. Mohseni, R. Verba, T. Brächer, Q. Wang, D. A. Bozhko, B. Hillebrands, and P. Pirro, *Backscattering Immunity of Dipole-Exchange Magnetostatic Surface Spin Waves,* Physical Review Letters **122**, 197201 (2019).

[17] T. Yu, Y. M. Blanter, and G. E. W. Bauer, *Chiral Pumping of Spin Waves,* Physical Review Letters **123**, 247202 (2019).

[18] P. Andrich, C. F. de las Casas, X. Liu, H. L. Bretscher, J. R. Berman, F. J. Heremans, P. F. Nealey, and D. D. Awschalom, *Long-range spin wave mediated control of defect qubits in nanodiamonds,* npj Quantum Information **3**, 28 (2017).

[19] P. Pincus, *Excitation of spin waves in ferromagnets: eddy current and boundary condition effects,* Physical Review **118**, 658 (1960).

[20] M. Kostylev, *Strong asymmetry of microwave absorption by bilayer conducting ferromagnetic films in the microstrip-line based broadband ferromagnetic resonance,* Journal of Applied Physics **106**, 043903 (2009).

[21] M. A. Schoen, J. M. Shaw, H. T. Nembach, M. Weiler, and T. J. Silva, *Radiative damping in waveguide-based ferromagnetic resonance measured via analysis of perpendicular standing spin waves in sputtered permalloy films,* Physical Review B **92**, 184417 (2015).

[22] Y. Li and W. E. Bailey, *Wave-Number-Dependent Gilbert Damping in Metallic Ferromagnets,* Physical Review Letters **116**, 117602 (2016).

[23] M. Kostylev, *Coupling of microwave magnetic dynamics in thin ferromagnetic films to stripline transducers in the geometry of the broadband stripline ferromagnetic resonance,* Journal of Applied Physics **119**, 013901 (2016).

[24] J. W. Rao, S. Kaur, X. L. Fan, D. S. Xue, B. M. Yao, Y. S. Gui, and C. M. Hu, *Characterization of the non-resonant radiation damping in coupled cavity photon magnon system,* Applied Physics Letters **110**, 262404 (2017).

[25] S. A. Bunyaev, R. O. Serha, H. Y. Musiienko-Shmarova, A. J. Kreil, P. Frey, D. A. Bozhko, V. I. Vasyuchka, R. V. Verba, M. Kostylev, B. Hillebrands, G. N. Kakazei, and A. A. Serga, *Spin-wave relaxation by Eddy Currents in Y3Fe5O12/Pt bilayers and a way to suppress it,* Physical Review Applied **14**, 024094 (2020).

[26] J. D. Cutnell and K. W. Johnson, *Physics*, 4th ed. (Wiley, Hoboken, 1997).

[27] C. Mathieu, V. T. Synogatch, and C. E. Patton, *Brillouin light scattering analysis of three-magnon splitting processes in yttrium iron garnet films,* Physical Review B **67**, 104402 (2003).

[28] H. Schultheiss, X. Janssens, M. Van Kampen, F. Ciubotaru, S. J. Hermsdoerfer, B. Obry, A. Laraoui, A. A. Serga, L. Lagae, A. N. Slavin, B. Leven, and B. Hillebrands, *Direct current control of three magnon scattering processes in spin-valve nanocontacts,* Physical Review Letters **103**, 157202 (2009).

[29] T. Schneider, A. A. Serga, A. V. Chumak, C. W. Sandweg, S. Trudel, S. Wolff, M. P. Kostylev, V. S. Tiberkevich, A. N. Slavin, and B. Hillebrands, *Nondiffractive subwavelength wave beams in a medium with externally controlled anisotropy,* Physical Review Letters **104**, 197203 (2010).

[30] T. Wimmer, M. Althammer, L. Liensberger, N. Vlietstra, S. Geprägs, M. Weiler, R. Gross, and H. Huebl, *Spin Transport in a Magnetic Insulator with Zero Effective Damping,* Physical Review Letters **123**, 257201 (2019).

[31] M. Schneider, T. Brächer, D. Breitbach, V. Lauer, P. Pirro, D. A. Bozhko, H. Y. Musiienko-Shmarova, B. Heinz, Q. Wang, T. Meyer, F. Heussner, S. Keller, E. T. Papaioannou, B. Lägel, T. Löber, C. Dubs, A. N. Slavin, V. S. Tiberkevich, A. A. Serga, B. Hillebrands, and A. V. Chumak, *Bose–Einstein condensation of quasiparticles by rapid cooling,* Nature Nanotechnology **15**, 457 (2020).

[32] T. L. Gilbert, *A phenomenological theory of damping in ferromagnetic materials,* IEEE Transactions on Magnetics **40**, 3443 (2004).

[33] K. Y. Guslienko and A. N. Slavin, *Magnetostatic Greens functions for the description of spin waves in finite rectangular magnetic dots and stripes,* Journal of Magnetism and Magnetic Materials **323**, 2418 (2011).

[34] A. Brataas, Y. Tserkovnyak, and G. E. Bauer, *Magnetization dissipation in ferromagnets from scattering theory,* Physical Review B **84**, 054416 (2011).

6

SENSING CHIRAL MAGNETIC NOISE VIA QUANTUM IMPURITY RELAXOMETRY

Via the fluctuation-dissipation theorem, the magnetic fluctuations of a system are related to its susceptibility, which provides information about the system's excitations. Thermally-excited spin waves are a source of such fluctuating magnetic fields, which can be locally probed by the electron spin of single NV centers in diamond. Focusing on a nickel thin film, we study the magnetic-noise spectrum of thermally-excited spin waves via relaxometry measurements. We further analyze the distance- and field-dependence of the magnetic fluctuations, finding a good agreement with a theoretical model based on the chiral coupling between the spin-wave stray fields and the NV transitions. We detect discrepancies at the ferromagnetic resonance frequency of nickel, which we address by performing additional measurements of coherent spin waves, suggesting the presence of spatial field inhomogeneities.

Parts of this chapter have been published in *Physical Review B* **102**, 220403 (2020) by A. Rustagi, **I. Bertelli**, T. van der Sar, P. Upadhyaya. Helena La provided the code for the magnetic noise calculations.

6.1. INTRODUCTION

Magnetic noise can be the result of charge[1, 2] and spin[3, 4] fluctuations. Via the fluctuation-dissipation theorem, such noise can be related to the intrinsic properties and excitations of a system[5], which are reflected in the conductivity and susceptibility tensors. Because of their non-invasive and point-like nature, single NV electron spins in diamond are well suited to probe such fluctuations locally and quantitatively via NV relaxometry. Therefore, single-NV relaxometry has been proposed as a tool to probe the normal metal-superconductor transition[6, 7], the antiferromagnet(AFM)-ferromagnet metamagnetic phase transition[8], the AFM chemical potential[9], AFM domain walls[10], the electron-phonon instability in graphene [11], the emergence of exotic quantum spin-liquid phases with topological character[4], magnetic monopoles in spin ice[12], one-dimensional edge states [13] and magnon sound modes in magnets in the hydrodynamic regime[14].

In a magnet, quantifying the magnetic field noise can grant access to the spin chemical potential[15], which indicates the tendency of spins to diffuse, or to the power spectral density of the magnetic field, which reflects the system's excitations[16, 17, 22]. It has been predicted that quantifying the distance dependence of magnetic noise in the spin-wave gap of a magnet is an effective tool in detecting a transition between the diffusive and ballistic-like transport of spin waves[3, 23]. The crossover between the different transport regimes should take place at a distance similar to the spin diffusion length[3].

Here, we investigate thermal spin waves by characterizing the relaxation rate of single NV centers at a distance of $\sim 0-300$ nm from a nickel thin film. We analyze these results according to the theoretical model describing the chiral coupling of the spin-wave fields with the NV transitions, developed in Chapter 3. We find a remarkable agreement between the measured distance- and field-dependence of the NV relaxation rates with the theoretical model. In particular, the model accurately predicts the amplitude of the magnetic-field noise without free parameters. We also detect the unexpected presence of a large noise at frequencies below the ferromagnetic resonance (FMR) of nickel, where the noise should be suppressed. We perform additional measurements of NV Rabi oscillations to probe coherent spin waves. Close to the FMR, we observe that the Rabi frequencies of NV centers in nickel-covered areas are strongly modified by the spin-wave modes in the magnetic film. This indicates that driving the system with a microwave field excites spin waves whose stray fields add to the direct drive field. The local variations between NV centers suggest the presence of inhomogeneities of the magnetic surface and granularity of the spacer layer, possibly causing large local stray fields variations.

6.2. RESULTS

SYSTEM GEOMETRY

To have access to isolated NV defects at different distances from a magnetic film, we fabricate a SiO_2 spacer layer of increasing thickness on a diamond with shallow single-NV centers, on top of which we grow a 40 nm-thick layer of nickel (Fig. 6.1a). Individual NV

spins are addressed from below, using a confocal microscope (Section 2.1.3), both in the bare diamond and under the nickel layer (Fig. 6.1b). All the NV defects investigated in this chapter possess the same crystallographic orientation.

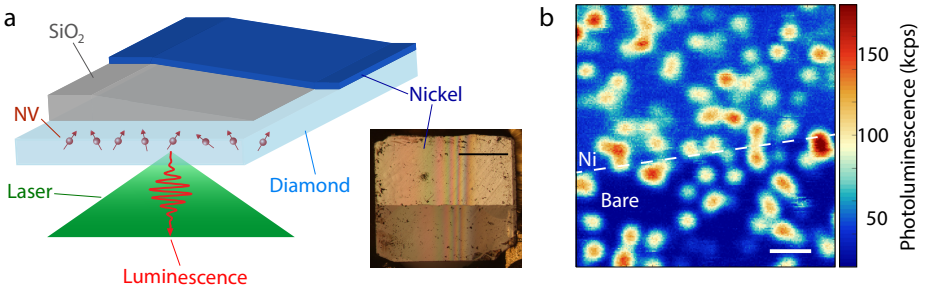

Figure 6.1: System geometry. (**a**) A SiO_2 spacer layer of varying thickness (0-1 μm) is grown on top of a diamond containing NV centers that can be individually addressed using a confocal microscope. A 40 nm-thick nickel layer is evaporated onto half of the diamond-spacer substrate. Inset: optical micrograph of the sample. The top half of the diamond is coated with nickel. The spacer layer thickness changes horizontally, as can be deduced from the optical interference fringes resulting from the commensurability of the light wavelength and the spacer thickness. Scale bar: 500 μm. (**b**) Photoluminescence image of the sample, showing (mostly) single NV centers as bright spots of ~120 thousands counts per second. Much brighter areas indicate the presence of more than one NV per diffraction-limited spot. The background signal is higher where the diamond is coated with the nickel film (top half). Scale bar: 1 μm.

CHARACTERIZING THE EXCITATIONS OF THE SYSTEM

We start characterizing the system by performing electron spin resonance (ESR) measurements (Section 2.2.2), at increasing values of the static field oriented along the NV center axis, at a location where the SiO_2 is absent (Fig. 6.2a). When the ω_- frequency is close to the FMR (bottom of the spin-wave band), the $|0\rangle \leftrightarrow |-1\rangle$ transition shows an increased contrast and width compared to $|0\rangle \leftrightarrow |+1\rangle$. This indicates an efficient driving of the NV spins by the stray fields of spin waves with frequencies close to the FMR. An increased contrast is consistent with the larger driving field (Section 2.2.2.2), and an increased width is consistent with a lifetime reduction caused by magnetic noise (Section 3.5). Surprisingly, at the exact field-and-frequency where the calculated FMR of the nickel film crosses the ω_- ESR transition, we notice a clear and abrupt reduction of the contrast and width of the ESR dip (Fig. 6.2b). At this moment, we do not know the cause of such changes.

DETECTING MAGNETIC NOISE BY NV RELAXOMETRY

The magnetic-noise spectrum of a system provides information regarding its excitations. We probe the magnetic fluctuations of thermal spin waves via NV relaxometry, which en-

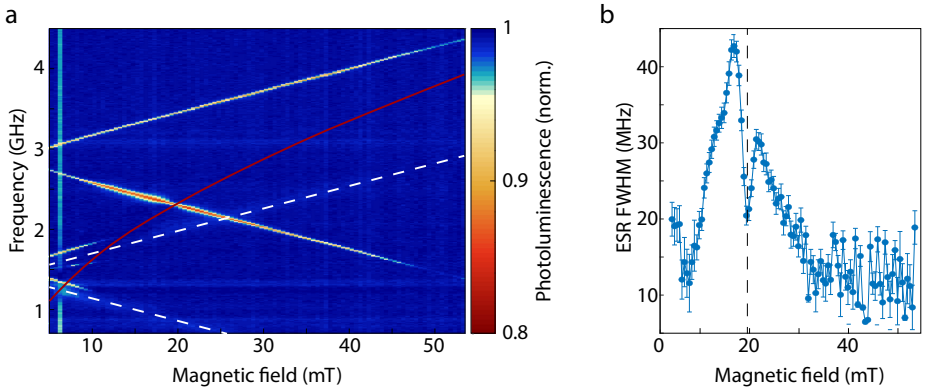

Figure 6.2: Electron spin resonance. (**a**) When an external microwave field is resonant with the NV ESR transitions, the NV spin is pumped into the dark $|\pm 1\rangle$ states, such that its luminescence is decreased. In the region close to where the ω_- transition crosses the calculated FMR of nickel (solid red line), the NV transition is additionally driven by the field of resonant spin waves. The dashed white lines indicate the frequency of ESR transitions in the NV excited states. (**b**) The full-width half-maximum (FWHM) of the ω_- transition is greatly enhanced close to the FMR of nickel, at a nickel-NV distance of 40±10 nm. Exactly at resonance (black dashed line), however, a sharp decrease is present.

6

tails preparing the NV spin in an eigenstate ($|0\rangle$, $|\pm 1\rangle$) and monitoring its time-relaxation caused by magnetic noise (Section 2.2.5). The spectrum of the magnetic noise can be probed by tuning the ESR transitions via the static field.

Close to the nickel film, the NV lifetime is reduced to few microseconds as a result of large transverse magnetic fluctuations at the NV ESR transitions (Fig. 6.3a-c). In the region of the diamond without nickel, the spin lifetime of NV centers is a few milliseconds (Fig. 6.3d), as expected[18–21] .

The spin-wave induced relaxation rates depends on several parameters, such as the NV-magnet distance, the spin-wavelength, the angle between the NV axis and the magnetization, the spin-wave propagation direction with respect to the magnetization, and the NV transition (Section 3.4, 3.5.2). As the distance is increased, the spin-wave stray field decays exponentially with distance, with a characteristic decay length similar to the spin-wavelength (Eq. 3.71-3.73). The spin-wave angle with respect with the magnetization, and the angle between the NV axis and the magnetization, influence the handedness and ellipticity of the spin-wave stray field at the NV location (Section 3.4). Finally, each NV transition is driven by a circularly polarized magnetic field, in the plane perpendicular to the NV axis, of opposite handedness (Section 2.2.4). Based on these considerations, we can draw some qualitative conclusions which are reflected in the measurements of Figure 6.3:

- The $|0\rangle \leftrightarrow |+1\rangle$ transition is not efficiently driven by spin-wave fields (Section 3.4-

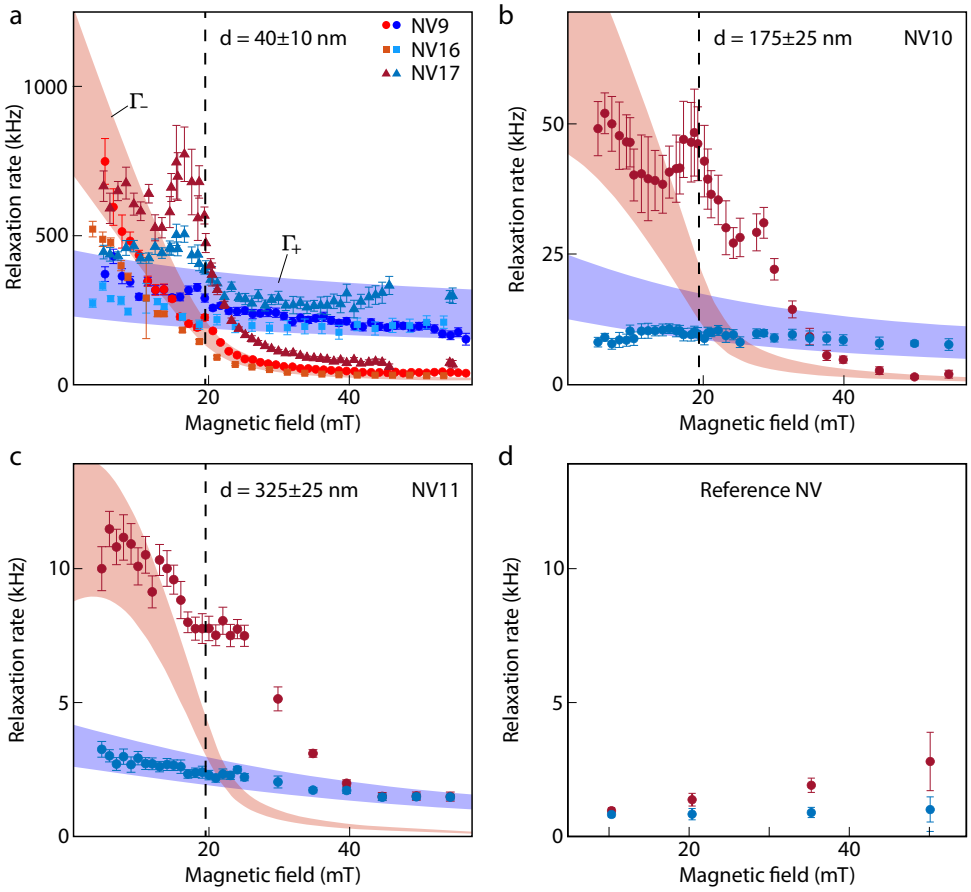

Figure 6.3: Probing the spin-wave spectrum via relaxometry. (**a**)-(**c**) Relaxation rate of NV centers at 40 ± 10, 175 ± 25 and 325 ± 25 nm from a nickel film, respectively. Red (blue) circles: Γ_- (Γ_+). The shaded red (blue) band is a calculations of Γ_- (Γ_+) based on the model of Chapter 3, taking into consideration the uncertainty on the NV-nickel distance. (**d**) The lifetime of shallow NV centers in bare diamond is typically between 0.5 and 5 ms (the latter being the coherence time in non-isotopically-purified bulk diamond at room temperature[18]). Red (blue) circles: Γ_- (Γ_+).

3.5.2). Additionally, its frequency runs almost parallel to the FMR (in Fig. 6.2a), such that spin waves of similar wavelength are probed at each field. Therefore, the relaxation rates Γ_+ is small, and almost constant with field.

- Conversely, the $|0\rangle \leftrightarrow |-1\rangle$ transition is efficiently driven by the spin-wave field. Above the FMR, this transition probes spin waves of different wavelength (longer wavelength towards the FMR), depending on the static field. At ~ 20 mT, ω_- crosses the FMR, such that at larger fields ω_- is not resonant with any spin-wave mode. Thus, Γ_- is large at small fields, and becomes much smaller than Γ_+ at large fields.

All these considerations are captured in the model introduced in Section 3.5.2, which is used to calculate the expected rates showed in figure 6.3 as shaded bands (which reflect the uncertainty on the NV-nickel distance). We find a generally good match between the model and the measurement. However, at the field where ω_- crosses the FMR of nickel (~ 20 mT), we observe discrepancies of unclear origin. Specifically, we detect relaxation rates for ω_- that, close to the FMR, exceeds the predicted ones by a factor 2-4, and that are dependent on which specific NV center is addressed.

It has been predicted that, below the FMR (i.e. in the spin-wave gap), two-magnon scattering events become important[3], while they are not captured by our theoretical model. Thus, this is a possible source of noise for fields larger than ~ 20 mT (i.e. below the FMR), but it does not justify the NV-specific variations. These variations could be partly explained by spatial inhomogeneities of the field, which we probe with additional measurements of NV Rabi frequencies (Section 6.5). An explanation of the possible mechanism responsible for the location-dependent variation of relaxation rates and Rabi frequency is in Section 6.5, corroborated by measurements of the film morphology (Section 6.4).

6.3. DISCUSSION

Using single NV sensor spins, we have probed the fluctuating magnetic fields generated by thermal spin waves in a nickel thin film. Our results are well-explained by the theory of chiral coupling between spin-wave fields and NV spins presented in Chapter 3. We find unexpected NV-specific variations of the Γ_- relaxation rate close to the FMR of nickel, which we investigate further by measuring NV Rabi frequencies, and that can be partially explained by local variations of the static field.

6.4. METHODS

The SiO_2 layer is grown by plasma-enhanced chemical vapor deposition (PECVD) at room temperature. The ramp is fabricated by shadowing half of the diamond with a rigid mask (a glass coverslide), suspended 1 µm above the diamond, similar to [1], during the SiO_2 growth. The ramp profile is measured with a profilometer (Fig. 6.4a). The resulting structure of the SiO_2 is granular, with grain size increasing with the layer thick-

ness (Fig. 6.4b-c). This is most likely due to the low temperature of the process, which was chosen in order to decrease the luminescence of the SiO_2 layer as much as possible, because films grown at high-temperature showed high luminescence that hampered the detection of single NV centers by drastically reducing the signal-to-noise ratio.

The nickel layer is evaporated on top of the diamond-SiO_2 substrate, masking half of the sample with tape to retain a nickel-free area of the diamond surface to use as location for reference measurements of NV relaxation rates.

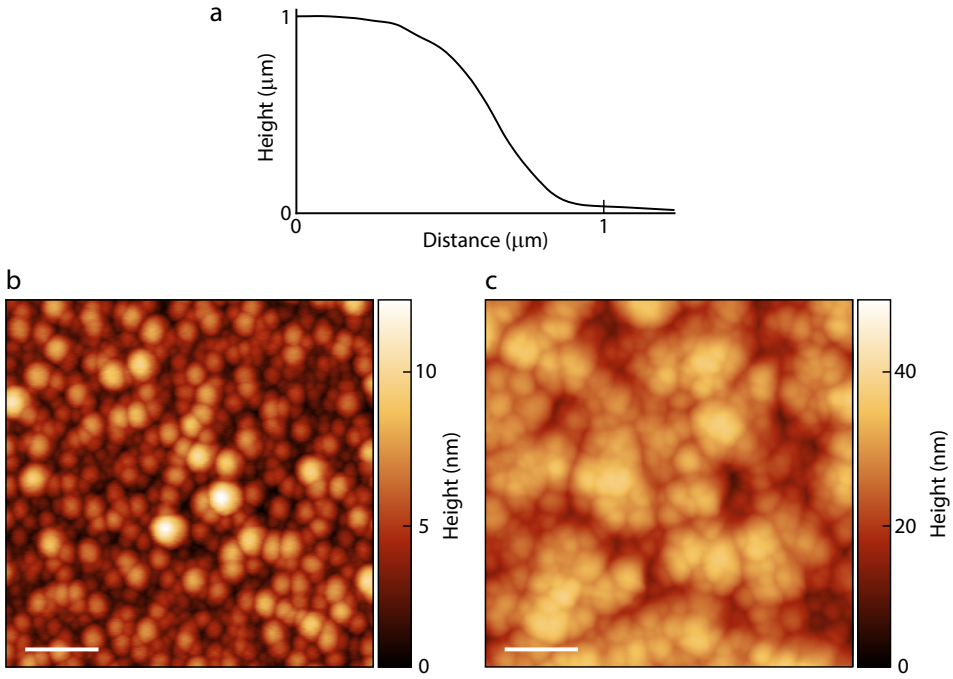

Figure 6.4: Ramp profile and structure. (**a**) Profilometry measurement of the SiO_2 spacer layer. (**b**)-(**c**) Atomic force microscope (AFM) measurement of the nickel film on a SiO_2 layer of thickness 50 nm and 1 μm, respectively. Scale bar, 100 nm.

6.5. ADDITIONAL MEASUREMENTS

PROBING COHERENT SPIN WAVES VIA RABI-FREQUENCY ENHANCEMENT

Because we find relevant discrepancies between the theoretically calculated and the experimentally measures relaxation rates, that seem to vary randomly with the specific NV center investigated, we perform additional measurements to uncover the reason of such local changes.

To probe the spin-wave driving of the NV spin, we perform Rabi oscillation measure-

ments (Section 2.2.4), which provide information regarding coherent spin waves. We first characterize the transmission through the microwave antenna used to excite spin waves by monitoring the Rabi frequency of an NV center in the bare diamond (Fig. 6.5a), which we use to normalize the measurements that follow, thereby making sure that the changes detected are caused by the magnetic film. While NV centers very close (30-50 nm) to the nickel present a large (~ 5-fold) change of the Rabi frequency (Fig. 6.5b), NVs that are hundreds of nanometers away show smaller (i.e. close to 20%) changes (Fig. 6.5c-d).

These results qualitatively remind of the Fano lineshape previously observed for NV centers interacting with a magnetic disk[16]. In the cited work, the variations were consistent with the NV location relative to the magnetic disk: the interference of the direct driving field and of that of the magnetic disk is position-dependent. In the present experiments we study a (supposedly) homogeneous film, which should induce no such variations. Thus, we deduce that the nickel film is, in fact, quite strongly not homogeneous, which is corroborated by the atomic force microscope measurements of Section 6.4. Assuming a granularity of the film allows to expect the presence of magnetic domains of diverse size and orientation, such that a situation similar to that of Ref. [16] is realized: the microwave driving field has a projection on the plane perpendicular to the magnetization that is position-dependent, and therefore a different driving efficiency (Section 3.2.1) in each domain, such that the amplitude of the spin-wave precession changes locally. Thus, the spin-wave field interferes with the direct field differently for each NV center, which can cause changes both in the amplitude and sign of the Fano lineshape[16].

It is reasonable to think that in our system there is an additional effect that stems from the domain structure[1]: the projection of the *static* magnetic field along the equilibrium magnetization of each domain is different. Thus, each magnetic domain possesses a distinct FMR frequency (according to Eq.3.42). This accounts for the frequency-shift of the center of the Fano-like resonances in Fig. 6.5.

INVESTIGATING THE LOCAL STRAY FIELD VARIATIONS

To corroborate the interpretation that the different response of each NV centers to spin-wave fields is caused by local inhomogeneities, we quantify the spatial variations of the stray magnetic field of the nickel film. To do so, we detect the local static field at the location of several neighbouring NV centers with the same orientation (Fig. 6.6), such that the field they experience should be equal[2]. In the space of just few micrometers, we find variations larger than 3 mT at an applied field of 20.5 mT. This confirms our assumptions regarding the possible presence of magnetic domains and inhomogeneities.

[1] If we assume that the structure of the nickel film is polycristalline, the non-negligible crystalline anisotropy of nickel results in each domain having the equilibrium magnetization oriented along different directions.

[2] A small field gradient is present, due to the finite size of the bar magnet used to apply the static field. Over an area of ~ 6 μm, such variations are in the tens of μT range.

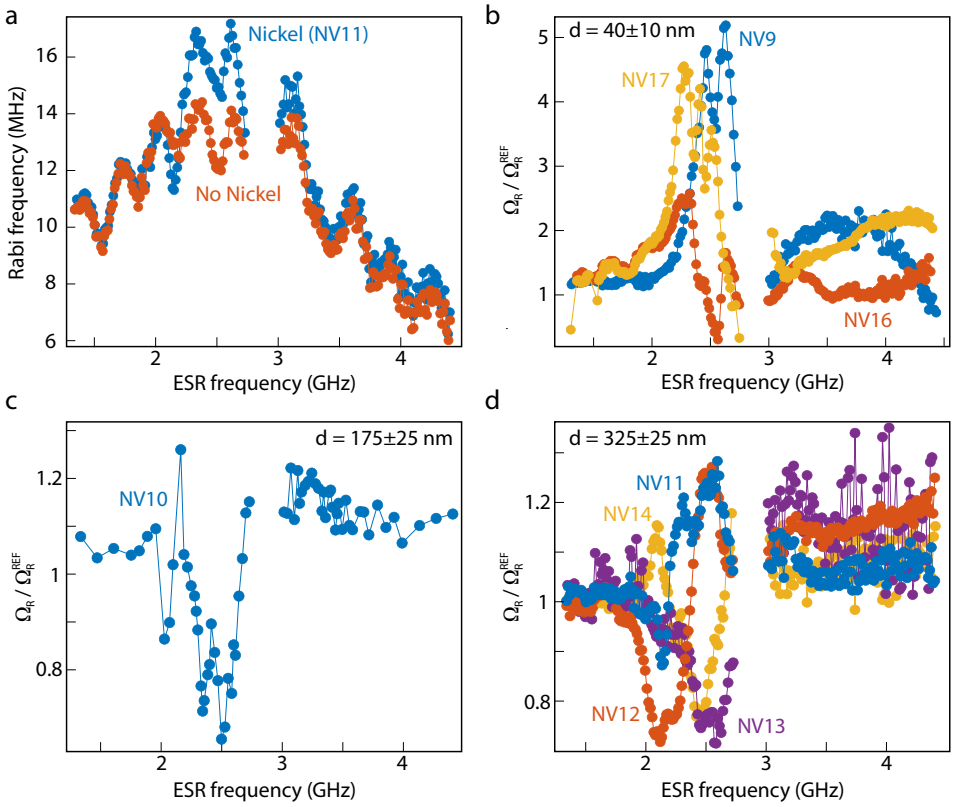

Figure 6.5: Detection of coherent spin-wave fields. (**a**) We calibrate the frequency-dependent delivery of microwaves through the electronics by characterizing the Rabi frequency of an NV center located in the bare diamond. An NV under the nickel shows a similar microwave transmission spectrum, on top of which are visible changes due to the magnetic film. Close to 2.87 GHz (the zero-field splitting of the NV center), the two ESR lines overlap, hindering a clean measurement of Rabi oscillations. (**b**) NV centers at 40 ± 10 nm from the nickel film show large changes of the Rabi frequency, between a ~5-fold enhancement and a reduction to almost zero. (**c**)-(**d**) At larger NV-Ni distances (175±25 and 325±25 nm, respectively), the spin-wave-induced changes are smaller. The variations of such changes, peculiar to each NV center, are discussed in the text.

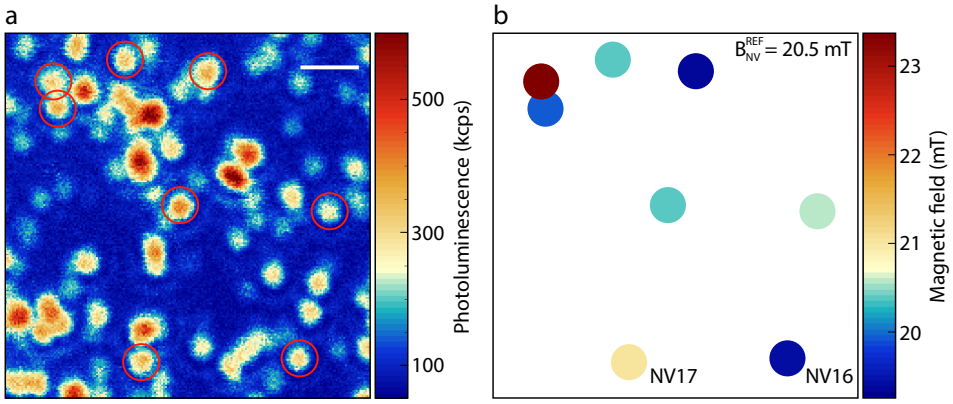

Figure 6.6: Local variations of the static stray field. (**a**) Photoluminescence image showing several NV centers close to each other. The circled NV centers have the same orientation of the NV axis, such that the stray field they experience should be the same. Scale bar: 1 µm . (**b**) For an applied static field of ~ 20.5 mT, the local field shows variations as large as 3 mT for NVs that are closer than 1 µm (top left corner).

6

REFERENCES

[1] S. Kolkowitz, A. Safira, A. A. High, R. C. Devlin, S. Choi, Q. P. Unterreithmeier, D. Patterson, A. S. Zibrov, V. E. Manucharyan, H. Park, and M. D. Lukin, *Probing Johnson noise and ballistic transport in normal metals with a single-spin qubit*, Science **347**, 1129 (2015).

[2] K. Agarwal, R. Schmidt, B. I. Halperin, V. Oganesyan, G. Zaránd, M. D. Lukin, and E. Demler, *Magnetic noise spectroscopy as a probe of local electronic correlations in two-dimensional systems*, Physical Review B **95**, 155107 (2017).

[3] B. Flebus and Y. Tserkovnyak, *Quantum-Impurity Relaxometry of Magnetization Dynamics*, Physical Review Letters **121**, 187204 (2018).

[4] S. Chatterjee, J. F. Rodriguez-Nieva, and E. Demler, *Diagnosing phases of magnetic insulators via noise magnetometry with spin qubits*, Physical Review B **99**, 104425 (2019).

[5] J. Cardellino, N. Scozzaro, M. Herman, A. J. Berger, C. Zhang, K. C. Fong, C. Jayaprakash, D. V. Pelekhov, and P. C. Hammel, *The effect of spin transport on spin lifetime in nanoscale systems*, Nature Nanotechnology **9**, 343 (2014).

[6] P. E. Dolgirev, S. Chatterjee, I. Esterlis, A. A. Zibrov, M. D. Lukin, N. Y. Yao, and E. Demler, *Characterizing two-dimensional superconductivity via nanoscale noise magnetometry with single-spin qubits*, (2021), arXiv:2106.05283v1 .

[7] N. J. McLaughlin, H. Wang, M. Huang, E. Lee-Wong, L. Hu, H. Lu, G. Q. Yan, G. D.

Gu, C. Wu, Y.-Z. You, and C. R. Du, *Observation of Superconductivity Induced Ferromagnetism in an Fe-Chalcogenide Superconductor,* (2021), arXiv:2106.15882 .

[8] G. Nava Antonio, I. Bertelli, B. G. Simon, R. Medapalli, D. Afanasiev, and T. van der Sar, *Magnetic imaging and statistical analysis of the metamagnetic phase transition of FeRh with electron spins in diamond,* Journal of Applied Physics **129**, 223904 (2021).

[9] B. Flebus, *Chemical potential of an antiferromagnetic magnon gas,* Physical Review B **100**, 064410 (2019).

[10] B. Flebus, H. Ochoa, P. Upadhyaya, and Y. Tserkovnyak, *Proposal for dynamic imaging of antiferromagnetic domain wall via quantum-impurity relaxometry,* Physical Review B **98**, 180409 (2018).

[11] T. I. Andersen, B. L. Dwyer, J. D. Sanchez-Yamagishi, J. F. Rodriguez-Nieva, K. Agarwal, K. Watanabe, T. Taniguchi, E. A. Demler, P. Kim, H. Park, and M. D. Lukin, *Electron-phonon instability in graphene revealed by global and local noise probes,* Science **364**, 154 (2019).

[12] F. K. K. Kirschner, F. Flicker, A. Yacoby, N. Y. Yao, and S. J. Blundell, *Proposal for the detection of magnetic monopoles in spin ice via nanoscale magnetometry,* Physical Review B **97**, 140402 (2018).

[13] J. F. Rodriguez-Nieva, K. Agarwal, T. Giamarchi, B. I. Halperin, M. D. Lukin, and E. Demler, *Probing one-dimensional systems via noise magnetometry with single spin qubits,* Physical Review B **98**, 195433 (2018).

[14] J. F. Rodriguez-Nieva, D. Podolsky, and E. Demler, *Hydrodynamic sound modes and Galilean symmetry breaking in a magnon fluid,* (2020), arXiv:1810.12333 .

[15] C. Du, T. van der Sar, T. X. Zhou, P. Upadhyaya, F. Casola, H. Zhang, M. C. Onbasli, C. A. Ross, R. L. Walsworth, Y. Tserkovnyak, and A. Yacoby, *Control and local measurement of the spin chemical potential in a magnetic insulator,* Science **357**, 195 (2017).

[16] T. van der Sar, F. Casola, R. Walsworth, and A. Yacoby, *Nanometre-scale probing of spin waves using single-electron spins,* Nature Communications **6**, 7886 (2015).

[17] F. Casola, T. van der Sar, and A. Yacoby, *Probing condensed matter physics with magnetometry based on nitrogen-vacancy centres in diamond,* Nature Reviews Materials **3**, 17088 (2018).

[18] A. Jarmola, A. Berzins, J. Smits, K. Smits, J. Prikulis, F. Gahbauer, R. Ferber, D. Erts, M. Auzinsh, and D. Budker, *Longitudinal spin-relaxation in nitrogen-vacancy centers in electron irradiated diamond,* Applied Physics Letters **107**, 242403 (2015).

[19] T. De Guillebon, B. Vindolet, J.-F. Roch, V. Jacques, and L. Rondin, *Temperature dependence of the longitudinal spin relaxation time T_1 of single nitrogen-vacancy centers in nanodiamonds,* Physical Review B **102**, 165427 (2020).

[20] M. Rollo, A. Finco, R. Tanos, F. Fabre, T. Devolder, I. Robert-Philip, and V. Jacques, *Quantitative study of the response of a single NV defect in diamond to magnetic noise,* Physical Review B **103**, 235418 (2021).

[21] A. Finco, A. Haykal, R. Tanos, F. Fabre, S. Chouaieb, W. Akhtar, I. Robert-Philip, W. Legrand, F. Ajejas, K. Bouzehouane, N. Reyren, T. Devolder, J.-P. Adam, J.-V. Kim, V. Cros, and V. Jacques, *Imaging non-collinear antiferromagnetic textures via single spin relaxometry,* Nature Communications 2021 12:1 **12**, 767 (2021).

[22] C. M. Purser, V. P. Bhallamudi, F. Guo, M. R. Page, Q. Guo, G. D. Fuchs, and P. C. Hammel, *Spinwave detection by nitrogen-vacancy centers in diamond as a function of probe-sample separation,* Applied Physics Letters **116**, 202401 (2020).

[23] B. A. McCullian, A. M. Thabt, B. A. Gray, A. L. Melendez, M. S. Wolf, V. L. Safonov, D. V. Pelekhov, V. P. Bhallamudi, M. R. Page, and P. C. Hammel, *Broadband multi-magnon relaxometry using a quantum spin sensor for high frequency ferromagnetic dynamics sensing,* Nature Communications **11**, 5229 (2020).

7

MAGNETIC IMAGING AND STATISTICAL ANALYSIS OF THE METAMAGNETIC PHASE TRANSITION OF FERH

Magnetic imaging based on nitrogen-vacancy (NV) centers in diamond has emerged as a powerful tool for probing magnetic phenomena in fields ranging from biology to physics. A key strength of NV sensing is its local-probe nature, enabling high-resolution spatial images of magnetic stray fields emanating from a sample. However, this local character can also form a drawback for analysing the global properties of a system, such as a phase transition temperature. Here, we address this challenge by using statistical analyses of magnetic-field maps to characterize the first-order temperature-driven metamagnetic phase transition from the antiferromagnetic to the ferromagnetic state in FeRh. After imaging the phase transition and identifying the regimes of nucleation, growth, and coalescence of ferromagnetic domains, we statistically characterize the spatial magnetic-field maps to extract the transition temperature and thermal hysteresis width. By analysing the spatial correlations of the maps in relation to the magnetocrystalline anisotropy and external magnetic field, we detect a reorientation of domain walls across the phase transition. The employed statistical approach can be extended to the study of other magnetic phenomena with NV magnetometry or other sensing techniques.

This chapter has been published in *Journal of Applied Physics* **129**, 223904 (2021) by G. Nava Antonio*, **I. Bertelli***, B. G. Simon, R. Medapalli, D. Afanasiev, T. van der Sar. * indicates equal contribution.

7.1. INTRODUCTION

Nitrogen-vacancy (NV) centers are point-like defects in the diamond lattice hosting an electron spin that can be used as a sensor of magnetic fields[1]. In the last decade, NV centers have been developed into powerful tools for probing magnetic phenomena in both condensed-matter and biological systems[2, 3]. Key strengths of the technique are its nanoscale spatial resolution[4], high magnetic field sensitivity[5], and its operability under cryogenic conditions to above room temperature[6]. However, its local-probe nature can also form a challenge for extracting quantities related to the macroscopic properties of a system such as its phase transition temperature and hysteresis width. In addition, while real-space images provide a powerful visualization of spatial textures such as domain structures, extracting the temperature- or field-driven evolution of important parameters such as domain sizes requires defining suitable figures of merit. On the other hand, global techniques for probing phase transitions are typically less sensitive to a sample's microscopic structure. Being able to combine the acquisition of local information with a simultaneous monitoring of macroscopic sample properties would provide insight into how microscopic mechanisms underlie the global sample behavior.

In this work, we image the magnetic stray fields generated by an FeRh thin film using an ensemble of NV centers in a diamond chip (Fig. 7.1a) and employ statistical methods[7] to characterize its temperature-driven metamagnetic phase transition (MMPT)[8]. By analyzing the spatial variations and correlations of measured stray fields as a function of temperature, we extract the transition temperature and hysteresis width of the phase transition. Furthermore, we identify a reorientation of ferromagnetic (FM) domain walls during the MMPT triggered by the application of a bias field along a magnetic hard axis. Our study of the MMPT in FeRh shows how combining real-space imaging with statistical figures of merit can enable a better understanding of how macroscopic properties arise from the local state of a system.

The alloy FeRh undergoes a first-order phase transition from an antiferromagnetic (AFM) to a FM state when increasing its temperature (Fig. 7.1b) above a transition temperature ($T_t \approx 370$ K) that depends on the strain[9], bias field[10], and stoichiometry of the sample[11]. This MMPT is accompanied by a volume expansion of $\sim 1\%$ and an abrupt decrease in the resistivity[12], as well as an interplay between AFM and FM domains that was recently shown to lead to an intricate domain structure[13]. As such, FeRh constitutes a platform that is well suited for investigating the interaction between magnetic, electronic, and structural degrees of freedom. The MMPT of FeRh is also of practical interest due to its potential for data storage technologies, such as AFM resistive memories[14], heat-assisted magnetic recording[15], and low-power spintronic devices[16].

7.2. RESULTS

NV IMAGING OF THE MMPT IN FERH

Our sensing platform is based on an NV-containing diamond chip positioned on top of a 20-nm-thick epitaxial FeRh film that is grown on MgO (Fig. 7.1a) by DC magnetron sputtering[17]. As shown by vibrating sample magnetometry, the transition temperature of the film is ~ 370 K with a hysteresis width of approximately 20 K under an in-plane bias field of 150 mT (Fig. 7.1b). The temperature-dependent changes of the FeRh magnetization cause variations of the stray magnetic field above the film, which, in turn, induce Zeeman shifts in the electron spin resonance (ESR) frequencies of the NV centers[1]. We polarize the NV spins by optical pumping and detect ESR transitions between their $|0\rangle$ and $|\pm1\rangle$ spin sublevels by applying a microwave (MW) field using a nearby bonding wire and monitoring the spin-dependent photoluminescence (Fig. 7.1c). A DC bias field $\mathbf{B_0}$ is applied along one of the four possible NV orientations (i.e., the $\langle 111\rangle$ directions of the diamond lattice) to select two ESR transitions among the eight possible ones and to magnetize the FeRh film. Specifically, the bias field is oriented at ~ 35° out of plane and has an in-plane component $\mathbf{B_0^{\parallel}}$ that we orient alternatively along a magnetic easy or hard axis of FeRh. The out-of-plane magnetization of FeRh induced by the field is negligible since the shape anisotropy of the film favors in-plane magnetization and the bias fields used in this work are much smaller than the saturation magnetization ($\mu_0 M_s \sim 1.5$ T[18]). This, together with the magnetocrystalline anisotropy of FeRh, results in four in-plane $\langle 100\rangle$ easy axes[19].

To determine the magnetic field , we measure the two ESR transition frequencies of the selected NV family (Fig. 7.1d), which yield the projection B_{NV} of the stray field onto the NV axis[1]. Performing this measurement at each pixel by sweeping the MW frequency while detecting the photoluminescence takes several hours for images of 100×100 pixels. Instead, we employ a feedback scheme[20] in which, at each pixel, the photoluminescence is only measured at two frequencies $\nu_{\pm}$ (Fig. 7.1d), thereby speeding up the data collection by about an order of magnitude.

Using this method, we map the stray field generated by the FeRh thin film across the MMPT, and in this way we image the evolution of its magnetic order, when $\mathbf{B_0^{\parallel}}$ is applied along a hard (Fig. 7.2a – g) or easy (see Supplementary Fig. 7.5)axis. Below the phase transition temperature (T_t), we observe a mostly vanishing B_{NV}, since AFM and nanometric FM domains generate negligible magnetic fields at the NV location. This is because the stray field of these features decays exponentially with the NV-FeRh distance[2], which is around 1 micrometer in our experiments. Thus, we cannot address the presence or absence of residual ferromagnetic domains of nanometric size at the FeRh/Pt interface reported in the literature[13, 19]. The appearance of regions of non-zero field at ~ 368 K indicates the nucleation of FM domains, which grow and coalesce as the temperature is increased further. The magnetization direction results from a competition between the Zeeman energy and the anisotropy energy, the former favoring the alignment of spins with the bias field and the latter with the in-plane easy axes.

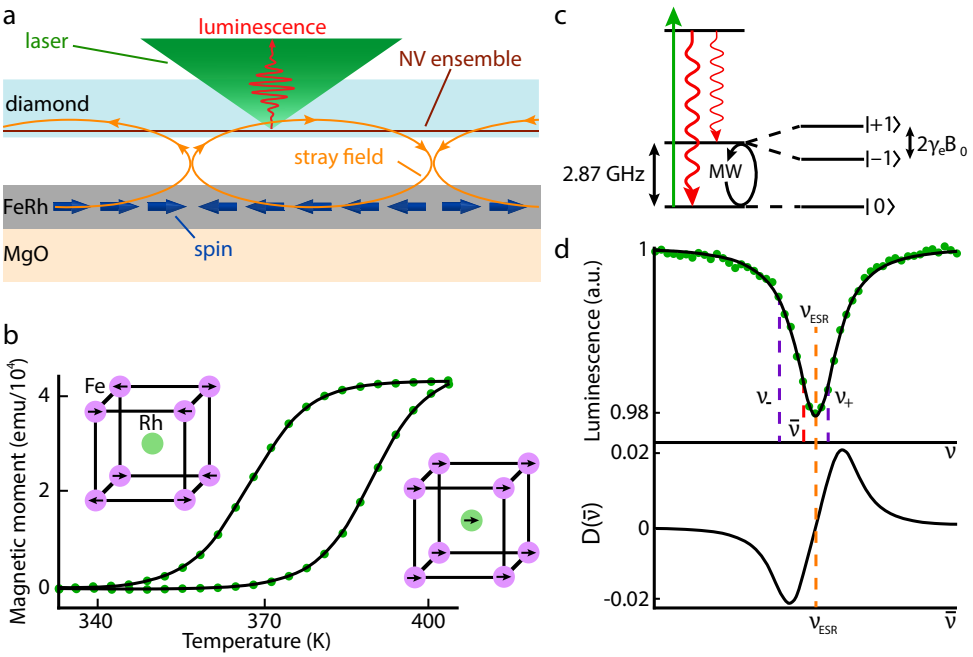

7

Figure 7.1: NV detection of the FeRh stray field. (**a**) Schematic of the experimental setup. The stray field of the FeRh film is detected by the NV sensing layer in a diamond chip. Scanning the laser allows to spatially map the FeRh stray field. (**b**) Temperature dependence of the magnetic moment of the 20-nm-thick FeRh film measured by vibrating sample magnetometry under an in-plane bias field of 150 mT, parallel to the [100] FeRh crystalline direction (easy axis). Below the transition temperature $T_t \approx 370$ K, the Fe spins are ordered in an AFM configuration and the Rh atoms carry no net magnetic moment (left inset). Above T_t, the Rh atoms gain a finite moment and align ferromagnetically parallel to the Fe spins (right inset)[8]. (**c**) Simplified energy level diagram of an NV center. The NV is optically excited with a green laser and its spin state monitored via spin-dependent photoluminescence. Microwaves drive ESR transitions between the $m_s = |0\rangle$ and $|\pm 1\rangle$ spin states. The magnetic field is extracted by measuring the Zeeman-split ESR frequencies. (**d**) Feedback measurement of NV ESR frequencies. Top: at the first pixel, we measure the full ESR spectrum, obtained by sweeping the MW frequency while recording the NV photoluminescence. The center frequency is used as an estimate for the next pixel. Bottom: error function employed to extract the ESR frequency with a feedback algorithm ($D = 0$ when $\bar{\nu} = \nu_{ESR}$). The error D is derived by modelling the ESR spectrum in the top panel as a Lorentzian and Taylor expanding $D(\bar{\nu}) = PL(\nu_+) - PL(\nu_-)$ about $\bar{\nu} = \nu_{ESR}$ to first order. In the feedback protocol, only two MW pulses are applied with frequencies $\nu_\pm$, symmetric around an estimate $\bar{\nu}$ of the ESR frequency ν_{ESR}. The photoluminescence difference at these frequencies, denoted $D(\bar{\nu})$, is proportional to the error $\bar{\nu} - \nu_{ESR}$, which we use as feedback signal to adjust the MW pulse frequencies while scanning.

Upon decreasing the temperature, we observe thermal hysteresis (i.e., by comparing Fig. 7.2a and 7.2g). This hysteretic behavior, together with the coexistence of different magnetic phases represented in Fig. 7.2a–b, are in line with the well-known first-order character of this phase transition[8].

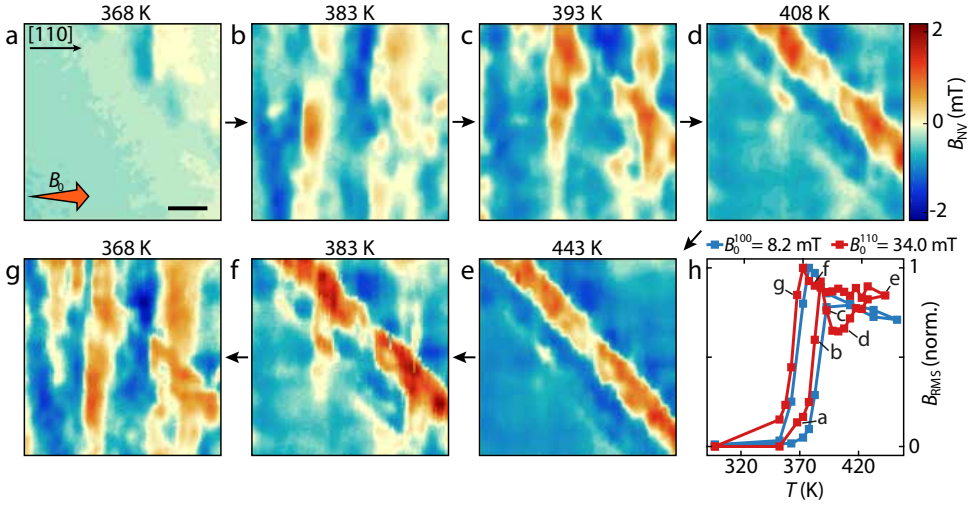

Figure 7.2: Imaging the meta-magnetic phase transition (MMPT) of FeRh with NV magnetometry. (**a**)-(**g**) Magnetic-field maps measured across the MMPT after subtraction of the bias field, in the heating (a - e) and cooling (e - g) branches of the experiment. The in-plane component of the bias field is parallel to the [110] FeRh direction. All maps in this work contain 100 × 100 pixels with a pixel size of 0.5 µm. Scale bar, 10 µm. B_0 = 34.0 mT. (**h**) Temperature evolution of the normalized RMS deviation of the measured stray-field maps. The blue (red) line corresponds to the in-plane component of the bias field being oriented along an easy (hard) axis and B_0 = 8.2 mT (B_0 = 34.0 mT).

QUANTITATIVE DETERMINATION OF T_t AND HYSTERESIS WIDTH

To quantitatively analyze the evolution of the stray field and the underlying changes in the magnetization of the FeRh film, we calculate the root-mean-square (RMS) deviation of the measured magnetic-field maps. This figure of merit, which gauges the spatial variations of the field, is computed as[7]

$$B_{RMS} = \sqrt{\frac{1}{n}\sum_{i=1}^{n}(B_{NV,i} - \langle B_{NV}\rangle)^2}, \tag{7.1}$$

where $B_{NV,i}$ is the field along the selected NV axis at pixel i, n is the total number of pixels, and $\langle B_{NV}\rangle$ is the average field over the region of interest. The temperature dependence of B_{RMS} (Fig. 7.2h) exhibits an abrupt increase at ~ 373 K, which gives a clear quantitative indication of the transition temperature, unlike the spatial magnetic-field

maps discussed previously.

Below T_t, B_{RMS} vanishes as there are no detectable FM domains within the AFM matrix[2]. As the FM domains start to appear, the homogeneity of the stray field is reduced, resulting in an increase of B_{RMS} between 368 K and 388 K. With $\mathbf{B_0^{\parallel}}$ parallel to an easy axis ([100]), the existing FM regions are expected to be magnetized along this direction and grow in size with increasing temperature, making the B_{NV} maps more uniform. The observed reduction of B_{RMS} with further increasing temperatures is expected as a consequence of the magnetization decrease due to thermally excited magnons.

For $\mathbf{B_0^{\parallel}} \parallel [110]$, the anisotropy and in-plane bias fields point along different directions. The magnetization direction of the FM domains results from a balance between these two contributions, which evolve in a non-trivial way as function of the sample temperature, leading to a non-monotonous T dependence of B_{RMS} above 388 K, which will be further investigated in the next sections. The quantitative character of the applied statistical tools enables detecting small differences between the $\mathbf{B_0^{\parallel}} \parallel [100]$ or [110] measurements. It also provides a figure of merit for quantifying the hysteresis of the MMPT: upon cooling the sample, the extracted RMS deviation of the magnetic-field maps shows a similar behavior as along the heating branch, but the curve is shifted ~ 20 K lower. This value agrees well with the hysteresis width extracted from the temperature-dependent vibrating-sample magnetometry measurements (Fig. 7.1b).

STATISTICAL ANALYSIS OF THE ANISOTROPY

Recent numerical studies have concluded that the magnetocrystalline anisotropy (MCA) of FeRh thin films depends on epitaxial strain[21, 22]. Indeed, samples fabricated under different experimental conditions have been found to exhibit different degrees of MCA[22–24]. We analyze the magnetocrystalline anisotropy of the sample using the two-dimensional autocorrelation function

$$R_{BB} = \sum_{x,y} B_{NV}(x+\delta x, y+\delta y) B_{NV}(x,y), \tag{7.2}$$

where we sum over each pixel, identified by its coordinates (x, y), and δx and δy are displacements in the $\hat{\mathbf{x}}$ and $\hat{\mathbf{y}}$ directions. This quantity gauges how similar the field at (x, y) is to that at $(x+\delta x, y+\delta y)$ and is therefore a useful tool for quantifying the characteristic length scales of a magnetic-field map.

For a relatively low bias field (~ 10 mT) and a temperature ~ 20 K above T_t (Fig. 7.3a-b), the measuredB_{NV} maps display patterns with diagonal or vertical stripe-like features, when $\mathbf{B_0^{\parallel}}$ is aligned with a magnetic easy or hard axis of the material, respectively. These directional features are reflected in the corresponding autocorrelation maps (Fig. 7.3e-f). Note that the vertical and diagonal stripes in Fig. 7.3a-b (and equivalently Fig. 7.3e-f) reflect a similarly oriented domain structure since the edges of the maps in Fig. 7.3a and 7.3e are parallel to the ⟨100⟩ directions, while those of the maps in Fig. 7.3b and 7.3f are parallel to the ⟨110⟩ directions.

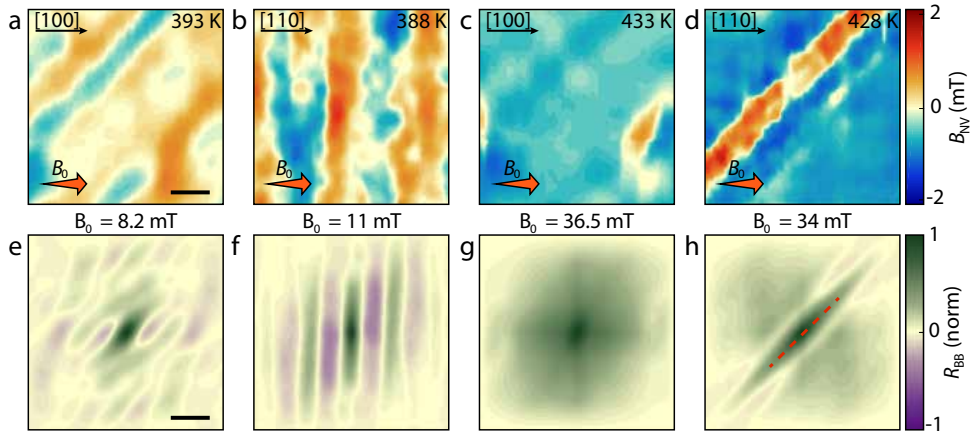

Figure 7.3: Statistical characterization of the magnetocrystalline anisotropy of FeRh. (**a**)-(**d**) Stray-field maps for small bias field and temperature moderately above T_t (a-b), and large bias field and temperature well above T_t (c-d). In (a), (c) the in-plane component of the bias field is parallel to an easy axis, while in (b), (d) it is parallel to a hard axis. Black arrows indicate crystalline directions of the FeRh lattice. Scale bar, 10 µm. (**e**)-(**h**) Normalized two-dimensional autocorrelation maps corresponding to the magnetic field distributions in (a) – (d), respectively. The scarlet dashed line in (h) indicates the FWHM of the central peak of the autocorrelation map, measured along [100]. Scale bar, 20 µm.

For temperatures well above (~ 40 K) T_t and relatively high magnetic field (~ 35 mT), the stray-field maps become nearly homogeneous when $\mathbf{B}_\mathbf{0}^{\parallel} \parallel [100]$ (easy axis), as FM domains start to occupy areas comparable to or larger than the imaged region (Fig. 7.3c). This translates into a broad central peak in the associated autocorrelation map (Fig. 7.3g), representing the large uniformity of the stray field. On the other hand, when $\mathbf{B}_\mathbf{0}^{\parallel} \parallel [110]$ (hard axis), the measured field distributions also become smoother, but with well-defined diagonal features (Fig. 7.3d), which are manifested in the autocorrelation maps as sharp central peaks elongated along a magnetic easy axis (Fig. 7.3h). This result agrees with the energy competition discussed in section 7.2 and highlights how the statistical approach strengthens the interpretation of real-space images.

MAGNETIC-FIELD DEPENDENCE OF THE MMPT

Next, we investigate the effect of the magnitude of the bias field on the magnetic configuration and show how the autocorrelation function enables a systematic study of the size and (re)orientation of FM domains. We find that while changing the magnitude of $\mathbf{B}_\mathbf{0}^{\parallel} \parallel [110]$ does not significantly affect the RMS deviation (Fig. 7.4a), it does alter the length scale of the spatial correlations (Fig. 7.4b). We evaluate this length scale by considering the full width at half maximum $\mathrm{FWHM}_{[100]}$ of the central peak of the autocorrelation maps taken along the [100] direction (dashed line in Fig. 7.3h). Since $\mathrm{FWHM}_{[100]}$ is a measure of the typical size of the features in the stray-field maps, it provides a figure

of merit that is well suited to study the evolution of the size of the magnetic domains. Below T_t, $\mathrm{FWHM}_{[100]}$ is large because of the presence of extensive AFM regions. At the onset of the phase transition, $\mathrm{FWHM}_{[100]}$ drops as small FM domains emerge and start producing highly granular stray-field configurations. This corresponds to the nucleation stage of the MMPT and is consistent with previous imaging studies of FeRh[19, 24, 25].

For higher temperatures, the growth and coalescence of FM domains cause an increment of $\mathrm{FWHM}_{[100]}$ that is larger for stronger bias fields. We interpret this as a result of the dominance of the Zeeman energy over the MCA energy in this temperature regime: as the bias field increases, FM domains with magnetization having a significant projection along the bias field start to expand to lower the Zeeman energy. These domains are predominantly elongated along [100] and, therefore, lead to higher $\mathrm{FWHM}_{[100]}$ values. This interpretation could be corroborated by determining the magnetization direction of the FM domains via e.g. scanning electron microscopy with polarization analysis[24] or X-ray photoemission electron microscopy[19]. We note that NV magnetometry does not allow an unambiguous reconstruction of the magnetization orientation from the measured stray field, as such reconstruction is an underconstrained inverse problem[2].

Interestingly, we detect a reorientation of the domain walls across the MMPT when the bias field is applied along a hard axis (Fig. 7.4c). This can be seen by analyzing the FWHM along different directions, which indicates the preferred direction of the spatial correlations in the stray-field maps. Specifically, by taking the ratio $\mathrm{FWHM}_{[110]}/\mathrm{FWHM}_{[100]}$, we observe domain walls that align with a hard axis from the start of the MMPT up to $T \sim 388$ K, as seen in Fig. 7.3b. Above this temperature, domain walls parallel to an easy axis start to become more recurrent. When the phase transition is completed, the orientation parallel to [100] is dominant in the case of relatively high B_0 (~ 35 mT), as illustrated in Fig. 7.3d.

The domain-wall realignment is concomitant with the sudden decrease of the RMS deviation (Fig. 7.2h). This decrease indicates a reorientation of the FM domains into a state that decreases the stray field. Thus, our results suggest that a reorientation of the FM domains is behind the domain-wall realignment. Such a rearrangement results from the changing balance between the anisotropy and Zeeman energies and could also be affected by the exchange coupling between FM and AFM regions that pins the FM domains in the first stages of the MMPT[13].

Our analysis demonstrates how the autocorrelation function and its width in different directions provide figures of merit that are well suited for tracking the evolution and orientation of magnetic domain walls as a function of control parameters (here, the bias field strength and its direction).

7.3. CONCLUSIONS

Our results show how imaging the local state of a system and simultaneously quantifying the corresponding global behavior using statistical tools yield complementary insight

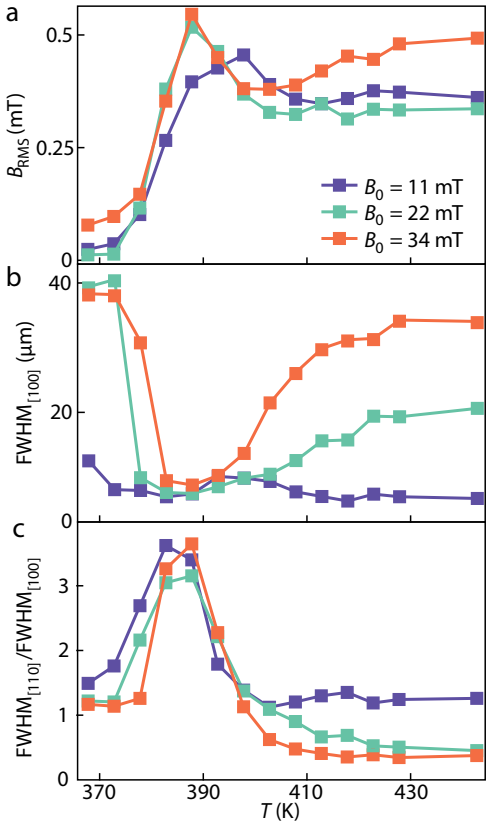

Figure 7.4: Magnetic-field dependence of the metamagnetic phase transition of FeRh. (**a**) RMS deviation of the measured stray field distributions as a function of temperature, for different values of the bias field along a hard axis. Each series of measurements is taken at a fixed bias field in the heating branch of the experiment. (**b**) Temperature dependence of the FWHM, measured along the [100] direction, of the central peak of the autocorrelation maps for the same values of the bias field as in (a). (**c**) Analysis of the rotation of domain walls in the magnetic texture of FeRh across the phase transition done by calculating the ratio of the FWHM of the central peak along [110] to the FWHM along [100], for the same bias field values of (a) and (b).

into the temperature- and bias-field dependence of phase transitions in a magnetic material. In particular, we extracted the transition temperature and hysteresis width of the MMPT in an FeRh thin film by means of a statistical analysis of spatial stray-field images. Furthermore, we characterized the spatial correlations of the measured stray-field maps and proposed a simple way of gauging the alignment and reorientation of ferromagnetic domain walls, based on quantifying the FWHM of the autocorrelation function.

The statistical methods employed here could be extended to characterize spatial correlations of stray fields generated by e.g. coherent[26] and incoherent spin-wave excitations[27, 28]. For maps of coherent spin waves, we anticipate that the spatial autocorrelation function could provide a useful figure of merit for assessing the predominant spin-wave directions and spatial periodicities. For incoherent spin waves, spatial maps of NV relaxation rates could provide insight into spatial variations of spin-wave densities. The methods could also be implemented in scanning-probe NV magnetometers to gain nanometric spatial resolution[29]. This would enable studying spatial correlations and phase separation and coexistence at the nanoscale, paving the way for the imaging and characterization of phase transitions in e.g. Kagome lattices[30], spin glasses[31] and monolayer magnets[32]. In such systems, the spatial autocorrelation function could, for instance, provide a figure of merit for assessing the spatial periodicity of the spin textures.

ACKNOWLEDGEMENTS

The authors thank Sheena K.K. Patel, Eric E. Fullerton, and Jan Aarts for their support, and Ray Descoteaux for technical assistance. T.v.d.S. acknowledges funding from the Dutch Research Council (NWO) as part of the Frontiers of Nanoscience (NanoFront) program through NWO Projectruimte grant 680.91.115. The work at CMRR, UCSD was funded by the DOE grant No. DE-SC0003678.

DATA AVAILABILITY STATEMENT

All data contained in the figures will be available upon publication at Zenodo.org with the identifier 10.5281/zenodo.4638723. Additional data related to this paper may be requested from the authors.

7.4. MATERIALS AND METHODS

7.4.1. SAMPLE FABRICATION

The diamond preparation procedure is described in [26]. We use CVD-grown, electronic-grade type IIa diamonds (Element 6), which are laser-cut and polished down to 2x2x0.05-mm chips (Almax easylabs). These chips were cleaned with nitric acid and the top $\sim$ 5 µm were removed using ICP reactive-ion etching (30 min Ar/Cl, 20 min O_2) to mitigate polishing damage. The chips were subsequently implanted with ^{15}N ions at 6 keV with a dose of 1×10^{13} ions/cm^2 (Innovion), tri-acid cleaned (mixture of nitric, sulphuric and perchloric acid 1:1:1), annealed at 800°C for 4 hours at 10^{-6} mbar, and tri-acid cleaned again to remove possibly graphitized layers on the surface, resulting in an estimated density of NV centers of $\sim 1 \times 10^{11}$ NV/cm^2 at a depth of $\sim 10-20$ nm.

The FeRh film is 20 nm thick, grown on an MgO substrate by DC magnetron sputtering at 450°C and under an Ar pressure of 2×10^{-3} mbar[17]. The sample was post-annealed at 800°C and capped with 4 nm of Pt. Due to the mismatch between the lattice constants of FeRh and MgO, the [100] direction of MgO is parallel to the [110] direction of FeRh.

To attach an NV-containing diamond to the FeRh sample, a small droplet of isopropanol was deposited onto the FeRh, on top of which a diamond chip was placed with the NV-surface facing down. The diamond chip was gently pressed down until the IPA had evaporated. The typical resulting NV-FeRh distance is around 1-2 μm (limited by e.g. dust particles) as reflected by the spatial resolution of our measurements.

7.4.2. MEASUREMENT SETUP

The optical setup used for all the measurements was a home-built confocal microscope. A 532 nm laser was used for optical excitation of the NV centers, focused to a diffraction limited spot by a 100X, NA=0.95 objective. The NV luminescence was collected by the same objective, separated from the excitation light by a dichroic mirror and long-pass filter (633 nm cutoff), spatially filtered by a multi-mode optical fiber with a 50 μm diameter core and detected using a Si-PIN photodiode. The laser beam was scanned by a dual-axis galvanometer mirror. The microwave field was generated by a wire located ~100 μm above the diamond.

7.4.3. NV MAGNETOMETRY

The NV spins are initialized and read out using non-resonant optical excitation at 532 nm. A microwave magnetic field drives ESR transitions between the NV spin states ($m_s = |0\rangle$ and $m_s = |\pm 1\rangle$). The NV spin state is read out by applying a laser pulse and measuring the spin-dependent photoluminescence that results from spin-selective non-radiative decay via a metastable singlet state. The ESR frequencies of the NV families in a magnetic field $\mathbf{B}$ are determined by the NV spin Hamiltonian $H = DS_z^2 + \gamma \mathbf{B} \cdot \mathbf{S}$ where γ is the electron gyromagnetic ratio, D the zero-field splitting (2.87 GHz) and $S_{(i=x,y,z)}$ the Pauli spin matrices for spin 1[33]. We apply the bias magnetic field $\mathbf{B_0}$ using a small permanent magnet (diameter 1 cm, height 2 cm).

All magnetic images in Figs. 2-3 are composed of 100×100 pixels (pixel size 0.5 μm). Both the $|0\rangle \leftrightarrow |-1\rangle$ and the $|0\rangle \leftrightarrow |+1\rangle$ ESR transitions are measured at each pixel, from which we extract the field components parallel (B_{NV}) and orthogonal to the NV axis, using a feedback algorithm[20]: At the first pixel we measure a full ESR spectrum (Fig. 7.1d, top panel), which we fit with a Lorentzian curve to extract its amplitude, width and ESR frequency ν_{ESR}. This ESR frequency is then used as an estimate ($\bar{\nu}$) for the ESR frequency at the next pixel. At this pixel, we measure the photoluminescence (PL) at two frequencies ($\nu_\pm$) symmetric around the estimated value $\bar{\nu}$. We then calculate the error signal $D(\bar{\nu}) = PL(\nu_+) - PL(\nu_-)$. The difference between the estimated value $\bar{\nu}$ and the real ESR frequency is, to first order, proportional to this error signal. This allows us to calculate ν_{ESR}, which we then use to change the two measurements frequencies ν_+ and ν_- when repeating the procedure on the following pixel.

7.5. SUPPLEMENTARY MATERIAL

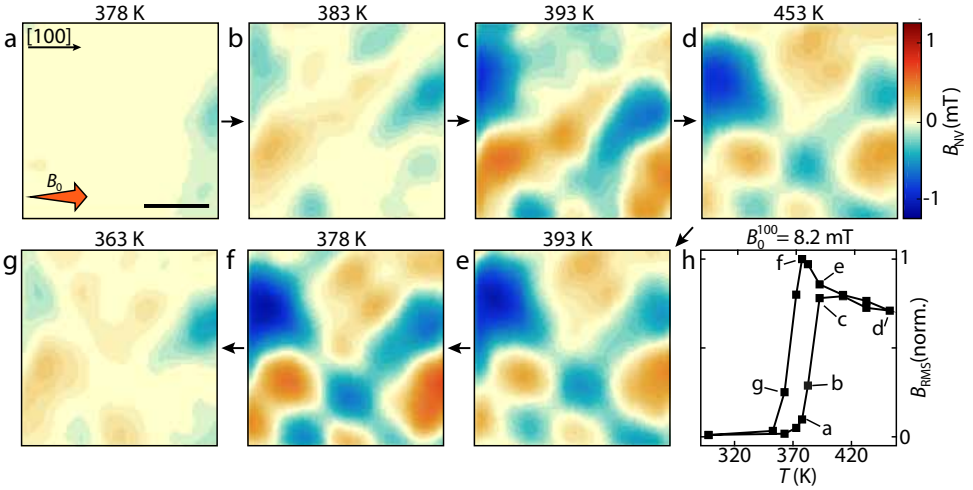

Figure 7.5: Imaging the meta-magnetic phase transition (MMPT) of FeRh with NV magnetometry with in-plane component of the bias field parallel to an easy axis. (**a**-**g**) Magnetic-field maps measured across the MMPT after subtraction of the bias field, in the heating (a - d) and cooling (d - g) branches of the experiment. The in-plane component of the bias field is parallel to the [100] FeRh direction. Scale bar, 10 μm. B_0 = 8.2 mT. (**h**) Temperature evolution of the normalized root-mean-squared (RMS) deviation of the measured stray-field maps. This curve is the same as the blue line in Fig. 7.2h of the main text, where the temperature dependence of the spatial variations of the stray field is explained.

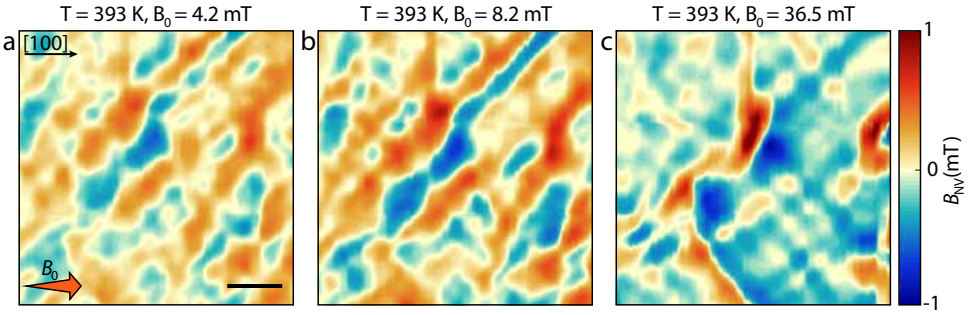

Figure 7.6: Effect of a magnetic field along the easy axis. (**a**-**c**) Magnetic field maps with the in-plane component of the bias field along the easy axis ([100] FeRh direction) for T = 393 K. Increasing the bias field does not produce a visible reorientation of domain walls. In (c), some features are more pronounced, but the shape of the domains is qualitatively similar. Scale bar, 20 μm.

REFERENCES

[1] L. Rondin, J. P. Tetienne, T. Hingant, J. F. Roch, P. Maletinsky, and V. Jacques, *Magnetometry with nitrogen-vacancy defects in diamond,* Reports on Progress in Physics **77**, 056503 (2014).

[2] F. Casola, T. van der Sar, and A. Yacoby, *Probing condensed matter physics with magnetometry based on nitrogen-vacancy centres in diamond,* Nature Reviews Materials **3**, 17088 (2018).

[3] R. Schirhagl, K. Chang, M. Loretz, and C. L. Degen, *Nitrogen-Vacancy Centers in Diamond: Nanoscale Sensors for Physics and Biology,* Annual Review of Physical Chemistry **65**, 83 (2014).

[4] M. H. Abobeih, J. Randall, C. E. Bradley, H. P. Bartling, M. A. Bakker, M. J. Degen, M. Markham, D. J. Twitchen, and T. H. Taminiau, *Atomic-scale imaging of a 27-nuclear-spin cluster using a quantum sensor,* Nature **576**, 411 (2019).

[5] J. F. Barry, J. M. Schloss, E. Bauch, M. J. Turner, C. A. Hart, L. M. Pham, and R. L. Walsworth, *Sensitivity optimization for NV-diamond magnetometry,* Reviews of Modern Physics **92**, 015004 (2020).

[6] G. Q. Liu, X. Feng, N. Wang, Q. Li, and R. B. Liu, *Coherent quantum control of nitrogen-vacancy center spins near 1000 kelvin,* Nature Communications **10**, 1344 (2019).

[7] P. Reith, X. Renshaw Wang, and H. Hilgenkamp, *Analysing magnetism using scanning SQUID microscopy,* Review of Scientific Instruments **88**, 123706 (2017).

[8] L. H. Lewis, C. H. Marrows, and S. Langridge, *Coupled magnetic, structural, and electronic phase transitions in FeRh,* Journal of Physics D: Applied Physics **49**, 323002 (2016).

[9] H. Kumar, D. R. Cornejo, S. L. Morelhao, S. Kycia, I. M. Montellano, N. R. Álvarez, G. Alejandro, and A. Butera, *Strain effects on the magnetic order of epitaxial FeRh thin films,* Journal of Applied Physics **124**, 085306 (2018).

[10] S. Maat, J. U. Thiele, and E. E. Fullerton, *Temperature and field hysteresis of the antiferromagnetic-to-ferromagnetic phase transition in epitaxial FeRh films,* Physical Review B **72**, 214432 (2005).

[11] M. Jiang, X. Z. Chen, X. J. Zhou, B. Cui, Y. N. Yan, H. Q. Wu, F. Pan, and C. Song, *Electrochemical control of the phase transition of ultrathin FeRh films,* Applied Physics Letters **108**, 202404 (2016).

[12] J. S. Kouvel and C. C. Hartelius, *Anomalous magnetic moments and transformations in the ordered alloy FeRh,* Journal of Applied Physics **33**, 1343 (1962).

[13] I. Gray, G. M. Stiehl, J. T. Heron, A. B. Mei, D. G. Schlom, R. Ramesh, D. C. Ralph, and G. D. Fuchs, *Imaging uncompensated moments and exchange-biased emergent ferromagnetism in FeRh thin films,* Physical Review Materials **3**, 124407 (2019).

[14] X. Marti, I. Fina, C. Frontera, J. Liu, P. Wadley, Q. He, R. J. Paull, J. D. Clarkson, J. Kudrnovský, I. Turek, J. Kuneš, D. Yi, J. H. Chu, C. T. Nelson, L. You, E. Arenholz, S. Salahuddin, J. Fontcuberta, T. Jungwirth, and R. Ramesh, *Room-temperature antiferromagnetic memory resistor,* Nature Materials **13**, 367 (2014).

[15] J. U. Thiele, S. Maat, and E. E. Fullerton, *FeRH/FePt exchange spring films for thermally assisted magnetic recording media,* Applied Physics Letters **82**, 2859 (2003).

[16] R. O. Cherifi, V. Ivanovskaya, L. C. Phillips, A. Zobelli, I. C. Infante, E. Jacquet, V. Garcia, S. Fusil, P. R. Briddon, N. Guiblin, A. Mougin, A. A. Ünal, F. Kronast, S. Valencia, B. Dkhil, A. Barthélémy, and M. Bibes, *Electric-field control of magnetic order above room temperature,* Nature Materials **13**, 345 (2014).

[17] V. Uhlíř, J. A. Arregi, and E. E. Fullerton, *Colossal magnetic phase transition asymmetry in mesoscale FeRh stripes,* Nature Communications **7**, 20018 (2016).

[18] R. Medapalli, G. Li, S. K. Patel, R. V. Mikhaylovskiy, T. Rasing, A. V. Kimel, and E. E. Fullerton, *Femtosecond photocurrents at the FeRh/Pt interface,* Applied Physics Letters **117**, 142406 (2020).

[19] C. Baldasseroni, C. Bordel, A. X. Gray, A. M. Kaiser, F. Kronast, J. Herrero-Albillos, C. M. Schneider, C. S. Fadley, and F. Hellman, *Temperature-driven nucleation of ferromagnetic domains in FeRh thin films,* Applied Physics Letters **100**, 262401 (2012).

[20] R. S. Schoenfeld and W. Harneit, *Real time magnetic field sensing and imaging using a single spin in diamond,* Physical Review Letters **106**, 030802 (2011).

[21] G. Zheng, S. H. Ke, M. Miao, J. Kim, R. Ramesh, and N. Kioussis, *Epitaxial strain controlled magnetocrystalline anisotropy in ultrathin FeRh/MgO bilayers,* AIP Advances **7**, 055914 (2017).

[22] C. Bordel, J. Juraszek, D. W. Cooke, C. Baldasseroni, S. Mankovsky, J. Minár, H. Ebert, S. Moyerman, E. E. Fullerton, and F. Hellman, *Fe spin reorientation across the metamagnetic transition in strained FeRh thin films,* Physical Review Letters **109**, 117201 (2012).

[23] E. Mancini, F. Pressacco, M. Haertinger, E. E. Fullerton, T. Suzuki, G. Woltersdorf, and C. H. Back, *Magnetic phase transition in iron-rhodium thin films probed by ferromagnetic resonance,* Journal of Physics D: Applied Physics **46**, 245302 (2013).

[24] X. Zhou, F. Matthes, D. E. Bürgler, and C. M. Schneider, *Magnetic surface domain imaging of uncapped epitaxial FeRh(001) thin films across the temperature-induced metamagnetic transition,* AIP Advances **6**, 015211 (2016).

[25] T. P. Almeida, R. Temple, J. Massey, K. Fallon, D. McGrouther, T. Moore, C. H. Marrows, and S. McVitie, *Quantitative TEM imaging of the magnetostructural and phase transitions in FeRh thin film systems,* Scientific Reports **7**, 17835 (2017).

[26] I. Bertelli, J. J. Carmiggelt, T. Yu, B. G. Simon, C. C. Pothoven, G. E. Bauer, Y. M. Blanter, J. Aarts, and T. van der Sar, *Magnetic resonance imaging of spin-wave transport and interference in a magnetic insulator,* Science advances **6**, eabd3556 (2020).

[27] C. S. Wolfe, V. P. Bhallamudi, H. L. Wang, C. H. Du, S. Manuilov, R. M. Teeling-Smith, a. J. Berger, R. Adur, F. Y. Yang, and P. C. Hammel, *Off-resonant manipulation of spins in diamond via precessing magnetization of a proximal ferromagnet,* Physical Review B **89**, 180406 (2014).

[28] E. Lee-Wong, R. Xue, F. Ye, A. Kreisel, T. Van Der Sar, A. Yacoby, and C. R. Du, *Nanoscale detection of magnon excitations with variable wavevectors through a quantum spin sensor,* Nano Letters **20**, 3284 (2020).

[29] L. Thiel, Z. Wang, M. A. Tschudin, D. Rohner, I. Gutiérrez-Lezama, N. Ubrig, M. Gibertini, E. Giannini, A. F. Morpurgo, and P. Maletinsky, *Probing magnetism in 2D materials at the nanoscale with single-spin microscopy,* Science **364**, 973 (2019).

[30] T. H. Han, J. S. Helton, S. Chu, D. G. Nocera, J. A. Rodriguez-Rivera, C. Broholm, and Y. S. Lee, *Fractionalized excitations in the spin-liquid state of a kagome-lattice antiferromagnet,* Nature **492**, 406 (2012).

[31] R. Harris, Y. Sato, A. J. Berkley, M. Reis, F. Altomare, M. H. Amin, K. Boothby, P. Bunyk, C. Deng, C. Enderud, S. Huang, E. Hoskinson, M. W. Johnson, E. Ladizinsky, N. Ladizinsky, T. Lanting, R. Li, T. Medina, R. Molavi, R. Neufeld, T. Oh, I. Pavlov, I. Perminov, G. Poulin-Lamarre, C. Rich, A. Smirnov, L. Swenson, N. Tsai, M. Volkmann, J. Whittaker, and J. Yao, *Phase transitions in a programmable quantum spin glass simulator,* Science **361**, 162 (2018).

[32] B. Huang, G. Clark, E. Navarro-Moratalla, D. R. Klein, R. Cheng, K. L. Seyler, D. Zhong, E. Schmidgall, M. A. McGuire, D. H. Cobden, W. Yao, D. Xiao, P. Jarillo-Herrero, and X. Xu, *Layer-dependent ferromagnetism in a van der Waals crystal down to the monolayer limit,* Nature **546**, 270 (2017).

[33] T. van der Sar, F. Casola, R. Walsworth, and A. Yacoby, *Nanometre-scale probing of spin waves using single-electron spins.* Nature communications **6**, 7886 (2015).

8

CONCLUSION

This chapter summarizes the most important results obtained throughout this thesis, and indicates possible future research directions.

8.1. CONCLUSION

The majority of this thesis is devoted to the investigation of spin waves and their properties. In Chapter 4 we established a new technique to image coherent spin waves using nitrogen-vacancy centers in diamond. We showed that such technique can be used to extract quantitative information - such as the spin-wave amplitude - and to measure the spin-wave velocity in real space. Our results suggest that the sensitivity of the technique should allow the detection of spin waves in monolayer magnets, such as Van der Waals materials.

In Chapter 5 we used such technique to study the spin-wave damping caused by metallic electrodes. We modelled the damping as being induced by eddy currents in the metal, which dissipate energy, obtaining a good match with the experimental results. We showed that the capability of our technique for imaging spin waves underneath optically opaque material (such as metals) makes it possible to characterize the quality of a buried interface.

In Chapter 6 we characterized the magnetic noise caused by thermally excited spin waves using NV relaxometry. We found a good agreement with a model based on the chiral coupling between the spin-wave fields and the NV spin, but we detected discrepancies at the ferromagnetic resonance (FMR) frequency, ascribed to local variations of the static field.

In Chapter 7 we studied a metamagnetic phase transition, showing that the use of statistical methods can enable the characterization of the global properties of a system, even using a local technique such as NV magnetometry.

Unlike the most common spin-wave imaging techniques, NV magnetometry detects spin waves via their stray magnetic field. While this could introduce uncertainty (reconstructing a magnetization pattern from the magnetic field is an underdefined problem), it also opens up several research directions. Additionally, some constrains on our technique can be addressed and made less severe. In the next section we will describe both aspects.

8.2. OUTLOOK

This thesis focused on establishing a new technique to image spin waves and using it to characterize various aspects of spin-wave propagation, rather than maximizing the spatial resolution or the magnetic field sensitivity. Future research can therefore improve on our results by implementing NV-based imaging of spin waves in a scanning geometry, i.e. embedding a single NV center into a pillar at the apex of a diamond AFM cantilever. The achievable NV-magnet distance should be of a few tens of nanometers, resulting in a spatial resolution on a similar scale, and an enhancement in magnetic field sensitivity of several orders of magnitude, since the spin-wave stray magnetic fields typically decay exponentially with the ratio of the distance over the wavelength. Additionally, the sensitivity could be increased by using NV ensembles in a wide-field setup, in which an image can be recorded at once, such that measurement time can be devoted to reducing noise

rather than scanning the laser spot on the diamond.

These advancements will enable several new research directions. The improved spatial resolution will allow to study spin waves with much shorter wavelength (i.e. tens of nanometers). These waves are more interesting for technological purposes, but also harder to excite inductively. New excitation strategies, effective at the nanoscale, could be designed and tested.

Investigating magnetic van der Waals materials (i.e. CrI_3 and $Cr_2Ge_2Te_6$) could provide information regarding spin waves in truly two-dimensional systems, which might be different (e.g. a different dispersion) from conventional ones. Even though it seems already possible to detect spin waves in such monolayer magnets (from the estimated sensitivity of our approach), an improved sensitivity would be beneficial to this end.

Additionally, detecting spin waves via their stray magnetic fields enables several research directions because it grants the possibility of imaging underneath non-magnetic material. Opportunities that appear within reach include studying the interactions of spin waves with electrical currents, with superconductors, and with van der Waals materials. In the first case, depositing a platinum electrode on YIG enables injecting spin waves via the spin-Hall effect. Imaging underneath the contacts could shed new light on the physical processes at play, including spin-wave damping via the inverse spin-Hall effect. Interesting phenomena stemming from the interactions of superconductors and spin waves could include the motion of superconducting vortices coupled to spin waves and the partial screening of the spin-wave fields by AC currents in the superconductor. Depositing a van der Waals material on another magnet (e.g. YIG) could lead to a coupling between the valley pseudo-spin and (coherent) spin waves propagating in YIG.

One constraint of our technique is the need for the resonance between the frequency of the NV electron spin resonance (ESR) and that of the spin waves. One possible future research direction involves trying to address this challenge, relaxing the constraint. One possibility is to rely on non-linear processes, such as four-magnon scattering, to reveal the presence of high-frequency modes (non resonant with the ESR): two spin waves of frequency above the ESR can simultaneously scatter to the ESR and to a higher frequency, if both modes are allowed in the magnet, and if the scattering event conserves frequency and momentum. When the high-frequency mode is populated to a higher degree, the scattering rate increases (similar to a stimulated emission process) and the contrast of the ESR increases as a consequence. A large population of the high-frequency mode could be the result of coupling the magnet with a different system - e.g. a magnet of unknown saturation magnetization where the ferromagnetic resonance (FMR) is driven - resulting in a signature at the ESR. This phenomenon could be used to detect any signals of frequency above the ESR, provided that it couples to existing modes in the magnet in which the non-linear scattering is taking place. Besides the extended capabilities of NV magnetometry, understanding non-linear scattering processes of spin waves is interesting *per se*. We could start by studying this process in YIG, i.e. characterizing the frequency range (and its power-dependence) and if higher-order processes are allowed

as well.

While it is interesting to improve the technique we developed, trying to compete with other spin-wave imaging techniques is not necessary. For example, performing time-resolved measurement is best left to techniques such as Brilouin light scattering (BLS) and magneto-optical Kerr effect (MOKE) microscopy, which can work with pump-probe schemes and reach femtosecond time resolution. Rather, NV-based imaging of spin waves should focus on the tasks that are virtually impossible to achieve with other techniques, such as studying phenomena at buried interfaces, characterizing the interaction of spin waves with other excitations that generate a magnetic stray field (i.e. currents, superconducting vortices), and exploiting the high sensitivity to probe monolayer van der Waals magnets.

SUMMARY

The elementary excitations of magnets are called *spin waves*, and their corresponding quasi-particles are known as *magnons*. The rapidly growing field of *Magnonics* aims at using them as information carriers in a new generation of electronic devices, (almost) free of electric currents. Encoding information in the amplitude and/or phase of these coherent waves could lead to a drastic decrease in dissipated power, typically related to the motion of electrons ("Joule" or "Ohmic" heating).

This dissertation describes the development and use of a new technique to study spin waves. This technique uses the electronic spins associated with nitrogen-vacancy (NV) centers as magnetic field sensors. An NV center is a light-emitting defect in the crystal lattice of diamond. Remarkably, the brightness of its emission depends on its spin state, sensitive to magnetic fields. This way, magnetic information can be investigated optically.

The aforementioned field of *magnonics* is described in Chapter 1, where we discuss its large potential for technological innovation, that in turn leads to several research directions and the development of magnetic imaging techniques. In Chapter 2 we present the structural, electronic and optical properties of NV centers and introduce the NV-based experimental techniques that are used throughout this thesis to sense static and oscillating magnetic fields.

In Chapter 3, we present a theoretical treatment of spin waves that encompasses deriving their dispersion from the equations of magnetization dynamics (Landau-Lifshitz-Gilbert equation). We then show the equations that govern the inductive excitation of spin waves (relevant to chapter 4-5), and the stray magnetic fields they generate, stepping stone for understanding the NV-based measurements of spin waves.

In Chapter 4 we establish a technique for imaging coherent spin waves via their magnetic stray field with phase sensitivity. This relies on the interference between the spin-wave field and the homogeneous field of an additional antenna, which are of the same frequency and phase-locked, such that their interference is stationary. This way, we can image the amplitude of spin waves resonant with the NV spin. Having knowledge of the auxiliary field allows to reconstruct the spin-wave field, such that in model configurations we can measure the spin-wave amplitude quantitatively.

Using the developed technique and its "see-through" capability, in Chapter 5 we image spin waves propagating underneath metallic electrodes and quantify the additional damping these cause. This phenomenon is relevant for devices in which spin-wave excitation, control and detection are achieved via metallic gates. We reveal a 100-fold in-

crease in spin-wave damping and show that this matches the effective damping calculated by including the eddy currents field into the LLG equations self-consistently.

In Chapter 6 we focus on thermally-excited spin waves and characterize the spectrum of the magnetic noise they generate via NV relaxometry - which involves preparing the NV spin in a determined state and measuring its decoherence over time. Such noise is related to the excitations of the system via the fluctuation-dissipation theorem. The results are well matched by a theoretical model based on the chiral coupling between spin-wave fields and NV spin. However, we find surprising discrepancies at the ferromagnetic resonance frequency, which suggest the presence of inhomogeneities in the system.

NV centers are excellent local probes of magnetic fields. One challenge related to the *locality* of the results is how to effectively quantify properties that are inherently *global*, such as the temperature of a phase transition. In Chapter 7 we show that a possible answer to this challenge is provided by the use of statistical analyses to quantify spatial correlations. We employ these methods to study the temperature-driven metamagnetic (i.e. from antiferromagnetic to ferromagnetic) phase transition of the metallic alloy FeRh. We image the nucleation, growth, and coalescence of magnetic domains, and find evidence that suggests the presence of a domain reorientation across the phase transition.

SAMENVATTING

De elementaire excitaties van magneten zijn spingolven en hun bijbehorende quasideeltjes heten *magnonen*. Het snelgroeiende veld van de *magnonica* poogt deze te gebruiken als informatiedrager in een nieuwe generatie elektronica, (bijna) gevrijwaard van elektrische stromen. Het coderen van informatie in de amplitude en/of fase van deze coherente golven zou kunnen leiden tot een drastische afname in gedissipeerd vermogen, wat typisch wordt veroorzaakt door de beweging van elektronen (het "joule-effect").

Dit proefschrift beschrijft zowel de ontwikkeling als het gebruik van een nieuwe techniek om spingolven te bestuderen. Deze techniek gebruikt de elektronenspins van stikstof-gat (NV) centra als magneetveldsensoren. Een NV centrum is een luminescerend defect in het kristalrooster van diamant. De helderheid van de emissie hangt af van de toestand van de spin, die gevoelig is voor magneetvelden. Op deze wijze kunnen magnetische eigenschappen met optische technieken bestudeerd worden.

Het hiervoor genoemde veld van de *magnonica* wordt beschreven in Hoofdstuk 1, waar we de grote potentie voor technologische innovatie bespreken, die leidt tot verschillende onderzoeksrichtingen en de ontwikkeling van magnetische beeldvormingstechnieken. In Hoofdstuk 2 zetten we de structurele, elektronische en optische eigenschappen van NV centra uiteen en worden de op NV centra gebaseerde experimentele technieken geïntroduceerd, die in dit proefschrift worden gebruikt om statische en oscillerende magnetische velden te detecteren.

In Hoofdstuk 3 presenteren we een theoretische beschrijving van spingolven, waar hun dispersierelatie wordt afgeleid uit de vergelijkingen van magnetisatiedynamica (de Landau-Lifshitz-Gilbert vergelijking). Vervolgens laten we vergelijkingen zien die de inductieve excitatie van spingolven beschrijven (relevant voor Hoofdstuk 4-5) en de demagnetiserende velden die zij genereren, wat een opstap vormt naar de op stikstof-gat centra gebaseerde detectie van spingolven.

In Hoofdstuk 4 presenteren we een techniek voor fasegevoelige beeldvorming van coherente spingolven via hun magnetisch demagnetisatieveld. Deze techniek maakt gebruik van de interferentie tussen het spingolf-veld en het homogene magneetveld van een nabije microgolfantenne, die dezelfde frequentie en een vaste faserelatie hebben, waardoor hun interferentie stationair is. Op deze wijze kunnen we de amplitude van spingolven, die resonant zijn met de NV spin, in kaart brengen. Met kennis van het homogene veld kan het spingolfveld gereconstrueerd worden, waardoor in modelleerbare geometrieën de amplitude van het spingolfveld zelfs kwantitatief gemeten kan worden.

De ontwikkelde techniek biedt de mogelijkheid om door materialen heen te kijken, een "doorzichtigeëigenschap die we in Hoofdstuk 5 inzetten om spingolven in beeld te brengen die zich voortplanten onder dunne metallische elektroden, waarbij we kwantitatief hun dempende werking karakteriseren. Deze techniek is relevant voor structuren waarin excitatie, controle en detectie van spingolven via metallische contacten bereikt wordt. We ontdekken een 100-voudige toename in spingolfdemping en laten zien dat dit overeenstemt met een effectieve demping die berekend wordt door wervelstromen in de LLG-vergelijking te implementeren op zelf-consistente wijze.

In Hoofdstuk 6 focussen we op thermisch geëxciteerde spingolven en karakteriseren we het magnetische ruisspectrum dat zij genereren via *relaxometry* – het initiëren van de spin in een deterministische staat, om vervolgens zijn decoherentie in de tijd te meten. Zulke ruis is gerelateerd aan de excitaties van het systeem via het fluctuatie-dissipatietheorema. De resultaten komen goed overeen met een theoretisch model gebaseerd op een chirale koppeling tussen de spingolven en de NV spin. Echter, wij observeren verrassende afwijkingen bij de ferromagnetische resonantiefrequentie, die op de aanwezigheid van inhomogeniteiten in het systeem duiden.

Stikstof-gat centra zijn uitstekende sensoren voor plaatselijke magneetvelden. Een uitdaging die met deze *plaatsgebondenheid* meekomt is het effectief detecteren van *globale* eigenschappen, zoals de temperatuur van een faseovergang. In Hoofdstuk 7 laten we zien dat een mogelijk antwoord op deze uitdaging gevormd wordt door statistische analyse om ruimtelijke correlaties te kwantificeren. We passen een dergelijke methode toe om de temperatuur-gedreven metamagnetische (i.e. van antiferromagnetisch naar ferromagnetisch) faseovergang van de metallische legering FeRh. We brengen de nucleatie, groei en samensmelting van magnetische domeinen in beeld en vinden bewijs voor de aanwezigheid van een heroriëntatie van domeinen door de faseovergang.

SOMMARIO

Le eccitazioni elementari dei materiali magnetici sono chiamate onde di spin (*spin waves*), e le corrispondenti quasiparticelle prendono il nome di *magnoni*. Il campo di studi della *Magnonica*, in rapida crescita, ha come obiettivo l'uso delle onde di spin per il trasporto ed elaborazione di informazione in una nuova generazione di dispositivi elettronici, (quasi) privi di correnti elettriche. La codifica dell'informazione nell'ampiezza e/o nella fase di queste onde coerenti potrebbe portare ad un decremento drastico dell'energia dissipata, solitamente collegata al movimento di elettroni (riscaldamento "Ohmico" o "Joule").

Questa tesi tratta lo sviluppo e l'uso di una nuova tecnica per studiare le onde di spin. Alla base di tale tecnica vi è l'utilizzo dello spin elettronico associato ai cosidetti "centri di colore" azoto-vacanza (nitrogen-vacancy, NV) come sensori di campo magnetico. Un centro NV è un difetto nel reticolo cristallino del diamante che emette luce. La luminosità dell'emissione dipende dallo stato del suo spin elettronico, rendendo possibile studiare proprietà magnetiche con mezzi ottici.

Il campo della magnonica viene descritto nel Capitolo 1, in cui si discute il vasto potenziale per l'innovazione tecnologica, che a sua volta conduce a diverse direzioni di ricerca e allo sviluppo di tecniche di *imaging*. Nel Capitolo 2 vengono trattate le proprietà strutturali, ottiche ed elettroniche dei centri NV, ed introdotte le tecniche sperimentali utilizzate in questa tesi per misurare campi magnetici statici o oscillanti.

Nel Capitolo 3 viene presentato un trattamento teorico delle onde di spin, che comprende la derivazione della loro dispersione a partire dalle equazioni della dinamica della magnetizzazione (equazioni di Landau-Lifshitz-Gilbert). Successivamente vengono introdotte le equazioni che governano l'eccitazione induttiva delle onde di spin (rilevante per i capitoli 4-5), e vengono discussi i campi magnetici da esse generati, punto di partenza per capire gli esperimenti sulle onde di spin basati sui centri NV.

Nel Capitolo 4 viene presentate una nuova tecnica di osservazione di onde di spin coerenti, tramite il loro campo magnetico, con sensibilità di fase. Questa tecnica si basa sull'interferenza tra il campo magnetico delle onde di spin ed il campo omogeneo di una antenna esterna, aventi la stessa frequenza e con differenza di fase costante, così che la loro interferenza è stazionaria. In questo modo possiamo osservare l'ampiezza delle onde di spin risonanti con lo spin dei centri NV. La conoscenza del campo ausiliario permette di ricostruire il campo magnetico dell'onda di spin così che, in configurazioni modello, possiamo misurare l'ampiezza dell'onda di spin in modo quantitativo.

Usando la tecnica sviluppata e la sua capacità di osservare attraverso materiali, nel Capitolo 5 viene descritta l'osservazione di onde di spin che si propagano al di sotto di elettrodi metallici, e viene quantificato l'aumento di smorzamento da essi causato. Questo fenomeno è rilevante in dispositivi in cui l'eccitazione, controllo e rilevamento delle onde di spin è realizzato attraverso *gate* metallici. Si rileva un aumento dello smorzamento delle onde di spin di un fattore 100, e mostriamo che questo è in linea con lo smorzamento effettivo calcolato includendo il campo magnetico delle correnti parassite all'interno delle equazioni LLG in modo autoconsistente.

Nel Capitolo 6 ci focalizziamo su onde di spin eccitate in modo termico, e caratterizziamo lo spettro delle fluttuazioni magnetiche che generano utilizzando la rilassometria NV - che comporta la preparazione dello spin del centro NV in un predeterminato stato e la misura della sua decoerenza nel tempo. Tali fluttuazioni sono collegate alle eccitazioni del sistema attraverso il teorema di fluttuazione-dissipazione. I risultati sono in accordo con un modello teorico basato sull'accoppiamento chirale tra i campi magnetici delle onde di spin e lo spin del centro NV. Tuttavia, riscontriamo incongruenze sorprendenti alla frequenza della risonanza ferromagnetica, che suggeriscono la presenza di disomogeneità nel sistema.

I centri NV sono eccellenti sensori locali di campi magnetici. Una sfida relativa alla *località* dei risultati è come quantificare efficacemente proprietà che sono intrinsecamente *globali*, come ad esempio la temperatura di una transizione di fase. Nel Capitolo 7 mostriamo che una possibile soluzione a questo problema è fornita dall'uso di analisi statistiche per quantificare le correlazioni spaziali. Utilizziamo questi metodi per studiare la transizione metamagnetica (da antiferromagnete a ferromagnete) di fase, guidata dalla temperatura, della lega magnetica FeRh. Osserviamo la nucleazione, crescita e coalescenza di domini magnetici, e troviamo evidenze sperimentali che indicano le presenza di un riorientamento dei domini magnetici durante la transizione di fase.

ACKNOWLEDGEMENTS

As I reflect about the last four years, I can't help but feeling grateful for the opportunities I had and, even more, for the people I met on my path, that contributed to this 4-year trip both from the scientific and the personal point of view.

The first and foremost *thank you* goes to Dr. van der Sar. Toeno, you hired me, helped me build up the lab when the group consisted only of us two, and gave me independence. You often had more confidence in me than I did, provided guidance, paying attention to all the small details, and taught me what it means to be a scientist. I appreciate all the discussions we had when we went into the tiniest details, and I am constantly blown away by your efficiency. I feel lucky and privileged to have been your first PhD student.

Jan, thank you for being my promotor. Even though the initially planned experiments never took place, such that our interactions were limited, I always appreciated and enjoyed your omnipresent good spirit, fascination and excitement about science (and anything remotely scientific), and kindness. This combination of qualities is not nearly as common as it should be.

Yaroslav, Gerrit, Tao, Avinash, I am grateful to have found theorists with such a flair for experiments. Trying to understand your derivations always provided me with new insights. Your work beautifully complements the spin-wave experiments of the Sar Lab. Last but not least, it is always an unexpected pleasure when each co-author responds within two days, removing a good deal of stress and frustration from the publishing process.

My PhD started as the only member of an empty lab at the end of a dark corridor in the basement, and was hit halfway by a pandemic. Despite this, I met a great number of talented, fun, like-minded people that really like science, but like having fun and socializing just as much - and often more. I truly enjoyed every single time we went to the TeePee café, every dinner, every party, every conference and spring/winter school. It is thanks to you (and that amazing espresso machine) that I enjoyed my PhD as much as I did. The gratitude I feel toward my colleagues - many of whom are now really more friends than anything - can't fit in two pages. I just want to mention here a few people that contributed to my PhD by providing a social environment in which I could work long hours and not be weighed down. In sparse order, I want to thank Nikos, Holger, Yildiz, Joris, Brecht, Michael, Samer, Yufan, Allard, Edouard, Luigi, Thierry, Jorrit, Rasa, Mattias, Lukas, Laëti, Dima, Adriàn, Sona, Nina, Ranko, Pascal, Dejan, Joeri, Marc, Dirk, Andreas. The people at QN will receive my full non-scientific acknowledgements separately.

During these 4 years, I have supervised several students, which taught me at least as much as I - hopefully - taught them. So, thank you Marten, Coosje, Guillermo, Roland. Helena, thank you for that beautiful piece of code.

Officially, I was part of two groups, the van der Sar Lab in Delft and the Aarts group in Leiden. Despite not spending much time in the latter, I always enjoyed my time there, because of the many stimulating scientific discussions and of the nice people: Kaveh, Remko, Nikita, Aymen, Chunhai, Kumar, Guerino, Junxiang, Marcel, Douwe, Thomas.

Being split in two groups was (usually...) not that hard. However, I can't imagine the bureaucratic hurdles behind the scenes. I want to thank Marijke, Daniëlle and Lizzy for making it as smooth as possible. Additionally, I'd like to thank the people that keep QN and Casimir running: Etty, Maria, Erika, Heleen, Dorine, Marije. Also, I would like to thank the people who work behind the scenes to allow us to do some fun research: Tom, Tino, and the whole Kavli cleanroom staff.

Several people outside academia also deserve a *thank you* for recharging my batteries in the weekends and holidays - without which my scientific efforts would suffer greatly. These include Julia, Maria, Frenci, Ana Victoria. Last, I'm grateful for living my life with Ana, and for the support that my parents, Sara and Andrea, always provided.

CURRICULUM VITÆ

Iacopo BERTELLI

11-06-1992 Born in Modena, Italy.

EDUCATION

2006-2011 High School
Liceo Scientifico Wiligelmo, Modena, Italy

2011-2014 B.Sc. in Physics
Università di Modena e Reggio Emilia, Modena, Italy

2014-2017 M.Sc. in Physics (*cum Laude*)
Università di Modena e Reggio Emilia, Modena, Italy
Thesis: Magnetic analysis of the subsurface region of ball bearing inner rings subject to rolling contact fatigue
Supervisor: Prof. dr. S. D'Addato
Supervisor: Prof. dr. A. Kirilyuk (Radboud University)

2015-2016 Erasmus Exchange Program
Radboud University, Nijmegen

2017-2021 Ph.D. in Physics
University of Leiden
Thesis: Magnetic imaging of spin waves and magnetic phase transitions with nitrogen-vacancy centers in diamond
Promotor: Prof. dr. J. Aarts
Co-Promotor: Dr. T. van der Sar

LIST OF PUBLICATIONS

* indicates equal contribution

7. B. G. Simon, S. Kurdi, H. La, **I. Bertelli**, J. J. Carmiggelt, M. T. Ruf, N. de Jong, H. van den Berg, A. Katan, T. van der Sar, *Directional Excitation of a High-Density Magnon Gas Using Coherently Driven Spin Waves*, Nano Letters **21**, 8213 (2021).

6. **I. Bertelli**, B. G. Simon, T. Yu, J. Aarts, G. E. W. Bauer, Y. M. Blanter, T. van der Sar, *Imaging spin-wave damping underneath metals using electron spins in diamond*, Advanced Quantum Technologies 2100094 (2021).

5. G. Nava Antonio*, **I. Bertelli***, B. G. Simon, R. Medapalli, D. Afanasiev, T. van der Sar, *Magnetic imaging and statistical analysis of the metamagnetic phase transition of FeRh with electron spins in diamond*, Journal of Applied Physics **129**, 223904 (2021).

4. J. J. Carmiggelt, B. G. Simon, **I. Bertelli**, T. van der Sar, *Spinsensoren in diamant onthullen golvende spinzee*, Nederlands Tijdschrift voor Natuurkunde, June (2021).

3. A. Rustagi, **I. Bertelli**, T. van der Sar, P. Upadhyaya, *Sensing chiral magnetic noise via quantum impurity relaxometry*, Physical Review B **102**, 220403 (2020).

2. **I. Bertelli**, J. J. Carmiggelt, T. Yu, B. G. Simon, C. C. Pothoven, G. E. W. Bauer, Y. M. Blanter, J. Aarts, T. van der Sar, *Magnetic resonance imaging of spin-wave transport and interference in a magnetic insulator*, Science Advances **6**, eabd3556 (2020).

1. Y. Kadin, **I. Bertelli**, A. Kirilyuk, *Magnetooptical Analysis of the Subsurface Region in a Bearing Ring Subjected to Rolling Contact Fatigue*, Tribology Transactions **61**, 4 (2018).